

# **Are Auxetics Better for Protection?**

On the Behaviour of Architected Metamaterials  
under High-Rate Loading Conditions



# **Are Auxetics Better for Protection?**

**On the Behaviour of Architected Metamaterials  
under High-Rate Loading Conditions**

## **Dissertation**

for the purpose of obtaining the degree of doctor  
at Delft University of Technology  
by the authority of the Rector Magnificus, prof.dr.ir. T.H.J.J. van der Hagen,  
chair of the Board for Doctorates  
to be defended publicly on  
Monday, November 3rd 2025 at 10:00 o'clock

by

**Til GÄRTNER**

Master of Science in Mechanical and Process Engineering,  
Technical University of Darmstadt, Germany  
born in Hanau, Germany

This dissertation has been approved by the

Promotor: Prof.dr.ir. L.J. Sluys  
Copromotor: Dr.ir. J. Weerheijm  
External Advisor: Dr.ir. S.J. van den Boom

Composition of the doctoral committee:

Rector Magnificus,	chairperson
Prof.dr.ir. L.J. Sluys,	Delft University of Technology, <i>promotor</i>
Dr.ir. J. Weerheijm,	Delft University of Technology, <i>copromotor</i>
Dr.ir. S.J. van den Boom,	Netherlands Organization for Applied Scientific Research (TNO), <i>external advisor</i>

*Independent members:*

Prof.dr.ir. M. Langelaar,	Delft University of Technology
Prof.dr. A.A. Zadpoor,	Delft University of Technology
Prof.dr. V.S. Deshpande,	University of Cambridge
Prof.dr.rer.nat. O. Weeger,	Technical University of Darmstadt
Dr.ir. F.P. van der Meer,	Delft University of Technology, <i>reserve member</i>



This research was financed by TNO through the  
PhD program of the Dutch Ministry of Defence.

*Keywords:* architected materials; auxetic materials; geometrically exact rods;

transient simulation; impact mitigation

*Printed by:* Ipskamp printing

*Cover by:* Renata Gjerrud

Copyright © 2025 by T. Gärtner

ISBN 978-94-6518-121-9

An electronic copy of this dissertation is available at

DOI [10.4233/uuid:9d0b230e-1008-46a2-a193-b9dd3f8c472f](https://doi.org/10.4233/uuid:9d0b230e-1008-46a2-a193-b9dd3f8c472f)

In Ehrfurcht und Dankbarkeit jenen gegenüber,  
die am 18. Juli 2018 mein Leben bewahrten.

In Schuld und Dankbarkeit denen gegenüber,  
die mir danach halfen, es wiederzuerlangen.



# SUMMARY

‘Auxetics are superior materials for impact mitigation’ is a common motif in scientific literature on the quest for lightweight, impact-resistant materials. This assertion is driven by the promising properties of auxetic materials, i.e. materials with a negative Poisson’s ratio. However, it is rarely subjected to rigorous scrutiny in direct comparison with positive Poisson’s ratio materials. The objective of the present dissertation is to challenge this assertion by investigation and comparison of architected metamaterials under high-rate loading conditions. Given the absence of relevant auxetic materials in nature, the negative Poisson’s ratio of a material is engineered through the careful architecture of its internal structure, leading to the creation of so-called *metamaterials*. In order to investigate these metamaterials under impact conditions, extensive physical set-ups are required while allowing only for global measurements. The present dissertation is thus concerned with the computational modelling of architected materials under high-rate compression.

In order to achieve a more profound comprehension of the processes within a range of different configurations for auxetic metamaterials, a first step is the development of an efficient numerical model based on nonlinear Timoshenko-Ehrenfest beams. The developed model is implemented in a finite element framework. In addition to geometric non-linearities, also nonlinear material behaviour within the beams needs to be accounted for. Here, a scaling strategy for the hardening behaviour of elastoplastic beams is proposed and implemented.

A set of four different auxetic architectures, based on distinct mechanisms, is employed to provide a comprehensive overview of the options for architected materials. These are re-entrant honeycombs, double arrowheads, chiral and anti-chiral architectures. The conventional honeycomb is used as a benchmark for a non-auxetic structure. In order to establish a baseline for the comparison of materials, a range of unit cells from all designs with identical linear elastic properties, such as the Young’s modulus and the density, are designed. Utilizing the developed numerical model, the evolution of the elastic properties throughout the deformation process is examined and correlated to alterations in the loading of the deformed beams. This evolution is linked to the energy absorption capabilities in an elastic environment for varying loading speeds and conditions. The findings of this study demonstrate that higher energy absorption is exhibited only by one of the investigated auxetic metamaterials, when compared to conventional honeycomb structures.

Furthermore, an experimental campaign is conducted with two reduced sets of unit cells, designed and manufactured to show the same mass and stiffness, respectively. During the campaign, the samples were subjected to high velocity impact loading. Particular emphasis is placed on the force transmission between the two sides of the beam structure. The distribution of these forces onto the back

side of the architected material is supplemented by additional numerical studies. In this campaign, auxetic materials have been found to demonstrate no advantage in terms of force transmission and distributions of these forces in comparison with their non-auxetic counterparts.

A final series of investigations is conducted to examine the impact of varying strain rates on the localization of deformation across different architectures. In this investigation, particular emphasis is placed on the patterns in which localized deformation occurs and the subsequent effects on the concentration of energy in the structure. In the tested conditions, auxetic materials demonstrate higher levels of transmitted forces and lower levels of absorbed energy, resulting in worse impact protection capabilities.

Consequently, the present dissertation challenges the prevailing consensus in literature that auxetic materials offer superior impact mitigation capabilities, both in terms of energy absorption and force transmission. The computational results demonstrate the deleterious effect of substantial deformations, as well as the neutralization of the Poisson effect at high compression rates. The results of the experimental campaign further support these findings.

# SAMENVATTING

“Auxetische materialen zijn superieure materialen voor het verminderen van inslag-effecten” is een veel voorkomende claim in de wetenschappelijke literatuur in de zoektocht naar lichte, stootbestendige materialen. Deze bewering is gebaseerd op de gunstige eigenschappen van auxetische materialen, d.w.z. materialen met een negatieve dwarscontractiecoëfficiënt. Een grondige vergelijking met materialen die een positieve dwarscontractiecoëfficiënt hebben, wordt echter zelden gemaakt. Het doel van dit proefschrift is om deze vergelijking van auxetische en niet-auxetische materialen bij hoge belastingssnelheden uit te voeren en zo de juistheid van die bewering te controleren. Aangezien er in de natuur nauwelijks auxetische materialen voorkomen, wordt de negatieve dwarscontractiecoëfficiënt verkregen door een zorgvuldig ontworpen interne structuur, wat leidt tot de creatie van zogenaamde metamaterialen. Het bestuderen van deze metamaterialen onder omstandigheden die voor inslag representatief zijn vereist uitgebreide fysieke proefopstellingen, die echter slechts globale metingen mogelijk maken. Daarom richt dit proefschrift zich op de rekenkundige modellering van geprogrammeerde metamaterialen bij compressie met hoge snelheid.

Om een dieper inzicht te verkrijgen in de vervormingsprocessen in verschillende configuraties van auxetische metamaterialen, is eerst een efficiënt numeriek model ontwikkeld, gebaseerd op niet-lineaire Timoshenko-Ehrenfest-balken. Het ontwikkelde model is geïmplementeerd in een eindige-elementenraamwerk. Naast geometrische niet-lineariteiten moet ook het niet-lineaire materiaalgedrag van de balken worden meegenomen. Hiertoe is een schaalmethodiek van het verstevigingsgedrag van elastoplastische balken ontwikkeld en geïmplementeerd.

Er is gebruik gemaakt van vier verschillende auxetische architecturen, gebaseerd op uiteenlopende mechanismen, om een volledig overzicht te geven van de mogelijkheden van geprogrammeerde metamaterialen. Het gaat hierbij om concave honingraten, dubbele pijlvormen, chirale en antichirale structuren. De conventionele honingraat is als referentie gebruikt voor een niet-auxetische structuur. Om een basis te creëren voor de vergelijking van de verschillende metamaterialen, is een reeks eenheidscellen ontworpen uit alle configuraties met identieke lineair-elastische eigenschappen, zoals de elasticiteitsmodulus en de dichtheid. Met behulp van het ontwikkelde numerieke model is de evolutie van de elastische eigenschappen tijdens het vervormingsproces onderzocht en gecorreleerd aan de veranderende belasting van de gedeformeerde balken. Deze evolutie is gekoppeld aan de energieabsorptiecapaciteit in een elastische omgeving bij verschillende belastingssnelheden en -omstandigheden. Uit de resultaten van deze studie blijkt dat slechts één van de onderzochte auxetische metamaterialen een hogere energieabsorptie vertoont dan conventionele honingraatstructuren.

Daarnaast is een experimentele campagne uitgevoerd met twee gereduceerde sets eenheidscellen, die zodanig zijn ontworpen en vervaardigd dat ze dezelfde massa en stijfheid bezitten. Tijdens deze campagne zijn de proefstukken onderworpen aan hogesnelheidsimpact, met bijzondere aandacht voor de krachtsoverdracht tussen de twee zijden van de balkstructuur. De verdeling van deze krachten aan de achterzijde van het materiaal is verder onderzocht met aanvullende numerieke studies. Uit deze campagne zijn geen voordelen gebleken van auxetische materialen, in vergelijking met hun niet-auxetische tegenhangers, wat betreft krachtsoverdracht en de verdeling van deze krachten. In een laatste studie is de invloed van verschillende rek- en vervormingssnelheden op de lokalisatie van de vervorming in uiteenlopende architecturen bestudeerd. Bij dit onderzoek lag de nadruk op de patronen waarin deze lokalisaties optreden en de daaropvolgende effecten op de energie-distributie in de structuur. Onder de geteste omstandigheden vertonen auxetische materialen hogere overgedragen krachten en lagere geabsorbeerde energie, wat resulteert in een slechtere bescherming tegen inslagen.

Daarom stelt dit proefschrift de heersende consensus in de literatuur ter discussie dat auxetische materialen superieure mogelijkheden bieden voor de vermindering van inslageffecten, zowel wat betreft energieabsorptie als krachtsoverdracht. Uit de berekende resultaten blijkt dat aanzienlijke vervormingen in auxetische materialen een nadelig effect hebben en dat de dwarscontractiecoëfficiënt bij hoge compressiesnelheden wordt geneutraliseerd. De resultaten van de experimentele campagne ondersteunen deze bevindingen.

# ZUSAMMENFASSUNG

„Auxetische Werkstoffe sind überlegene Materialien zur Minderung von Einschlagsereignissen“ ist ein häufiges Narrativ in der wissenschaftlichen Literatur bei der Suche nach leichten, stoßbeständigen Materialien. Diese Behauptung stützt sich auf die vorteilhaften Eigenschaften von auxetischen Werkstoffen, d. h. von Werkstoffen mit einer negativen Querkontraktionszahl. Ein gründlicher Vergleich gegenüber Werkstoffen mit positiver Querkontraktionszahl wird jedoch selten vorgenommen. Ziel der vorliegenden Dissertation ist es, diesen Vergleich anzustellen und zu hinterfragen, inwiefern auxetische Materialien vorteilhaft zur Einschlagsminderung sind. Da es in der Natur keine auxetischen Materialien gibt, wird die negative Querkontraktionszahl eines Materials durch sorgfältige Gestaltung seiner inneren Struktur erzeugt, was zur Schaffung sogenannter Metamaterialien führt. Um diese Metamaterialien unter Aufprallbedingungen zu untersuchen, sind umfangreiche physikalische Versuchsaufbauten erforderlich, die nur globale Messungen zulassen. Die vorliegende Dissertation befasst sich daher mit der rechnergestützten Modellierung von Balken-basierten Metamaterialien unter Hochgeschwindigkeitskompression.

Um ein vertieftes Verständnis der Vorgänge innerhalb verschiedener Strukturen für auxetische Metamaterialien zu erreichen, wird in einem ersten Schritt ein effizientes numerisches Modell auf der Basis nichtlinearer Timoschenko-Ehrenfest-Balken entwickelt. Das entwickelte Modell wird in einem Finite-Elemente-System implementiert. Zusätzlich zu den geometrischen Nichtlinearitäten muss auch das nichtlineare Materialverhalten innerhalb der Balken berücksichtigt werden. Hier wird eine Strategie für die Skalierung des Verfestigungsverhaltens von elasto-plastischen Balken vorgeschlagen und implementiert.

Um einen umfassenden Überblick über die Architekturen von Balken-basierten Metamaterialien zu geben, wird eine Reihe von vier verschiedenen auxetischen Architekturen verwendet, die auf unterschiedlichen Mechanismen basieren. Dabei handelt es sich um konkave Bienenwaben, Doppelpfeilspitzen, chirale und antichirale Architekturen. Die konventionelle Bienenwabe dient als Referenz für eine nicht auxetische Struktur. Um eine Grundlage für den Vergleich von Materialien zu schaffen, wird eine Reihe von Einheitszellen aller Architekturen mit identischen linear-elastischen Eigenschaften in Stoßrichtung entworfen. Unter Verwendung des entwickelten numerischen Modells wird die Entwicklung der elastischen Eigenschaften während des Kompression untersucht und mit den Änderungen der Belastung der verformten Balken korreliert. Diese Entwicklung wird mit den Energieabsorptionsfähigkeiten in einer elastischen Umgebung für unterschiedliche Belastungsgeschwindigkeiten und -bedingungen verknüpft. Die Ergebnisse dieser Studie zeigen, dass auxetische Materialien nur in einer begrenzten Anzahl von Szenarien eine höhere Energieabsorption aufweisen.

Außerdem wird eine Versuchsreihe mit einer reduzierten Anzahl von Einheitszellen durchgeführt. Dabei wird besonderes Augenmerk auf die Kraftübertragung zwischen den beiden Seiten der Balkenstruktur gelegt. Die Verteilung dieser Kräfte auf die Rückseite des strukturierten Materials wird durch zusätzliche numerische Studien ergänzt. In diesen Versuchen kann gesehen werden, dass auxetische Materialien im Vergleich zu ihren nicht auxetischen Gegenstücken keinen Vorteil in Bezug auf die Kraftübertragung und die Verteilung dieser Kräfte aufweisen.

In einer abschließenden Reihe von Untersuchungen werden die Auswirkungen unterschiedlicher Dehnungsgeschwindigkeiten auf die Lokalisierung der Verformung in verschiedenen Architekturen untersucht. Bei dieser Untersuchung wird besonderes Augenmerk auf die Muster gelegt, in denen diese Lokalisierungen auftreten, sowie auf die nachfolgenden Auswirkungen auf die Energiekonzentration in der Struktur. In diesem Fall zeigen auxetische Materialien höhere übertragene Kräfte und geringere absorbierte Energie, was zu einem schlechteren Schutz bei Einschlägen führt.

Folglich stellt die vorliegende Arbeit den in der Literatur vorherrschenden Konsens infrage, dass auxetische Werkstoffe sowohl in Bezug auf die Energieabsorption als auch auf die Kraftübertragung bessere Fähigkeiten zur Minderung von Stößen bieten. Die vorliegenden Simulationsresultate zeigen die nachteilige Wirkung großer Verformungen sowie die Negierung von Querkontraktionen bei hohen Kompressionsraten. Die Ergebnisse der experimentellen Versuchsreihe stützen diese Erkenntnisse.

# PREFACE

*There is only one thing in the long run more expensive than education:  
no education.*

John F. Kennedy

*Science, my lad, is made up of mistakes,  
but they are mistakes which it is useful to make,  
because they lead little by little to the truth.*

Jules Verne

Stepping into the train to Amsterdam (and then Delft) on April 1<sup>st</sup> 2021—carrying a single suitcase containing my household, in the middle of the Covid-pandemic—might be viewed as a mistake. But it was a useful mistake. A useful mistake, I am more than happy to have made. The following journey provided me with many more, happy, but also some not-so-happy mistakes. Mistakes for myself, mistakes for my colleagues, and mistakes for science. This book will not tell you all the mistakes I made throughout my journey, but it will give you the fruit of these mistakes, the truth to which the mistakes led me. I will not take you up to an epic journey to the centre of the earth, or around the moon, or 20 000 leagues below the sea. But I will provide you with the little insight I gained in my journey around the world of auxetics and all the wonders I saw during just a little more than 80 days.

I hope you will enjoy following me on this journey, I hope you will see the little fruit my mistakes brought me to, I hope you can take away a bit of new knowledge, enabling you to do more mistakes, take more fruitful steps, that lead little by little to the truth.

I will continue doing mistakes, useful mistakes, and maybe also not-so-useful mistakes—sometimes they are the little ones, that brighten our day the most. My sincere wish is to meet many of you along the way and that you join me in doing the mistakes, that still need to be made to inch just a little closer to the truth.

Til Gärtner  
Delft, Summer 2025



# CONTENTS

<b>Summary</b>	<b>vii</b>
<b>Samenvatting</b>	<b>ix</b>
<b>Zusammenfassung</b>	<b>xi</b>
<b>Preface</b>	<b>xiii</b>
<b>Contents</b>	<b>xvi</b>
<b>1. Introduction</b>	<b>1</b>
1.1. Computational modelling of architected metamaterials . . . . .	4
1.2. Influence of the Poisson effect on energy absorption . . . . .	6
1.3. Influence of the Poisson effect on force transmission . . . . .	7
<b>2. Beam kinematics and their numerical description</b>	<b>13</b>
2.1. Introduction . . . . .	15
2.2. Beams undergoing large deformations . . . . .	15
2.3. Beams in contact . . . . .	20
2.4. Adaptive time marching . . . . .	27
<b>3. Numerical modelling of the material behaviour</b>	<b>35</b>
3.1. Introduction . . . . .	37
3.2. Theoretical background . . . . .	38
3.3. Effects of mesh size . . . . .	43
3.4. Effects of geometrical scaling . . . . .	47
3.5. Strategies for the consistent geometric scaling of hardening . . . . .	50
3.6. Conclusion . . . . .	55
<b>4. Elastic behaviour under impact</b>	<b>59</b>
4.1. Introduction . . . . .	61
4.2. Auxetic architectures . . . . .	63
4.3. Numerical framework . . . . .	68
4.4. Numerical results . . . . .	69
4.5. Varying the effective properties . . . . .	86
4.6. Conclusion . . . . .	88

<b>5. Efficacy of auxetics in physical impact simulations</b>	<b>93</b>
5.1. Introduction . . . . .	95
5.2. Investigated architectures . . . . .	99
5.3. Methods . . . . .	103
5.4. Results . . . . .	108
5.5. Discussion & conclusion . . . . .	118
<b>6. Inelastic behaviour under different strain rate regimes</b>	<b>123</b>
6.1. Introduction . . . . .	125
6.2. Investigated architectures . . . . .	127
6.3. Numerical framework . . . . .	128
6.4. Effects of the number of unit cells . . . . .	131
6.5. Effects of strain rate on the force transmission . . . . .	141
6.6. Local energy distributions . . . . .	150
6.7. Conclusion . . . . .	157
<b>7. Conclusion &amp; Outlook</b>	<b>163</b>
7.1. Computational modelling of architected metamaterials . . . . .	165
7.2. Influence of the Poisson effect on energy absorption . . . . .	166
7.3. Influence of the Poisson effect on force transmission . . . . .	167
7.4. Conclusion . . . . .	168
7.5. Recommendations for further research . . . . .	169
<b>A. Elastic behaviour under impact</b>	<b>175</b>
A.1. Structural configurations . . . . .	177
A.2. Boundary conditions and tangent properties . . . . .	179
<b>B. Efficacy of auxetics in physical impact simulations</b>	<b>191</b>
B.1. Construction drawings . . . . .	193
B.2. Experimental and numerical comparisons . . . . .	193
B.3. Structural samples comparisons . . . . .	194
B.4. Deformation patterns at different speeds . . . . .	197
<b>C. Inelastic behaviour under different strain rate regimes</b>	<b>205</b>
C.1. Additional number of unit cells plots . . . . .	207
C.2. Additional strain rate plots . . . . .	213
<b>Acknowledgements</b>	<b>217</b>
<b>Contributions</b>	<b>219</b>
<b>Curriculum Vitae</b>	<b>222</b>







# INTRODUCTION

*The sky may fall on our heads tomorrow,  
but today we'll go for a walk in the forest.*

Asterix the Gaul

To achieve properties, that are *beyond* the limits given set by the physics of a homogenous material, scientists and engineers are in the last decades moving to synthetic structural materials, so-called *metamaterials*. Careful design of the internal structure can be used to tune the metamaterial's effective properties in a wide range of physical domains, from electromagnetism to acoustics and mechanics [Dav<sup>&al</sup>25]. Among the wide range of properties that can be influenced in mechanical metamaterials ([Bon<sup>&al</sup>24; Jia<sup>&al</sup>23]), is the Poisson's ratio, describing the lateral contraction of the material during tension. The Poisson's ratio is positive for nearly all naturally occurring materials, with the exceptions of e.g. mammal teat skin [LVH91] and crystalline silica [KC92], that are of no industrial relevance. The thus architected negative Poisson's ratio metamaterials are also called *auxetics*, a term coined by Evans et al. [Eva<sup>&al</sup>91] from the Greek *auxetos* "that may be increased". These negative Poisson's ratio metamaterials have been a topic of research, especially for the mitigation of impact phenomena [Boh<sup>&al</sup>23; KZ17; Ren<sup>&al</sup>18; SDC16; TZH22]. Literature suggests auxetic materials to exhibit a higher shear resistance [CL92] and an increased fracture toughness [CL96], that together with the higher indentation resistance [AGS12] and increased energy absorption [JH17] promise improved protection against impact events. The two basic prin-

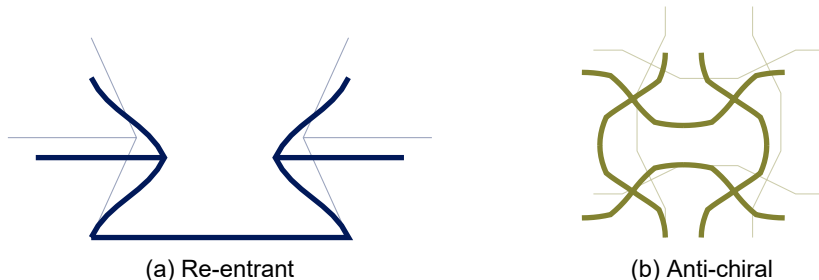


Figure 1.1.: Example unit cells for two auxetic mechanisms.

ciples to achieve a negative Poisson's ratio in an architected material is either by inwards folding at the joints as seen in the re-entrant honeycomb cell depicted in Figure 1.1a, or by rotation of parts of the unit cell, as shown by the anti-chiral unit cell depicted in Figure 1.1b.<sup>1</sup> More auxetic unit cells and their deformation mechanisms are explained in Chapter 4. As this presentation is concerned with the effects of the structure in a 2.5-dimensional setting,<sup>2</sup> the focus is put on beam-based lattice structures.

Impact events are a common occurrence across in vastly different scenarios. From micrometeorites and space debris endangering satellites [PA99] over personal protective equipment in sports [San<sup>&al</sup>14] and protection against detonation debris [Cro19] to metal roofs needing to withstand hail [SS19], all these events can essentially be abstracted the same way: An impactor with a set velocity is colliding

<sup>1</sup>This illustration as well as all visualizations and the theme of this dissertation make use the *batlow* colour scheme from *scientific colour maps* [Cra23].

<sup>2</sup>See physical samples in Chapter 5 for an illustration.

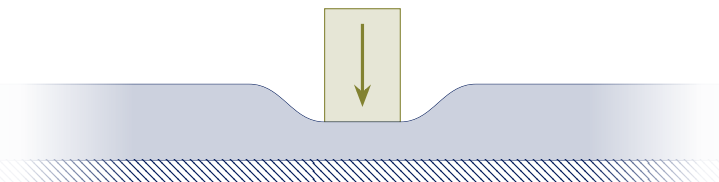


Figure 1.2.: Abstraction of an impact event.

with a material layer of finite thickness fixed at the back side. This abstraction, illustrated in [Figure 1.2](#), will serve as the fundamental model for this dissertation. Once the impactor and the material layer are in contact, the material itself undergoes high-rate compressive loading. These effects of large deformations at high rates in an architected material have not yet been addressed systematically in literature.

To establish a systematic comparison of auxetic with non-auxetic metamaterials is the goal of this dissertation. This results in the overarching research question (and title of the thesis):

**TITLE QUESTION**

Are auxetics better for protection?

In order to answer this question, it is subdivided into three research questions, that each contribute towards a better understanding of high-rate effects in architected materials.

## 1.1. COMPUTATIONAL MODELLING OF ARCHITECTED METAMATERIALS

The assessment of different architected metamaterials for impact mitigation typically involves high velocities and high amplitude forces. Conducting such experiments in a physical testing location is challenging and requires large amounts of time and monetary commitment. The physical experiments are additionally limited in the insight they can give, since measurements can only be taken from the outside of the material. Numerical experiments provide a way of performing different tests in a comparatively fast and inexpensive manner, whilst at the same time being able to provide more detailed insight into the internal material dynamics of the structure. It is therefore crucial to develop a numerical model, that is both, complex enough to capture relevant non-linearities in the material behaviour and at the same time as inexpensive as possible to allow for fast experimentation with different configurations. Such a model allows the researcher to investigate different architectures and shed light on their differences, advantages and disadvantages. This dissertation is focusing on metamaterials architected from beams forming lattice structures. Thus, the first research question is formulated as:

## RESEARCH QUESTION #1

How can lattice structures be efficiently and accurately modelled using numerical tools?

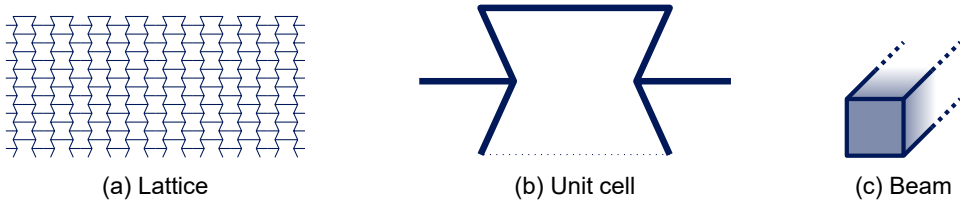


Figure 1.3.: Modelling of architected metamaterials as collection of beams.

To answer this question, the lattice structures are abstracted as a collection of beams and the beams are modelled individually. An exemplary lattice as well as the corresponding unit cell and beam are shown in Figure 1.3. These beams are modelled as geometrically nonlinear Timoshenko-Ehrenfest beams, also known as Simo-Reissner beams, geometrically exact beams or special Cosserat rods [Ant05; Eug15; Rei81; Sim85]. The geometrical description of these beams is well-developed in the mechanics community and summarized in Chapter 2. Next to the kinematic description of the deformation of the beams a description of the discretization into a finite element (FE) model and the implementation in [JIVE] used for the investigations, following [CJ99; SV86], is given. The present implementation uses an explicit time marching scheme with variable step size and finally considers contact between the beams, as laid out in Chapter 2.

Besides these kinematic considerations, the material behaviour of the beams and the corresponding kinetics have to be taken into account. During an impact event, the material is expected to experience large deformations at high rates. Such deformations include severe inelastic non-linearities. These non-linearities stemming from the behaviour of the constituting material in the architecture need to be accounted for in the numerical model as well. Whilst the inclusion of the modelling of inelastic behaviour into the description of the beams is as old as the description of the beams itself (e.g. [DC90; SHT84]), the adaptability of these models for different scenarios is limited. More recently Smriti et al. [Smr<sup>et al.</sup>18] developed a thermodynamically consistent theory to describe the inelastic behaviour of beams. Methods to acquire the plastic material constants for selected cross-sections have been shown by Herrnböck, Kumar and Steinmann [HKS21; HKS22]. The plastic material constants are, however, fitted for a single cross-section size and lack the flexibility to model lattice architectures employing different material cross-sections. In Chapter 3, a scaling strategy is developed and presented to augment the previously developed methods and make them feasible for the investigation of diverse metamaterial architectures in impact scenarios.

## 1.2. INFLUENCE OF THE POISSON EFFECT ON ENERGY ABSORPTION

The fundamental question of this dissertation pertains to the performance of auxetic metamaterials in impact scenarios for protection purposes. As the *negative* Poisson's ratio is—by definition—what sets auxetic materials fundamentally apart from other structures, it is of paramount importance to investigate influence of the Poisson effect during an impact event. These investigations are condensed first into the following research question:

### RESEARCH QUESTION #2

How does the Poisson effect influence energy absorption in architected materials?

Answering this question will allow not only for a better understanding of the impact response of architected materials, but also will allow a critical assessment of the fundamental arguments in favour of auxetics for impact mitigation.

From the plethora of investigations into auxetic metamaterials there are only few, that critically compare the effects between structures or analyse the fundamental deformation of singular unit cells. Tatlier [Tat22] compares different architectures, all showcasing a negative Poisson's ratio, tuned to the same density. They analyse the differences in energy absorption and collapse patterns of the patches without commenting on the behaviour of singular unit cells. The collapse patterns of patches made from architected materials are described in literature for different unit cells (double arrowheads [Zha<sup>&al</sup>18], conventional honeycombs [Rua<sup>&al</sup>03], and re-entrant honeycombs [Mer<sup>&al</sup>22]) without a comparison between different architectures using the same material parameters or similar effective properties. Farshbaf, Dialami and Cervera [FDC25] investigate the compressive and tensile properties of both conventional and re-entrant honeycomb structures made from the same material and using the same beams resulting in different effective properties.

In order to overcome the issue of comparability, distinct unit cell designs achieving the same linear elastic properties for different material architectures are developed in [Chapter 4](#). An initially purely elastic investigation is conducted into these unit cells determining the development of the stiffness properties of the unit cells under compression and shear loading conditions. The observed changes in properties are then related to the geometric effects seen throughout the deformation. [Chapter 4](#) closes with a comparison of the effects of geometry on the elastic energy absorption behaviour at different compression rates and an investigation into the effects of lateral material on the elastic response of different architectures.

To also investigate inelastic material responses in a realistic setting, this study is followed up by an experimental comparison between a single auxetic and a single non-auxetic architecture in different configurations in [Chapter 5](#). In this experimental and numerical campaign the differences between a set of auxetic and non-auxetic patches are investigated for both, a comparable mass and a comparable stiffness.

## 1.3. INFLUENCE OF THE POISSON EFFECT ON FORCE TRANSMISSION

The forces transmitted through the metamaterial structure are, next to the absorption of the energy of the impactor, a crucial measure for the efficacy of a protective layer. For a good protection, these forces should not exceed limits set by the fragility of the material to be protected. In literature, there is not yet a systematic overview regarding the transmission of forces through an architected material at high rates. This gap in literature motivates the final research question:

### RESEARCH QUESTION #3

How does the Poisson effect influence force transmission in architected materials?

Chapter 5 investigates both the temporal and spatial distribution of forces on the back side of the protective metamaterial for different Poisson's ratios by a distinct set of architectures, designed to have either comparable mass or stiffness. In Chapter 6, these investigations are supplemented by simulations of the material behaviour under different strain rates. Including material non-linearities, it is demonstrated, how the force levels differ between the two sides of the patch. The observed differences in the force transmission through the various architectures and the effect of different compression rates are attributable to the different observed patterns in deformation of the structures. The differences seen in the deformation patterns are related to the size of single unit cells and localized deformations are motivated by static mechanisms and dynamic force concentrations. Whilst during static compression auxetic architectures show a stronger embrittlement for smaller unit cells due to localized deformation, the investigated non-auxetic structure appears stronger for smaller unit cells. During dynamic compression, a concentration of deformation is observed adjacent to the edge that is subject to compressive loading (top edge in Figure 1.2). These localized deformations are investigated both from a global force level and for the local distribution of different types of energy. Chapter 6 closes with a comparison between impact mitigation capabilities of the investigated structures.

## REFERENCES

[AGS12] I. I. Argatov, R. Guinovart-Díaz and F. J. Sabina. ‘On local indentation and impact compliance of isotropic auxetic materials from the continuum mechanics viewpoint’. *Int. J. Eng. Sci.* **54** (2012), pp. 42–57.

[Ant05] S. S. Antman. *Nonlinear Problems of Elasticity*. 2nd ed. Applied Mathematical Sciences. Springer, 2005.

[Boh<sup>&a/</sup>23] R. P. Bohara et al. ‘Anti-blast and -impact performances of auxetic structures: A review of structures, materials, methods, and fabrications’. *Eng. Struct.* **276**, 115377 (2023).

[Bon<sup>&a/</sup>24] S. Bonfanti et al. ‘Computational design of mechanical metamaterials’. *Nat Comput. Sci* **4** (2024), pp. 574–583.

[CJ99] M. A. Crisfield and G. Jelenić. ‘Objectivity of strain measures in the geometrically exact three-dimensional beam theory and its finite-element implementation’. *Proc. R. Soc. A-Math. Phys. Eng. Sci.* **455** (1999), pp. 1125–1147.

[CL92] J. B. Choi and R. S. Lakes. ‘Non-linear properties of metallic cellular materials with a negative Poisson’s ratio’. *J. Mater. Sci.* **27** (1992), pp. 5375–5381.

[CL96] J. B. Choi and R. S. Lakes. ‘Fracture toughness of re-entrant foam materials with a negative Poisson’s ratio: experiment and analysis’. *Int. J. Fract.* **80** (1996), pp. 73–83.

[Cra23] F. Cramer. *Scientific colour maps*. Version 8.0.1. Oct. 2023.

[Cro19] I. G. Crouch. ‘Body armour – New materials, new systems’. *Def. Technol.* **15** (2019), pp. 241–253.

[Dav<sup>&a/</sup>25] B. Davies et al. ‘Roadmap on metamaterial theory, modelling and design’. *J. Phys. D: Appl. Phys.* **58**, 203002 (2025).

[DC90] L. Duan and W.-F. Chen. ‘A yield surface equation for doubly symmetrical sections’. *Eng. Struct.* **12** (1990), pp. 114–119.

[Eug15] S. R. Eugster. *Geometric Continuum Mechanics and Induced Beam Theories*. Lecture Notes in Applied and Computational Mechanics. Springer, 2015.

[Eva<sup>&a/</sup>91] K. E. Evans et al. ‘Molecular network design’. *Nature* **353** (1991), p. 124.

[FDC25] S. Farshbaf, N. Dialami and M. Cervera. ‘Large deformation and collapse analysis of re-entrant auxetic and hexagonal honeycomb lattice structures subjected to tension and compression’. *Mech. Mater.* **210**, 105457 (2025).

[HKS21] L. Herrnböck, A. Kumar and P. Steinmann. ‘Geometrically exact elastoplastic rods: determination of yield surface in terms of stress resultants’. *Comput. Mech.* **67** (2021), pp. 723–742.

[HKS22] L. Herrnböck, A. Kumar and P. Steinmann. 'Two-scale off-and online approaches to geometrically exact elastoplastic rods'. *Comput. Mech.* **71** (2022), pp. 1–24.

[JH17] L. Jiang and H. Hu. 'Low-velocity impact response of multilayer orthogonal structural composite with auxetic effect'. *Compos. Struct.* **169** (2017), pp. 62–68.

[Jia<sup>&al</sup>23] P. Jiao et al. 'Mechanical metamaterials and beyond'. *Nat. Commun.* **14**, 6004 (2023).

[JIVE] Dynaflow Research Group. *JIVE*. Version 3.0. 1st Apr. 2021.

[KC92] N. R. Keskar and J. R. Chelikowsky. 'Negative Poisson ratios in crystalline SiO<sub>2</sub> from first-principles calculations'. *Nature* **358** (1992), pp. 222–224.

[KZ17] H. M. A. Kolken and A. A. Zadpoor. 'Auxetic mechanical metamaterials'. *RSC Adv.* **7** (2017), pp. 5111–5129.

[LVH91] C. Lees, J. F. V. Vincent and J. E. Hillerton. 'Poisson's Ratio in Skin'. *Bio-Med. Mater. Eng.* **1** (1991), pp. 19–23.

[Mer<sup>&al</sup>22] C. Mercer et al. 'Effects of geometry and boundary constraint on the stiffness and negative Poisson's ratio behaviour of auxetic metamaterials under quasi-static and impact loading'. *Int. J. Impact Eng.* **169**, 104315 (2022).

[PA99] C. Pardini and L. Anselmo. 'Assessing the Risk of Orbital Debris Impact'. *Space Debris* **1** (1999), pp. 59–80.

[Rei81] E. Reissner. 'On Finite Deformations of Space-Curved Beams'. *Z. Angew. Math. Phys.* **32** (1981), pp. 734–744.

[Ren<sup>&al</sup>18] X. Ren et al. 'Auxetic metamaterials and structures: a review'. *Smart Mater. Struct.* **27**, 023001 (2018).

[Rua<sup>&al</sup>03] D. Ruan et al. 'In-plane dynamic crushing of honeycombs—a finite element study'. *Int. J. Impact Eng.* **28** (2003), pp. 161–182.

[San<sup>&al</sup>14] M. Sanami et al. 'Auxetic Materials for Sports Applications'. *Procedia Eng.* **72** (2014), pp. 453–458.

[SDC16] K. K. Saxena, R. Das and E. P. Calius. 'Three Decades of Auxetics Research – Materials with Negative Poisson's Ratio: A Review'. *Adv. Eng. Mater.* **18** (2016), pp. 1847–1870.

[SHT84] J. C. Simo, K. D. Hjelmstad and R. L. Taylor. 'Numerical Formulations of Elasto-Viscoplastic Response of Beams Accounting for the Effect of Shear'. *Comput. Methods Appl. Mech. Eng.* **42** (1984), pp. 301–330.

[Sim85] J. C. Simo. 'A finite strain beam formulation. The three-dimensional dynamic problem. Part I'. *Comput. Methods Appl. Mech. Eng.* **49** (1985), pp. 55–70.

[Smr<sup>&al</sup>18] Smriti et al. 'A thermoelastoplastic theory for special Cosserat rods'. *Math. Mech. Solids* **24** (2018), pp. 686–700.

- [SS19] D. Saini and B. Shafei. 'Prediction of extent of damage to metal roof panels under hail impact'. *Eng. Struct.* **187** (2019), pp. 362–371.
- [SV86] J. C. Simo and L. Vu-Quoc. 'A three-dimensional finite-strain rod model. part II: Computational aspects'. *Comput. Methods Appl. Mech. Eng.* **58** (1986), pp. 79–116.
- [Tat22] M. S. Tatlier. 'A comparative analysis of the in-plane energy absorption capacities of auxetic structures'. *Trans. Can. Soc. Mech. Eng.* **46** (2022), pp. 216–224.
- [TZH22] D. Tahir, M. Zhang and H. Hu. 'Auxetic Materials for Personal Protection: A Review'. *phys. status solidi (b)* **259**, 2200324 (2022).
- [Zha<sup>&al</sup>/18] X. Zhao et al. 'Dynamic crushing of double-arrowed auxetic structure under impact loading'. *Mater.& Des.* **160** (2018), pp. 527–537.





# 2

## **BEAM KINEMATICS AND THEIR NUMERICAL DESCRIPTION**

*During their education, engineers invariably encounter beams as a foundational concept of mechanics. Starting from simple rods that only deform in the axial direction, moving to Euler-Bernoulli beams, considering bending but not shear, and finally, Timoshenko-Ehrenfest beams, which include shear deformation, various concepts are introduced. All of these concepts are first taught in an infinitesimal context, without consideration of any non-linearities, either geometric or material. Although starting from simple concepts, they have been extended over the last century to include non-linearities while maintaining the simplicity of a one-dimensional continuum. The following chapter will establish the kinematic description of beam deformation and the numerical treatment that is employed throughout the remainder of this dissertation.*

## 2.1. INTRODUCTION

Beams are used to describe structures that have a single predominant direction, i.e.  $l \gg d$  where  $l$  represents the length of the beam and  $d$  a measure of the cross-sectional size. The most common description of these beams is the Euler-Bernoulli beam theory, which assumes, that **a)** the cross-section of the beam is infinitely rigid in its own plane, **b)** the cross-section remains plane throughout the deformation, and **c)**, the cross-section remains perpendicular to the centreline of the beam. These assumptions do not allow the modelling of shear deformation or rotational inertia, which become significant for fast and large deformations. Therefore, in this work, assumption that the cross-section remains perpendicular to the centreline is dropped, while keeping the notion of a plane, rigid cross-section. The resulting theory is known as Timoshenko-Ehrenfest beam theory. In the following, the analytical description of the beam as static one-dimensional continuum is laid out in Section 2.2, followed by the description of beam contact kinematics in Section 2.3. The chapter is then closed with an explanation of the time marching scheme employed for the investigations in Section 2.4.

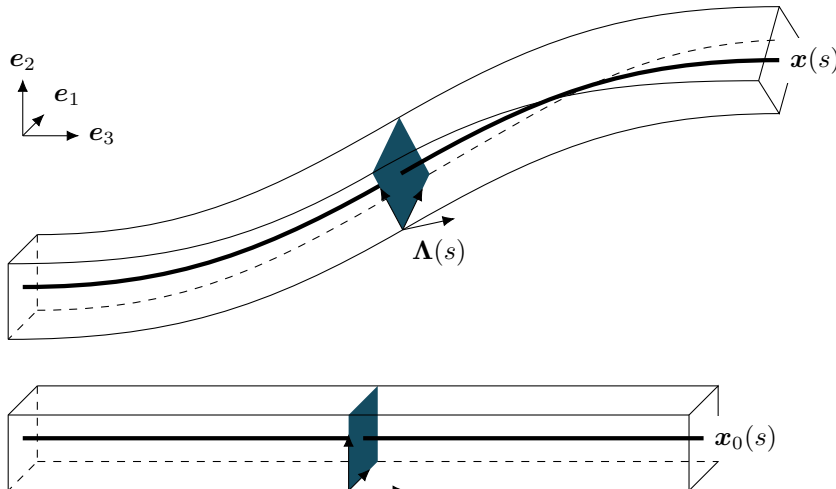


Figure 2.1.: Beam undergoing large deformation.

## 2.2. BEAMS UNDERGOING LARGE DEFORMATIONS

The aforementioned Timoshenko-Ehrenfest theory is extended to nonlinear deformation, resulting in nonlinear Timoshenko-Ehrenfest beams. These are also known as Simo-Reissner beams (after [Rei81; Sim85]), geometrically exact beams, or special Cosserat rods [Ant05; Eug15]. The following deliberations on the beam configuration follow Antman [Ant05] and Eugster [Eug15]. For a deeper mathematical treatise the reader is also referred to Rubin [Rub00].

### 2.2.1. ANALYTICAL DESCRIPTION OF THE BEAM

A schematic showing the concept is given in Figure 2.1. A beam is described with the centreline  $\mathbf{x}(s)$ , where  $s \in [s_0, s_1]$  is the measure along the length of the beam, with two orthonormal directors attached to it  $\mathbf{d}_1(s), \mathbf{d}_2(s)$ . A third director is introduced orthogonal to the first two  $\mathbf{d}_3(s) = \mathbf{d}_1(s) \times \mathbf{d}_2(s)$ . These three orthonormal directors may be viewed as the column vectors of a matrix, which represents the rotation between the global reference frame and the local coordinate frame of the beam:

$$\Lambda(s) = \mathbf{d}_i(s) \otimes \mathbf{e}_i = [\mathbf{d}_1(s) \quad \mathbf{d}_2(s) \quad \mathbf{d}_3(s)]. \quad (2.1)$$

This rotation represents the orientation of the rigid cross-section of the beam at a point along the centreline of the beam  $\mathbf{x}(s)$ . To account for extension and shear of the beam, the centre line is described as a sum of the centreline in the undeformed configuration  $\mathbf{x}_0$  and a deformation  $\mathbf{u}$  according to

$$\mathbf{x}(s) = \mathbf{x}_0(s) + \mathbf{u}(s). \quad (2.2)$$

The description of the total deformation as a mapping from the length coordinate to the current position as well as rotation is given by

$$s \mapsto (\Lambda, \mathbf{x}) \quad \mathbb{R} \mapsto \text{SO}(3) \times \mathbb{R}^3. \quad (2.3)$$

One can express the translational strain-prescriptors (shear, extension)  $\gamma(s)$  as well as rotational strain-prescriptors (bending, torsion)  $\kappa(s)$  with the given deformations and rotations in the global frame of reference as:

$$\gamma(s) = \mathbf{x}'(s) - \mathbf{d}_3(s), \quad (2.4)$$

$$\tilde{\kappa}(s) = \Lambda'(s)\Lambda^T(s), \quad (2.5)$$

where  $(\cdot)$  denotes the skew symmetric matrix with associated axial vector and  $(\cdot)'$  the derivative with respect to  $s$ . The strain-prescriptors in the material frame ( $\Gamma(s)$  for the translational part,  $\mathcal{K}(s)$  for the rotational part) are expressed as:

$$\Gamma(s) = \Lambda^T(s)(\mathbf{x}'(s) - \mathbf{d}_3(s)), \quad (2.6)$$

$$\tilde{\mathcal{K}}(s) = \Lambda^T(s)\Lambda'(s). \quad (2.7)$$

In order to calculate the stress-resultants, a general function relating material strain-prescriptors to material stress-resultants ( $\mathbf{N}(s)$  for the translational parts and  $\mathbf{M}(s)$  for the rotational parts) is assumed to exist:

$$\begin{bmatrix} \mathbf{N}(s) \\ \mathbf{M}(s) \end{bmatrix} = f \left( \begin{Bmatrix} \Gamma(s) \\ \mathcal{K}(s) \end{Bmatrix} \right). \quad (2.8)$$

This constitutive model will be detailed in Chapter 3. The resulting stress-resultants are then transformed back to the inertial frame of reference, denoted again by lower case symbols ( $\mathbf{n}(s), \mathbf{m}(s)$ ):

$$\mathbf{n}(s) = \Lambda(s)\mathbf{N}(s), \quad (2.9)$$

$$\mathbf{m}(s) = \Lambda(s)\mathbf{M}(s). \quad (2.10)$$

### 2.2.2. DISCRETIZATION OF THE BEAM

The discretization of the beam into finite elements, as proposed by Simo and Vu-Quoc [SV86] and subsequent improvements due to Crisfield and Jelenić [CJ99], are laid out in the following. Initially, the displacement  $\mathbf{u}(s)$  is interpolated using standard Lagrangian shape functions  $\mathcal{L}_i$ :

$$\mathbf{u}(s) \approx \mathbf{u}^*(s) = \sum_i \mathcal{L}_i(s) \mathbf{u}_i. \quad (2.11)$$

Here and in the following the superscript  $(\cdot)^*$  refers to the discretized, interpolated quantities. The orientation of the cross-section is then interpolated using spherical interpolation as proposed by [CJ99]. For this interpolation, a central rotation  $\Lambda_r$  is found as

$$\Lambda_r = \Lambda_i \exp(0.5 \log \Lambda_i^T \Lambda_j), \quad (2.12)$$

where  $\Lambda_i$  denotes the rotation at the node on one side and  $\Lambda_j$  at the node on the other side the centre of the element. Here,  $\log$  refers to the operation that maps a rotation matrix, that is part of the special orthogonal group  $\text{SO}(3)$ , to an element of the corresponding Lie-algebra  $\mathfrak{so}(3)$ . This can be interpreted in the context of rotation as the skew symmetric matrix associated with the rotation vector representing the rotation between the two central nodes. By multiplying half of this rotation vector again with the rotation of the first node, the overall central rotation is obtained. For elements with an odd number of nodes the result is simply  $\Lambda_i = \Lambda_j = \Lambda_r$ . Then for every node the corresponding (local) rotation vectors  $\Phi_i$  are computed using the same matrix logarithm as

$$\tilde{\Phi}_i = \log \left( \Lambda_r^T \Lambda_i \right), \quad (2.13)$$

where again  $(\tilde{\cdot})$  represents the skew symmetric matrix. These local vectors are interpolated using the same standard Lagrangian shape functions used for the displacements:

$$\Phi(s) \approx \Phi^*(s) = \sum_i \mathcal{L}_i(s) \Phi_i. \quad (2.14)$$

At each point along the centre line, one can reconstruct the rotation by simple consecutive rotation of the local rotation followed by the reference rotation as

$$\Lambda(s) \approx \Lambda^*(s) = \Lambda_r \exp \tilde{\Phi}^*(s). \quad (2.15)$$

From these interpolated kinematic properties, one can construct the strain-pre-criptors and stress-resultants at every quadrature point as described in Equations (2.4) to (2.8).

For brevity the dependency on  $s$  is not spelled out explicitly in the following. Starting from the static equilibrium equations along the beam with the external translational line load  $\mathbf{n}_{\text{ext}}$  and the external rotational line load  $\mathbf{m}_{\text{ext}}$ :

$$\mathbf{n}' = \mathbf{n}_{\text{ext}}, \quad (2.16)$$

$$\mathbf{m}' + \mathbf{n} \times \mathbf{x}' = \mathbf{m}_{\text{ext}}, \quad (2.17)$$

the virtual work can be computed by multiplying these equations with an arbitrary, but admissible variation in the displacements  $\delta u$  as well as in the rotations  $\delta \vartheta$ :

$$\delta W = \int_{s_0}^{s_1} [(\mathbf{n}_{\text{ext}} - \mathbf{n}') \cdot \delta \mathbf{u} + (\mathbf{m}_{\text{ext}} - \mathbf{m}' - \mathbf{n} \times \mathbf{x}') \cdot \delta \vartheta] \, ds. \quad (2.18)$$

For a static solution procedure, which tries to find a point where the virtual work vanishes for any admissible variation by applying a Newton-Raphson scheme, one needs to calculate the unbalanced forces first. This is done for every element  $e$  by numerically computing the internal force integral collecting the contributions of every node  $i$ :

$$\mathbf{f}_{\text{int}}^{e,i} = \int_e \boldsymbol{\Xi}_i \begin{bmatrix} \mathbf{n} \\ \mathbf{m} \end{bmatrix} \, ds, \quad (2.19)$$

with

$$\boldsymbol{\Xi}_i = \begin{bmatrix} \mathcal{L}'_i \mathbb{1} & \mathbb{0} \\ -\mathcal{L}_i \widetilde{\mathbf{x}^*} & \mathcal{L}'_i \mathbb{1} \end{bmatrix}. \quad (2.20)$$

Where  $\mathbb{1}$  denotes the  $3 \times 3$  identity matrix and  $\mathbb{0}$  a  $3 \times 3$  zero matrix. It should be noted, that these integrals are numerically integrated by reduced integration in order to prevent shear locking. These individual contributions to the global internal force vector  $\mathbf{f}_{\text{int}}$  are subsequently assembled using standard FE procedures (see e.g. [Bat06; Sch99]), with  $\mathbf{A}$  denoting the assembly operator:

$$\mathbf{f}_{\text{int}} = \mathbf{A} \sum_{e,i} \mathbf{f}_{\text{int}}^{e,i}. \quad (2.21)$$

With the (nodal) external forces  $\mathbf{f}_{\text{ext}} = [\mathbf{n}_{\text{ext}} \quad \mathbf{m}_{\text{ext}}]^T$  given by the boundary conditions they result in the out-of-balance force vector  $\mathbf{f}_{\text{res}}$ :

$$\mathbf{f}_{\text{res}} = \mathbf{f}_{\text{ext}} - \mathbf{f}_{\text{int}}. \quad (2.22)$$

Subsequently, the tangent stiffness matrix is computed as well. This can be done by differentiating the internal force components with respect to the displacements. In a discrete scheme, the stiffness contributions  $\mathbf{K}^{e,ij}$  can be additively split into the contributions of the symmetric material stiffness  $\mathbf{S}^{e,ij}$  and a non-symmetric geometric stiffness contribution  $\mathbf{T}^{e,ij}$ :

$$\mathbf{K}^{e,ij} = \mathbf{S}^{e,ij} + \mathbf{T}^{e,ij}. \quad (2.23)$$

The symmetric contribution is computed from the material tangent stiffness  $\mathbf{C}$  defined in [Chapter 3](#) as

$$\mathbf{S}^{e,ij} = \int_e \boldsymbol{\Xi}_i \mathbf{\Pi}_i \mathbf{C} \mathbf{\Pi}_j^T \boldsymbol{\Xi}_j^T \, ds, \quad (2.24)$$

with

$$\mathbf{\Pi}_i = \begin{bmatrix} \mathbf{\Lambda}_i & \mathbb{0} \\ \mathbb{0} & \mathbf{\Lambda}_i \end{bmatrix}, \quad (2.25)$$

and the geometric contribution is computed as

$$T^{e,ij} = \int_e \Psi_i^* B^* \Psi_j^{*T} ds, \quad (2.26)$$

with

$$\Psi_i^* = \begin{bmatrix} \mathcal{L}'_i \mathbb{1} & 0 & 0 \\ 0 & \mathcal{L}'_i \mathbb{1} & \mathcal{L}_i \mathbb{1} \end{bmatrix} \quad (2.27)$$

and

$$B^* = \begin{bmatrix} 0 & 0 & -\tilde{\mathbf{n}}^* \\ 0 & 0 & -\tilde{\mathbf{m}}^* \\ \tilde{\mathbf{n}}^* & 0 & \mathbf{n}^* \otimes \mathbf{x}^* - (\mathbf{n}^* \cdot \mathbf{x}^*) \mathbb{1} \end{bmatrix}. \quad (2.28)$$

After the tangent stiffness and the internal force vector are assembled, the system is solved.

#### NUMERICAL BENCHMARKS

In order to verify the implementation done using [JIVE](#), selected results from literature were re-implemented and compared with the custom implementation.

**Convergence** As a first test, the quadratic convergence behaviour of the algorithm is confirmed comparing it to *Example 7.1* from [\[SV86\]](#). In this example a cantilever is subjected to pure bending by applying a moment at the free end, the beam is set to have the unitless bending stiffness  $EI = 2$  and be of unit length. The moment is chosen so that the beam curls up twice ( $M = 8\pi$ ). The test is conducted using 5 linear elements. The minor differences in [Table 2.1](#) for the numerical values of the

Table 2.1.: Residuals for the bent cantilever.

Iteration	Simo and Vu-Quoc <a href="#">[SV86]</a>	This implementation
0	$0.251 \times 10^2$	$0.251 \times 10^2$
1	$0.425 \times 10^2$	$0.283 \times 10^2$
2	$0.441 \times 10^{-13}$	$0.691 \times 10^{-13}$

residual are attributed to differences in nearly 4 decades of changes in hard- and software. The configuration and the deformed beam can be seen in [Figure 2.2](#).

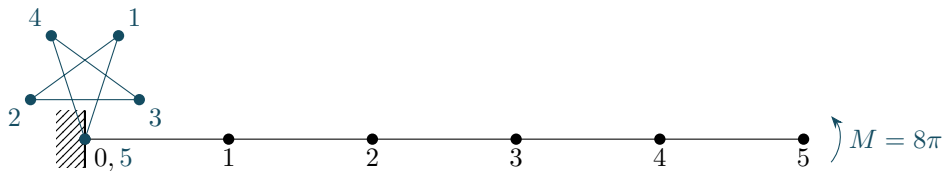


Figure 2.2.: Twice rolled up beam with 5 linear elements [\[SV86\]](#).

**Ability to model complex deformation** To showcase the abilities of the implementation, *Example 7.5* from [SV86] is implemented and compared with the reported results. This example shows the loading of a cantilever, bent by  $45^\circ$  with a radius of 100 m, in the third direction. The material parameters are taken to be  $E = 10^7 \text{ Pa}$ ,  $G = 5 \times 10^6 \text{ Pa}$ ,  $A = 1 \text{ m}$ ,  $I = 0.083 \text{ m}^4$ <sup>1</sup> and the system is modelled with 8 linear elements. The setup for this test can be seen in Figure 2.3. In Figure 2.4 the excellent agreement between the custom implementation and the reported results from literature can be seen. Minor differences may be attributed to the limited resolution available in the literature graphs. The curves were extracted using the WebPlotDigitizer [WPD].

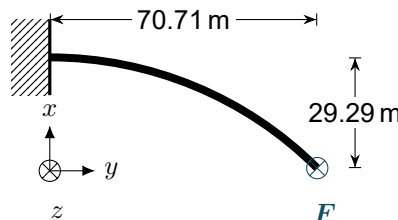


Figure 2.3.: Depiction of the test configuration and loading conditions.

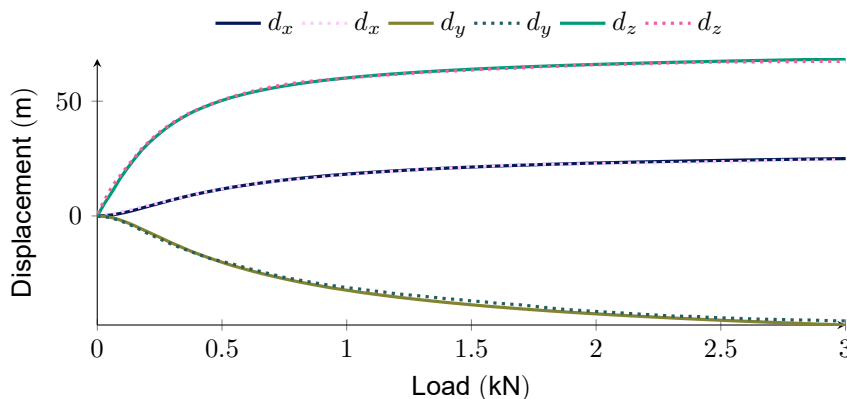


Figure 2.4.: Load-deflection curves for a curved beam under a point load. Solid lines depict this work, dotted lines the reference [SV86].

## 2.3. BEAMS IN CONTACT

The following section describes two beams in contact according to the work of Wriggers [Wri06].

<sup>1</sup>See Chapter 3 for details and explanation of the material modelling.

### 2.3.1. ANALYTICAL DESCRIPTION OF CONTACT

Two beams  $a, b$ , with radii  $r_a, r_b$  are in contact if the gap function  $g$  at  $x(s_a)$  and  $x(s_b)$  is negative:

$$g = |x(s_a) - x(s_b)| - r_a - r_b. \quad (2.29)$$

For description of the behaviour of two bodies in contact, two options exist which are widely discussed in literature. On the one hand, one can introduce Lagrangian multipliers. Lagrangian multipliers ensure no interpenetration and serve as representation for the contact forces effected from the contact. They increase the size of the discretized system, and are therefore not considered for this work. On the other hand, penalty parameters provide a solution to the contact problem, that simply adds new terms to the force computations without increasing the overall number of variables for any implementation. Penalty parameters introduce the contact force  $f_{\text{con}}$  as a function of the gap, which is assumed linear for the remainder of this work

$$f_{\text{con}} = \begin{cases} \varepsilon g, & \text{if } g < 0 \\ 0, & \text{otherwise} \end{cases}, \quad (2.30)$$

with the penalty parameter  $\varepsilon$  needing to be chosen carefully. The numerical implementation of the contact is laid out in the following.

### 2.3.2. NUMERICAL IMPLEMENTATION OF CONTACT

#### CONTACT SEARCH

As the number of possible contact pairs between the elements increases quadratically with the number of elements, the search for the contact is implemented in a staggered three-step scheme:

**Coarse, beam-level search** First, in a lattice with many beams, the beams are checked for potential contact between them. To this end, the boxes spanning two beams are computed, resulting in two corners at the minimum and maximum coordinates for each beam  $a$  and  $b$  in the pairing:

$$x_{\min,a}^{\text{coord}}, \quad x_{\max,a}^{\text{coord}}, \quad \text{and} \quad x_{\min,b}^{\text{coord}}, \quad x_{\max,b}^{\text{coord}}. \quad (2.31)$$

These boxes are now extended by the radii of both beams

$$x_{\min,a} = x_{\min,a}^{\text{coord}} - \begin{bmatrix} r_a \\ r_a \\ r_a \end{bmatrix}, \quad x_{\max,a} = x_{\max,a}^{\text{coord}} + \begin{bmatrix} r_a \\ r_a \\ r_a \end{bmatrix}, \quad \text{likewise for } b, \quad (2.32)$$

after which, it can be computed, whether there is any intersection between those two boxes by simple geometric operations. The construction of these boxes is visualized for an example in [Figure 2.5](#). The beams are in potential contact, if for every coordinate  $x^k$ ,  $k = 1, 2, 3$  the following condition is fulfilled:

$$(x_{\max,a}^k \geq x_{\min,b}^k) \wedge (x_{\max,b}^k \geq x_{\min,a}^k). \quad (2.33)$$

If the beams  $a, b$  are found to be in potential contact, they are added to a list of beam pairings to be investigated in the next step.

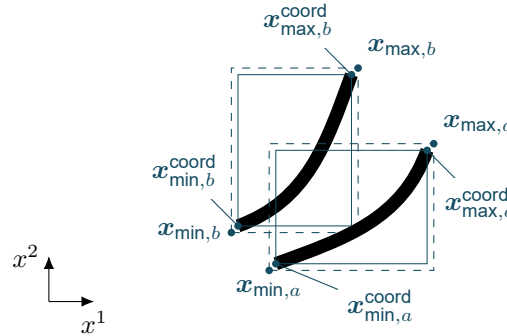


Figure 2.5.: Schematic illustration of the coarse, beam-level search.

**Coarse, element-level search** For each of those pairings, the search is refined on the element level, and again boxes spanning element  $i$  of the beam  $a$  and an element  $j$  of beam  $b$  are computed as described above for entire beams. Here, the algorithm is employed to fill a list with potential pairs of elements in contact. For these pairs a finer computation determining the contact point is then started.

**Fine, element-level search** In the computations performed in this work, only linear elements are used for contact computation. Therefore, the following deliberations depend crucially on the representation of the elements by simple lines in space. Using local coordinates, element  $i$ , with its nodal position vectors  $\mathbf{x}_i^1, \mathbf{x}_i^2$ , is described using the local coordinate  $\xi_i$ :

$$\mathbf{x}(\xi_i) = \frac{1}{2}(1 - \xi_i)\mathbf{x}_i^1 + \frac{1}{2}(1 + \xi_i)\mathbf{x}_i^2. \quad (2.34)$$

Element  $j$  is described similarly,

$$\mathbf{x}(\xi_j) = \frac{1}{2}(1 - \xi_j)\mathbf{x}_j^1 + \frac{1}{2}(1 + \xi_j)\mathbf{x}_j^2. \quad (2.35)$$

Following now [WZ97], the values of  $\xi_i^{\text{con}}$  and  $\xi_j^{\text{con}}$  for the point of the closest approach of the two lines are computed:

$$\begin{aligned} \xi_i^{\text{con}} &= -(\mathbf{b}_j - \mathbf{b}_i) \cdot \frac{\mathbf{t}_j (\mathbf{t}_j \cdot \mathbf{t}_i) - \mathbf{t}_i (\mathbf{t}_j \cdot \mathbf{t}_j)}{(\mathbf{t}_j \cdot \mathbf{t}_j)(\mathbf{t}_i \cdot \mathbf{t}_i) - (\mathbf{t}_j \cdot \mathbf{t}_i)^2}, \\ \xi_j^{\text{con}} &= (\mathbf{b}_j - \mathbf{b}_i) \cdot \frac{\mathbf{t}_i (\mathbf{t}_j \cdot \mathbf{t}_i) - \mathbf{t}_j (\mathbf{t}_i \cdot \mathbf{t}_i)}{(\mathbf{t}_j \cdot \mathbf{t}_j)(\mathbf{t}_i \cdot \mathbf{t}_i) - (\mathbf{t}_j \cdot \mathbf{t}_i)^2}, \end{aligned} \quad (2.36)$$

with  $\mathbf{b} = \mathbf{x}^2 - \mathbf{x}^1$  and  $\mathbf{t} = \mathbf{x}^2 - \mathbf{x}^1$ . Using these calculated values, the actual contact computation is performed.

#### CONTACT COMPUTATION

Based on the results for  $\xi_i^{\text{con}}, \xi_j^{\text{con}}$  from the last step of the contact search, different contact algorithms are employed.

**Closest approach within both elements** In the simple case, when the closest distance of the lines is within both elements, i.e.

$$\xi_i^{\text{con}} \in [-1, 1] \wedge \xi_j^{\text{con}} \in [-1, 1], \quad (2.37)$$

point-wise contact between the two beams is assumed and the algorithms from Wriggers and Zavarise [WZ97] for a segment-to-segment contact are employed. The gap for this contact is computed from the two positions directly

$$\mathbf{g} = \mathbf{x}_i^{\text{con}} - \mathbf{x}_j^{\text{con}}, \quad g = |\mathbf{g}| - r_i - r_j, \quad (2.38)$$

with the contact normal as

$$\hat{\mathbf{n}} = \frac{\mathbf{g}}{|\mathbf{g}|}. \quad (2.39)$$

For this segment-to-segment contact, the force contribution is computed as

$$\mathbf{f}_{\text{con}} = \begin{bmatrix} \mathbf{f}_{\text{con}}^{i_1} \\ \mathbf{f}_{\text{con}}^{i_2} \\ \mathbf{f}_{\text{con}}^{j_1} \\ \mathbf{f}_{\text{con}}^{j_2} \end{bmatrix} = \varepsilon_{\text{STS}} \langle g \rangle^1 \tilde{\mathbf{H}}^T \cdot \hat{\mathbf{n}}, \quad (2.40)$$

with the segment-to-segment penalty  $\varepsilon_{\text{STS}}$  and

$$\tilde{\mathbf{H}} = \begin{bmatrix} -\mathcal{L}_{i,1}^{\text{con}} \mathbb{1} & -\mathcal{L}_{i,2}^{\text{con}} \mathbb{1} & \mathcal{L}_{j,1}^{\text{con}} \mathbb{1} & \mathcal{L}_{j,2}^{\text{con}} \mathbb{1} \end{bmatrix}. \quad (2.41)$$

The contact stiffness contribution is computed using the abbreviation

$$\hat{\mathbf{H}} = \begin{bmatrix} \mathcal{L}_{i,1}^{\text{con}} \mathbb{1} & \mathcal{L}_{i,2}^{\text{con}} \mathbb{1} & \mathbf{0} & \mathbf{0} \\ \mathbf{0} & \mathbf{0} & \mathcal{L}_{j,1}^{\text{con}} \mathbb{1} & \mathcal{L}_{j,2}^{\text{con}} \mathbb{1} \end{bmatrix}, \quad (2.42)$$

and with the matrices

$$\bar{\mathbf{A}} = \begin{bmatrix} -\mathbf{x}_i^{\text{con}'} \cdot \mathbf{x}_i^{\text{con}'} & \mathbf{x}_j^{\text{con}'} \cdot \mathbf{x}_i^{\text{con}'} \\ -\mathbf{x}_i^{\text{con}'} \cdot \mathbf{x}_j^{\text{con}'} & \mathbf{x}_j^{\text{con}'} \cdot \mathbf{x}_j^{\text{con}'} \end{bmatrix}, \quad (2.43)$$

$$\bar{\mathbf{B}} = \begin{bmatrix} \mathbf{x}_i^{\text{con}'T} & -\mathbf{x}_i^{\text{con}'T} \\ \mathbf{x}_j^{\text{con}'T} & -\mathbf{x}_j^{\text{con}'T} \end{bmatrix}, \quad (2.44)$$

$$\bar{\mathbf{C}} = \begin{bmatrix} -\mathbf{x}_i^{\text{con}T} - \mathbf{x}_j^{\text{con}T} & \mathbf{0} \\ \mathbf{0} & \mathbf{x}_i^{\text{con}T} - \mathbf{x}_j^{\text{con}T} \end{bmatrix}, \quad (2.45)$$

$$\bar{\mathbf{D}} = \left[ \bar{\mathbf{A}}^{-1} \left( \bar{\mathbf{B}} \hat{\mathbf{H}} + \bar{\mathbf{C}} \hat{\mathbf{H}}' \right) \right] = \begin{bmatrix} \mathbf{d}_{ii} & \mathbf{d}_{ij} \\ \mathbf{d}_{ji} & \mathbf{d}_{jj} \end{bmatrix}, \quad (2.46)$$

$$\bar{\mathbf{E}} = \begin{bmatrix} \left[ -\mathcal{L}_{i,1}^{\text{con}'} \mathbb{1} \quad -\mathcal{L}_{i,2}^{\text{con}'} \mathbb{1} \right]^T \hat{\mathbf{n}} \left[ \mathbf{d}_{ii} \quad \mathbf{d}_{ij} \right] \\ \left[ \mathcal{L}_{j,1}^{\text{con}'} \mathbb{1} \quad \mathcal{L}_{j,2}^{\text{con}'} \mathbb{1} \right]^T \hat{\mathbf{n}} \left[ \mathbf{d}_{ji} \quad \mathbf{d}_{jj} \right] \end{bmatrix}, \quad (2.47)$$

and

$$G_1 = \tilde{\mathbf{H}}^T + [\mathbf{d}_{ji} \quad \mathbf{d}_{jj}]^T \mathbf{x}'_j^T - [\mathbf{d}_{ii} \quad \mathbf{d}_{ij}]^T \mathbf{x}'_i^T, \quad (2.48)$$

$$G_2 = \mathbb{1} - \hat{\mathbf{n}}\hat{\mathbf{n}}^T, \quad (2.49)$$

$$G_3 = \tilde{\mathbf{H}} + [\mathbf{d}_{ji} \quad \mathbf{d}_{jj}] \mathbf{x}'_j - [\mathbf{d}_{ii} \quad \mathbf{d}_{ij}] \mathbf{x}'_i, \quad (2.50)$$

$$\bar{\mathbf{G}} = \frac{\mathbf{G}_1 \mathbf{G}_2 \mathbf{G}_3}{g}, \quad (2.51)$$

as

$$\mathbf{K}_{\text{con}} = \begin{bmatrix} \mathbf{K}_{\text{con}}^{i_1 i_1} & \mathbf{K}_{\text{con}}^{i_1 i_2} & \mathbf{K}_{\text{con}}^{i_1 j_1} & \mathbf{K}_{\text{con}}^{i_1 j_2} \\ \mathbf{K}_{\text{con}}^{i_2 i_1} & \mathbf{K}_{\text{con}}^{i_2 i_2} & \mathbf{K}_{\text{con}}^{i_2 j_1} & \mathbf{K}_{\text{con}}^{i_2 j_2} \\ \mathbf{K}_{\text{con}}^{j_1 i_1} & \mathbf{K}_{\text{con}}^{j_1 i_2} & \mathbf{K}_{\text{con}}^{j_1 j_1} & \mathbf{K}_{\text{con}}^{j_1 j_2} \\ \mathbf{K}_{\text{con}}^{j_2 i_1} & \mathbf{K}_{\text{con}}^{j_2 i_2} & \mathbf{K}_{\text{con}}^{j_2 j_1} & \mathbf{K}_{\text{con}}^{j_2 j_2} \end{bmatrix} = \varepsilon \left( \tilde{\mathbf{H}}^T \hat{\mathbf{n}}\hat{\mathbf{n}}^T \tilde{\mathbf{H}} + g (\bar{\mathbf{E}} + \bar{\mathbf{E}}^T + \bar{\mathbf{G}}) \right). \quad (2.52)$$

The superscripts  $i_{1,2}, j_{1,2}$  correspond to the degrees of freedom (DOFs) for the first and second node of the element pair  $i$  and  $j$ .

**Closest approach within one element** In the case, when the point of the closest approach is contained within one element but outside the other element, i.e.

$$\xi_i^{\text{con}} \in [-1, 1] \oplus \xi_j^{\text{con}} \in [-1, 1], \quad (2.53)$$

initially, it is checked which end of the non-included beam is closer to the included beam. For the remainder of this explanation, it is assumed, that the closest approach is within element  $i$  ( $\xi_i^{\text{con}} \in [-1, 1]$ ), but outside element  $j$  ( $\xi_j^{\text{con}} \notin [-1, 1]$ ). By simple exchange of the indices, the same procedure may also be employed for the case with  $\xi_i^{\text{con}} \notin [-1, 1]$  and  $\xi_j^{\text{con}} \in [-1, 1]$ . For the further computation a non-symmetric contact formulation, which is based on the two-dimensional node-to-segment discretization from [WS85], is employed. In a first step, the end of element  $j$ , that is taking the role of the secondary node  $\mathbf{x}_j^s$  is determined

$$\mathbf{x}_j^s = \begin{cases} \mathbf{x}_j^1, & \text{for } \xi_j^{\text{con}} < -1 \\ \mathbf{x}_j^2, & \text{for } \xi_j^{\text{con}} > 1 \end{cases}. \quad (2.54)$$

The next step is to calculate the closest point  $\xi_i^m$  on the main element  $i$  to this node  $\mathbf{x}_j^s$  to ensure orthogonality on the segment for the contact using

$$\xi_i^m = \frac{2(\mathbf{x}_j^s \cdot \mathbf{t}_i) - (\mathbf{t}_i \cdot \mathbf{b}_i)}{(\mathbf{t}_i \cdot \mathbf{t}_i)} \quad (2.55)$$

If this point is outside the element  $\xi_i^m \notin [-1, 1]$  no contact is found, and the algorithm is terminated for this pairing. Otherwise, with the contact position on the main element  $\mathbf{x}_i^m = \mathbf{x}(\xi_i^m)$ , and the contact normal  $\hat{\mathbf{n}} = (\mathbf{x}_j^s - \mathbf{x}_i^m) / |\mathbf{x}_j^s - \mathbf{x}_i^m|$ , three matrices are constructed:

$$\hat{\mathbf{N}}_s = \begin{bmatrix} \hat{\mathbf{n}} \\ -\frac{1}{2}(1 - \xi_i^m) \hat{\mathbf{n}} \\ -\frac{1}{2}(1 + \xi_i^m) \hat{\mathbf{n}} \end{bmatrix}, \quad \mathbf{T}_s = \begin{bmatrix} \mathbf{t}_i \\ -\frac{1}{2}(1 - \xi_i^m) \mathbf{t}_i \\ -\frac{1}{2}(1 + \xi_i^m) \mathbf{t}_i \end{bmatrix}, \quad \hat{\mathbf{N}} = \begin{bmatrix} \mathbf{0} \\ \mathbf{0} \\ \hat{\mathbf{n}} \end{bmatrix}. \quad (2.56)$$

Using these matrices, the nodal forces as well as the stiffness contributions can be computed with the independent node-to-segment penalty parameter  $\varepsilon_{\text{NTS}}$  as

$$\mathbf{f}_{\text{con}} = \varepsilon_{\text{NTS}} \langle g \rangle^1 \hat{\mathbf{N}}_s, \quad (2.57)$$

$$\mathbf{K}_{\text{con}} = \varepsilon_{\text{NTS}} \langle g \rangle^0 \hat{\mathbf{N}}_s \otimes \hat{\mathbf{N}}_s - \frac{\langle g \rangle^1}{|t_i|} \left( \hat{\mathbf{N}} \otimes \mathbf{T}_s + \mathbf{T}_s \otimes \hat{\mathbf{N}} + \frac{\langle g \rangle^1}{|t_i|} \hat{\mathbf{N}} \otimes \hat{\mathbf{N}} \right). \quad (2.58)$$

With the nodal indices sorted for the superscript  $s$  as secondary node and  $m_{1,2}$  for the two nodes of the main element:

$$\mathbf{f}_{\text{con}} = \begin{bmatrix} \mathbf{f}_{\text{con}}^s \\ \mathbf{f}_{\text{con}}^{m_1} \\ \mathbf{f}_{\text{con}}^{m_2} \end{bmatrix}, \quad (2.59)$$

$$\mathbf{K}_{\text{con}} = \begin{bmatrix} \mathbf{K}_{\text{con}}^{ss} & \mathbf{K}_{\text{con}}^{sm_1} & \mathbf{K}_{\text{con}}^{sm_2} \\ \mathbf{K}_{\text{con}}^{m_1s} & \mathbf{K}_{\text{con}}^{m_1m_1} & \mathbf{K}_{\text{con}}^{m_1m_2} \\ \mathbf{K}_{\text{con}}^{m_2s} & \mathbf{K}_{\text{con}}^{m_2m_1} & \mathbf{K}_{\text{con}}^{m_2m_2} \end{bmatrix}. \quad (2.60)$$

**Closest approach outside both elements** In the case, when the point of the closest approach is outside both elements, i.e.

$$\xi_i^{\text{con}} \notin [-1, 1] \wedge \xi_j^{\text{con}} \notin [-1, 1], \quad (2.61)$$

again, a node-to-segment contact is assumed. For all four nodes potentially included in this contact, the algorithm described in the previous paragraph is employed, i.e. four potential contacts are computed.

### JOINT CONTACT

Besides the contact between different structural members of the truss, also contact between joints, i.e. end-points of the beams is implemented. For this a simple contact formulation between two spheres with a radius equivalent to that of the beams is used. For every pair of nodes representing joints  $i, j$ , the gap is defined as

$$g = |\mathbf{x}_i - \mathbf{x}_j| - r_i - r_j. \quad (2.62)$$

The corresponding force is again defined with the independent node-to-node penalty  $\varepsilon_{\text{NTN}}$  as

$$\mathbf{f}_{\text{con}} = \varepsilon_{\text{NTN}} \langle g \rangle^1, \quad (2.63)$$

and is added to the nodal forces of the joints in a straightforward manner

$$\mathbf{f}_{\text{con}}^i = f_{\text{con}} \hat{\mathbf{n}}, \quad \mathbf{f}_{\text{con}}^j = -f_{\text{con}} \hat{\mathbf{n}}, \quad (2.64)$$

with the contact normal defined as

$$\hat{\mathbf{n}} = \frac{\mathbf{x}_i - \mathbf{x}_j}{|\mathbf{x}_i - \mathbf{x}_j|}. \quad (2.65)$$

The transformation matrix from the local system of the contact to the global system can be defined as the dyadic product of the normal vector as

$$T_{\text{con}} = \hat{\mathbf{n}} \otimes \hat{\mathbf{n}}, \quad (2.66)$$

and the stiffness contributions can then be written in compact form as

$$\mathbf{K}_{\text{con}} = \begin{bmatrix} \mathbf{K}_{\text{con}}^{ii} & \mathbf{K}_{\text{con}}^{ij} \\ \mathbf{K}_{\text{con}}^{ji} & \mathbf{K}_{\text{con}}^{jj} \end{bmatrix} = \begin{bmatrix} \varepsilon_{\text{NTN}} \mathbf{T}_{\text{con}} & -\varepsilon_{\text{NTN}} \mathbf{T}_{\text{con}} \\ -\varepsilon_{\text{NTN}} \mathbf{T}_{\text{con}} & \varepsilon_{\text{NTN}} \mathbf{T}_{\text{con}} \end{bmatrix} \quad (2.67)$$

### ASSEMBLY

Finally, all contact contributions can be assembled into the global force vector

$$\mathbf{f}_{\text{res}} = \mathbf{f}_{\text{ext}} - \sum_{e,i} \mathbf{f}_{\text{int}}^{e,i} - \sum_{c,i} \mathbf{f}_{\text{con}}^{c,i}, \quad (2.68)$$

where the assembly operation for the contact is iterating over the contacts  $c$  and nodes  $i$  as opposed to the elements  $e$  and nodes  $i$  for the internal force vector. Similar procedures are employed for the global tangent matrix.

### NUMERICAL BENCHMARK

To ensure the correct implementation of the contact algorithm, a comparison with *Example 2* from [ZW00] is undertaken. In this case, two circular beams are modelled using two node linear elements. The horizontal beam is 14 units long, the vertical one 10 units and the distance between the centrelines is 1 unit. The geometric configuration can be seen in Figure 2.6. The material is assumed to be elastic with  $E = 10^8$  and  $\nu = 0$ .<sup>2</sup> The area and moments of inertia are assumed to be  $A = 4 \times 10^{-2}$ ,  $I = 2 \times 10^{-4}$  and the contact radius is taken to be  $r = 0.2$ . The contact parameters for beam contact are set to be  $\varepsilon_{\text{STS}} = \varepsilon_{\text{NTS}} = 10^4$ . The horizontal

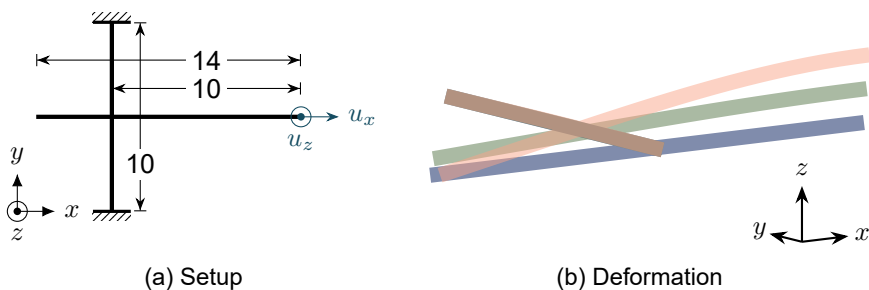


Figure 2.6.: Setup of *Example 2* from [ZW00] and deformed configurations of the beams at different steps. Colours correspond to the steps in Figure 2.7.

beam is free at the left end and a movement of  $u_z = 0.3$  per step and  $u_x = 0.03$  per

<sup>2</sup>See Chapter 3 for details and explanation of the material modelling.

step are imposed on the right end. The vertical beam is clamped at both ends. The simulation is run for 6 steps. The setup for the simulation is visualized in Figure 2.6a and the deformation of the beams for different steps is presented in Figure 2.6. We

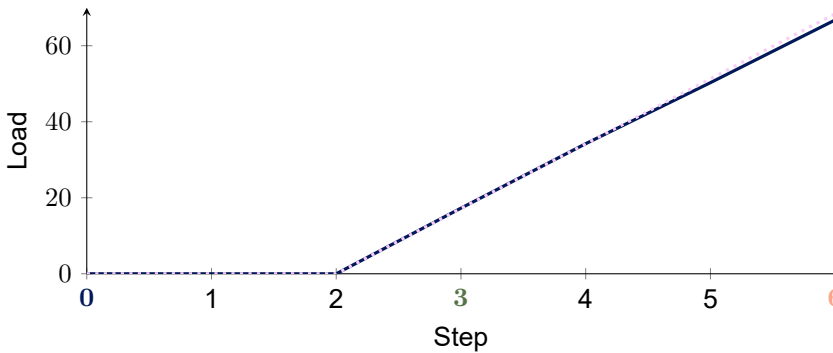


Figure 2.7.: Load-deflection curves for two beams in (frictionless) contact. Solid lines depict this work, dotted lines the reference [ZW00].

can see the good agreement between the present implementation and the results in literature in Figure 2.7, where the contact force per loading step is depicted.

## 2.4. ADAPTIVE TIME MARCHING

The methodology discussed so far is for static problems, but impact events consist not only of large but also of fast deformations. Thus, the implementation also needs to be able to represent dynamic effects. For this work a simple predictor-corrector approach with step size control is implemented to accommodate dynamic loading and is presented in the following.

The second order differential equation system describing the motion of the beam is,

$$\begin{aligned} \mathbf{n}_{\text{ext}} - \mathbf{n}'(s) &= \rho A \ddot{\mathbf{x}}(s), \\ \mathbf{m}_{\text{ext}} - (\mathbf{m}'(s) + \mathbf{n}(s) \times \mathbf{x}'(s)) &= \Theta(s) \dot{\omega}(s) + \omega(s) \times \Theta(s) \omega(s), \end{aligned} \quad (2.69)$$

with  $\Theta$  denoting the rotational inertia of the rigid cross-section and a superimposed dot representing time derivatives. This is discretized for the FE system as

$$\begin{bmatrix} \ddot{\mathbf{u}} \\ \dot{\omega} \end{bmatrix} = \begin{bmatrix} \mathcal{M} & 0 \\ 0 & \Theta \end{bmatrix}^{-1} \left( \begin{bmatrix} \mathbf{n}_{\text{ext}} \\ \mathbf{m}_{\text{ext}} \end{bmatrix} - \begin{bmatrix} \mathbf{n}' \\ \mathbf{m}' + \mathbf{n} \times \mathbf{x}' \end{bmatrix} - \begin{bmatrix} 0 \\ \omega \times \Theta \omega \end{bmatrix} \right), \quad (2.70)$$

and transformed into a first order system by introducing the velocities (translational velocity  $\mathbf{v}$  and angular velocity  $\omega$ ) as additional state variables:

$$\begin{bmatrix} \dot{\mathbf{v}} \\ \dot{\omega} \\ \dot{\mathbf{u}} \\ \dot{\Lambda} \end{bmatrix} = \begin{bmatrix} \begin{bmatrix} \mathcal{M} & 0 \\ 0 & \Theta \end{bmatrix}^{-1} (\mathbf{f}_{\text{ext}} - \mathbf{f}_{\text{int}} - \mathbf{f}_{\text{gyro}} - \mathbf{f}_{\text{con}}) \\ \begin{bmatrix} \mathbf{v} \\ \tilde{\omega} \Lambda \end{bmatrix} \end{bmatrix}. \quad (2.71)$$

The translational part of the inertia matrix  $\mathcal{M}$  is consistently assembled, while the rotational part  $\Theta$  is *lumped* at each node resulting in the equivalent of a rigid body (with regard to the rotational DOFs) at each node. It should also be noted, that the angular velocity is not equal to the derivative of the rotation vector, as the latter is only a numerical representation of rotation  $\Lambda \in \text{SO}(3)$ . Also, the gyroscopic force vector  $f_{\text{gyro}}$  is defined and added to the resulting dynamic forces  $f_{\text{res}}$ :

$$\begin{aligned} f_{\text{gyro}} &= \begin{bmatrix} \mathbf{0} \\ \boldsymbol{\omega} \times \boldsymbol{\Theta} \boldsymbol{\omega} \end{bmatrix}, \\ f_{\text{res}} &= f_{\text{ext}} - f_{\text{int}} - f_{\text{gyro}} - f_{\text{con}}. \end{aligned} \quad (2.72)$$

In this work, the predictor-corrector scheme was accompanied by adaptive time stepping using a Milne-Device<sup>3</sup> as estimator for the error. A pair of explicit and implicit Euler schemes as predictor-corrector pair is chosen for simplicity. In the prediction step, the state variables are updated with time step  $\Delta t_n$  according to the explicit Euler rule, where the resulting force vector is assembled as described in the previous sections:

$$\begin{aligned} \begin{bmatrix} \mathbf{v}_{n+1}^p \\ \boldsymbol{\omega}_{n+1}^p \end{bmatrix} &= \begin{bmatrix} \mathbf{v}_n \\ \boldsymbol{\omega}_n \end{bmatrix} + \Delta t_n \left( \begin{bmatrix} \mathcal{M}_n & \mathbf{0} \\ \mathbf{0} & \boldsymbol{\Theta}_n \end{bmatrix}^{-1} \cdot f_{\text{res},n} \right), \\ \begin{bmatrix} \mathbf{u}_{n+1}^p \\ \boldsymbol{\Lambda}_{n+1}^p \end{bmatrix} &= \begin{bmatrix} \mathbf{u}_n + \Delta t_n \mathbf{v}_n \\ \exp(\Delta t_n \boldsymbol{\omega}_n) \cdot \boldsymbol{\Lambda}_n \end{bmatrix}. \end{aligned} \quad (2.73)$$

The integration of the rotational displacements is done using an exponential integrator (see e.g. [Mun15]).

The forces associated with the predicted values  $f_{\text{res},n+1}^p$  are computed and then used in the corrector step using the implicit Euler rule:

$$\begin{aligned} \begin{bmatrix} \mathbf{v}_{n+1}^c \\ \boldsymbol{\omega}_{n+1}^c \end{bmatrix} &= \begin{bmatrix} \mathbf{v}_n \\ \boldsymbol{\omega}_n \end{bmatrix} + \Delta t_n \left( \begin{bmatrix} \mathcal{M}_n & \mathbf{0} \\ \mathbf{0} & \boldsymbol{\Theta}_n \end{bmatrix}^{-1} \cdot f_{\text{res},n+1}^p \right), \\ \begin{bmatrix} \mathbf{u}_{n+1}^c \\ \boldsymbol{\Lambda}_{n+1}^c \end{bmatrix} &= \begin{bmatrix} \mathbf{u}_n + \Delta t_n \widetilde{\mathbf{v}_{n+1}^p} \\ \exp(\Delta t_n \widetilde{\boldsymbol{\omega}_{n+1}^p}) \cdot \boldsymbol{\Lambda}_n \end{bmatrix}. \end{aligned} \quad (2.74)$$

Next, in order to obtain an estimate for the error introduced by the time stepping, the results of the predictor stage and the results of the corrector stage are compared and used to compute an estimation for the current error  $e_{\text{est}}$ :

$$e_{\text{est}} = \frac{\left\| \begin{bmatrix} l_0^{-1} \\ \mathbf{0} \end{bmatrix} \cdot \left( \begin{bmatrix} \mathbf{u}_{n+1}^p \\ \boldsymbol{\vartheta}_{n+1}^p \end{bmatrix} - \begin{bmatrix} \mathbf{u}_{n+1}^c \\ \boldsymbol{\vartheta}_{n+1}^c \end{bmatrix} \right) \right\|}{\sqrt{n_{\text{dof}}} + \Delta t_n \frac{\left\| \begin{bmatrix} l_0^{-1} \\ \mathbf{0} \end{bmatrix} \cdot \left( \begin{bmatrix} \mathbf{v}_{n+1}^p \\ \boldsymbol{\omega}_{n+1}^p \end{bmatrix} - \begin{bmatrix} \mathbf{v}_{n+1}^c \\ \boldsymbol{\omega}_{n+1}^c \end{bmatrix} \right) \right\|}{\sqrt{n_{\text{dof}}}}. \quad (2.75)$$

<sup>3</sup>Named after Milne [Mil26], the error is estimated by comparing the leading terms of the local truncation error of two different methods of the same order

Here the translational DOFs are scaled with the inverse size of the typical critical length scale of the problem  $l_0$ . For example in the case of contact it is set to one tenth of the contact radius, i.e.  $l_0 = \frac{r_{\text{con}}}{10}$ . Using this estimated error the next step size is computed to result in a desired error of  $e_{\text{tol}}$ :

$$\Delta t_n^{\text{opt}} = \Delta t_n \sqrt{\frac{e_{\text{tol}}}{0.5e_{\text{est}}}}. \quad (2.76)$$

Based on the estimated error it is also decided whether to accept the current step. The step is accepted if  $e_{\text{est}} < e_{\text{tol}}$  or if the step was calculated with the minimal step size  $\Delta t_n = \Delta t_{\text{min}}$ . If the solution is accepted the step size for the following step is determined by

$$\Delta t_{n+1} = \max (\min (r_{\text{safe}} \Delta t_n^{\text{opt}}, r_{\text{incr}} \Delta t_n, \Delta t_{\text{max}}), r_{\text{decr}} \Delta t_n, \Delta t_{\text{min}}), \quad (2.77)$$

where  $r_{\text{safe}} < 1$  is the safety factor for the optimal step size,  $r_{\text{decr}} < 1$  the decrease factor and  $r_{\text{incr}} > 1$  the increase factor from the current step size. If the step is not accepted, the solution is rejected and the step is restarted with a smaller step size determined from

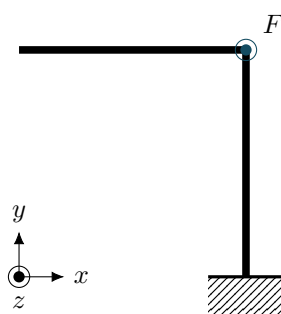
$$\Delta t_n^{\text{rep}} = \max (r_{\text{safe}} \Delta t_n^{\text{opt}}, r_{\text{decr}} \Delta t_n, \Delta t_{\text{min}}). \quad (2.78)$$

The next step is then calculated with the same procedure, starting again at Equation (2.73).

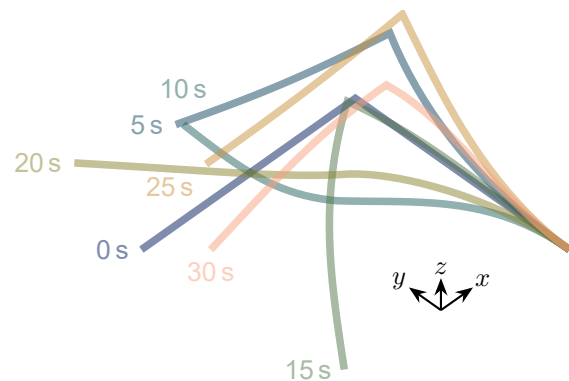
### NUMERICAL BENCHMARK

In order to ensure correct implementation of the algorithm, it is benchmarked against *Example 5.2* from [SV88]. In this benchmark, an angled cantilever beam is loaded for a short period at the elbow and left swinging freely. The initial time step size was set to  $\Delta t_0 = 10^{-5}$  s with a desired error of  $e_{\text{tol}} = 10^{-4}$ . The material properties are without units set such, that  $kG = EA = 10^6$  and  $EI = GJ = 10^3$  are resulting for the static properties and  $A\varrho = 1$ ,  $I\varrho = 10$ , and  $J\varrho = 20$  for the dynamic properties.<sup>4</sup> The legs of the beam are each 10 units long, and the beam is discretized using 10 quadratic elements per leg. A load  $F$  is applied at the elbow in  $z$ -direction, that is linearly rising over to first second up to a value of 50 and linearly falling again to reach 0 at  $t = 2$  s. A top view of this setup is shown in Figure 2.8a. The movement of the beam over 30 s can be seen in Figure 2.8b. We can see a good agreement between the present implementation and the results in literature in Figure 2.9. The minor differences may be again explained by the software used to acquire the data from the limited resolution in the graphs of [SV88].

<sup>4</sup>See Chapter 3 for details and explanation of the material modelling.



(a) Setup of the Benchmark



(b) Deformed configurations

Figure 2.8.: Setup and deformed configurations of the angled cantilever beam swinging at time steps  $t = 0\text{ s}$ ,  $5\text{ s}$ ,  $10\text{ s}$ ,  $15\text{ s}$ ,  $20\text{ s}$ ,  $25\text{ s}$  and  $30\text{ s}$ .

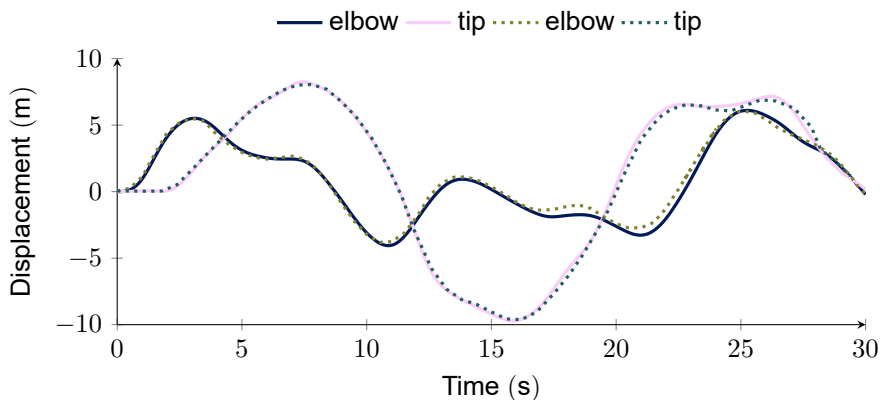


Figure 2.9.: Displacement in loading direction over time for the elbow and tip of the system. Solid lines depict this work, dotted lines the reference [SV88].

## REFERENCES

[Ant05] S. S. Antman. *Nonlinear Problems of Elasticity*. 2nd ed. Applied Mathematical Sciences. Springer, 2005.

[Bat06] K.-J. Bathe. *Finite element procedures*. 2nd ed. 2006.

[CJ99] M. A. Crisfield and G. Jelenić. 'Objectivity of strain measures in the geometrically exact three-dimensional beam theory and its finite-element implementation'. *Proc. R. Soc. A-Math. Phys. Eng. Sci.* **455** (1999), pp. 1125–1147.

[Eug15] S. R. Eugster. *Geometric Continuum Mechanics and Induced Beam Theories*. Lecture Notes in Applied and Computational Mechanics. Springer, 2015.

[JIVE] Dynaflow Research Group. *JIVE*. Version 3.0. 1st Apr. 2021.

[Mil26] W. E. Milne. 'Numerical Integration of Ordinary Differential Equations'. *Am. Math. Mon.* **33** (1926), pp. 455–460.

[Mun15] H. Z. Munthe-Kaas. 'Lie Group Integrators'. In: *Encyclopedia of Applied and Computational Mathematics*. Springer, 2015, pp. 787–790.

[Rei81] E. Reissner. 'On Finite Deformations of Space-Curved Beams'. *Z. Angew. Math. Phys.* **32** (1981), pp. 734–744.

[Rub00] M. B. Rubin. *Cosserat Theories: Shells, Rods and Points*. Solid Mechanics and Its Applications. Springer, 2000.

[Sch99] M. Schäfer. *Numerik im Maschinenbau*. Springer-Lehrbuch. Springer, 1999.

[Sim85] J. C. Simo. 'A finite strain beam formulation. The three-dimensional dynamic problem. Part I'. *Comput. Methods Appl. Mech. Eng.* **49** (1985), pp. 55–70.

[SV86] J. C. Simo and L. Vu-Quoc. 'A three-dimensional finite-strain rod model. part II: Computational aspects'. *Comput. Methods Appl. Mech. Eng.* **58** (1986), pp. 79–116.

[SV88] J. C. Simo and L. Vu-Quoc. 'On the dynamics in space of rods undergoing large motions — A geometrically exact approach'. *Comput. Methods Appl. Mech. Eng.* **66** (1988), pp. 125–161.

[WPD] A. Rohatgi. *WebPlotDigitizer*. Version 4.6. 1st Dec. 2022.

[Wri06] P. Wriggers. *Computational Contact Mechanics*. 2nd ed. Springer, 2006.

[WS85] P. Wriggers and J. C. Simo. 'A Note on Tangent Stiffness for Fully Nonlinear Contact Problems'. *Commun. Appl. Numer. Methods* **1** (1985), pp. 199–203.

[WZ97] P. Wriggers and G. Zavarise. 'On contact between three-dimensional beams undergoing large deflections'. *Commun. Numer. Methods Eng.* **13** (1997), pp. 429–438.

[ZW00] G. Zavarise and P. Wriggers. 'Contact with friction between beams in 3-D space'. *Int. J. Numer. Methods Eng.* **49** (2000), pp. 977–1006.





# 3

## **NUMERICAL MODELLING OF THE MATERIAL BEHAVIOUR**

*A yield function in the stress-resultant space of geometrically exact beams based on the elastoplastic cross-sectional warping problem has been proposed by Herrmböck, Kumar and Steinmann (2021). This plasticity framework has been extended with a hardening tensor to model the kinematic hardening effects in Herrmböck, Kumar and Steinmann (2022). While this framework provides scaling for the yield surface in ideal plasticity, scaling in hardening plasticity has not yet been explored. This chapter focuses on the numeric modelling of hardening beams and beam assemblies at different geometric scales. Discretization effects from the introduction of plasticity into the geometrically exact beam model are demonstrated. Furthermore, the effects of scaling are explored, and a method to mitigate undesirable effects in order to achieve a size-agnostic formulation is proposed. Consistent geometric scaling is demonstrated for two alternative scaling approaches of the yield function.*

## 3.1. INTRODUCTION

Beams undergo large, plastic deformations in various applications, such as the weaving of chain-link fences, the production of paper clips, or the crushing of architected lattice materials. The latter are man-made structures in demand for a wide range of applications, from sports equipment to protective systems in a military context [Cro19; SDC16; TZH22]. These lattice materials, can be seen as a collection of beams, and are represented accordingly in an FE context. In the given applications, metal lattices undergo large deformations that may include material non-linearities. In order to design such materials, a proper representation of the beams undergoing large deformations with the corresponding inelastic material behaviour is required. The representation of beams undergoing large deformations with elastic material behaviour following the Simo-Reissner (after [Rei81; Sim85]) beam theory is well established as laid out in [Chapter 2](#).

Irreversible deformation of the beam structures, i.e., plasticity, is not considered in these formulations. When including plasticity into the beam models, one has two options: The plastic deformation can be concentrated at distinct cross-sections throughout the beam, or it can be distributed over the entire beam. The first approach corresponds to so-called *plastic hinges*, represented by strong discontinuities along the beam and thus introduced as such into the FE model [TJ21; Toj<sup>&al</sup>23]. The second approach is to introduce plasticity into the description of the beam-type strain-prescriptors itself. Smriti et al. [Smr<sup>&al</sup>18] present a thermo-elasto-plastic formulation for such an approach, with an FE implementation described in [SKS20]. A similar approach is taken by Weeger et al. [Wee<sup>&al</sup>23], where a formulation for elasto-visco-plastic beams is presented in an isogeometric framework. The introduction of plasticity into the strain-prescriptors of the beam is closest to traditional continuum plasticity and straightforward to be implemented in an existing framework, as no changes in the geometric representation are required. One problem not solved in these approaches is, however, the determination of a yield criterion for the formulation at hand. This issue could be relegated back to the material scale by introducing a *subintegration* across the cross-section in each integration point of the beam element, as presented in [Kar<sup>&al</sup>23]. This approach is also used in most commercial FE codes.

For the purpose of this investigation, a yield surface in the six-dimensional stress-resultant space is chosen, in order to ensure fast computation. Early approaches to this are limited to simple deformations and do not include any hardening behaviour of the material [DC90; SHT84]. More recently, Herrnböck, Kumar and Steinmann [HKS21] formulate an approach to systematically determine the yield surface using the formulation of [SKS20; Smr<sup>&al</sup>18] for a given cross-section and material model, based on simulations of the cross-section on the material scale. The procedure is demonstrated with a J2-plasticity model for a generic steel in beams with circular and square cross-sections. The authors also demonstrate the geometric scaling behaviour of the resulting yield surface. This can be motivated based on the fact, that the beam-type stress-resultants are essentially cross-sectional forces and moments. They extend their approach to kinematic hardening in [HKS22] for the circular cross-section without considering geometric scaling. The extension demon-

strates a good agreement with a FE<sup>2</sup> approach utilizing the identical plasticity model in their test cases. The discrepancies observed can be attributed to the fact that, in the stress-resultant approach, the entire cross-section plastifies simultaneously, whereas in reality a more gradual plastification process occurs [HKS22]. It is shown how the kinematic hardening tensor is a full matrix and that it relates to microscale isotropic hardening, that is assumed for the underlying material behaviour. The geometric scaling of hardening plasticity in beam formulations has not been investigated so far in literature. However, it is of paramount importance for the targeted design of lattice materials structures exposed to severe straining.

In this chapter, the geometric scaling behaviour of the kinematic hardening formulation from Herrnböck, Kumar and Steinmann [HKS22] is investigated. An adequate scaling approach to be used in the design process of lattice structures representing metal metamaterials undergoing large inelastic deformations for the remainder of this dissertation is introduced. In Section 3.2 the theoretical background for the investigations is laid out, followed by a mesh convergence study in Section 3.3. The extent of the geometric scaling in the existing formulation, not considering the hardening tensor, is demonstrated in Section 3.4 using a simple bending cantilever together with its limitations, followed by the proposal to mitigate this effect. In Section 3.5 it is demonstrated, how to apply the proposed strategy to different yield functions, and the results in a three-dimensional setting are presented.

## 3.2. THEORETICAL BACKGROUND

The following treatise extends the geometric description of the geometrically exact beam given in Chapter 2 by incorporating the material behaviour in the laid out framework.

Summarizing the material strain-prescriptors  $\Gamma, \mathcal{K}$  in  $\mathcal{E} = [\Gamma \quad \mathcal{K}]^T$ , their initial, elastic relation to the material stress-resultants  $N, M$ , summarized as  $\Sigma$ , is usually described using the following formula:

$$\Sigma = \begin{bmatrix} N \\ M \end{bmatrix} = C \begin{bmatrix} \Gamma \\ \mathcal{K} \end{bmatrix} = C\mathcal{E}, \quad (3.1)$$

where the material stiffness matrix  $C$  already introduced earlier, in the context of point-symmetric cross-sections showing homogeneous, isotropic material distributions, is expressed using the engineering constants  $E$  as the Young's modulus,  $G$  as the shear modulus,  $A$  as the area of the cross-section,  $I_1, I_2$  as the area moments of inertia in the directions of the directors  $d_1, d_2$ ,  $J$  as the polar moment of inertia, and  $k$  as the shear correction coefficient:

$$C = \begin{bmatrix} kGA & 0 & 0 & 0 & 0 & 0 \\ 0 & kGA & 0 & 0 & 0 & 0 \\ 0 & 0 & EA & 0 & 0 & 0 \\ 0 & 0 & 0 & EI_1 & 0 & 0 \\ 0 & 0 & 0 & 0 & EI_2 & 0 \\ 0 & 0 & 0 & 0 & 0 & GJ \end{bmatrix}. \quad (3.2)$$

It should be mentioned here, that this material stiffness matrix *implicitly* scales with changes in the geometry, as the area and its second moments are defined using the geometry of the cross-section. This implicit scaling refers to the fact that the terms do not have a geometric scaling factor *explicitly* present in their analytical definition, but are naturally adapted based on the geometry. For instance, the area  $A = \pi r^2$  is not defined by a scaling factor, but it is defined by the radius  $r$ , which is assumed to be scaled with the rest of the geometry. The stress-resultants are again expressed in the inertial frame of reference, using lower case symbols  $\sigma = [n \ m]^T$ :

$$n = \Lambda N, \quad (3.3)$$

$$m = \Lambda M. \quad (3.4)$$

While the description thus far is purely elastic, beams undergoing large deformations are expected to exhibit inelastic behaviour. This inelastic behaviour must be captured in the numerical description as well. Here, we focus our attention on the description of kinematic hardening plasticity in the six-dimensional stress-resultant space of a beam, following [HKS21; HKS22; Smr<sup>&al</sup>18].

First, the strain-prescriptors are additively decomposed into elastic and plastic parts as in [Smr<sup>&al</sup>18]:

$$\mathcal{E} = \mathcal{E}^e + \mathcal{E}^p. \quad (3.5)$$

Using this decomposition, we can introduce the Helmholtz energy density  $\Psi$  from [Smr<sup>&al</sup>18]:

$$\Psi = \frac{1}{2} \mathcal{E}^{eT} C \mathcal{E}^e + \frac{1}{2} \mathcal{M}^T H \mathcal{M}, \quad (3.6)$$

with the invertible, symmetric, constant  $6 \times 6$  hardening tensor  $H$  and the internal hardening variables  $\mathcal{M} = [\mathcal{M}_1^\Gamma \ \mathcal{M}_2^\Gamma \ \mathcal{M}_3^\Gamma \ \mathcal{M}_1^K \ \mathcal{M}_2^K \ \mathcal{M}_3^K]^T$ . Furthermore, the yield function in the stress-resultant space as proposed in [HKS22] is introduced as

$$\Phi = \left| \frac{N_1}{N_1^y - N_1^h} \right|^{\alpha_1^N} + \left| \frac{N_2}{N_2^y - N_2^h} \right|^{\alpha_2^N} + \left| \frac{N_3}{N_3^y - N_3^h} \right|^{\alpha_3^N} + \left| \frac{M_1}{M_1^y - M_1^h} \right|^{\alpha_1^M} + \left| \frac{M_2}{M_2^y - M_2^h} \right|^{\alpha_2^M} + \left| \frac{M_3}{M_3^y - M_3^h} \right|^{\alpha_3^M} - 1 \leq 0. \quad (3.7)$$

The hardening stress-resultants  $\Sigma^h = [N^h \ M^h]^T$  in this equation can be determined using the internal hardening variables  $\mathcal{M}$  and the hardening tensor  $H$  as shown in [Smr<sup>&al</sup>18]:

$$\Sigma^h = -\frac{\partial \Psi}{\partial \mathcal{M}} = -\frac{1}{2} \frac{\partial (\mathcal{M}^T H \mathcal{M})}{\partial \mathcal{M}} = -H \mathcal{M}. \quad (3.8)$$

The associative flow rule introduced in [Smr<sup>&al</sup>18] is expressed for the rate of the plastic strain-prescriptors  $\mathcal{E}^p$  and for the rate of the internal hardening variables  $\mathcal{M}$ :

$$\dot{\mathcal{E}}^p = \dot{\lambda} \frac{\partial \Phi}{\partial \Sigma^h}, \quad \dot{\mathcal{M}} = \dot{\lambda} \frac{\partial \Phi}{\partial \Sigma^h}, \quad (3.9)$$

with the plastic multiplier  $\dot{\lambda}$  from [SKS20]

$$\dot{\lambda} = \frac{\frac{\partial \Phi}{\partial \Sigma} C \dot{\epsilon}}{\frac{\partial \Phi}{\partial \Sigma} C \frac{\partial \Phi}{\partial \Sigma} + \frac{\partial \Phi}{\partial \Sigma^h} H \frac{\partial \Phi}{\partial \Sigma^h}}, \quad (3.10)$$

3

and the Karush-Kuhn-Tucker conditions:

$$\dot{\lambda} \geq 0, \quad \Phi \leq 0, \quad \dot{\lambda} \Phi = 0. \quad (3.11)$$

### 3.2.1. FE FORMULATION

For the FE discretization, this study follows the approach presented earlier in Section 2.2 for the determination of the stiffness matrices and the resulting nodal forces.

For plasticity an explicit convex cutting-plane algorithm following [SH98] is implemented in the [JIVE]-framework. This leads to the loss of global quadratic convergence in an implicit, static solution scheme. However, it provides a fast and accurate solution in the context of an explicit scheme. In the following the explicit procedure is laid out following [SH98] using the notation used in this dissertation with an overview given in Algorithm 1.

**Step 1** We initialize the local iteration variable  $l = 0$ , the linearized plastic flow  $\Delta \lambda^{(0)} = 0$ , the plastic strain-prescriptor  $\mathcal{E}_{n+1}^{p(0)} = \mathcal{E}_n^p$ , and the hardening variables  $\mathcal{M}_{n+1}^{(0)} = \mathcal{M}_n$ , where the index  $n$  represents the converged solution for the last load step and  $n + 1$  the load step of the current global Newton-Raphson iteration.

**Step 2** The stress-resultants and hardening contributions are computed according to the constitutive relationships and subsequently the yield function at the current iteration  $\Phi_{n+1}^{(l)}$  is evaluated using Equation (3.7). If the yield function is smaller than a predefined tolerance  $\Phi_{n+1}^{(l)} < \Phi_{\text{tol}}$ , the iterative procedure has converged, and we can move forward with the global iterations, if not, we proceed with the next step.

**Step 3** The derivatives of the yield function at the current point are evaluated

$$\begin{aligned} \partial_{\Sigma} \Phi^{(l)} &= \frac{\partial \Phi}{\partial \Sigma} (\Sigma^{(l)}, \Sigma^{h(l)}), \\ \partial_{\Sigma^h} \Phi^{(l)} &= \frac{\partial \Phi}{\partial \Sigma^h} (\Sigma^{(l)}, \Sigma^{h(l)}). \end{aligned}$$

Next, the increment  $\Delta^2 \lambda$  to the linearized plastic flow  $\Delta \lambda^{(l)}$  is computed.

**Step 4** Finally, we update the plastic flow, plastic strain-prescriptor, and internal hardening variables using the flow rules from Equation (3.9). After incrementing the local iteration variable  $l = l + 1$ , one returns to **Step 2**.

The yield surface is in [HKS21] derived for J2-plasticity and isotropic hardening with

$$\begin{aligned} N_1^y &= N_2^y = 700 \text{ N}, \\ N_3^y &= 1470 \text{ N}, \\ M_1^y &= M_2^y = 0.62 \text{ N m}, \\ M_3^y &= 0.56 \text{ N m}, \end{aligned} \quad (3.12)$$

3

and the exponents for the yield function Equation (3.7) as

$$\begin{aligned} \alpha_1^N &= \alpha_2^N = 2.04, \\ \alpha_3^N &= 1.76, \\ \alpha_1^M &= \alpha_2^M = 2.09, \\ \alpha_3^M &= 1.73. \end{aligned} \quad (3.13)$$

For details regarding the used model, the reader is referred to the original contribution [HKS21]. The authors also report an *implicit* scaling of the yield surface is with the area for the stress-resultant force  $N^y$  components, by showing an excellent fit of the reported values with  $\vartheta^2$ , where  $\vartheta$  represents a geometric scaling factor. The stress-resultant moments  $M^y$  are likewise *implicitly* scaled by the volume, as is demonstrated by the fit to  $\vartheta^3$ . For hardening plasticity, the hardening tensor  $\mathbf{H}$  was

---

### Algorithm 1 Explicit return mapping iterations.

---

**Step 1:** Initialize

$$\begin{aligned} \mathcal{E}_{n+1}^{p(0)} &= \mathcal{E}_n^p \\ \mathcal{M}_{n+1}^{(0)} &= \mathcal{M}_n \\ \Delta\lambda^{(0)} &= 0 \\ l &= 0 \end{aligned}$$

**Step 2:** Compute stress-resultants and yield function

$$\begin{aligned} \Sigma &= \mathbf{C} \left( \mathcal{E}_{n+1} - \mathcal{E}_{n+1}^{p(l)} \right) \\ \Sigma^h &= -\mathbf{H} \mathcal{M}_{n+1}^{(l)} \\ \Phi_{n+1}^{(l)} &= \Phi(\Sigma, \Sigma^h) \text{ using Eq. (3.7)} \end{aligned}$$

If  $\Phi_{n+1}^{(l)} < \Phi_{\text{tol}}$   
Finish procedure

**Step 3:** Compute plastic flow update

$$\Delta^2\lambda = \frac{\Phi_{n+1}^{(l)}}{\partial_{\Sigma} \Phi^{(l)} \mathbf{C} \partial_{\Sigma} \Phi^{(l)} + \partial_{\Sigma^h} \Phi^{(l)} \mathbf{H} \partial_{\Sigma^h} \Phi^{(l)}}$$

**Step 4:** Update plastic variables

$$\begin{aligned} \Delta\lambda^{(l+1)} &= \Delta\lambda^{(l)} + \Delta^2\lambda \\ \mathcal{E}_{n+1}^{p(l+1)} &= \mathcal{E}_{n+1}^{p(l)} + \Delta^2\lambda \partial_{\Sigma} \Phi^{(l)} \\ \mathcal{M}_{n+1}^{(l+1)} &= \mathcal{M}_{n+1}^{(l)} + \Delta^2\lambda \partial_{\Sigma^h} \Phi^{(l)} \end{aligned}$$

Increase local iteration variable  $l = l + 1$   
and go to **Step 2**

---

derived in [HKS22], again for the identical plasticity model on the microscale:

$$\mathbf{H} = \begin{bmatrix} \mathbf{H}_{\varepsilon\varepsilon} & \mathbf{H}_{\varepsilon\kappa} \\ \mathbf{H}_{\kappa\varepsilon} & \mathbf{H}_{\kappa\kappa} \end{bmatrix}, \quad (3.14)$$

3

with submatrices:

$$\begin{aligned} \mathbf{H}_{\varepsilon\varepsilon} &= \begin{bmatrix} 19014 & 17547 & 33121 \\ & 19014 & 33121 \\ \text{sym} & & 56864 \end{bmatrix} \text{ N,} \\ \mathbf{H}_{\varepsilon\kappa} &= \begin{bmatrix} 16.069 & 16.743 & 15.552 \\ 16.743 & 16.069 & 15.556 \\ 24.578 & 24.578 & 26.757 \end{bmatrix} \text{ N m} = \mathbf{H}_{\kappa\varepsilon}^T, \\ \mathbf{H}_{\kappa\kappa} &= \begin{bmatrix} 0.015015 & 0.015009 & 0.012715 \\ & 0.016015 & 0.012715 \\ \text{sym} & & 0.010434 \end{bmatrix} \text{ N m}^2. \end{aligned}$$

In [HKS22], the authors demonstrate the applicability of this approach with several examples of complex three-dimensional loading scenarios for beams. These examples also illustrate the limitations of this approach, which is that the entire cross-section plasticizes at once, as opposed to a gradual plastification when the cross-section is resolved at the microscale. This is particularly evident at the onset of plasticity in bending or torsion, where the fully resolved model shows a gradual transition from the elastic to the plastic regime. The stress-resultant approach used here shows a sharp kink in the corresponding global load-displacement curves for the onset of plasticity over the entire cross-section. For further details and illustration of this process, the reader is referred to Herrnböck, Kumar and Steinmann [HKS22].

#### NUMERICAL BENCHMARK

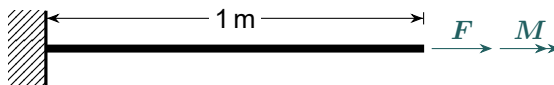


Figure 3.1.: Example 5.1 taken from [SKS20].

To ensure the correct implementation and applicability of the in [Algorithm 1](#) described algorithm to beam plasticity, *Example 5.1* from [SKS20] is modelled and compared to the results in literature. A straight rod, depicted in [Figure 3.1](#), of length  $l = 1 \text{ m}$  and diameter  $d = 0.1 \text{ m}$  is taken to have the Young's modulus  $E = 1 \text{ MPa}$ , the shear correction coefficient  $k = 0.792453$ , and the Poisson's ratio  $\nu = 0.4$ . The beam is discretized using 5 linear elements. In the yield function

$$\Phi = \left| \frac{n_3}{n_3^p} \right| + \left| \frac{m_3}{m_3^p} \right| - \zeta_{y0},$$

the yield limit for axial tension is set to be  $n_3^p = 1 \text{ N}$  and for axial torsion  $m_3^p = 0.12 \text{ N m}$  at an initial yield limit  $\zeta_{y0} = 10$ . The beam is fixed at the left end and subjected to a constant twist of  $0.18 \text{ rad} \approx 10.3^\circ$  at the right end. It is subsequently stretched and compressed, with the corresponding load-displacement curve depicted in Figure 3.2. The good fit between the implementation for this work and the

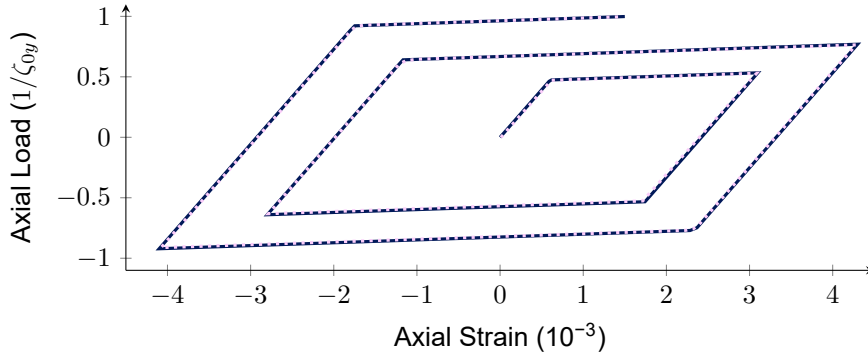


Figure 3.2.: Load-displacement curve for the benchmark problem. The solid line depicts this work, the dotted line [SKS20].

reported results from literature demonstrates the applicability of the explicit return mapping scheme for problems of beam plasticity. It is noteworthy here, that the apparent hardening after yielding is not due to hardening in the model, but rather due to the geometric interaction between torsion and tension in the beam. For further details the reader is referred to [SKS20].

### 3.3. EFFECTS OF MESH SIZE

To ensure that the results of the investigation into the geometric scaling are independent of the discretization a mesh sensitivity study was carried out first. For this



Figure 3.3.: Schematic of a cantilever beam under load.

purpose, a straight cantilever beam, as represented in Figure 3.3, is chosen as a reference case. The free end of this cantilever beam is subjected to a displacement  $u$  and the reaction force  $F$  is recorded. The beam is  $l = 0.1 \text{ m}$  long and has a solid circular cross-section with a radius of  $r = 1 \text{ mm}$ , resulting in a slenderness-ratio  $S = l/r = 100$ . The material has a Young's modulus of  $210 \text{ GPa}$  and a Poisson's

ratio of 0.3. All runs are investigated for elastic material behaviour as well as ideal plastic and kinematic hardening plastic behaviour. In order to gain insight into the effects of softening as well, runs are also conducted with the hardening tensor  $H$  given in Equation (3.14) multiplied by  $-1$ . In this initial investigation a simplified yield surface with only yielding in the out of plane bending direction is used. This reduces Equation (3.7) to:

$$\Phi = \left| \frac{M_1}{M_1^y - M_1^h} \right|^{\alpha_1^M} - 1 \leq 0. \quad (3.15)$$

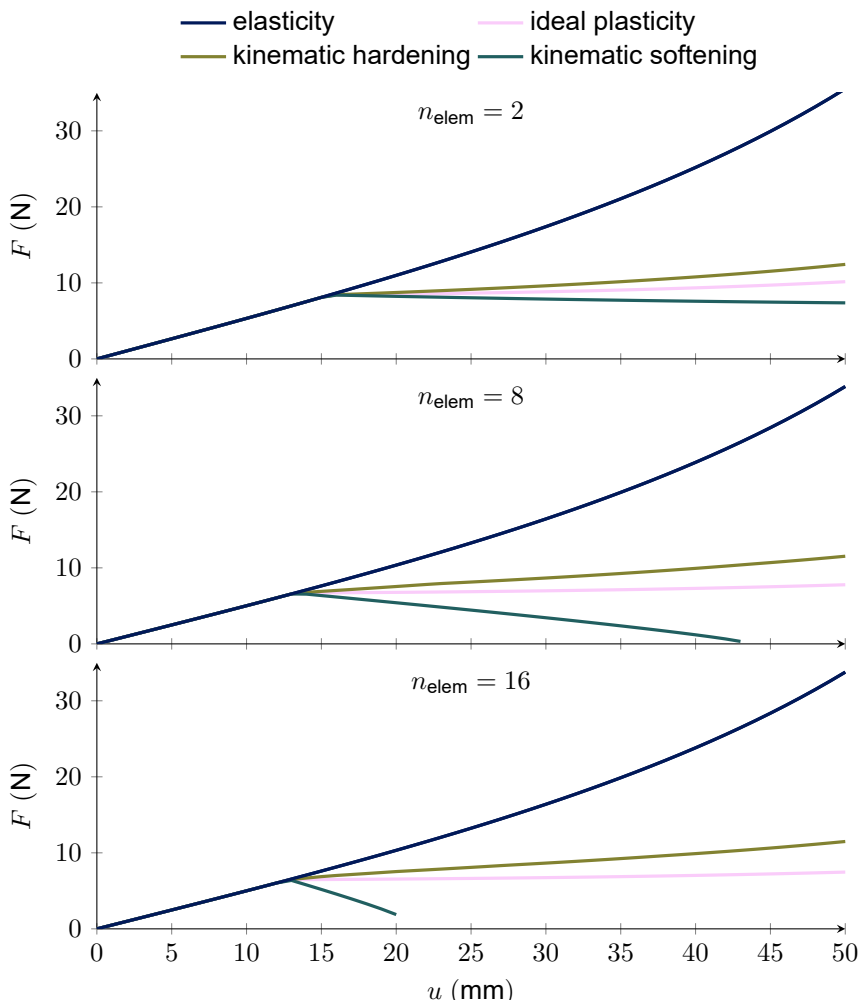


Figure 3.4.: Load displacement curves cantilever beam.

Initially, simulations are done with  $n_{\text{elem}} = 2, 8$  and  $16$  linear elements, respectively. The load displacement curves are depicted in Figure 3.4. One can see a clear difference between the upper ( $n_{\text{elem}} = 2$ ) and middle ( $n_{\text{elem}} = 8$ ) discretization depicted for all investigated material models. This difference disappears when comparing the middle and the lower graph, corresponding to  $n_{\text{elem}} = 16$  elements. Following the onset of plasticity, the expected behaviour can be observed in Figure 3.4. In the case of ideal plasticity, a constant force is maintained after yielding. In contrast, models of hardening and softening plasticity exhibit a positive and negative slope, respectively, in the load displacement curve. In Figure 3.5a the distribution

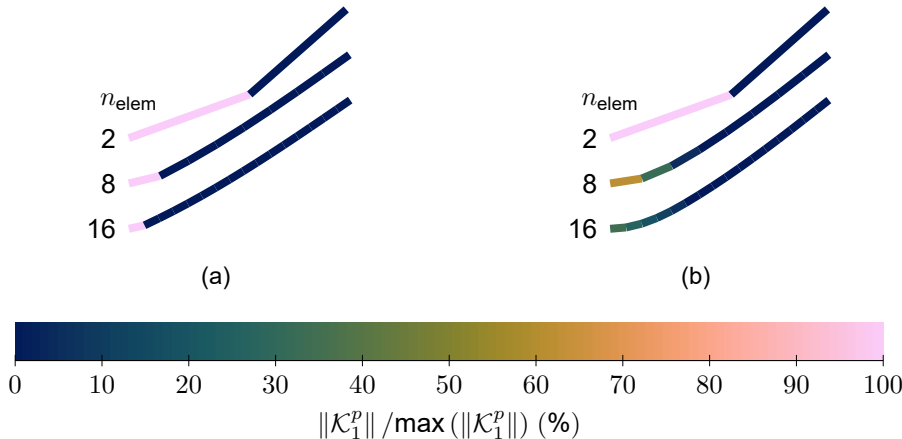


Figure 3.5.: Localization of plasticity for (a) ideal plasticity and (b) kinematic hardening plasticity ( $n_{\text{elem}} = 2, 8$  and  $16$  from top to bottom; colours depict the relative distribution of plastic curvature).

of the plastic curvature  $\mathcal{K}_1^p$  is shown for a displacement of  $50$  mm using an ideally plastic material model. Again, in the figure, the three mesh refinements shown in the load-displacement curves are visualized, with  $n_{\text{elem}} = 2, 8$  and  $16$  from top to bottom. It is clearly visible that plasticity is localized in one element at the clamped end of the beam. This stems from the fact, that the moment carried by the beam, due to the point load at the end, has its highest value at the left boundary. As soon as one element yields, this highest value is limited, thus limiting in turn the load the beam can bear. In the hardening case, the transmitted cross-sectional moment may increase due to hardening, leading to more subsequent elements starting to yield. This is visualized in Figure 3.5b, where again the colour corresponds to the plastic curvature  $\mathcal{K}_1^p$  at a tip displacement of  $50$  mm. Again, the three refinements  $n = 2, 8$  and  $16$  are shown from top to bottom. The softening case is not depicted due to the inability to achieve a converged solution at  $u = 50$  mm. To assess mesh sensitivity of the different material models, in Figure 3.6 the forces for a deformation shortly after the onset of yielding at  $u = 20$  mm in the upper graph and after a larger deformation at  $u = 50$  mm in the lower graph are shown as function

of the discretization of the beam. The comparison between the two graphs shows that the forces using ideal plasticity do not significantly change between the two displacement levels, which can be motivated by the fact, that as soon as a single element starts yielding, this element limits the effective load bearing capacity of the entire beam. In elasticity, however, the load bearing capacity is not limited and thus increases with increased displacement level. When introducing kinematic hardening into the formulation, one can clearly see, that the load limiting effect of yielding still persists, however less strong as in the ideal plastic case. Softening behaviour, achieved by multiplying the hardening tensor  $H$  by  $-1$ , results in a clear mesh sensitivity as can be seen in the softening graphs in Figure 3.6 at the two displacement levels. This mesh sensitivity problem is well-known and relates to the mathematical ill-posedness of the problem. Opposite to this, for the three cases of elasticity, ideal plasticity and kinematic hardening plasticity, one can observe mesh insensitivity for a large enough number of elements. For the investigated cantilever beam, eight elements are determined as sufficient to represent the global behaviour of the

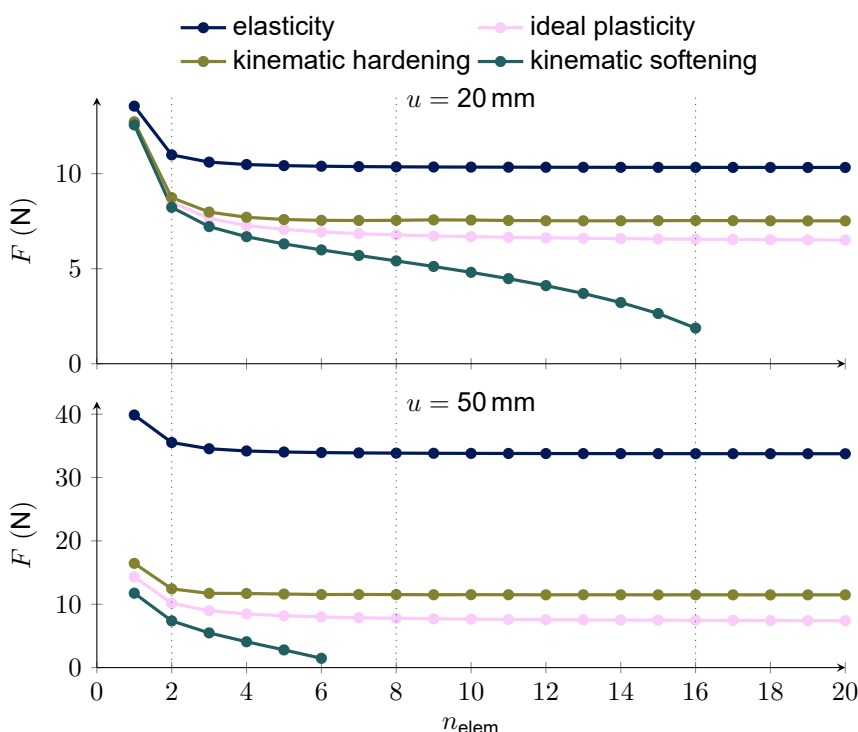


Figure 3.6.: Mesh convergence cantilever beam.

system in these models. One should note, that this does not necessarily relate to the local phenomena, as seen in Figure 3.5a, where a difference between the local distribution of plasticity for  $n_{\text{elem}} = 8$  and  $n_{\text{elem}} = 16$  can be observed around the left boundary. However, this has no effect on the global force response.

## 3.4. EFFECTS OF GEOMETRICAL SCALING

A key aspect of the design of lattice materials is the alteration of the length and orientation of the constituent beams, as well as the dimensions of the cross-section. As shown by Herrnböck, Kumar and Steinmann [HKS21] for circular and square cross-sections, the yield surface is dependent on the scale of the geometric cross-section. Herrnböck, Kumar and Steinmann [HKS22] demonstrated the scaling of the hardening tensor with the microscale hardening parameter and its influence on the yield behaviour of the beam for a circular cross-section. However, no attention has been given to the geometric scaling of this hardening tensor. In order to investigate this, the same cantilever beam as in Section 3.3 is investigated first. The material models for the beam are elasticity, ideal plasticity and kinematic hardening plasticity. Both geometric parameters, length and radius of the beam, are scaled uniformly with a scaling parameter  $\vartheta \in [0.01, 100]$ , resulting in the same slenderness ratio across the scales. The same simplified yield surface from the previous section as reported in Equation (3.15) is employed and the *initial* yield stress-resultant bending moment  $M_1^y$  is scaled with volume  $\vartheta^3$  since the elastic bending moment in a beam will scale likewise, as can be seen in the *implicit* scaling of the elastic stiffness tensor shown in Equation (3.2).

### 3.4.1. UNSCALED HARDENING TENSOR

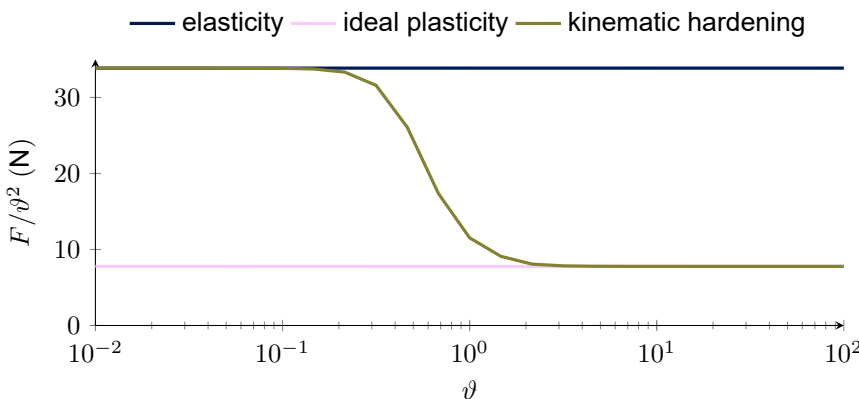


Figure 3.7.: Scaling study with an unscaled hardening tensor at  $u = 50$  mm for the unscaled case.

Table 3.1.: Comparative iteration 0 and 1 through Algorithm 1 for the different material models.

		Ideal Plasticity		Hardening Plasticity	
				unscaled $H$	scaled $H$
<b>Step 1</b>	$\Delta\lambda^{(0)}$ =	0		0	0
	$\mathcal{K}_1^P{}^{(0)}$ =	0		0	0
	$\mathcal{M}_1^K{}^{(0)}$ =	—		0	0
<b>Iteration 0</b>					
<b>Step 2</b>	$M_1$ =	0.6262 $\vartheta^3$		0.6262 $\vartheta^3$	0.6262 $\vartheta^3$
	$M_1^h$ =	—		$0\vartheta^0$	$0\vartheta^3$
	$\Phi^{(0)}$ =	0.02101		0.02101	0.02101
<b>Step 3</b>	$\partial_{M_1}\Phi$ =	3.408 $\vartheta^{-3}$		3.408 $\vartheta^{-3}$	3.408 $\vartheta^{-3}$
	$\partial_{M_1^h}\Phi$ =	—		3.442 $\vartheta^{-3}$	3.442 $\vartheta^{-3}$
	$\Delta^2\lambda$ =	0.01097 $\vartheta^2$		$\frac{0.02101}{1.915\vartheta^{-2}+0.1779\vartheta^{-6}}$	0.01004 $\vartheta^2$
<b>Step 4</b>	$\Delta\lambda^{(1)}$ =	0.01097 $\vartheta^2$		—	0.01004 $\vartheta^2$
	$\mathcal{K}_1^P{}^{(1)}$ =	0.03739 $\vartheta^{-1}$			0.03421 $\vartheta^{-1}$
	$\mathcal{M}_1^K{}^{(1)}$ =	—			0.03455 $\vartheta^{-1}$
<b>Iteration 1</b>					
<b>Step 2</b>	$M_1$ =	0.62 $\vartheta^3$			0.6206 $\vartheta^3$
	$M_1^h$ =	—			-0.0005188 $\vartheta^3$
	$\Phi^{(1)}$ =	0.0001127			0.0001301

In Figure 3.7 the scaling behaviour of the reaction force  $F/\vartheta^2$  is shown for the three investigated material models (elastic, ideal plastic and kinematic hardening) and the scaling parameter  $\vartheta$ . The force is scaled back with  $\vartheta^{-2}$ , since the force, similar to the moment, scales *implicitly* based on the elastic stiffness tensor from Equation (3.2). For the elastic case as well for the ideal plastic case, no scale effect is observed. In the case of the kinematic hardening material model, however, a clear effect of the geometric scale is observed. For larger scaling factors  $\vartheta > 1$  the behaviour approaches the ideal plastic case, indicating a vanishing hardening effect, whereas for smaller scaling factors  $\vartheta < 1$  the elastic case is approached, indicating an increase of the hardening effect relative to plasticity present in the model. In the following, we will investigate the cause for this spurious scale effect and propose a mitigation strategy.

### 3.4.2. INVESTIGATION INTO SCALING EFFECTS

As previously demonstrated, the scale effect can be attributed to the kinematic hardening contribution. Therefore, the development of the hardening variables, denoted by  $\mathcal{M}$ , as well as the hardening contributions, denoted by  $\Sigma^h$ , is investigated. In order to investigate this, a single iteration of the return mapping scheme from Algorithm 1 in Section 3.2.1 is performed, initially for ideal plasticity and subsequently for hardening plasticity. Both the *implicit* scaling of the elastic properties and the yield surface are present throughout, with the scale variable,  $\vartheta$ , *explicitly* given. To illustrate the scaling behaviour at different stages of return mapping, we

compute a single integration point with a bending moment of  $M_1 = 0.6262 \text{ N m}^{\vartheta^3}$ , just 1 % above the yield limit of  $M_1^y = 0.62 \text{ N m}^{\vartheta^3}$ , stemming from a curvature of  $\kappa_1 = M_1/EI_1 = 3.79 \text{ m}^{-1}\vartheta^{-1}$ . For ideal plasticity the calculation is depicted in the first column of [Table 3.1](#).

These results illustrate two characteristics of the underlying plasticity scheme. Firstly, plastic flow  $\lambda$  scales with area  $\sim \vartheta^2$ , which seems natural because in the present framework the stress-resultant space is referred back to the rigid cross-section of the beam. Secondly, the presented return mapping scheme converges for the assumed simple yield surface in one iteration.

Next, we investigate the same problem with kinematic hardening. Here again, the elastic properties and the yield surface are scaled *implicitly*, without considering any scaling for the hardening tensor  $\mathbf{H}$ . The scale variable  $\vartheta$  is again *explicitly* given. This is depicted in the second column of [Table 3.1](#). Already at the end of **Step 3** it can be seen, that the update of plastic flow cannot be computed consistently with the *implicit, geometric* scaling in the stiffness tensor and no scaling in the hardening tensor. Comparing the results of the ideal plasticity term  $\partial_{\Sigma}\Phi C \partial_{\Sigma}\Phi = 1.915\vartheta^{-2}$  with the hardening plastic term  $\partial_{\Sigma^h}\Phi \mathbf{H} \partial_{\Sigma^h}\Phi = 0.1779\vartheta^{-6}$  in the denominator of the computation of the plastic flow update (compare **Step 3** of [Algorithm 1](#)), we can now explain the behaviour observed in [Figure 3.7](#). For small  $\vartheta$ , hardening behaviour dominates, leading to an almost elastic model, and for large  $\vartheta$ , plastic behaviour dominates, leading to an almost ideal plastic model.

### 3.4.3. PROPOSED MITIGATION STRATEGY

To mitigate these spurious scale effects and ensure stable scaling in the computation of the plastic flow update, these two terms in the denominator will be further investigated. The *ideal plastic* term  $\partial_{\Sigma}\Phi C \partial_{\Sigma}\Phi$  scales with the area inverse  $\sim \vartheta^{-2}$  due to the construction of the yield function and the *implicit* scaling of the stiffness matrix  $\mathbf{C}$ . The *hardening plastic* term  $\partial_{\Sigma^h}\Phi \mathbf{H} \partial_{\Sigma^h}\Phi$  on the other hand, needs to be adapted to obtain scaling with the area inverse and compute the same plastic flow for different geometric scales. As the partial derivative of the yield function is determined by the definition of the yield function, the only adaptable parameter is the hardening tensor  $\mathbf{H}$ . In the given case, it needs to be scaled similar to the material stiffness (for the bending moment  $\sim \vartheta^4$ ) in order to achieve consistent geometrical scaling. With this, we can compute the return mapping again, as depicted in the last column of [Table 3.1](#). Here, it becomes clear that the proposed approach to scale the hardening tensor leads to an elimination of the scaling inconsistencies and also to an algorithm that converges to the desired accuracy of  $\Phi_{\text{tol}} = 10^{-3}$  within one iteration. This demonstrates, that the proposed strategy ensures the continuation of the return mapping scheme, without inconsistent scaling factors.

We will now examine the results of the proposed strategy for the response of the cantilever beam from [Figure 3.7](#). [Figure 3.8](#) depicts the same loading cases, but with the hardening tensor scaled as explained earlier. The elastic and ideal plastic behaviour is the same as reported in [Figure 3.7](#). The kinematic hardening plastic behaviour shows the initially expected behaviour, namely not exhibiting any

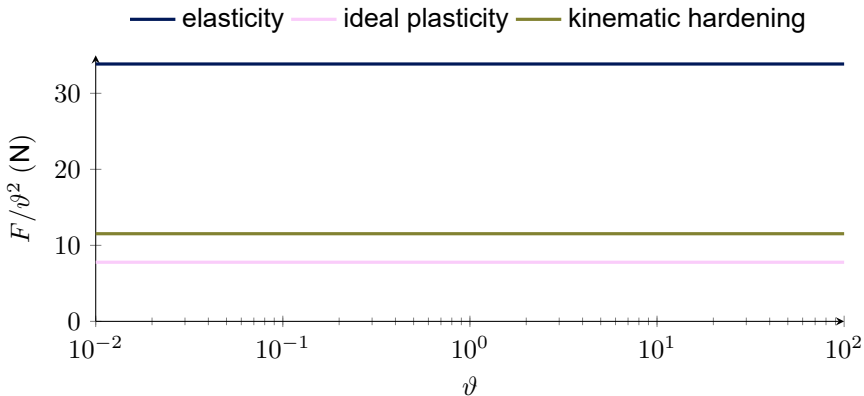


Figure 3.8.: Scaling study with a scaled hardening tensor (for the bending moment  $\sim \vartheta^4$ ) at  $u = 50$  mm for the unscaled case.

scale effect. This demonstrates the applicability of the proposed strategy to mitigate scaling effects in hardening plasticity. This strategy will be explained in the next section for the generic yield function Equation (3.7) together with an alternative strategy to scale the yield surface.

### 3.5. STRATEGIES FOR THE CONSISTENT GEOMETRIC SCALING OF HARDENING

When considering the yield function Equation (3.7), we can derive the necessary scaling following the same approach. Initially, we assume again only the initial yield surface to be scaled. Investigation of the scaling of  $\frac{\partial \Phi}{\partial \Sigma^h}$  leads to the following:

$$\frac{\partial \Phi}{\partial \Sigma^h} = \begin{bmatrix} (\dots) \frac{N_1}{(N_1^y - N_1^h)^2} \\ (\dots) \frac{N_2}{(N_2^y - N_2^h)^2} \\ (\dots) \frac{N_3}{(N_3^y - N_3^h)^2} \\ (\dots) \frac{M_1}{(M_1^y - M_1^h)^2} \\ (\dots) \frac{M_2}{(M_2^y - M_2^h)^2} \\ (\dots) \frac{M_3}{(M_3^y - M_3^h)^2} \end{bmatrix} \sim \begin{bmatrix} \vartheta^{-2} \\ \vartheta^{-2} \\ \vartheta^{-2} \\ \vartheta^{-3} \\ \vartheta^{-3} \\ \vartheta^{-3} \end{bmatrix}. \quad (3.16)$$

Taking this into account, we can derive, that the hardening tensor  $\mathbf{H}$  needs to scale as

$$\mathbf{H}^* = \begin{bmatrix} \mathbf{H}_{\varepsilon\varepsilon} \vartheta^2 & \mathbf{H}_{\varepsilon\kappa} \vartheta^3 \\ \mathbf{H}_{\kappa\varepsilon} \vartheta^3 & \mathbf{H}_{\kappa\kappa} \vartheta^4 \end{bmatrix}, \quad (3.17)$$

to ensure consistency of the plastic strain-prescriptors and internal hardening variables for different geometric scales. This scaling behaviour is consistent with the *implicit* scaling of the elastic stiffness tensor  $\mathbf{C}$  from Equation (3.2). If, on the other hand, the scaling of the yield surface from [HKS21] is interpreted not only for the *ini-*

tial yield surface but for the *entire* yield surface, the yield function from Equation (3.7) becomes

$$\Phi = \left| \frac{N_1}{(N_1^y - N_1^h)\vartheta^2} \right|^{\alpha_1^N} + \left| \frac{N_2}{(N_2^y - N_2^h)\vartheta^2} \right|^{\alpha_2^N} + \left| \frac{N_3}{(N_3^y - N_3^h)\vartheta^2} \right|^{\alpha_3^N} + \left| \frac{M_1}{(M_1^y - M_1^h)\vartheta^3} \right|^{\alpha_1^M} + \left| \frac{M_2}{(M_2^y - M_2^h)\vartheta^3} \right|^{\alpha_2^M} + \left| \frac{M_3}{(M_3^y - M_3^h)\vartheta^3} \right|^{\alpha_3^M} - 1 \leq 0, \quad (3.18)$$

where the initial yield stress-resultant forces and moments are *not* implicitly scaled and are taken as reported in Equation (3.12). The derivative of the yield function with respect to the hardening stress-resultants is then

$$\frac{\partial \Phi}{\partial \Sigma^h} = \begin{bmatrix} (\dots) \frac{N_1}{(N_1^y - N_1^h)^2 \vartheta^2} \\ (\dots) \frac{N_2}{(N_2^y - N_2^h)^2 \vartheta^2} \\ (\dots) \frac{N_3}{(N_3^y - N_3^h)^2 \vartheta^2} \\ (\dots) \frac{M_1}{(M_1^y - M_1^h)^2 \vartheta^3} \\ (\dots) \frac{M_2}{(M_2^y - M_2^h)^2 \vartheta^3} \\ (\dots) \frac{M_3}{(M_3^y - M_3^h)^2 \vartheta^3} \end{bmatrix} \sim \begin{bmatrix} \vartheta^0 \\ \vartheta^0 \\ \vartheta^0 \\ \vartheta^0 \\ \vartheta^0 \\ \vartheta^0 \end{bmatrix}, \quad (3.19)$$

where we again need to keep in mind, that the current stress-resultants are scaled *implicitly* via the scaling of the material stiffness tensor  $C$ . In order to ensure, that the hardening term  $\frac{\partial \Phi}{\partial \Sigma^h} \mathbf{H} \frac{\partial \Phi}{\partial \Sigma^h}$  scales with the area inverse  $\vartheta^{-2}$ , the hardening tensor  $\mathbf{H}$  needs to be scaled according to:

$$\mathbf{H}^* = \mathbf{H} \vartheta^{-2}. \quad (3.20)$$

This strategy leads to identical results as scaling only the initial yield surface combined with the scaled hardening tensor in Equation (3.17).

When using isotropic hardening of the form  $\Phi = \dots + \Phi_y(1 + h_0)$ , one can derive, that the hardening factor associated with the isotropic hardening variable needs to scale with the area inverse  $\vartheta^{-2}$ , in the same manner.

### 3.5.1. COMPARISON OF DIFFERENT HARDENING BEHAVIOUR IN THREE DIMENSIONS

For an investigation in a fully three-dimensional setting, we use the same beam as previously, but it is now curved in a way, that the point of loading is angled 45°, resulting in a radius of  $\approx 0.127$  m. As illustrated in Figure 3.9, the beam is loaded out of plane. Again, for all cases, 8 linear elements are used to describe the geometry. Load displacement curves for the material models, considered in Section 3.3, are shown in Figure 3.10. To illustrate the scaling effect, different yielding behaviour (kinematic hardening and softening with scaling of the *initial* and scaling of the *entire* yield surface as well as isotropic hardening) is investigated. For the kinematic

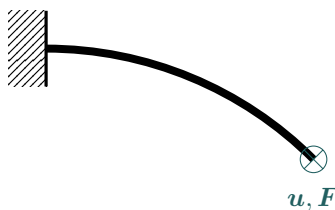


Figure 3.9.: Schematic of a bent cantilever beam under load.

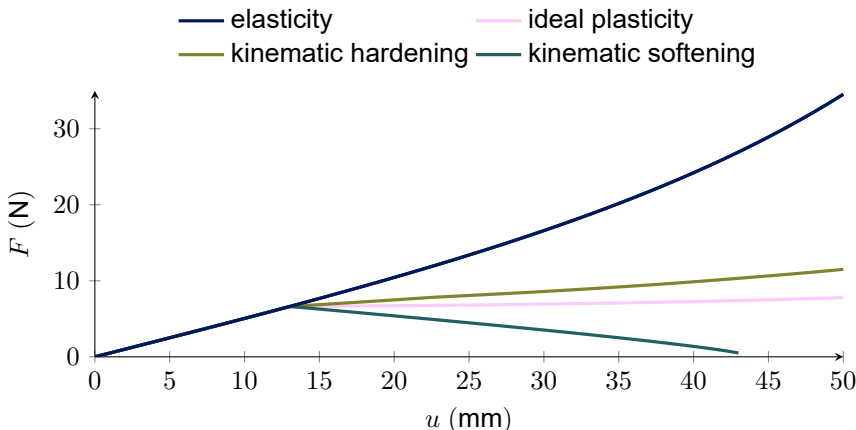


Figure 3.10.: Load displacement curves for the bent cantilever beam.

hardening cases, the values as given in [Section 3.2.1](#) are used. For the scaling of the *initial* yield surface case, the yield function as given in [Equation \(3.7\)](#) is employed, whereas in the case of scaling the *entire* yield surface, the modified surface as given in [Equation \(3.18\)](#) is used. In the isotropic hardening case the same elastic properties are used. The yield function is constructed by taking [Equation \(3.7\)](#) and adding the isotropic hardening term

$$\Phi_{\text{iso}} = \Phi - \zeta_H. \quad (3.21)$$

The hardening factor used in the corresponding calculations is set to be  $H_{00} = 50$ . The softening investigations are performed with the same values as the kinematic hardening investigations with the hardening tensor in [Equation \(3.14\)](#) multiplied with  $-1$ . For isotropic softening, the hardening factor is set to  $H_{00} = -50$ . Initially, without the adaptation of the proposed scaling factors, clear scale effects are visible in the upper graph of [Figure 3.11](#) as well as non-physical behaviour in the softening cases. The effect previously observed in [Section 3.4.1](#), whereby the kinematic hardening model approaches the elastic case for  $\vartheta$  and the ideal plastic case for large  $\vartheta$ , is once again identified here for the model with the *initial* yield surface scaled. In contrast, the model with the *entire* yield surface scaled exhibits the opposite behaviour, approaching the elastic case for large  $\vartheta$  and the ideal plastic case for

small  $\vartheta$ . The non-physical effect, that softening computations show an even stiffer response at certain scaling factors compared to the purely elastic material is based in the fact, that the denominator in **Step 3** of **Algorithm 1** can become negative if the second term with a negative  $H$  dominates the first term. This leads, under violation of the Karush-Kuhn-Tucker conditions in [Equation \(3.11\)](#), to the non-physical effect of *negative* plastic flow. Therefore, plastic strain-prescriptors develop in the opposite direction of the total strain-prescriptor, which gives elastic strain-prescriptors being higher than total strain-prescriptors, and higher stress-resultants than expected.

In consideration of the identified conditions, it is necessary to apply a scaling factor to the hardening tensor (or factor in the case of isotropic hardening) in accordance with the proposed mitigation strategy fitting to the yield surface. In the bottom graph of [Figure 3.11](#) it can be observed that the proposed strategy to modify the

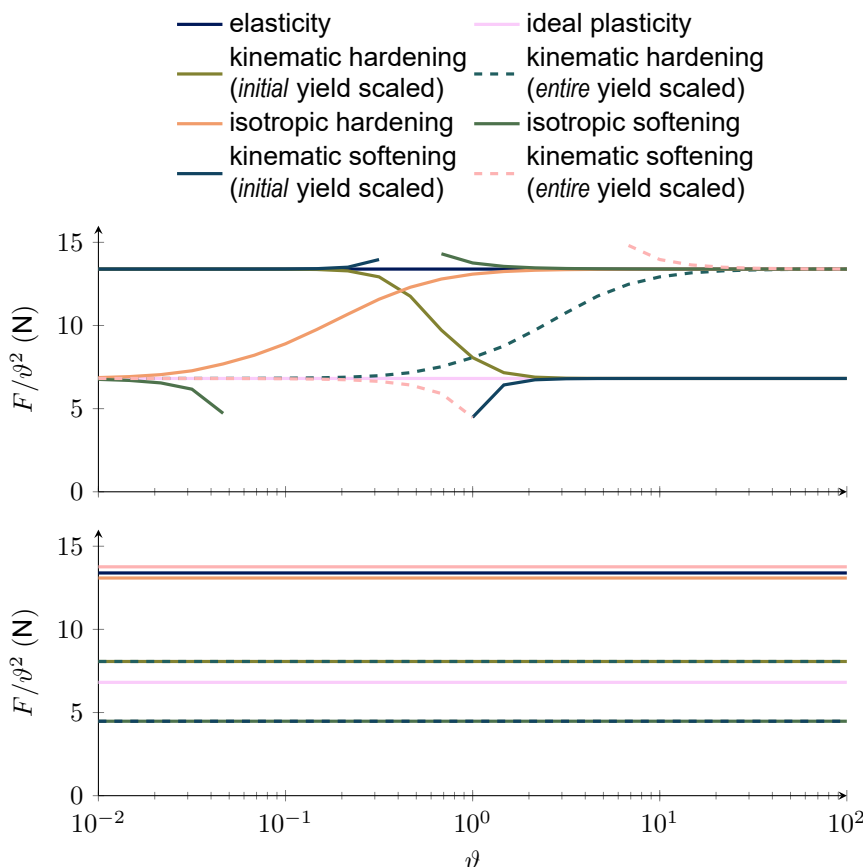


Figure 3.11.: Behaviour of different yield functions, with the hardening tensor scaled (bottom), and with the hardening tensor unscaled (top) at  $u = 25$  mm for the unscaled case.

hardening tensor effectively eliminates the scale dependency of the behaviour observed in all investigated cases. One has to note, that the chosen isotropic softening parameter is clearly non-physical as can be seen by the fact, that the response is stiffer than the purely elastic response.

### 3.5.2. INVESTIGATION OF DIFFERENT SLENDERNESS RATIOS

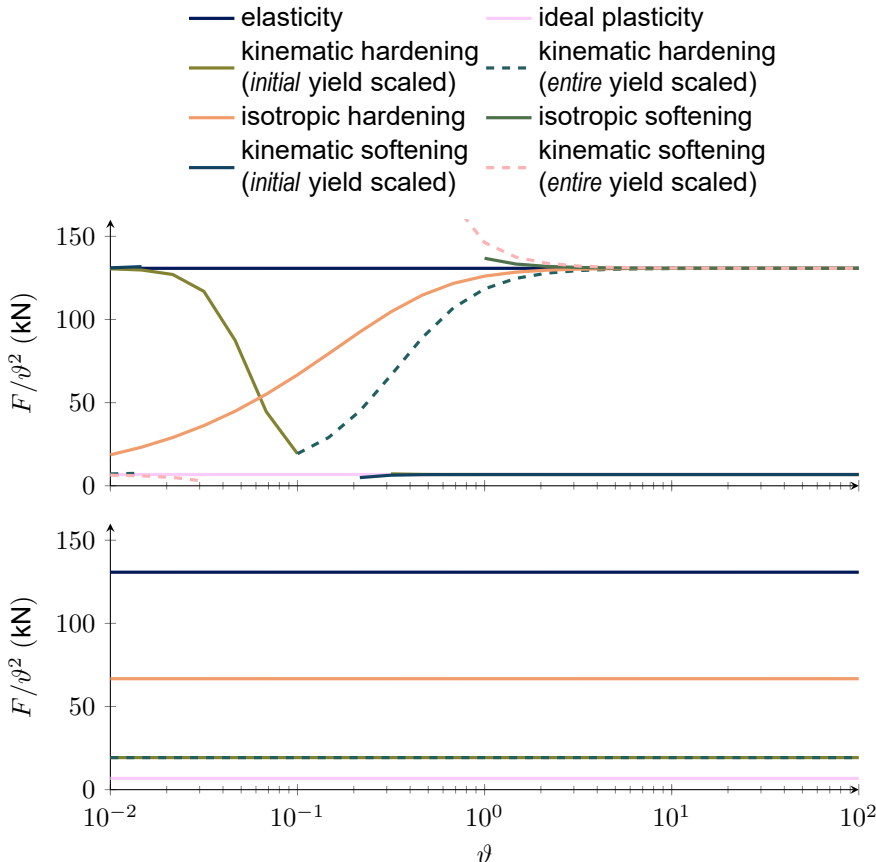


Figure 3.12.: Behaviour of different yield functions, with the hardening tensor scaled (bottom), and with the hardening tensor unscaled (top) at  $u = 25$  mm for the unscaled case ( $S = 10$ ).

Finally, we examine the behaviour for different slenderness ratios  $S = l/r$ , with the length  $l$  and radius  $r$  of the beam. For this effect, we repeat the investigation from the previous section with two additional beams with different slenderness ratios  $S = 10$  and  $1000$  as opposed to  $S = 100$  as discussed above. For the slenderness ratio  $S = 1000$ , corresponding to a radius of  $r = 0.1$  mm for  $\vartheta = 1$ , we do not

observe any plasticity in the thin beams. This can be explained by the fact that all the material is relatively close to the neutral fibre of the beam and thus experiences less strain, leading to less plasticity effects when considering full cross-sections. Furthermore, by scaling only the cross-section, the stress-resultant moments scale with  $\vartheta^4$ , while the yield surface scales with  $\vartheta^3$ . The curvature as a beam level strain-prescriptor, corresponding to the stress-resultant bending moment, scales with  $\vartheta^{-1}$ , requiring the scaling of the beam length as well as the boundary conditions with the geometry to maintain geometric similitude. On the other hand, the results for a beam with slenderness ratio  $S = 10$ , corresponding to  $r = 10$  mm for  $\vartheta = 1$ , in Figure 3.12, evidently show stronger plastic effects. While for the cross-section in Figure 3.11 the relative reduction of the force required to enforce the deformation associated with ideal plasticity compared to elasticity is about a factor of 0.5, for the examined thicker beams this ratio is closer to 0.1. The stronger plastic effect can again be explained by the fact that the material is relatively further away from the neutral fibre and thus experiences more strain. This example again emphasizes the applicability of the proposed scaling strategy, as in the lower graph of Figure 3.12 all size effects observed in the upper graph have been eliminated.

## 3.6. CONCLUSION

The incorporation of geometric scaling into the kinematic hardening of beams, has been demonstrated to successfully mitigate undesirable scale effects. We present a strategy for determining appropriate scaling of hardening parameters based on the yield function and its derivatives, and illustrate its applicability in a variety of scenarios with different yield functions as well as hardening or softening behaviour. Herrnböck, Kumar and Steinmann [HKS21] have shown the issue of geometric scaling of the yield surface in ideal plasticity. This scaling can be interpreted in the kinematic hardening model derived by Herrnböck, Kumar and Steinmann [HKS22] in two ways: Either as *implicit* scaling of the *initial* yield surface by adapting the yield limits in the six directions depending on the size of the cross-section, or as *explicit* scaling of the *entire* yield surface. The proposed strategy is independent of the interpretation of the scaling of the yield surface, as it derives the scaling factors analytically from a given yield surface formulation. It is demonstrated that the undesirable scale effects can be mitigated and that the definition of a hardening tensor dependent on a specific geometric scale can be avoided. This approach will be particularly beneficial for the targeted architecture of nonlinear mechanical metamaterials undergoing large inelastic deformations. At large deformations, the influence of geometric properties on the nonlinear response of the structure is unknown and requires the fitting of model parameters for a large set of geometric scales. An easily adaptable plasticity formulation that incorporates the effects of geometric scale also in the hardening will circumvent the need for model calibration at a wide range of sizes. This framework enables the rapid design of architected nonlinear materials with lattice structures and their accurate representation at arbitrary scales.

## REFERENCES

**3**

- [Cro19] I. G. Crouch. 'Body armour – New materials, new systems'. *Def. Technol.* **15** (2019), pp. 241–253.
- [DC90] L. Duan and W.-F. Chen. 'A yield surface equation for doubly symmetrical sections'. *Eng. Struct.* **12** (1990), pp. 114–119.
- [Gär<sup>&al</sup>25] T. Gärtner et al. 'A strategy for scaling the hardening behavior in finite element modelling of geometrically exact beams'. *Comput. Mech.* **75** (2025), pp. 1471–1482.
- [HKS21] L. Herrnböck, A. Kumar and P. Steinmann. 'Geometrically exact elastoplastic rods: determination of yield surface in terms of stress resultants'. *Comput. Mech.* **67** (2021), pp. 723–742.
- [HKS22] L. Herrnböck, A. Kumar and P. Steinmann. 'Two-scale off-and online approaches to geometrically exact elastoplastic rods'. *Comput. Mech.* **71** (2022), pp. 1–24.
- [JIVE] Dynaflow Research Group. *JIVE*. Version 3.0. 1st Apr. 2021.
- [Kar<sup>&al</sup>23] K. Karapiperis et al. 'A Variational Beam Model for Failure of Cellular and Truss-Based Architected Materials'. *Adv. Eng. Mater.*, 2300947 (2023).
- [Rei81] E. Reissner. 'On Finite Deformations of Space-Curved Beams'. *Z. Angew. Math. Phys.* **32** (1981), pp. 734–744.
- [SDC16] K. K. Saxena, R. Das and E. P. Calius. 'Three Decades of Auxetics Research – Materials with Negative Poisson's Ratio: A Review'. *Adv. Eng. Mater.* **18** (2016), pp. 1847–1870.
- [SH98] J. Simo and T. Hughes. *Computational Inelasticity*. Interdisciplinary Applied Mathematics. Springer, 1998.
- [SHT84] J. C. Simo, K. D. Hjelmstad and R. L. Taylor. 'Numerical Formulations of Elasto-Viscoplastic Response of Beams Accounting for the Effect of Shear'. *Comput. Methods Appl. Mech. Eng.* **42** (1984), pp. 301–330.
- [Sim85] J. C. Simo. 'A finite strain beam formulation. The three-dimensional dynamic problem. Part I'. *Comput. Methods Appl. Mech. Eng.* **49** (1985), pp. 55–70.
- [SKS20] Smriti, A. Kumar and P. Steinmann. 'A finite element formulation for a direct approach to elastoplasticity in special Cosserat rods'. *Int. J. Numer. Methods Eng.* (2020), pp. 1262–1282.
- [Smr<sup>&al</sup>18] Smriti et al. 'A thermoelastoplastic theory for special Cosserat rods'. *Math. Mech. Solids* **24** (2018), pp. 686–700.
- [TJ21] E. Tenorio-Montero and G. Juárez-Luna. 'Beam-column finite element with embedded discontinuities for modelling damage in reinforced concrete prismatic elements'. *Structures* **29** (2021), pp. 1934–1953.

[Toj<sup>&al</sup>23] V. Tojaga et al. 'Geometrically exact beam theory with embedded strong discontinuities for the modeling of failure in structures. Part I: Formulation and finite element implementation'. *Comput. Methods Appl. Mech. Eng.* **410**, 116013 (2023).

[TZH22] D. Tahir, M. Zhang and H. Hu. 'Auxetic Materials for Personal Protection: A Review'. *phys. status solidi (b)* **259**, 2200324 (2022).

[Wee<sup>&al</sup>23] O. Weeger et al. 'Inelastic finite deformation beam modeling, simulation, and validation of additively manufactured lattice structures'. *Addit. Manuf. Lett.* **4**, 100111 (2023).



# 4

## **ELASTIC BEHAVIOUR UNDER IMPACT**

*Lightweight materials used for impact mitigation must be able to resist impact and absorb the maximum amount of energy from the impactor. Auxetic materials have the potential to achieve high resistance by drawing material into the impact zone and providing higher indentation and shear resistance. However, these materials must be artificially designed, and the large deformation dynamic effects of the created structures must be taken into consideration when deciding on a protection concept. Despite their promise, little attention has been given to understanding the working mechanisms of high-rate and finite deformation effects of architected auxetic lattice structures. This study compares the static and dynamic elastic properties of different auxetic structures with a honeycomb structure, a typical non-auxetic lattice, at equivalent mass and stiffness levels. In this study, we limit the investigation to elastic material behaviour and do not consider contact between the beams of the lattices. It is demonstrated that the equivalent static and dynamic properties of individual lattices at an undeformed state are insufficient to explain the variations observed in impact situations. In particular, the initial Poisson's ratio does not determine the ability of a structure to resist impact. To gain a thorough comprehension of the overall behaviour of these structures during localized, high rate compression, the evolution of the elastic tangent properties under compression and shear deformation was monitored, leading to a more profound understanding. Observations made in one configuration of stiffness and mass are replicated and analysed in related configurations.*

## 4.1. INTRODUCTION

Impact events occur on various types of structures, ranging from roofs damaged by hailstorms [SS19] to civil structures exposed to accidents, such as a car hitting a bridge pillar [Pan<sup>&al</sup>18]. Detonation debris hitting personal protective equipment (see e.g. [Cro19]) or satellites in orbit threatened by micrometeorites and space debris [PA99] are examples of high impact velocity scenarios that occur in a military or space context. In the quest for better mitigation of these impacts, auxetic materials—materials with a negative Poisson’s ratio—exhibit several beneficial properties, such as higher indentation resistance [AGS12] and shear resistance [CL92], as well as increased fracture toughness [CL96] and energy absorption [JH17]. These properties are promising in the quest for lightweight materials for impact protection.

The differences in deformation behaviour between non-auxetic and auxetic materials are visualized in Figure 4.1. On the left, the lateral expansion is sketched during compression, as expected for materials with a positive Poisson’s ratio. The right side of the figure shows the lateral contraction after compression, as indicated by a negative Poisson’s ratio. This lateral contraction leads to a densification of the material at the point of impact. In addition to the properties mentioned above, this promises additional impact resistance.

Auxetic materials are rarely found in nature (e.g. cow teat skin [LVH91] or crystalline silica [KC92]), but they can be artificially constructed through careful design, as shown in various reviews [Boh<sup>&al</sup>23; Ren<sup>&al</sup>18; Wan<sup>&al</sup>20; ZLY20]. As the reviews show, the approach to designing auxetic metamaterials is well understood, but limited to static problems, and there are myriad types of auxetic architectures (see also [ÁD12]). Since the understanding of internal deformation patterns in dynamic environments and the resulting implications for the use of auxetic metamaterials in protective layers is limited and mostly based on macro-scale investigations with little insight into the workings at meso-scale, there is a need for a better understanding of the dynamic properties of these structures. Tatler [Tat22] compares different auxetic structures with comparable weight in crushing events without discussing the equivalent properties of the unit cells or their internal deformation mechanism. Even when the deformation mechanisms are described, the authors focus on one type of lattice only (e.g. Zhao et al. [Zha<sup>&al</sup>18] describe the dynamic performance of arrowhead structures, Mercer et al. [Mer<sup>&al</sup>22] investigate different re-entrant lattices).

As can be seen from the reviews on the subject, there are many possibilities for designing auxetic metamaterials. The linear, static properties of all these structures in the undeformed state are well understood [Ren<sup>&al</sup>18; Wan<sup>&al</sup>20]. In [Red<sup>&al</sup>18], the interaction between anisotropy and finite strains up to 10 % on the resulting static properties is studied together with the phase velocities of acoustic waves propagating through the lattice for Euler-Bernoulli beam structures with negligible bending stiffness. In impact scenarios, however, larger deformations (up to full densification) are expected with nonlinear waves propagating through the lattice structure. The

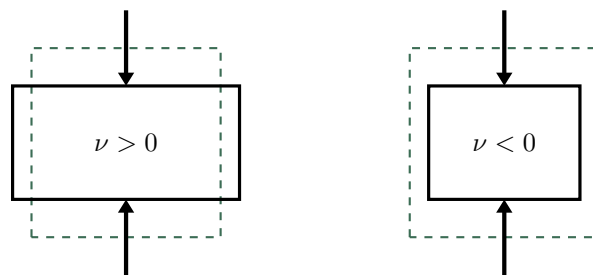


Figure 4.1.: Positive Poisson's ratio materials ( $\nu > 0$ ) and negative Poisson's ratio or auxetic materials ( $\nu < 0$ ) under compression (adapted from [Lim15]).

dynamic properties of different auxetics—and the influence on impact mitigation—are mainly reported phenomenologically for singular auxetic architectures without any comparison of different architectures under similar circumstances (see among others [Alo<sup>&al</sup>20; Che<sup>&al</sup>21; Gál<sup>&al</sup>21]).

This study contributes a first step in addressing the lack of understanding of the deformation behaviour of (auxetic) architected materials under high-rate localized compression by comparing the geometrically nonlinear static and dynamic properties of different architectures in a purely elastic environment. Our focus is on two-dimensional structures in order to identify the interdependencies between the lattice architecture and the resulting dynamic behaviour. We compare a set of different architectures based on the underlying mechanisms that produce auxeticity, all designed to exhibit the same linear-elastic properties and mass density. The study is carried out for nonlinear and dynamic problems and offers explanations for the observed differences. The different auxetic architectures are studied using a custom FE implementation of Simo-Reissner beams as explained in [Chapters 2 and 3](#). In this study material non-linearities and contact between the bars are ignored.

The chapter is structured as follows: In [Section 4.2](#) an overview of the possibilities to generate auxeticity in architected materials is given. Then, in [Section 4.3](#), the numerical framework and its mechanical background are discussed. In [Section 4.4](#), linear, static studies are performed on unit cells to find comparable configurations of different architectures. It is shown how these linear properties change when entering the nonlinear regime. The resulting dynamic effects are reported in a localized impact test including a study on strain rate effects. In [Section 4.5](#), the performance implications of the different architectural approaches are discussed. Finally, conclusions are drawn, and limitations of this study are presented.

## 4.2. AUXETIC ARCHITECTURES

### 4.2.1. DESIGN OPTIONS

The auxetic effect is based on the lateral inward movement of parts of the structure under uniaxial compression. This inward movement can be explained by two main mechanisms: rotation and inward folding.<sup>1</sup> In the following, different unit cell architectures and the corresponding design parameters will be explained. A unit cell, in the context of this publication, is the smallest part of a lattice that can be copied and connected to create the entire lattice.

The first class of auxetic architectures is constituted by those that derive their negative Poisson's ratio from rotation at the joints. These so-called *chiral* structures generate a rotating effect with circularly oriented beams, thus inducing rotation under compression. The chiral structure considered is the model introduced by Smith, Grima and Evans [SGE00], under a different name, to describe the behaviour of auxetic foams. In [BL19], the effects of geometrical parameters on the linear effective properties of the structure are described. A schematic of the chiral architecture is shown in Figure 4.2a and its auxetic mechanism is illustrated in Figure 4.2b. For the design of this architecture, it should be noted that due to the linear elasticity model on the material level, structures with geometric similitude exhibit the same equivalent properties. Thus, the width  $b$  and the thickness of the bars  $d$  are not chosen as independent parameters but rather the ratio  $t = d/l_c$ , with  $l_c = 0.5b/\cos\alpha$  as the length of a central bar. Next to this ratio, the angle of the bars  $\alpha$  is a variable measure. The colours in the mentioned and the following figures represent the same architecture throughout the chapter in all illustrations and graphs.

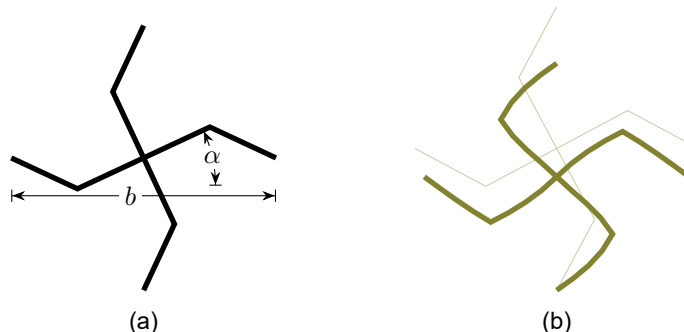


Figure 4.2.: Chiral architecture. (a) shows the design and geometric parameters, (b) illustrates uniaxial compression.

<sup>1</sup>Körner and Liebold-Ribeiro [KL15] argue that these two effects can be further reduced to a single mechanism, namely rotation. They describe a workflow to generate arbitrary auxetic structures based on eigenmode analysis. To explain the folding mechanism, they consider out-of-plane modes and recover the rotation mechanism by projecting the eigenmodes onto a plane. This results in beam rotation as opposed to joint rotation.

Taking four chiral unit cells and mirroring every other cell creates an *antichiral* structure, where a single unit cell consists of four rotational centres with alternating directions. The antichiral architecture is presented in Figure 4.3a with its deformation mechanism in Figure 4.3b.

4

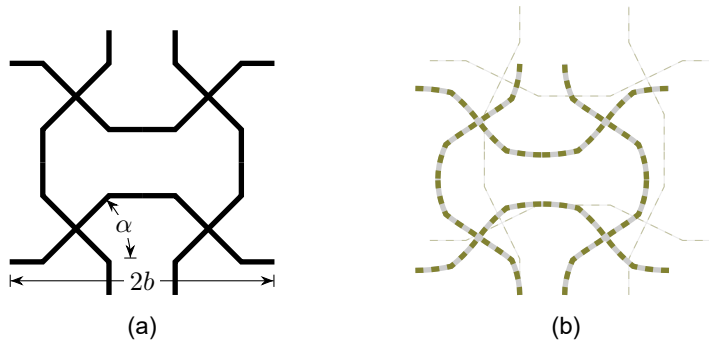


Figure 4.3.: Antichiral architecture. (a) shows the design and geometric parameters, (b) illustrates uniaxial compression.

The second class of architectures is composed of lattice structures that fold at the joints. In order to create an auxetic effect, this class consists of non-convex polygons, i.e. polygons with a reflex angle ( $\theta > 180^\circ$ ). The auxetic effect is caused by the non-convexity of the re-entrant structures, which causes them to fold laterally inwards under compression. The most prominent example of this is a *re-entrant honeycomb* (see among others [Gib<sup>&al</sup>97]). The parameters of this architecture are shown in Figure 4.4a and the working mechanism is illustrated in Figure 4.4b. Again, due to geometric similitude the properties do not change with absolute scale, instead of the lengths,  $l$  and  $b$ , individually their ratio  $r = \frac{l}{b}$  is taken as design variable and instead the thickness of a single beam  $d$ , the thickness scaled to the base length  $t = \frac{d}{b}$  is taken as variable. Finally, the angle between the base and the angled beams  $\alpha$  is added to the set of variables for this architecture. Since the properties of this architecture are not invariant to the orientation, this architecture will also be investigated rotated by  $90^\circ$ . The corresponding deformation mechanism is shown in Figure 4.4c.

While the re-entrant structure has two opposing folds, another architecture with two folds in the same direction is the *arrowhead* structure. This commonly investigated auxetic structure was originally the result of a topology optimization for negative Poisson's ratio [LSB97]. The architecture is visualized in Figure 4.5a along with its parameters and the working mechanism shown in Figure 4.5b. In this structure, the beam thickness  $d$  is scaled with the height of the unit cell  $t = \frac{d}{h}$ . The three variables, that determine the properties of this structure are the two angles of the longer beam  $\beta$  as well as the shorter beam  $\alpha$  and the height  $h$ . As with the re-entrant honeycomb structure, this architecture is also studied rotated by  $90^\circ$ . The corresponding deformation mechanism is shown in Figure 4.5c.

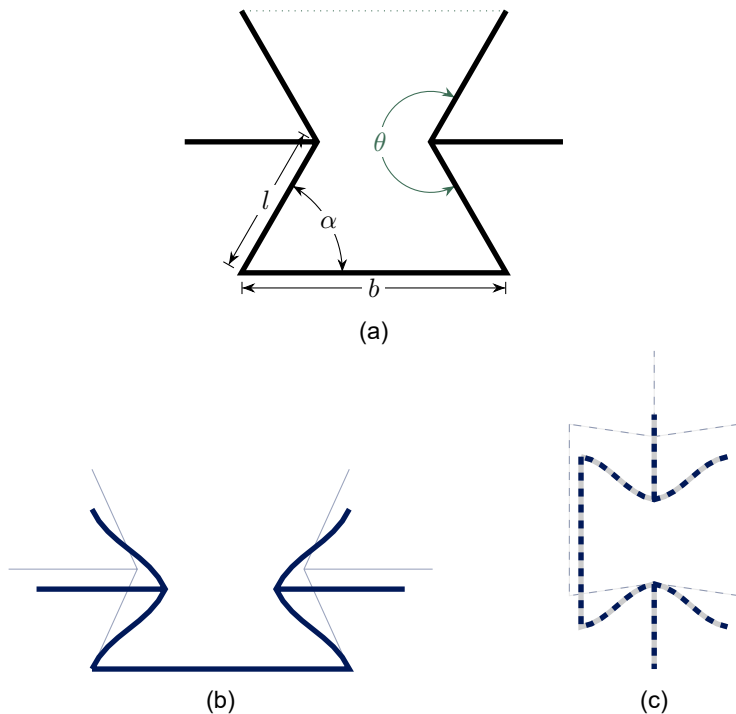


Figure 4.4.: Re-entrant honeycomb architecture. (a) shows the design and geometric parameters, uniaxial compression is illustrated in (b) for  $0^\circ$  orientation and in (c) for  $90^\circ$  orientation.

To allow for a comparison of the different architectures, a non-auxetic architecture is also included as a reference. Since the *normal honeycomb* is based on the same architecture as the re-entrant honeycomb, it is included in the study. Due to this similarity, its properties are determined by the same geometry factors as the re-entrant honeycombs, namely the ratio between the beam lengths  $r = \frac{l}{b}$ , the ratio between the thickness and the base length  $t = \frac{d}{b}$  and the angle between the base beams  $\alpha$ . Similar to the argumentation in the re-entrant architecture, investigations are also conducted with the structures rotated by  $90^\circ$ . The general configuration is depicted in Figure 4.6a, with the deformation mechanisms are shown in Figure 4.6b and Figure 4.6c for the  $0^\circ$  and  $90^\circ$  orientation respectively.

Table 4.1.: Range of properties for different architectures.

Architecture	$\alpha$	$t$	$r$	$\beta$	design constraint
re-entrant	$(20^\circ, 85^\circ)$	$(0.01, 0.1)$	$(\frac{1}{3}, \frac{4}{3})$	—	$r < \frac{1}{2 \cos \alpha}$
arrowhead	$(5^\circ, 45^\circ)$	$(0.01, 0.1)$	—	$(50^\circ, 80^\circ)$	$3 \tan \alpha < \tan \beta$
chiral	$(5^\circ, 60^\circ)$	$(0.01, 0.1)$	—	—	
antichiral	$(5^\circ, 60^\circ)$	$(0.01, 0.1)$	—	—	
honeycomb	$(95^\circ, 145^\circ)$	$(0.01, 0.1)$	$(\frac{1}{3}, \frac{4}{3})$	—	

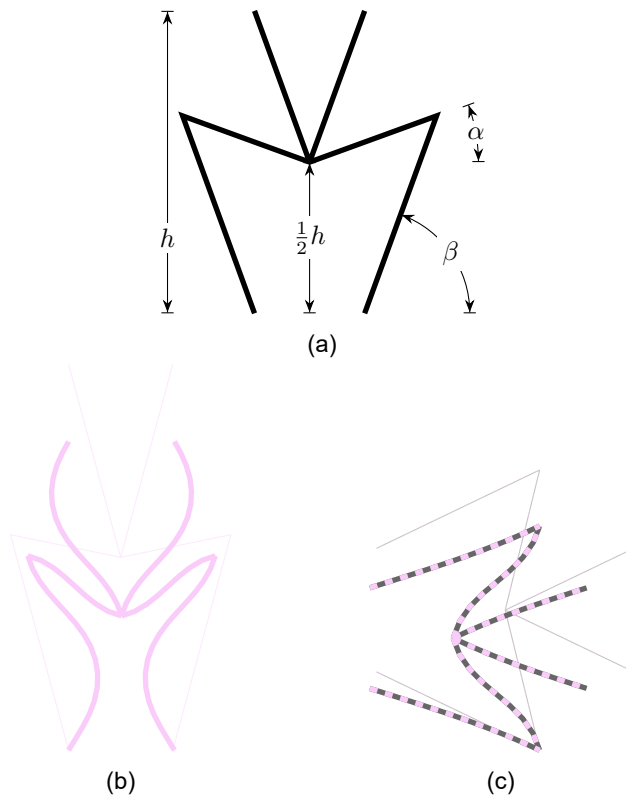


Figure 4.5.: Arrowhead architecture. (a) shows the design and geometric parameters, uniaxial compression is illustrated in (b) for 0° orientation and in (c) for 90° orientation.

### 4.2.2. DESIGN SELECTION

The parameters of all the selected architectures are tuned so that all the lattices in the undeformed configuration have the same Young's modulus in the vertical direction and the same relative density. The following is a brief explanation of the procedure for metamaterials with a density relative to the constituent material

$$\rho_{\text{rel}}^* = \frac{\rho}{\rho_{\text{mat}}} = 0.1$$

and an equivalent Young's modulus  $E_y^* = 300 \text{ MPa}$ , where  $(\cdot)^*$  represents target properties. For all investigations, the base material of the structures is set as a generic metal with  $E_{\text{mat}} = 210 \text{ GPa}$ ,  $\nu_{\text{mat}} = 0.3$ , and  $\rho_{\text{mat}} = 7850 \text{ kg m}^{-3}$ .

Since this study assumes linear elastic material behaviour at the microscale, structures with geometric similitude can be assumed to have identical properties. Thus, as explained above, the thickness  $t$  of the beams related to the primary length of the unit cell as well as the ratio between the beam lengths  $r$  are taken as free

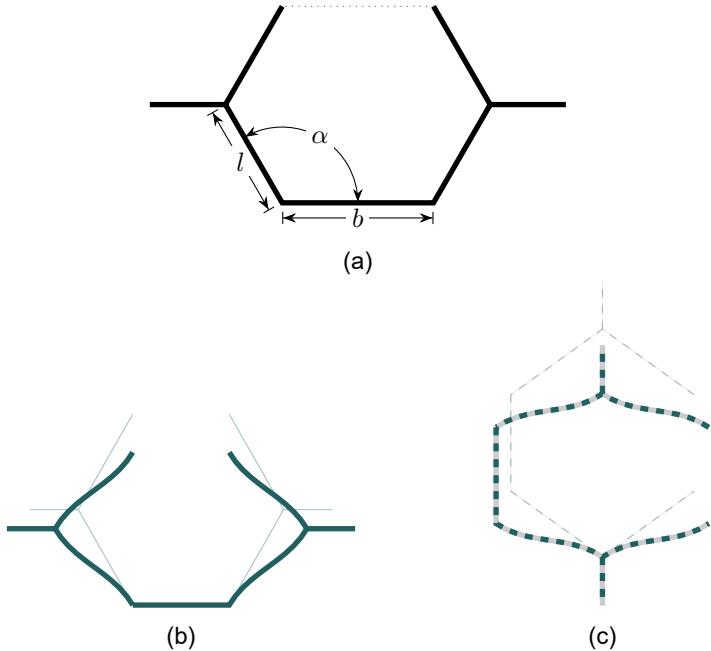


Figure 4.6.: Honeycomb architecture. (a) shows the design and geometric parameters, uniaxial compression is illustrated in (b) for 0° orientation and in (c) for 90° orientation.

Table 4.2.: Resulting properties and unit cells of the investigated architectures with target properties  $E_y^* = 300 \text{ MPa}$ ,  $\rho_{\text{rel}}^* = 0.1$   
Angles  $\alpha, \beta$  are given in degrees and the moduli  $E_x, E_y, G_{xy}, G_{yx}$  in MPa.

Geometry	$t$	$\alpha$	$\beta$	$r$	$\rho_{\text{rel}}$	$E_y$	$E_x$	$\nu_{yx}$	$\nu_{xy}$	$G_{xy}$	$G_{yx}$
re-entrant	0.035	65.62	—	0.43	0.100	297	273	-1.00	-0.92	8	8
re-entrant (90°)	0.046	81.67	—	0.50	0.100	297	2,937	-0.26	-2.60	15	15
arrowhead	0.021	11.60	74.90	—	0.100	296	468	-0.73	-1.16	924	924
arrowhead (90°)	0.030	13.81	64.34	—	0.100	295	80	-1.85	-0.50	1,583	1,583
chiral	0.078	28.11	—	—	0.100	299	299	-0.38	-0.38	53	19
antichiral	0.085	26.09	—	—	0.100	299	299	-0.69	-0.69	10	10
honeycomb	0.094	119.69	—	1.14	0.100	302	246	1.08	0.88	88	88
honeycomb (90°)	0.096	125.63	—	1.17	0.100	302	189	1.23	0.77	101	101



variables. All free variables are tuned within their ranges and conditions reported in Table 4.1 to ensure realistic structures. The ranges and conditions are explained in more detail in Appendix A.1. Given these design ranges, the individual structures are subsequently tuned to exhibit properties as close to the targets as possible. The resulting properties as well as visualizations of the corresponding unit cells are shown in Table 4.2. Details of the tuning process and results for different target lattice properties are shown in Appendix A.1.

### 4.3. NUMERICAL FRAMEWORK

The aforementioned lattice structures are implemented as Simo-Reissner beams, as laid out in Chapters 2 and 3. For the initial investigations in this chapter, the material behaviour is limited to the linear elastic case and no contact detection is employed. The implementation for this work is carried out using the JIVE-Framework [JIVE].

#### 4.3.1. TANGENT PROPERTY COMPUTATION

The linear equivalent properties of a unit cell need to be computed for simple deformation modes. In order to do so, periodic boundary conditions (PBCs) were implemented. Since the investigated architectures do not possess nodes in the corners, *ghost* nodes have been introduced for the application of the PBCs. The implementation of this procedure is explained in A.2.1.

In order to determine the equivalent elastic properties in a deformed state, a simple approach using finite differences was chosen. The incremental displacement gradient  $\delta \mathbf{H}$  is related to incremental Piola-Kirchhoff stresses  $\delta \mathbf{P}$  by tangent stiffness tensor  $\mathbb{C}^4$

$$\delta \mathbf{P} = \mathbb{C}^4 : \delta \mathbf{H}. \quad (4.1)$$

In order to estimate the elastic properties at a fixed deformation in a first step, the displacement gradient at this deformation  $\mathbf{H}_o$  is recorded. Then in a next step, this displacement gradient is perturbed in one direction

$$\mathbf{H}^{ij\pm} = \mathbf{H}_o \pm 0.5 \times 10^{-9} \begin{bmatrix} \delta_{i1}\delta_{j1} & \delta_{i1}\delta_{j2} \\ \delta_{i2}\delta_{j1} & \delta_{i2}\delta_{j2} \end{bmatrix} \quad i, j \in [1, 2] \quad (4.2)$$

with the Kronecker delta  $\delta_{kl}$ . The corresponding 1st Piola-Kirchhoff stress tensors  $\mathbf{P}^{ij\pm}$ ,  $i, j \in [1, 2]$  are then recorded. For all directions, corresponding tangent properties are first computed by addition of the recorded values

$$\begin{aligned} \Delta \mathbf{H}^{ij} &= \mathbf{H}^{ij+} - \mathbf{H}^{ij-} \\ \Delta \mathbf{P}^{ij} &= \mathbf{P}^{ij+} - \mathbf{P}^{ij-} \end{aligned} \quad i, j \in [1, 2]. \quad (4.3)$$

Then the coefficients of the tangent stiffness tensor are determined by dividing the stresses by the corresponding strains:

$$c_{ijkl} = \frac{\Delta P_{ij}^{kl}}{\Delta H_{kl}^{ij}}. \quad (4.4)$$

Finally, using the inverse of the stiffness tensor  $\mathbb{C}^4$ , the compliance tensor  $\mathbb{S}^4$ , the equivalent tangent Young's modulus is calculated by rearranging the equation

$$\begin{bmatrix} \delta H_{11} & 0 \\ 0 & \delta H_{22} \end{bmatrix} = \mathbb{S}^4 : \begin{bmatrix} \delta P_{11} & \delta P_{12} \\ \delta P_{21} & 0 \end{bmatrix} \quad (4.5)$$

for

$$\delta H_{11} = \frac{1}{E_{11}} \delta P_{11}. \quad (4.6)$$

The Poisson's ratio is then found by further rearrangements leading to

$$\delta H_{22} = -\nu_{12} \delta H_{11}. \quad (4.7)$$

Similar procedures are employed to determine the tangent properties  $E_{22}$  and  $\nu_{21}$ .

The constrained moduli  $M_{11}$ ,  $M_{22}$  and shear moduli  $G_{12}$ ,  $G_{21}$  are determined by rearrangements of the equation

$$\begin{bmatrix} \delta H_{11} & 0 \\ 0 & 0 \end{bmatrix} = \mathbb{S}^4 : \begin{bmatrix} \delta P_{11} & \delta P_{12} \\ \delta P_{21} & \delta P_{22} \end{bmatrix} \quad (4.8)$$

for

$$\delta H_{11} = \frac{1}{M_{11}} \delta P_{11}. \quad (4.9)$$

Again, identical procedures are employed to determine  $G_{12}$ ,  $G_{21}$ , and  $M_{22}$ . Details are found in A.2.2

## 4.4. NUMERICAL RESULTS

Using the methods described in Section 4.3 and the unit cells derived from the architectures as described in Section 4.2, the changes in the properties of unit cells subjected to large deformations are discussed below. First, the equivalent Young's modulus and Poisson's ratio as static properties are presented, followed by an overview of the equivalent lateral to the impact ( $x$ -direction) pressure and shear wave speeds as well as the longitudinal to the impact ( $y$ -direction) pressure wave speeds as dynamic properties of the different architectures. Finally, the behaviour of the different architectures under high strain rate and localized compression is examined and discussed.

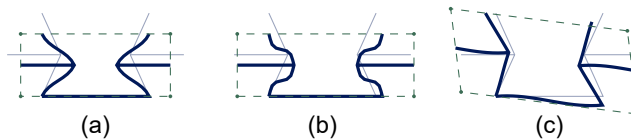


Figure 4.7.: (a) uniaxial compression (Equation (4.10)), (b) planar compression (Equation (4.11)) and (c) pure shear deformation (Equation (4.12)) of the re-entrant unit cell using the PBCs as in Figure A.1.

#### 4.4.1. STATIC PROPERTIES OF THE ARCHITECTURES

The evolution of the initial static properties of each architecture, reported in Table 4.2, is investigated with the procedures described in Section 4.3.1 applied to single unit cells. Structures that maintain high stiffness over a wide range of deformations are expected to have higher resistance in an impact scenario, as the decelerating forces on the impactor are high over the range of deformation to be expected during impact. To estimate this, three types of deformation are considered: (a) unconstrained uniaxial compression (in the following called uniaxial), (b) constrained uniaxial (in the following called planar) compression, and (c) pure shear deformation, as visualized in Figure 4.7.

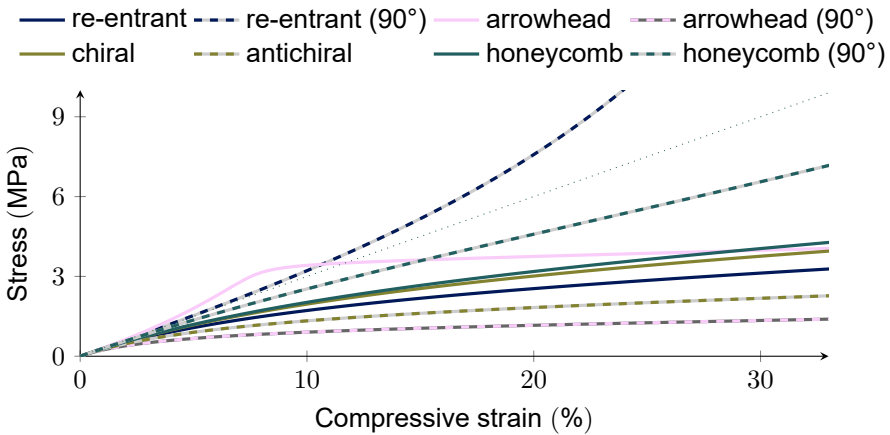


Figure 4.8.: Stress-strain curves in uniaxial (unconstrained) compression for different architectures.

The architectures are first exposed to uniaxial compression. This is done by applying the displacement gradients

$$\mathbf{H} = k \begin{bmatrix} \bullet & 0 \\ 0 & -1 \end{bmatrix} \quad k \in [0, 0.33], \quad (4.10)$$

where  $\bullet$  denotes no constraint. This deformation mode is illustrated in Figure 4.7a. At each deformation step the corresponding equivalent elastic tangent properties are recorded as well as the current stresses and strains at the four boundaries. Since contact and interpenetration of different beams, which is not modelled by the numerical framework, occur at later stages of deformation, in the following only compression up to  $k = 33\%$  will be discussed.

In the stress-strain curve (Figure 4.8), it is shown that all but two structures show a reduced stiffness under uniaxial compression. The *rotated* re-entrant honeycomb structure (depicted by the dashed blue line) is the only structure that keeps stiffening. This effect is due to the fact, that the folding mechanism aligns the beams in vertical direction, promoting axial loading over bending in uniaxial compression. The

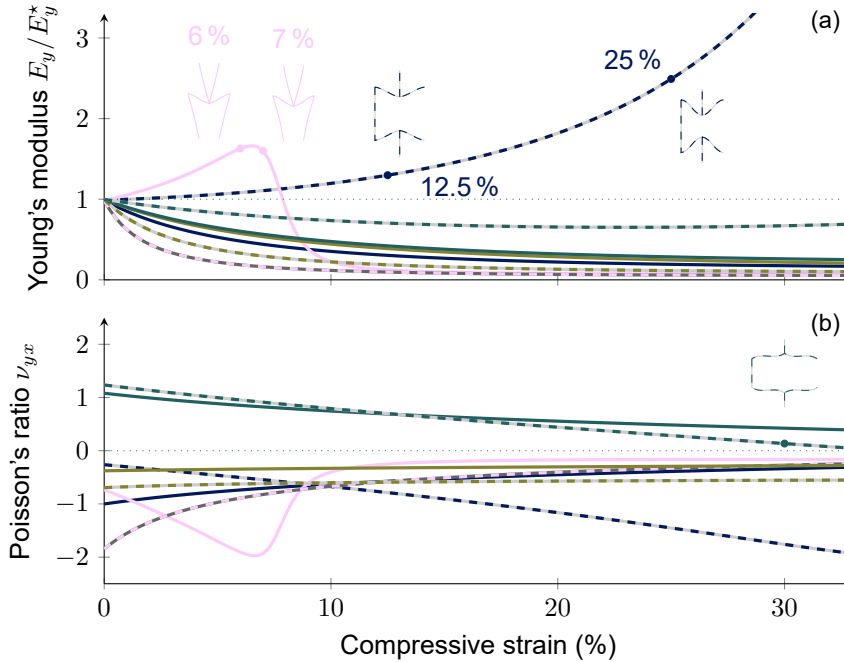


Figure 4.9.: Change of properties under uniaxial (unconstrained) compression for different architectures, namely (a) the normalized (unconstrained) Young's modulus  $E_y$  and (b) the Poisson's ratio  $\nu_{yx}$ .

same explanation holds for the initial stiffening of the arrowhead structure. However, at approximately 6.5 % compression the beams start to buckle, leading to a transition from axial loading to loading in bending and thus an overall weakening at larger deformations. These effects are depicted as well in Figure 4.9a, where the normalized equivalent Young's modulus  $E_y$  is plotted against the compressive strain. In this figure some relevant deformation patterns of the architectures are visualized as well. The buckling of the arrowhead structure (depicted in solid orange) can be seen at the plotted deformation patterns at 6 % and at 7 % compression. Prior to buckling the alignment of the beams is in vertical direction, leading to more axial loading. After buckling, the beams are loaded in bending again. Similarly, the vertical alignment of the beams in the rotated re-entrant honeycomb structure is clearly visible in the deformation sketches in Figure 4.9a at 12.5 % and 25 %. Additionally, in the lower graph Figure 4.9b, the Poisson's ratio  $\nu_{yx}$  is plotted against compression. Structures with a reduced stiffness also exhibit a decrease in involvement of lateral material in larger patches, i.e. a Poisson's ratio developing towards zero. This results in auxetic architectures exhibiting a less pronounced negative Poisson's ratio, thus reducing the effect of lateral material involvement. Noteworthy is the fact, that the rotated regular honeycomb structure, upon compression, resembles the

rotated re-entrant honeycomb structure. This is visualized in the deformation pattern at 30 %, and supported by the approximately linear decrease of the Poisson's ratio, leading to a change from non-auxetic to auxetic behaviour at high (> 33 %) compression.

4

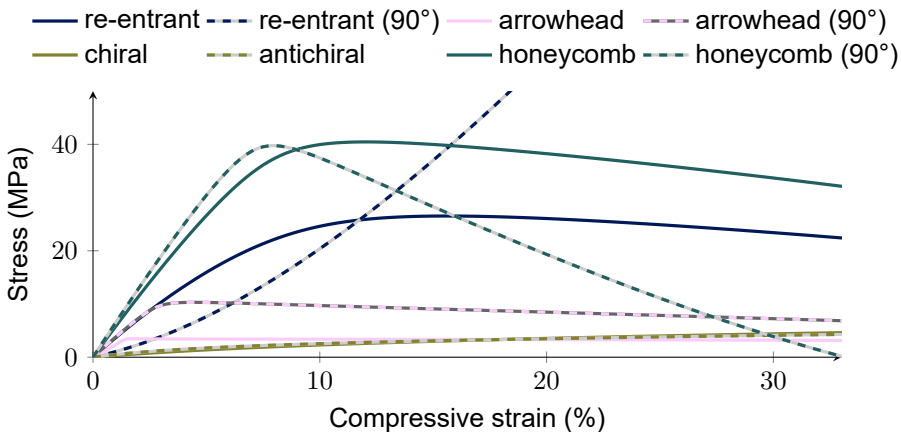


Figure 4.10.: Stress-strain curves in planar (constrained) compression for different architectures.

During impact, lateral material is confining the lateral displacement of the impacted lattice, thus constrained uniaxial or planar compression resembles an impact scenario better. For the assessment of the impact performance of metamaterials it is therefore valuable to also consider planar compression. This planar compression is described by the displacement gradients

$$\mathbf{H} = k \begin{bmatrix} 0 & 0 \\ 0 & -1 \end{bmatrix} \quad k \in [0, 0.33]. \quad (4.11)$$

This deformation mode is illustrated in Figure 4.7b. In Figure 4.10 the corresponding stress-strain curves are plotted. It should be noted, that the stresses are much higher compared with the stresses in uniaxial compression (in Figure 4.8). In planar compression only the rotated re-entrant honeycomb structure exhibits stiffening behaviour. The regular honeycomb and arrowhead architectures both display reduced stiffness leading to snap-through, resulting in negative slopes of the stress-strain curve following substantial planar compression. An illustration of the corresponding deformed structures is provided in Figure 4.11 for the rotated honeycomb unit cell. This behaviour is also observed in the re-entrant honeycomb unit cell. The normalized Young's modulus  $E_y$  plotted against the deformation as done in Figure 4.11a shows a similar behaviour. It should be noted here, that the Young's modulus as proxy for the *unconstrained* uniaxial tangent stiffness in Figure 4.11a is not equal to the derivative of the constrained stress-strain curve in Figure 4.10. The stiffness for all but the (anti-)chiral and the rotated re-entrant honeycomb architecture become negative, resulting in loss of resistance against unconstrained compression.

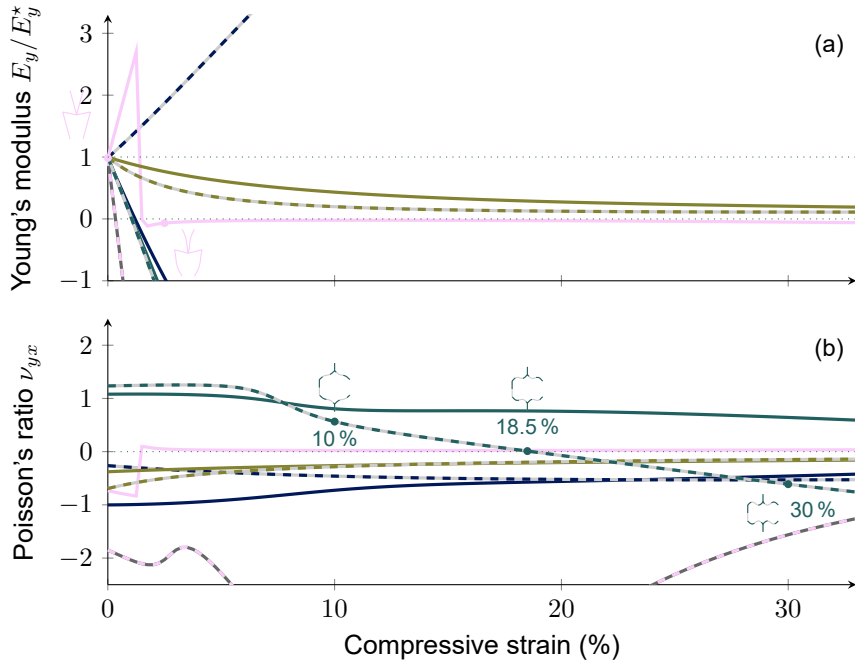


Figure 4.11.: Change of vertical properties in planar (constrained) compression for different architectures, namely (a) the normalized (unconstrained) Young's modulus  $E_y$  and (b) the Poisson's ratio  $\nu_{yx}$ .

In the lower graph, Figure 4.11b, the Poisson's ratio  $\nu_{yx}$  is plotted against the compressive strain. Here, the rotated regular honeycomb's transition from non-auxetic to auxetic behaviour is even more pronounced than for uniaxial compression and can be observed around 18.5 % compression. The deformation patterns at 10 % and 30 % planar compression show the transitions from the convex honeycomb shape towards a non-convex shape resembling—like in the uniaxial case—a re-entrant honeycomb structure. Also, the arrowhead structure transfers from auxetic behaviour into non-auxetic behaviour after buckling (in planar compression at approximately 1.5 %). This buckling is visualized in the deformation patterns at 0 % and 2.5 % planar compression in Figure 4.11a.

In an impact scenario also significant shear deformation may be expected. The development of different architectures under shear deformation is thus investigated by applying the displacement gradient

$$\mathbf{H} = k \begin{bmatrix} 0 & -0.5 \\ -0.5 & 0 \end{bmatrix} \quad k \in [0, 0.33]. \quad (4.12)$$

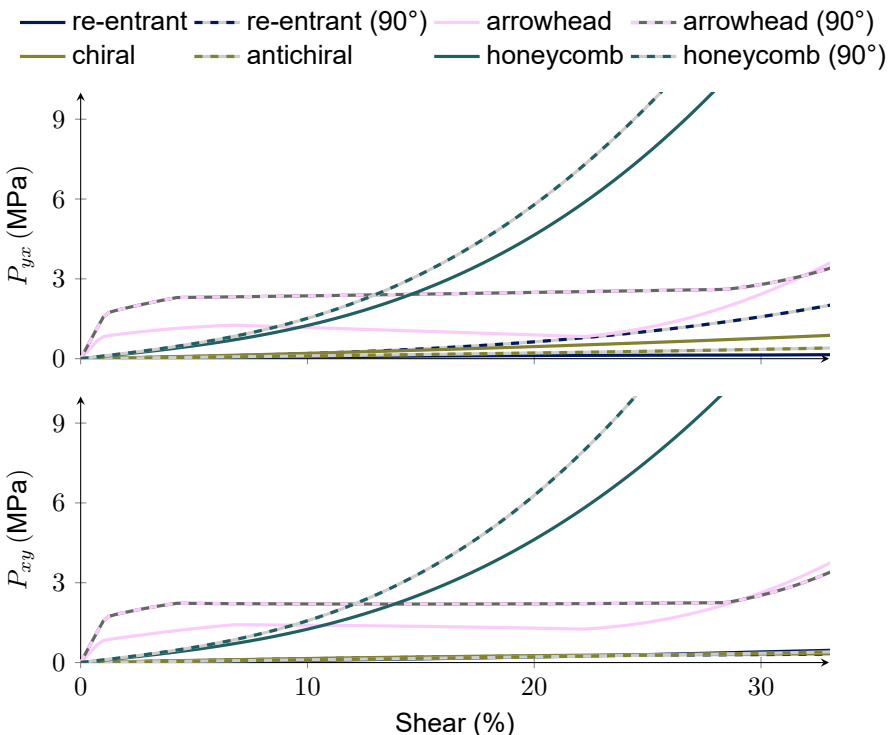


Figure 4.12.: Stress-strain curves in pure shear for different architectures.

This deformation mode is illustrated in Figure 4.7c. In Figure 4.12, the stress-strain curves for both shear components are shown. In the stress-strain curves, the regular honeycomb structures show the strongest resistance towards shear at higher deformations. The arrowhead structures show a steep decline in shear resistance, as they initially show the highest stresses upon shear deformation, followed by only minor increase in stresses at increasing strains. In Figure 4.13 the normalized Young's modulus and the Poisson's ratio are plotted against shear deformation. Here, apart from the arrowhead structures, all structures show an increasing Young's modulus. Especially the non-auxetic honeycomb structures show an increase, which is significantly larger compared to the corresponding auxetic structures. The arrowhead structures exhibit three regimes across the range of shear deformation examined. The progressive deformation patterns throughout shear deformation are shown in Figure 4.14. After a steep initial decline in Young's modulus, an almost constant modulus is seen before the Young's modulus finally starts to increase. These regions in the stiffness properties for the arrowhead architecture are explained by the fact that the two central beams in the unit cell initially form a downwards facing half-wave. Throughout deformation, the amplitude of this half-wave is decreasing, leading to load transfer by bending and pre-stresses even leading

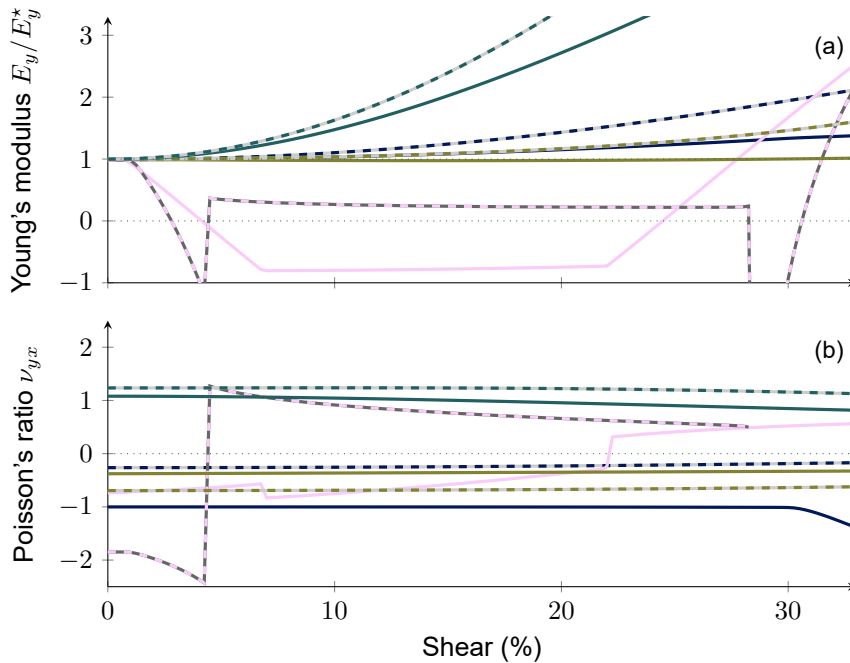


Figure 4.13.: Change of vertical properties under pure shear deformation for different architectures, namely (a) the normalized Young's modulus  $E_y$  and (b) the Poisson's ratio  $\nu_{yx}$ .

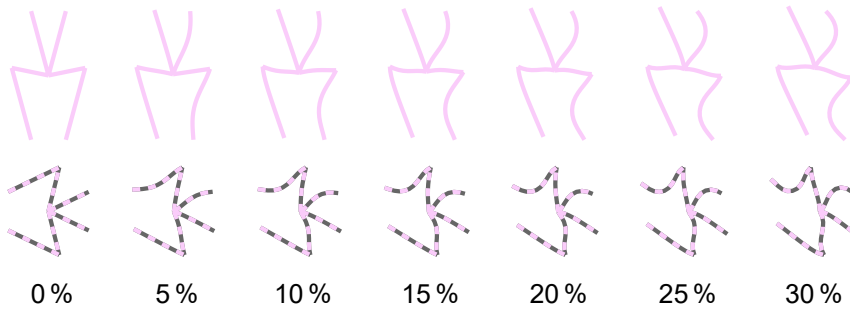


Figure 4.14.: Pure shear deformation pattern of arrowhead structures.

to negative Young's moduli, as can be seen in Figure 4.13a. After some deformation one of the two central beams suddenly shows large deformation, leading to the two central beams resembling a full sine wave with one node of the wave at the central joint. This is occurring at 4 % for the rotated and 7 % for the unrotated variant. Here, further deformation does not change the overall vertical stiffness of the unit cell, as the connecting joint is now resembling the node of the wave. At 28 %

for the rotated and 22 % for the unrotated variant the second beam again shows a sudden deformation in such a way, that the two central beams again resemble a (now upwards facing) half-wave. The connecting joint is located on the peak of this half-wave leading again to stiffening, as every displacement of the joint has the resistance of the beams working against it. Lastly, the Poisson's ratio (as seen in the lower graph Figure 4.13b) almost remains unchanged under shear deformation for all but the arrowhead architectures. The arrowhead architectures again show two jumps in their tangent properties, coinciding with the earlier mentioned configuration changes.

#### 4.4.2. DYNAMIC PROPERTIES OF THE ARCHITECTURES

In the assessment of the effects of different architectures in impact scenarios, not only the (static) loading resistance, as discussed in Section 4.4.1, is of importance, but also the behaviour of the architectures in dynamic loading is relevant. First measures to assess this dynamic behaviour are the pressure wave speed  $c_{P_x}$  and shear wave speed  $c_{S_x}$  lateral to the impact direction, as well as the pressure wave speed  $c_{P_y}$  longitudinal to the direction of impact. They are computed with the following formulae

$$c_{P_x} = \sqrt{\frac{M_x}{\rho}}, \quad c_{S_x} = \sqrt{\frac{G_{yx}}{\rho}}, \quad c_{P_y} = \sqrt{\frac{M_y}{\rho}} \quad (4.13)$$

where  $M_x$ ,  $G_{yx}$ , and  $M_y$  are determined during deformation as described in Section 4.3.1. The density  $\rho$  is updated with the deformation as well. As these wave speeds are calculated for homogenized cells, wave phenomena with wave lengths smaller than the size of each unit cell are not captured in this approach. Considering the development of the wave speeds  $c_{P_x}$ ,  $c_{S_x}$ ,  $c_{P_y}$  in the three cases described in Section 4.4.1—uniaxial compression, planar compression, and pure shear—offers more insight into the behaviour of different architectures under dynamic loading conditions. Higher lateral wave speeds lead to a higher involvement of the lateral material, since the stress concentrations move faster to the sides, i.e. the not impacted sections of the patch leading to a better distribution of energy.

In Figure 4.15 the wave speeds are plotted against uniaxial compression for all eight architectures. In the top graph (Figure 4.15a), the lateral pressure wave speed  $c_{P_x}$  is shown. It can be seen, that in the undeformed state, the rotated re-entrant unit cell has the highest lateral pressure wave speed of the investigated structures with an obvious decline upon compressive deformation. In the middle graph Figure 4.15b, the lateral shear wave speeds of the different structures and their development under uniaxial compression are shown. It can be seen, that the lateral shear wave speeds, compared to the lateral pressure wave speeds, are significantly smaller for all architectures but the arrowhead ones. In the lower graph Figure 4.15c, the longitudinal pressure wave speeds  $c_{P_y}$  are shown. They show similar behaviour to

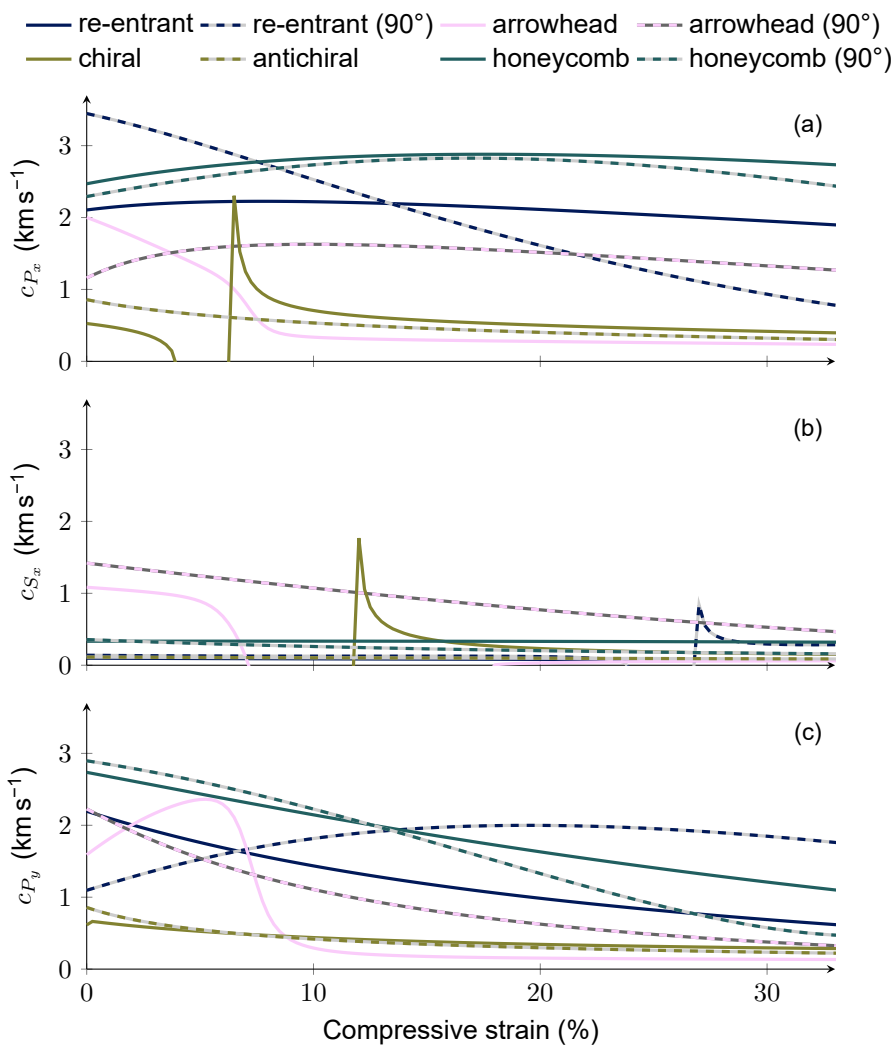


Figure 4.15.: Change of the lateral pressure and shear wave speed under uniaxial compression, (a) shows the lateral pressure wave speed  $c_{P_x}$ , (b) shows the lateral shear wave speed  $c_{S_x}$ , (c) shows the pressure wave speed in impact direction  $c_{P_y}$ .

the Young's moduli in impact direction  $E_y$  (compare Figure 4.9a). The differences are due to the constrained modulus  $M_y$  in the formula for the wave speed instead of the (unconstrained) Young's modulus  $E_y$  as well as in the consideration of the changing density  $\rho$  throughout the deformation.

The peaks in the chiral structure wave speeds in both graphs, Figure 4.15a and Figure 4.15b, as well as in the rotated re-entrant honeycomb structure in the  $c_{S_x}$  graph, are caused by instabilities of the pre-stressed beams undergoing small changes in loading direction leading to 'micro'-buckling, during the finite difference determination of the tangent stiffness tensor  $\mathbb{C}^4$ . This leads to the structure appearing with greatly exaggerated or reduced stiffness around polar points corresponding to the peaks.

Similar behaviour of the wave speeds can be seen in Figure 4.16, where the wave speeds are plotted against planar compressive strains. Compared with the uniaxial case previously discussed, the rotated re-entrant structure also tends to lose some of its lateral pressure wave speed, as can be seen in Figure 4.16a. This is, however, less pronounced and since all other structures show a substantial decrease, it maintains the highest wave speed. The shear wave speeds in Figure 4.16b show similarly low levels as in the uniaxial case. The pressure wave speeds in the impact direction are depicted in Figure 4.16c. The various peaks, that can be seen, again stem from the pre-stress in the singular beam elements at the various stages of compression corresponding instabilities during the finite difference calculation.

In the shear deformation case, as shown in Figure 4.17a, all architectures show a positive lateral pressure wave speed throughout the shear deformation except for the arrowhead unit cell in the  $90^\circ$  case. In the middle graph, Figure 4.17b, again, all architectures but the arrowhead ones show an ability to maintain their pressure wave speeds. The lower graph in Figure 4.17c depicts the development of the longitudinal pressure wave speeds over the shear deformation. The negative range of wave speeds for the arrowhead lattices is due to the subsequent flipping of the two central beams as explained in Section 4.4.1 and shown in Figure 4.13. In Figure 4.17 as before, the peaks and apparent infinite wave speeds stem from instabilities in the finite difference computation of the tangent stiffness tensor  $\mathbb{C}^4$ .

#### 4.4.3. IMPACT PERFORMANCE OF ARCHITECTURES

The impact protection of the different architectures is assessed by assembling the unit cells into a bigger patch. A schematic of the setup is shown in Figure 4.18 and will be subsequently explained. These patches are designed to have an initial height  $h_0 \approx 1$  cm, width  $w_0 \approx 1$  cm, and depth  $d_0 = 10$  cm. Due to the fact, that the different unit cells have different sizes patches of similar size contain different numbers of unit cells for the different architectures. Initially, these patches are globally compressed statically and dynamically at strain rates  $H$  of  $2.5 \text{ ms}^{-1}$ ,  $5 \text{ ms}^{-1}$ ,  $7.5 \text{ ms}^{-1}$  and  $10 \text{ ms}^{-1}$ . Later, additional material is added to the sides to investigate the effects of lateral material involvement. The width of the impact loading is kept constant with the overall material width changing, resulting in width-to-impact ratios

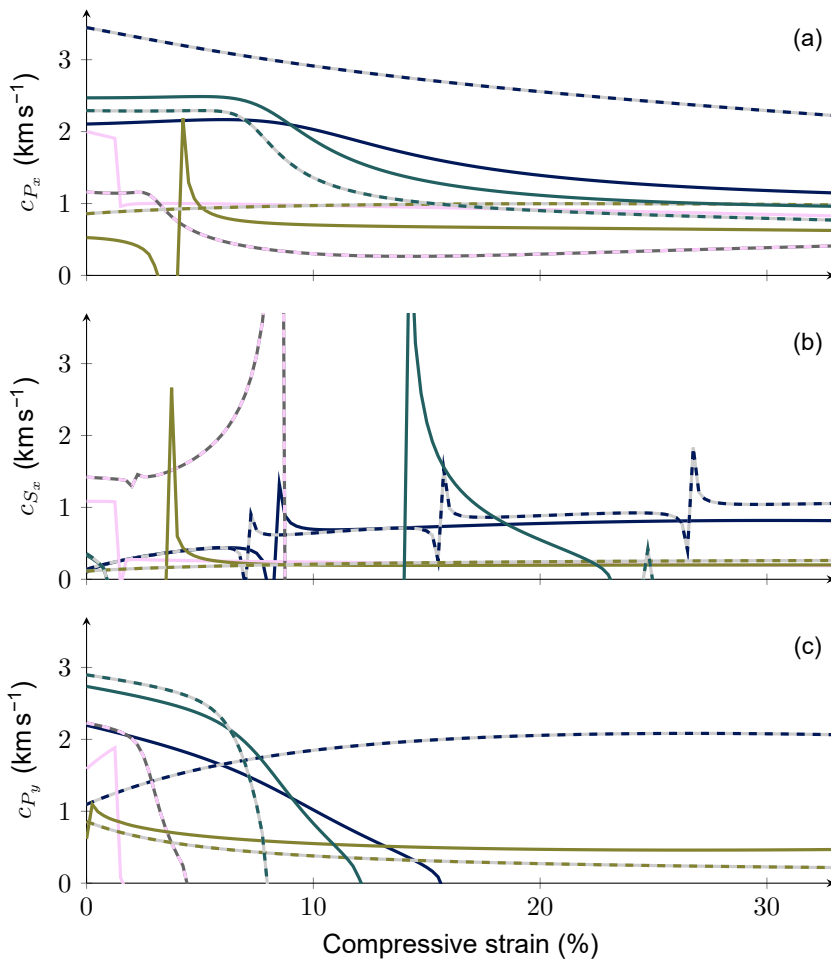


Figure 4.16.: Change of the lateral pressure and shear wave speed under planar compression, (a) shows the lateral pressure wave speed  $c_{P_x}$ , (b) shows the lateral shear wave speed  $c_{S_x}$ , (c) shows the pressure wave speed in impact direction  $c_{P_y}$ .

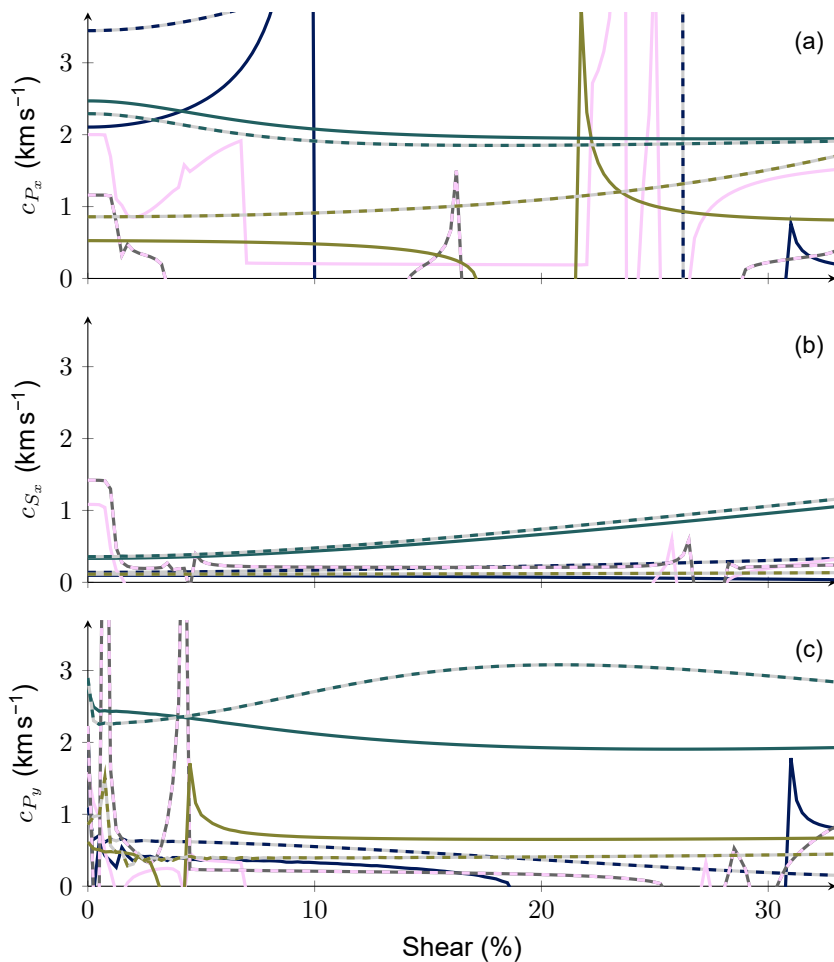


Figure 4.17.: Change of the lateral pressure and shear wave speed under shear, (a) shows the lateral pressure wave speed  $c_{P_x}$ , (b) shows the lateral shear wave speed  $c_{S_x}$ , (c) shows the pressure wave speed in impact direction  $c_{P_y}$ .

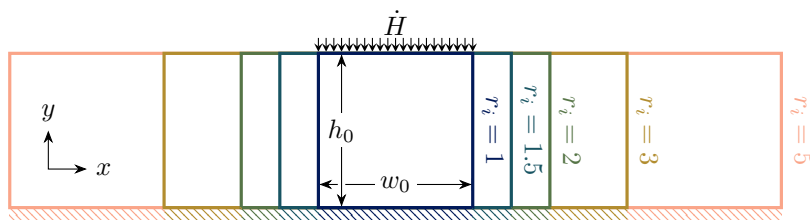


Figure 4.18.: Sketch of the setup used for the simulations.

of  $r_i = 1, 1.5, 2, 3$  and  $5$ . The compression is induced with changing Dirichlet boundary conditions on the top boundary over the constant impact width, whilst the reaction forces are recorded. The bottom boundary is fully fixed, and the sides are free.

During the computation, the displacements of the boundary subjected to movement  $u_t(t)$  are stored as prescribed. The total force needed to achieve this displacement  $f_t(t)$  and the total reaction force at the lower boundary  $f_b(t)$  are recorded as well. In post-processing, the specific energy absorption (SEA) for the undeformed volume under the impacted boundary is computed as:<sup>2</sup>

$$\text{SEA}(t) = \frac{1}{\rho_0} \int_{\tau < t} \frac{u_t(\tau)}{h_0} \frac{f_t(\tau)}{w_0 d_0}. \quad (4.14)$$

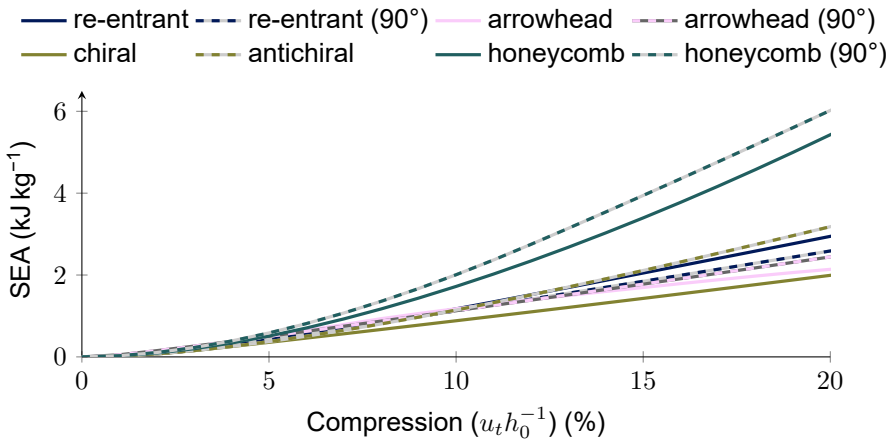


Figure 4.19.: SEA at non-localized ( $r_i = 1$ ), static ( $\dot{H} = 0 \text{ ms}^{-1}$ ) compression.

The results of non-localized ( $r_i = 1$ ), static ( $\dot{H} = 0 \text{ ms}^{-1}$ ) compression are shown in Figure 4.19. It should be noted, that here only deformations up to 20 % are discussed in order to exclude interpenetration of beams, which may happen because contact is not considered in the numerical framework. In the graph the SEA is plotted against the compressive strain. The patches consisting of arrowhead unit cells (both rotated and not) could not be computed for the desired compression of 20 % due to a plethora of local buckling points in the singular structural members. The compression of the regular honeycomb structures (rotated and not rotated) requires most work especially in the later stages. Given the static nature of this experiment, only the static properties described in Section 4.4.1 have an effect. Here, especially

<sup>2</sup>normalization for the initial volume is taking place to eliminate differences between the aspect ratios of the architectures and subsequent differences in initial volume

the vertical stiffness during shear deformation as seen in Figure 4.13a and the constrained stiffness related to the constrained stress-strain curve in Figure 4.10 are of importance. In both of these figures the regular honeycomb structures show the stiffest response over a wide range of deformation.

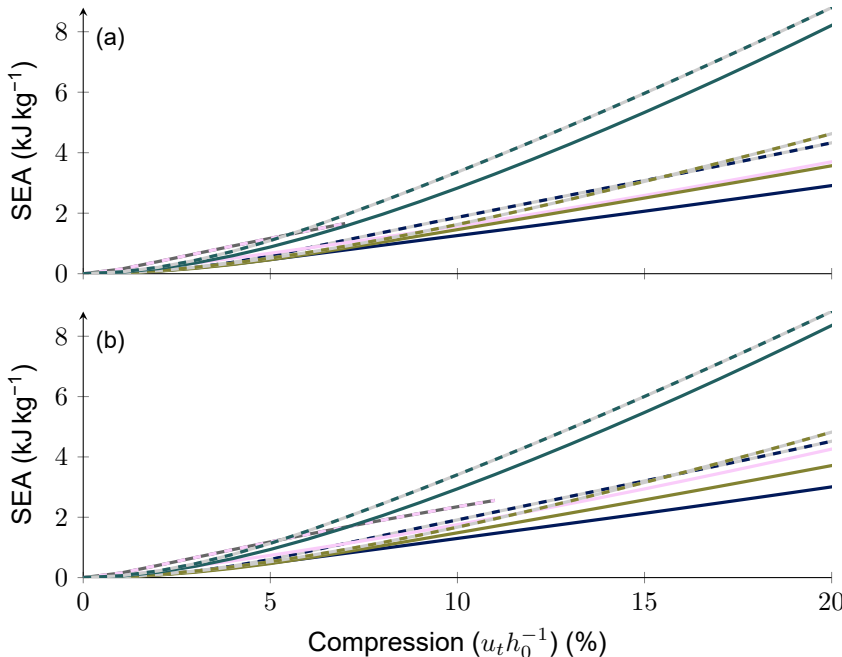


Figure 4.20.: SEA at localized ((a)  $r_i = 3$ , (b)  $r_i = 5$ ), static ( $\dot{H} = 0 \text{ ms}^{-1}$ ) compression.

The next experiments are conducted with increased width of the patches ( $r_i > 1$ ), but still under static loading ( $\dot{H} = 0 \text{ ms}^{-1}$ ) and reported in Figure 4.20. The SEA is again plotted against the (local) compression, in Figure 4.20a for  $r_i = 3$  and in Figure 4.20b for  $r_i = 5$ . Given the static context of this analysis, no fundamental changes are observed apart from the overall rise in work needed to compress the supported structure (compare the ranges of the y-axes of Figure 4.19 and Figure 4.20). It should be noted, that the patches of the arrowhead architectures could not be computed to the desired compression level again due to reasons as mentioned before.

Next, the dynamic behaviour is investigated using moderately localized impact conditions ( $r_i = 3$ ) and a set of strain rates ( $\dot{H} = 5 \text{ ms}^{-1}$  and  $10 \text{ ms}^{-1}$ ). The SEA of the different structures is shown in Figure 4.21. The corresponding static compression is shown in Figure 4.20a, whereas the upper graph (Figure 4.21a) shows the SEA at a compression speed of  $\dot{H} = 5 \text{ ms}^{-1}$ , which is doubled to  $\dot{H} = 10 \text{ ms}^{-1}$  in the lower graph Figure 4.21b. At moderate impact speeds ( $\dot{H} = 5 \text{ ms}^{-1}$  in the upper graph), the difference between the structures in static compression are small,

but the fact that the two regular honeycomb structure show a higher absorption compared to the auxetic structures, does not change. Only at the highest compression speeds ( $10 \text{ ms}^{-1}$ ), the re-entrant honeycomb, in its  $90^\circ$  configuration, is able to match with the regular honeycomb structures. As shown in Figure 4.16a and Figure 4.17a the re-entrant honeycomb shows the highest lateral pressure wave speeds, which in turn relates to a good involvement of the surrounding material. The regular honeycomb architectures show the highest values in the SEA throughout deformation, which is due to their ability to maintain a high stiffness in loading direction (as seen in Figure 4.11a and Figure 4.13a).

A second set of investigations discussed in the following is conducted with stronger localized impact conditions ( $r_i = 5$ ) at the same set of speeds ( $\dot{H} = 5 \text{ ms}^{-1}$  and  $\dot{H} = 10 \text{ ms}^{-1}$ ). In both graphs in Figure 4.22, when compared to the corresponding graphs in Figure 4.21, it can be observed that the effect of more lateral material is negligible for all architectures except from the rotated re-entrant honeycomb depicted in dashed blue. This effect, when comparing Figure 4.21b and Figure 4.22b even results in a better energy absorption capability of the re-entrant honeycomb structure compared to the regular honeycomb structure at high strain rates. This is due to the capability to involve the lateral material under strong deformation, which becomes more relevant with more lateral material (higher  $r_i$ ) and at higher strain rates, as in Figure 4.22a the rotated re-entrant honeycomb is not

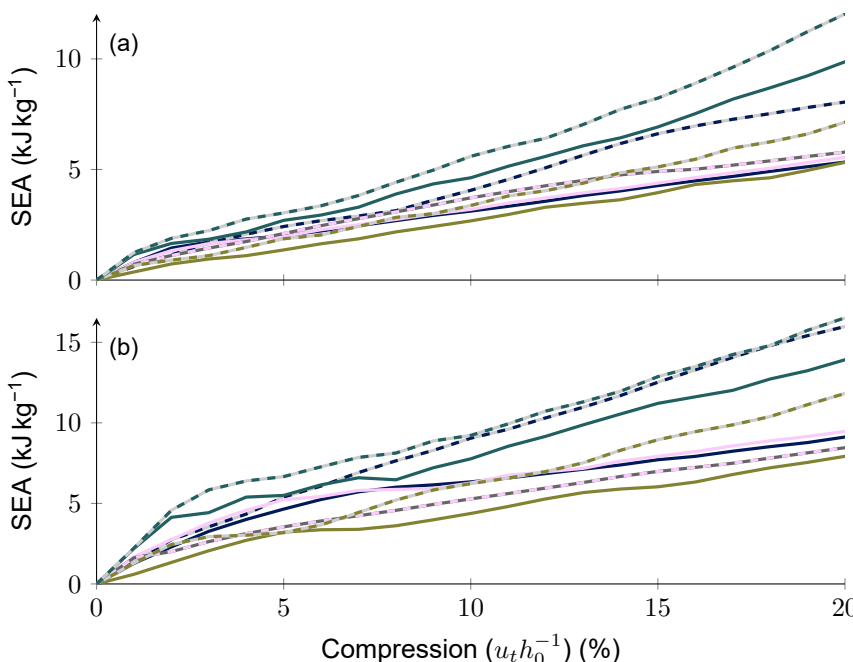


Figure 4.21.: SEA at localized ( $r_i = 3$ ), dynamic ((a)  $\dot{H} = 5 \text{ ms}^{-1}$ , (b)  $\dot{H} = 10 \text{ ms}^{-1}$ ) compression.

able to surpass the rotated regular honeycomb architecture. Figure 4.23 further illustrates this effect. The top Figure 4.23a depicts the left half of the regular honeycomb lattice and the right half of the re-entrant honeycomb lattice, both in their 90° orientation, in the undeformed state. The line thicknesses correspond to the beam thicknesses in the simulations, it should however be noted, that the re-entrant structure has been enlarged by about 9 % in order to reach the same height and better visual comparability with the regular honeycomb. In the lower graphs, the deformed halves of the lattices are shown at  $\sim 10\%$  (Figure 4.23b) and  $\sim 20\%$  (Figure 4.23c) compression, with their respective undeformed configuration in the background. Here, the involvement of the surrounding material by lateral pressure wave speeds can be clearly seen. At 10 % compression, the re-entrant honeycomb lattice shows already deformation in the upper right corner of the lattice, whereas the regular honeycomb lattice shows deformation only up to roughly one third of the width. Up until this point, as can be seen in Figure 4.22b, the regular honeycomb absorbs more energy, which can be motivated by the higher stiffness observed in Section 4.4.1. Only at later stages the higher material involvement as discussed in Section 4.4.2 contributes to the energy absorption. This can be more clearly seen in Figure 4.23c. Here the further involvement of the surrounding material for the regular honeycomb lattice is low when compared to the involvement of lateral material by the re-entrant honeycomb lattice on the right side, where the right edge

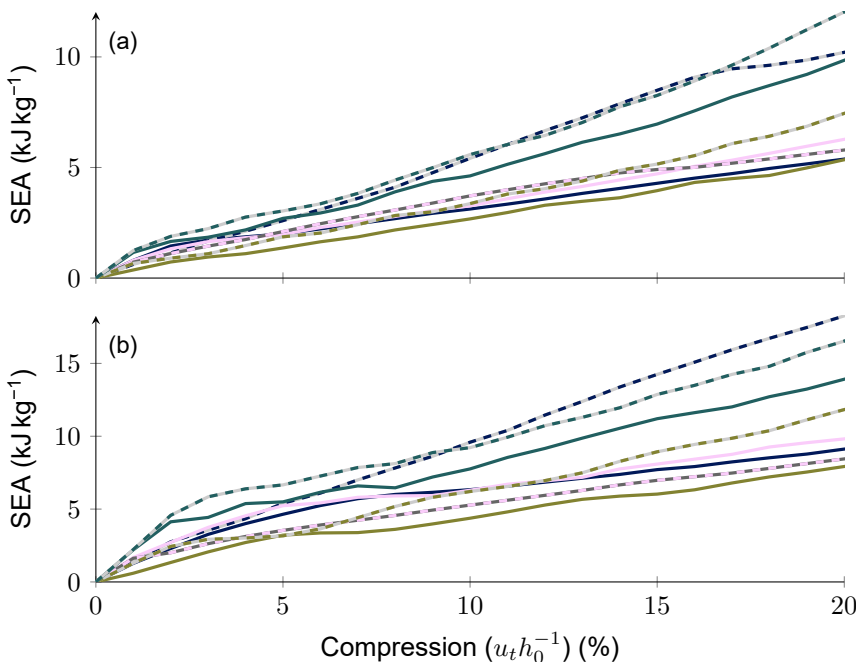


Figure 4.22.: SEA at localized ( $r_i = 5$ ), dynamic ((a)  $\dot{H} = 5 \text{ ms}^{-1}$ , (b)  $\dot{H} = 10 \text{ ms}^{-1}$ ) compression.

shows deformation all the way down to the back face. These deformations clearly show the activation of the lateral material, leading to the dispersion of the impact energy into kinetic and elastic potential energy of the material far away from the impact zone. However, for the example of the rotated regular honeycomb structure, it can be seen that this effect does not simply originate from a negative Poisson's ratio, but rather from the ability to maintain its stiffness at different deformations modes as discussed in Section 4.4.1 whilst at the same time providing the ability to involve the lateral material as discussed in Section 4.4.2.

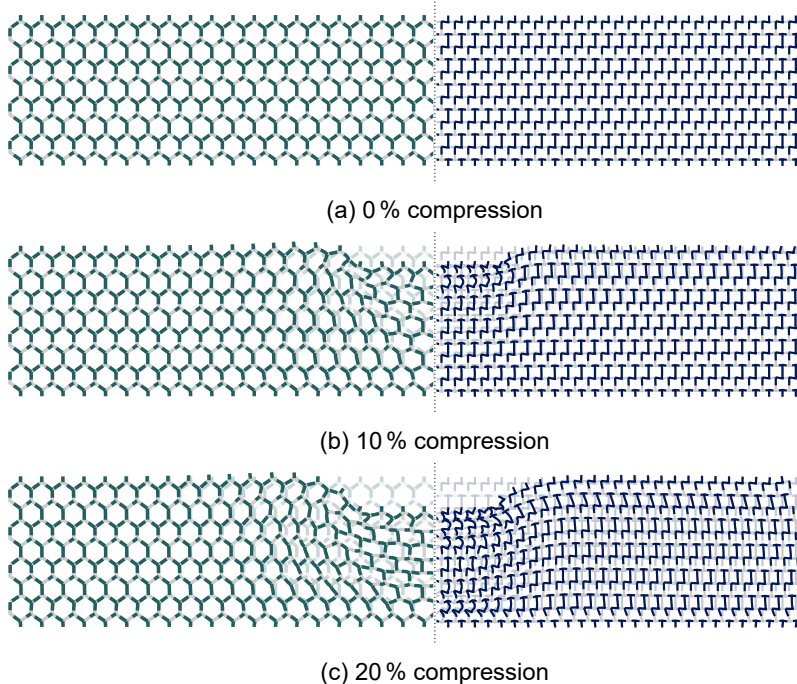


Figure 4.23.: Comparison of the regular and re-entrant honeycomb under localized ( $r_i = 5$ ), dynamic ( $\dot{H} = 10 \text{ ms}^{-1}$ ) compression.

In Figure 4.24 the effect of the lateral material as expressed by the impact ratio  $r_i$  is shown as the SEA is plotted against the impact ratio for different levels of compression. In this graph, it is shown that while most structures tend to obtain less additional benefit from additional lateral material, the rotated re-entrant honeycomb exhibits even at  $r_i = 5$  a positive slope of the SEA-curve, resulting in an added benefit of a further extension of the lattice to the sides, in other words for higher  $r_i$  values. This suggests, that when analysing the elastic energy absorption capabilities of different architected materials, the Poisson's ratio in itself is not sufficient in order to determine the performance of a particular architecture in impact scenarios.

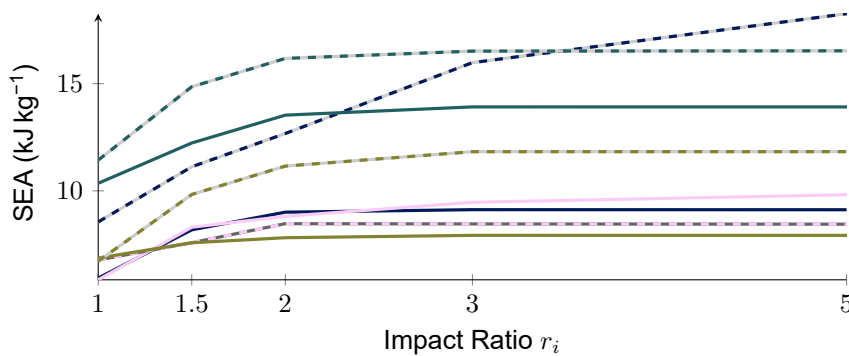


Figure 4.24.: SEA against impact ratio at  $\dot{H} = 10 \text{ ms}^{-1}$  and a strain level of 20 %.

## 4.5. VARYING THE EFFECTIVE PROPERTIES

As mentioned before, all observations have been made using the target properties  $E_y^* = 300 \text{ MPa}$  and  $\rho_{\text{rel}}^* = 0.1$ . In the following section, these observations are summarized and their applicability and limitations in a wider range of properties are shown. For this, both  $E_y^*$  and  $\rho_{\text{rel}}^*$  are individually increased and decreased by a third. This results in three measures  $E_y^* = 200 \text{ MPa}$ ,  $300 \text{ MPa}$  and  $400 \text{ MPa}$  for the effective Young's modulus and  $\rho_{\text{rel}}^* = 0.067$ ,  $0.100$  and  $0.133$  for the relative density and all nine combinations of the two effective measures are investigated. The structures are first designed following the optimization procedure described in Section 4.2.2 and subsequently investigated in the same way as described earlier. The behaviour at different configurations is shown in Figure 4.25, while the structures itself together with their properties can be found in Appendix A.1. In the figure, the SEA is plotted for different impact ratios  $r_i$  at 20 % compression level for dynamic compression at  $\dot{H} = 10 \text{ ms}^{-1}$ . The central graph shows the observations at  $E_y^* = 300 \text{ MPa}$  and  $\rho_{\text{rel}}^* = 0.1$ .

As discussed earlier, the honeycomb structures show the highest absorption of energy for no or small lateral material around the impact zone, due to their high stiffness during pure shear and resistance during planar compression. In Section 4.4.1 the development of the Young's modulus  $E_y$  for uniaxial compression, planar compression and pure shear deformation is shown. It is demonstrated, that structures where the load is carried predominately by axial forces rather than bending moments experience an increase in  $E_y$  whereas structures with more bending loading during deformation experience a decrease.

The only structure able to gain further benefits from more lateral material is the re-entrant honeycomb in its 90° configuration, due to the consistently high lateral pressure wave speeds allowing the involvement of a wide amount of lateral material. This is due to the fact, that next to the pure static resistance to impact, also the dynamic properties play an important role in the response of a patch towards localized, high rate compression. These dynamic properties are reported in Section 4.4.2. Here it is also shown, that the lateral shear wave speeds are smaller

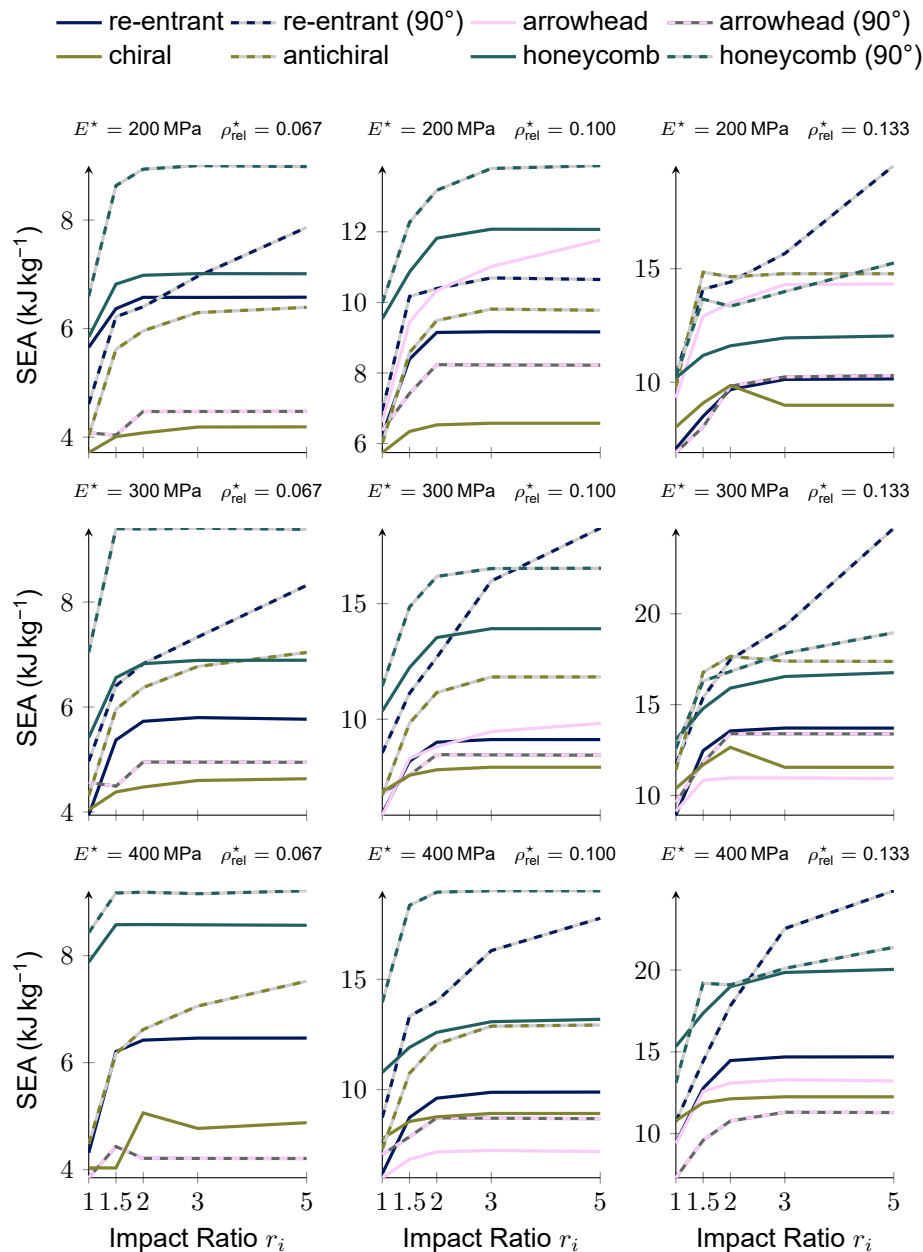


Figure 4.25.: SEA at 20 % compression at  $\dot{H} = 10 \text{ ms}^{-1}$ .

than the lateral pressure wave speeds for all architectures. Section 4.4.3 relates a consistently high lateral pressure wave speed to the energy absorption of the architectures in impact events. Planar compression and pure shear deformation are considered the most relevant deformation patterns in impact scenarios. For these two deformation patterns, it is essential for both critical factors, stiffness in the loading direction ( $E_y$ ), and the lateral pressure wave speed ( $c_{P_x}$ ), to remain at a high level in order to absorb the most impact energy. Comparable results can be achieved in all investigated configurations.

It should be noted, that the rotated re-entrant honeycomb structure at  $E_y^* = 200 \text{ MPa}$  and  $\rho_{\text{rel}}^* = 0.1$ , the antichiral structures at  $\rho_{\text{rel}}^* = 0.067$ , and the rotated regular honeycomb structures at  $\rho_{\text{rel}}^* = 0.133$  show a different behaviour than their counterparts at  $E_y^* = 300 \text{ MPa}$  and  $\rho_{\text{rel}}^* = 0.1$ . However, these different observations can be explained by differences in the evolution of the equivalent properties during the discussed simple deformation modes.

## 4.6. CONCLUSION

The Poisson's ratio alone is not sufficient to explain the differences in elastic impact mitigation behaviour between different lattice architectures. The working mechanisms of the lattice must be taken into account as well to explain these differences. While the exact internal deformation patterns are complex and highly dependent on the exact boundary conditions, a clear dependency can be established between the static properties and the ability of the architectures to adsorb and disperse energy. The evolution of the stiffness in the direction of impact, as well as the lateral pressure wave speed through the deformation modes typical for impact scenarios, namely planar compression and pure shear deformation, give an indication of the performance of the architecture in highly localized impact scenarios. First, the stiffness in loading direction must remain sufficiently high under both planar compression and pure shear deformation. In particular, architectures that exhibit folding in the impact direction, which results in higher axial loading of the members, show stiffer responses throughout deformation. However, they are prone to buckling in their axially loaded members, which can cancel this effect. Second, the lateral material involvement, here estimated by the lateral pressure wave speed, must remain at a sufficiently high level during deformation to allow the impact energy to be distributed to the surrounding material.

The choice of the optimal material architecture is a difficult task when designing protection concepts for different kinds of threats and environments. This work provides the design engineer with a first insight into the effects of different architectural choices in mechanical metamaterials used in impact protection scenarios. It also provides a solid foundation for further investigation into dynamic deformation patterns of architected materials by demonstrating the effects of geometry in an elastic setting.

## REFERENCES

[ÁD12] J. C. Álvarez Elipe and A. Díaz Lantada. 'Comparative study of auxetic geometries by means of computer-aided design and engineering'. *Smart Mater. Struct.* **21**, 105004 (2012).

[AGS12] I. I. Argatov, R. Guinovart-Díaz and F. J. Sabina. 'On local indentation and impact compliance of isotropic auxetic materials from the continuum mechanics viewpoint'. *Int. J. Eng. Sci.* **54** (2012), pp. 42–57.

[Alo<sup>&al</sup>20] A. Alomarah et al. 'Dynamic performance of auxetic structures: experiments and simulation'. *Smart Mater. Struct.* **29**, 055031 (2020).

[BL19] H. Bahaloo and Y. Li. 'Micropolar Modeling of Auxetic Chiral Lattices With Tunable Internal Rotation'. *J. Appl. Mech.* **86**, 041002 (2019).

[Boh<sup>&al</sup>23] R. P. Bohara et al. 'Anti-blast and -impact performances of auxetic structures: A review of structures, materials, methods, and fabrications'. *Eng. Struct.* **276**, 115377 (2023).

[Che<sup>&al</sup>21] Z. Chen et al. 'Dynamic response of sandwich beam with star-shaped reentrant honeycomb core subjected to local impulsive loading'. *Thin-Walled Struct.* **161**, 107420 (2021).

[CL92] J. B. Choi and R. S. Lakes. 'Non-linear properties of metallic cellular materials with a negative Poisson's ratio'. *J. Mater. Sci.* **27** (1992), pp. 5375–5381.

[CL96] J. B. Choi and R. S. Lakes. 'Fracture toughness of re-entrant foam materials with a negative Poisson's ratio: experiment and analysis'. *Int. J. Fract.* **80** (1996), pp. 73–83.

[Cro19] I. G. Crouch. 'Body armour – New materials, new systems'. *Def. Technol.* **15** (2019), pp. 241–253.

[Gál<sup>&al</sup>21] F. Gálvez Díaz-Rubio et al. 'On the study of the dynamic response in 3D additively manufactured auxetic structures'. *EPJ Web Conf.* **250**, 06004 (2021).

[Gär<sup>&al</sup>24] T. Gärtner et al. 'Geometric effects on impact mitigation in architected auxetic metamaterials'. *Mech. Mater.* **191**, 104952 (2024).

[Gib<sup>&al</sup>97] L. J. Gibson et al. 'The mechanics of two-dimensional cellular materials'. *Proc. R. Soc. Lond., A. Math. Phys. Sci.* **382** (1997), pp. 25–42.

[JH17] L. Jiang and H. Hu. 'Low-velocity impact response of multilayer orthogonal structural composite with auxetic effect'. *Compos. Struct.* **169** (2017), pp. 62–68.

[JIVE] Dynaflow Research Group. *JIVE*. Version 3.0. 1st Apr. 2021.

[KC92] N. R. Keskar and J. R. Chelikowsky. 'Negative Poisson ratios in crystalline SiO<sub>2</sub> from first-principles calculations'. *Nature* **358** (1992), pp. 222–224.

[KL15] C. Körner and Y. Liebold-Ribeiro. 'A systematic approach to identify cellular auxetic materials'. *Smart Mater. Struct.* **24**, 025013 (2015).

**4**

- [Lim15] T.-C. Lim. *Auxetic Materials and Structures*. Engineering Materials. Springer, 2015.
- [LSB97] U. D. Larsen, O. Sigmund and S. Bouwsta. 'Design and fabrication of compliant micromechanisms and structures with negative Poisson's ratio'. *J. Microelectromechanical Syst.* **6** (1997), pp. 99–106.
- [LVH91] C. Lees, J. F. V. Vincent and J. E. Hillerton. 'Poisson's Ratio in Skin'. *Bio-Med. Mater. Eng.* **1** (1991), pp. 19–23.
- [Mer<sup>&al</sup>22] C. Mercer et al. 'Effects of geometry and boundary constraint on the stiffness and negative Poisson's ratio behaviour of auxetic metamaterials under quasi-static and impact loading'. *Int. J. Impact Eng.* **169**, 104315 (2022).
- [PA99] C. Pardini and L. Anselmo. 'Assessing the Risk of Orbital Debris Impact'. *Space Debris* **1** (1999), pp. 59–80.
- [Pan<sup>&al</sup>18] J. Pan et al. 'Study on the performance of energy absorption structure of bridge piers against vehicle collision'. *Thin-Walled Struct.* **130** (2018), pp. 85–100.
- [Red<sup>&al</sup>18] H. Reda et al. 'The role of anisotropy on the static and wave propagation characteristics of two-dimensional architectured materials under finite strains'. *Mater.& Des.* **147** (2018), pp. 134–145.
- [Ren<sup>&al</sup>18] X. Ren et al. 'Auxetic metamaterials and structures: a review'. *Smart Mater. Struct.* **27**, 023001 (2018).
- [SGE00] C. W. Smith, J. N. Grima and K. E. Evans. 'A novel mechanism for generating auxetic behaviour in reticulated foams: missing rib foam model'. *Acta Mater.* **48** (2000), pp. 4349–4356.
- [SS19] D. Saini and B. Shafei. 'Prediction of extent of damage to metal roof panels under hail impact'. *Eng. Struct.* **187** (2019), pp. 362–371.
- [Tat22] M. S. Tatlier. 'A comparative analysis of the in-plane energy absorption capacities of auxetic structures'. *Trans. Can. Soc. Mech. Eng.* **46** (2022), pp. 216–224.
- [Wan<sup>&al</sup>20] Z. Wang et al. 'Progress in Auxetic Mechanical Metamaterials: Structures, Characteristics, Manufacturing Methods, and Applications'. *Adv. Eng. Mater.* **22**, 2000312 (2020).
- [Zha<sup>&al</sup>18] X. Zhao et al. 'Dynamic crushing of double-arrowed auxetic structure under impact loading'. *Mater.& Des.* **160** (2018), pp. 527–537.
- [ZLY20] J. Zhang, G. Lu and Z. You. 'Large deformation and energy absorption of additively manufactured auxetic materials and structures: A review'. *Compos. B: Eng.* **201**, 108340 (2020).







# **EFFICACY OF AUXETICS IN PHYSICAL IMPACT SIMULATIONS**

*It has been demonstrated that auxetic materials, characterized by a negative Poisson's ratio, offer enhanced resistance to indentation, shear forces, fracture toughness and the absorption of energy. As such, they are reported in literature to be promising options for impact mitigation in military and space contexts. Auxetic materials are rare in nature, and must therefore be designed and manufactured artificially in order to be applied. Densification of auxetic materials in order to absorb impact energy in a limited area has been the focus in the literature to date. However, this results in a concentration of the force paths, which is not desirable for impact mitigation. In this work, the effects of auxetic densification on the stress distribution over the backside of the auxetic material are addressed using both experimental and simulative trials. In this study, the distinction between auxetic and conventional honeycombs in force transmission characteristics is examined. This is achieved through an analysis of experimental data and the utilization of numerical techniques to enhance comprehension of the internal mechanisms of architected materials in response to impact.*

## 5.1. INTRODUCTION

Lightweight impact protection, formerly a concern of aerospace designers due to the typical weight constraints of aircraft, has also become of interest for other applications such as vehicles, ships and infrastructure protection. Lightweight design allows for more fuel efficiency and better mobility of platforms [Fin00], and also for using less material in infrastructure construction, contributing to sustainability goals and energy efficiency. Amongst different innovative solutions for lightweight impact protection, auxetic structures have received significant attention in recent research [Boh<sup>&al</sup>23; Gal<sup>&al</sup>24; Ren<sup>&al</sup>18]. Due to the negative Poisson's ratio of auxetic materials, densification occurs when such materials are impacted, drawing material towards the impacted area, such as illustrated in Figure 5.1. Because of this negative Poisson's ratio effect, auxetics are often considered as promising candidates to include in lightweight impact protection [Boh<sup>&al</sup>23; Gal<sup>&al</sup>24].

Given the absence of natural materials exhibiting negative Poisson's ratio, auxetic structures need to be architected from artificial materials to exhibit such negative Poisson's ratio for practical use. Whilst creating auxetic foams is possible [Cri<sup>&al</sup>13], in impact protection literature the negative Poisson's ratio is however mostly achieved by designing auxetic lattice structures [Boh<sup>&al</sup>23], such as exemplified by the unit cell in Figure 5.2b. These unit cells can be repeated to create a larger lattice structure with properties resembling the unit cell. Figure 5.2a shows the conventional honeycomb (CH), a non-auxetic unit cell, while Figure 5.2b shows the auxetic re-entrant honeycomb (ARH), an auxetic unit cell. The use of such auxetic lattices for impact protection reaches back decades [SDC16], but widespread experimentation with such designs has recently become popular due to advances in manufacturing techniques such as 3D printing. Whilst experimental campaigns require significant efforts in time and money, FE modelling approaches provide a fast way to supplement the experimental findings and have been a staple in designing and improving auxetic materials in the last decades [Gal<sup>&al</sup>24]. Within the FE modelling, one can speed up the computation even further by abstracting the present structure into its structural elements instead of viewing the structure as three-dimensional solids (e.g. [Gär<sup>&al</sup>24; Kap<sup>&al</sup>23; Wee<sup>&al</sup>23]).

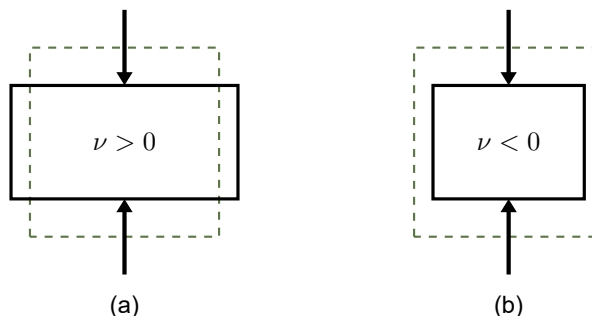


Figure 5.1.: (a)Positive Poisson's ratio materials ( $\nu > 0$ ) and (b) negative Poisson's ratio or auxetic materials ( $\nu < 0$ ) under compression.

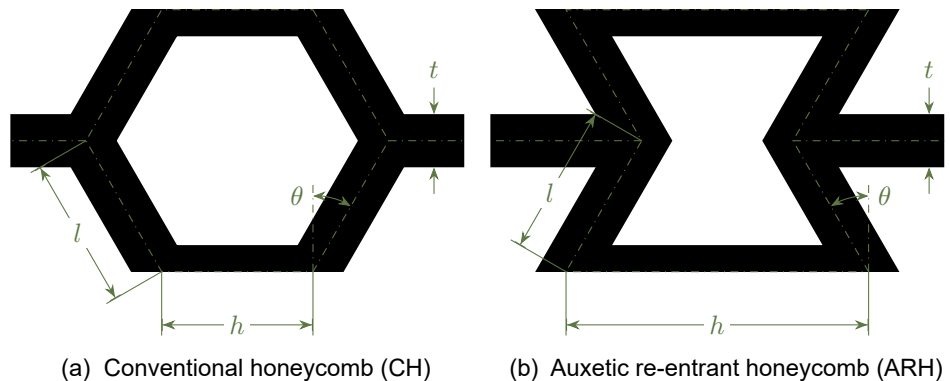


Figure 5.2.: Comparison of (a) conventional and (b) auxetic re-entrant honeycomb lattice structures.

Because the beneficial properties of auxetic materials are promising in the search for lightweight impact protection, a plethora of studies on auxetic lattices used as blast and ballistic protection has been published in the past years, many of them focusing on the ARH as a simple auxetic solution [Boh<sup>&al</sup>23]. Although such studies indicate the ARH almost unanimously as a better choice for impact and blast protection than conventional lattices [Boh<sup>&al</sup>22; Boh<sup>&al</sup>23; Qi<sup>&al</sup>17], the published research fails to articulate why or how designers should incorporate such auxetic lattices in real applications, and what design parameters the designer should focus on to enable impact mitigation.

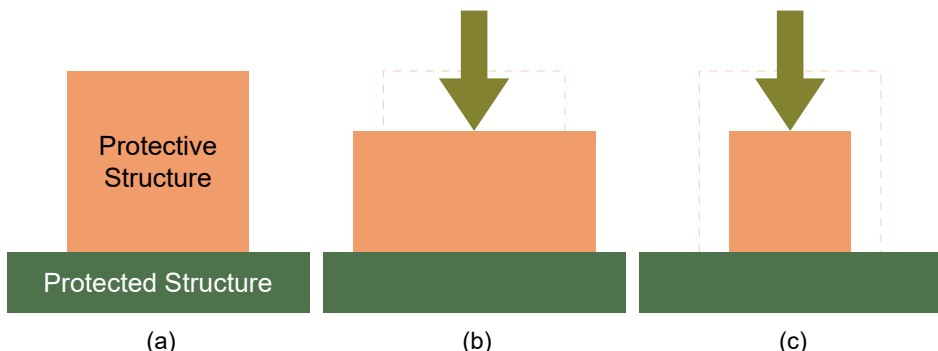


Figure 5.3.: Illustration of an example where auxetic lattices might be detrimental to the structure to be protected. (a) Unloaded structure; (b) structure with positive Poisson's ratio under load; (c) structure with a negative Poisson's ratio under load. Contact area is larger for structure with positive Poisson's ratio, transferring smaller stresses to underlying structure. Dashed lines represent the shape of the undeformed structure.

Consider, as an example, the illustration in Figure 5.3. Materials with a positive Poisson's ratio will spread the load onto a wider area, as illustrated in Figure 5.3b. Negative Poisson's ratio materials (Figure 5.3c) on the other hand, concentrate the load onto a smaller area. This effectively means that the distributed force results in less pressure being exerted on the protected structure. This anecdotal example aims to illustrate in simple terms that not in all cases auxetic protection systems will outperform non-auxetic conventional protection systems, contrary to what is concluded in [Boh<sup>&al</sup>23].

Compared to the non-auxetic CH, the ARH has been shown to fold more easily upon impact, leading to earlier densification [Liu<sup>&al</sup>16; Qi<sup>&al</sup>17]. This earlier densification is related to the inwards folding of the ARH structures, generating the auxetic effect. Once the material is densified, it acts as a conventional solid material and thus generates a substantially higher stress level, contributing to energy dissipation. Available research focuses its conclusions on the higher energy dissipated by auxetic lattices [Liu<sup>&al</sup>16; Qi<sup>&al</sup>17], to claim the better performance in impact scenarios, but little is reported about other metrics to evaluate performance under impact and where this dissipated energy goes to. The effects of high peak reaction forces generated by the impacted ARH due to its densification, being transferred to the underlying structure, is currently not addressed in the available literature. The temporal and spatial distribution of the impact energy and the subsequent effects on the protection capabilities of different lattice structures have not been addressed in sufficient detail thus far. However, some studies have shown in the past that load spreading is essential for effective impact protection [GD02]. The transfer of a substantial quantity of energy over a brief time span to a restricted area, as a consequence of the densification of the distinct lattice structures, may prove detrimental to the efficacy of the protective measures in question. More specifically, Gupta and Ding [GD02] mention that absorbing energy is not enough, but that momentum has to be diverted from the impactor and distributed laterally. The structure underlying the protective layer is usually not designed to withstand high, localized loads and thus is dependent on the protective layer to spread out the load over both time and space. To the best knowledge of the author, the only instance found in literature where the auxetic lattices are actually shown to transfer less force to the underlying structure than the CH is described in Bohara et al. [Boh<sup>&al</sup>22]. The authors show that, under close-in blast load, the ARH deflects part of the blast overpressure load. The increased densification of the ARH, by drawing material to the blast-impacted zone, makes the core stiffer under the close-in blast area and more compliant on the edges of the panel, contributing to the deflection of the blast pressure. [Boh<sup>&al</sup>22]

In addition to the load transfer of single lattice structures, the design parameters for auxetic lattice structures, including the design choices in relation to impact loads, had not been discussed in-depth until the investigations in Chapter 4. In this publication, it is shown that, for the effect of the auxeticity to have the greatest energy absorption, the impact should be localized and not over the complete length of the architected material. Localized impact results in the drawing of unloaded ma-

terial from the sides toward the impact zone, thereby facilitating a wider degree of densification. Furthermore, the impact energy can be transported further laterally. However, only geometric non-linear elastic models without contact were used in that study, and no experimental validation was presented.

It is currently unclear whether auxetic lattices can be shown to outperform conventional lattices in impact protection applications in the real world, particularly in cases where energy dissipation is not the sole measure of performance. This contribution thus proposes an integrated approach to the design and evaluation of auxetic lattice structures for protection, which goes beyond mere consideration of their energy dissipation capabilities. It is important to note that the objective of this study is not to disprove the use of auxetics. Instead, it is to subject the metrics of performance applied to auxetics in impact protection, as well as the underlying physical mechanisms, to rigorous scrutiny. The aim is to provide a better foundation for the application of auxetic or conventional lattices as protective structures.

## 5

### 5.1.1. OBJECTIVES

The aim of this study is twofold:

Firstly, this study aims to use different metrics to evaluate and compare the performance under impact of both auxetic and conventional lattice structures. The use of different metrics, such as load transferred to the underlying structure and the distribution of the pressure at the back-face of the protective structure can give new insights in the mechanisms of impact protection of different lattices, enabling the guided design of lattice structures for impact mitigation in relation to different loading scenarios.

Secondly, in order to produce guidelines for load localization for impact protection design, the present study aims to test the hypothesis of [Chapter 4](#), which states that in order for auxeticity to have more effect and a better impact protection, it is crucial, that the impact is localized and does not cover the complete auxetic lattice surface area.

To complete the overview of the design and analysis process of auxetic lattices, the present study combines experiments and non-linear numerical models. Furthermore, this study offers an insight into the numerical assessment methods available for architected lattices used for impact protection, by showcasing investigations possible with both detailed, continuum-based and efficient, beam-based numerical models. The continuum-based numerical model is employed to gain a deeper insight into the details of the inner deformation and load transmission processes of the experimental campaign. To supplement these investigations, the beam-based numerical model is chosen due to its efficiency to enable fast explorations into different scenarios.

### 5.1.2. ORGANIZATION

The lattice structures analysed are presented in Section 5.2. The different physical and numerical settings employed to assess the performance of different lattice architectures in a protection lay-up are explained in Section 5.3. Subsequently, the results of the different analyses will be laid out in Section 5.4, and the advantages and limitations of each analysis will be discussed. A comparison between the different methods will be done in Section 5.5, as well as a discussion on the efficacy of auxeticity in protective systems and the metrics useful in entertaining this assessment and suggestions for further research.

## 5.2. INVESTIGATED ARCHITECTURES

Table 5.1.: Dimensions, mass and initial elastic stiffness along impact direction of the unit cells considered in the present study (see Figure 5.2 for the definitions of the dimensions).

Unit cell	$l$ (mm)	$h$ (mm)	$\theta$ (°)	$t$ (mm)	mass (g)	stiffness (GPa)
SS	ARH	4.8831	8.30	35	0.750	5.50
	ARH90	4.8831	8.30	35	0.820	5.98
	CHW	4.8831	2.65	35	0.854	3.99
SM	CHL	4.8831	2.65	35	0.884	4.12
	ARH90	4.8831	8.30	35	0.750	5.50
	CHW	4.8831	2.65	35	1.100	5.04
	CHL	4.8831	2.65	35	1.100	5.04

Table 5.2.: Dimensionless properties of the unit cells considered in the present study

Unit cell	rel. density (%)	rel. stiffness (%)	max. slenderness	Poisson's ratio
SS	ARH	31.25	1.19	-0.95
	ARH90	33.98	1.19	-0.77
	CHW	22.67	1.18	0.95
SM	CHL	23.41	1.19	0.86
	ARH90	31.25	0.91	-0.80
	CHW	28.64	2.48	0.89
	CHL	28.64	2.24	0.82

This study investigates architected materials, as shown in Figure 5.2, where Figure 5.2b shows the auxetic re-entrant honeycomb (ARH), an auxetic lattice, while Figure 5.2a shows a conventional honeycomb (CH), a non-auxetic lattice. The ARH has been chosen as the baseline auxetic lattice for comparison. This choice is based on its widespread use in literature (e.g., [Boh<sup>&al</sup>22; Boh<sup>&al</sup>23; Liu<sup>&al</sup>16; Qi<sup>&al</sup>17]), and the dimensions of the baseline ARH are described in Table 5.1 together with the estimated mass and stiffness of one unit cell. The initial elastic stiffness of the samples in Figure 5.4 was estimated using linear elastic, small deformation FE analyses considering an elastic modulus of 210 GPa and a Poisson's ratio of 0.265, corresponding to the steel grade used to manufacture the samples.

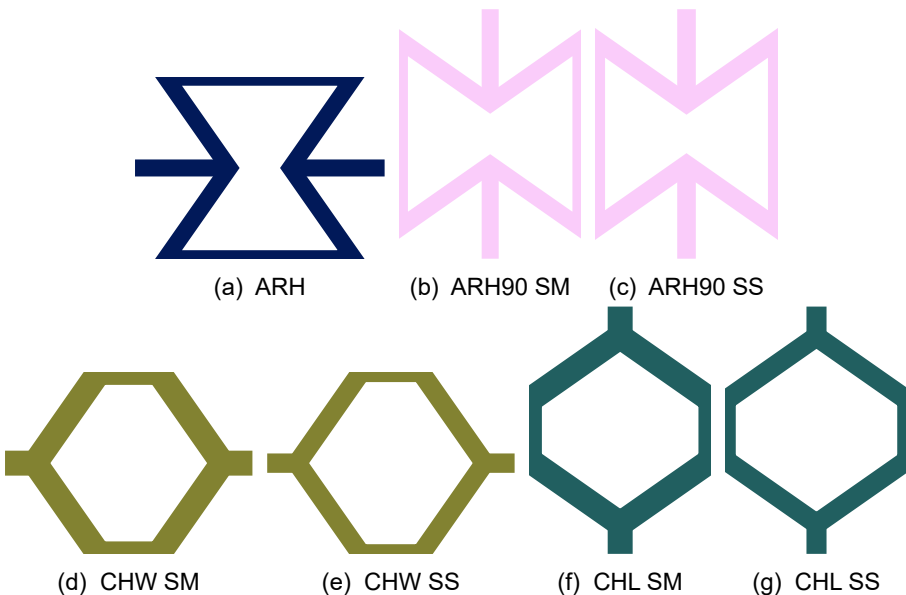
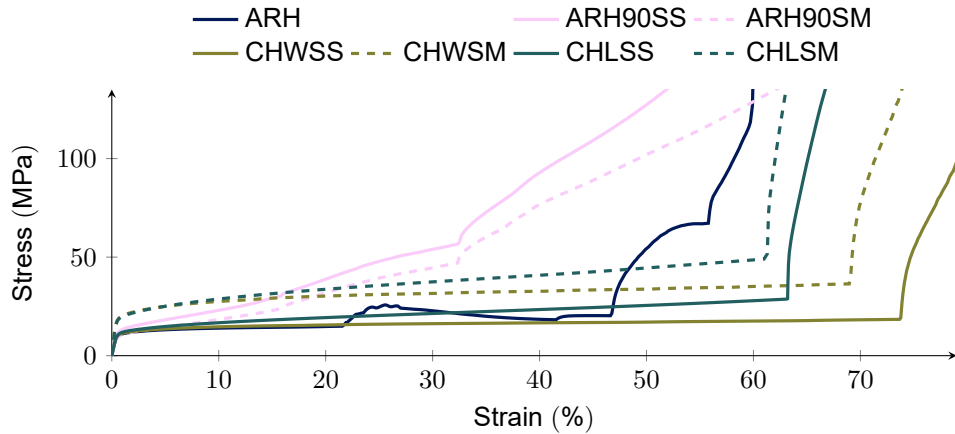


Figure 5.4.: Unit cells.

Linear elastic FE analyses were conducted instead of analytical models (such as the one from Gibson et al. [Gib<sup>&al</sup>97]) to estimate the initial elastic stiffnesses of the samples due to the relatively thick struts of the lattice structures. In addition, the impact protection performance of the ARH is compared to the same structure rotated by 90°, in the following called auxetic re-entrant honeycomb (90° d) (ARH90). In order to shed light on the effects of auxeticity in comparable circumstances, the non-auxetic unit cells conventional honeycomb (W-configuration) (CHW) and conventional honeycomb (L-configuration) (CHL) are investigated as well. The dimensions of the struts of the ARH90, CHW, and CHL samples were selected to guarantee that a set of such samples with the similar mass (SM) as the ARH is obtained. Additionally, another set of unit cells with the same initial elastic stiffness (SS) as the ARH in the impact direction is designed and evaluated throughout the study. The unit cells of each investigated lattice are illustrated in Figure 5.4, while the unit cell masses, dimensions and initial elastic stiffnesses are described in Table 5.1. In order to give a better estimation for the overall behaviour of the unit cells, the relative density and relative stiffness related to the base material are reported in Table 5.2. In this table, also the maximum slenderness, i.e. the length of the longest beam divide by the thickness of the beams is reported. It can be seen, that the re-entrant types are more slender, and thus more prone to buckling. The vertical Poisson's ratio relates the horizontal compression or extension with the compression in impact direction and is reported in Table 5.2 as well. It should be noted here, that the Poisson's ratios greater than 0.5 reported for the honeycomb unit cells do not violate any bounds on the Poisson's ratio given the orthotropic nature of these metamaterials.



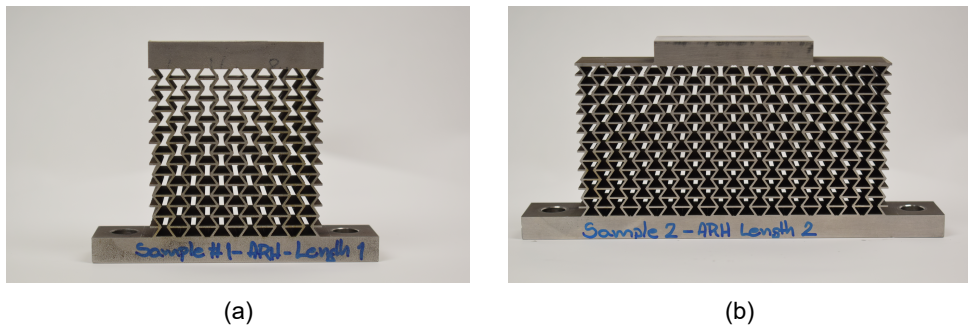
5

Figure 5.5.: Static compression response of single unit cells.

In addition to the initial elastic stiffness, quasi-static stress-strain curves were extracted for the investigated unit cells. These investigations were done using fully nonlinear FE analyses using planar boundary conditions, that ensure all edges remain plane but are free to move. The resulting curves are shown in Figure 5.5 up to the point of full densification. The onset of plasticity after around 1 % compression is clearly visible in all architectures. Within the elastic range of deformation, the differences in initial stiffness between the architectures are emphasized, particularly the substantially increased stiffness of the CH architectures of similar mass. This results in a higher stress at the yield point and subsequently higher stresses throughout the plateau stage. Comparing the SS and SM variants of all unit cells, the higher initial stiffness reported in Table 5.1 also correlates with a higher energy absorption potential in all cases. It should be noted as well, that buckling of the load-carrying beams at the lateral edges of the ARH90 and CHL unit cells is prevented by the planar boundary conditions. This results in an overestimation of the stresses for these particular unit cells. The effects of contact can distinctly be seen in all architectures up to the point of total densification. The auxetic structures densify earlier due to their convex nature. As densification leads to direct force transmission through the sample, the longer plateau phase of the CH architectures is beneficial in practical applications if sufficient to absorb the impactor's energy before densification.

### 5.2.1. SAMPLE CONFIGURATION

The previously described unit cells are assembled into lattice structures with two sizes of the entire patch: One size, in the following denoted as *Length 1*, has approximate measures of 65 mm  $\times$  65 mm. A sample twice as wide and denoted as *Length 2*, measures approximately 130 mm  $\times$  65 mm. To achieve these measures multiple units cells were stacked both vertically and horizontally, with a base of solid steel,



5

Figure 5.6.: Assembly of ARH unit cells into patches to be investigated, (a) *Length 1* and (b) *Length 2*.

Table 5.3.: Measured or estimated mass of the auxetic samples which are shown in Figure 5.6. The samples of *Length 1* were not measured with a digital scale but, instead, the mass was estimated via CAD model assuming a density of  $8000 \text{ kg m}^{-3}$ .

	Unit cell	Length 1			Length 2		
		$n_x$	$n_y$	mass (g)	$n_x$	$n_y$	mass (g)
SM	ARH	6	8	733.08	12	8	976.75
	ARH90	8	6	733.15	16	6	977.05
	CHW	6	8	732.61	12	8	970.15
SS	CHL	8	6	732.75	16	6	971.21
	ARH90	8	6	742.35	16	6	1023.05
	CHW	6	8	669.46	12	8	872.96
	CHL	8	6	688.43	16	6	884.48

10 mm high, and a strike face on the upper side being 65 mm wide and likewise 10 mm high. The physical samples produced for the ARH architecture are shown in Figure 5.6 for both lengths investigated. An overview over the number of unit cells in each direction and the resulting mass for the samples is given in Table 5.3. These patches with a depth of 25 mm are investigated for all further experimental and numerical studies unless otherwise noted.

## 5.2.2. TEST MATRIX

Table 5.4.: Physical & numerical investigation matrix.

	Unit cell	Length 1		Length 2	
		ARH	physical/numerical	ARH	physical/numerical
SM	ARH90		only numerical		physical/numerical
	CHW		only numerical		physical/numerical
	CHL		only numerical		physical/numerical
SS	ARH90		only numerical		physical/numerical
	CHW		only numerical		physical/numerical
	CHL		only numerical		physical/numerical

In order to assess the effects of the different lattice architectures as well as the effect of localization of an impact, as was suggested in [Chapter 4](#), all architectures are tested according to the test matrix shown in [Table 5.4](#). A physical comparison for the effect of impact localization between the *Length 1* and *Length 2* samples is experimentally carried out only for the ARH as baseline architecture. For the other lattice architectures physical experiments for *Length 2* samples and additional FE analyses for the *Length 1* samples are conducted.

## 5.3. METHODS

### 5.3.1. EXPERIMENTAL SET-UP

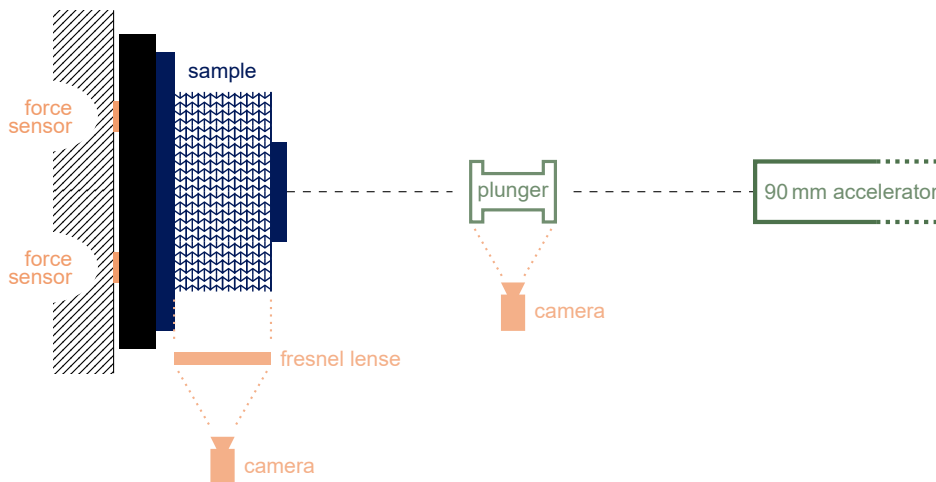


Figure 5.7.: Schematic view of the experimental set-up.

#### SAMPLE MANUFACTURING

The samples, with geometries as described in the previous section, have been manufactured by electric discharge machining (EDM). EDM was chosen for its tight geometric tolerances, which are required to ensure that the radii in the corners of the structures are sufficiently small to ensure that the physical samples resemble the desired structures. EDM is an inherently precise method, with the accuracy only limited by the size of the electrode, and maintains this accuracy for relatively large material depths.

A good material for lattice samples in impact condition will have a high yield strength and stiffness, in combination with being very ductile. These properties ensure sufficient energy can be dissipated during the deformation. The only condition that EDM poses on the material is that it conducts electricity, rendering metals a prime choice. After careful evaluation 316 stainless steel (AISI 316L) was chosen

for producing the sample set later used in the experimental campaign. This was motivated mainly by the high strain to failure ( $> 25\%$ ), ensuring the structure folding neatly without hinges breaking and losing structural integrity. This high toughness additionally absorbs a significant amount of energy in the process.

### TESTING SET-UP

## 5

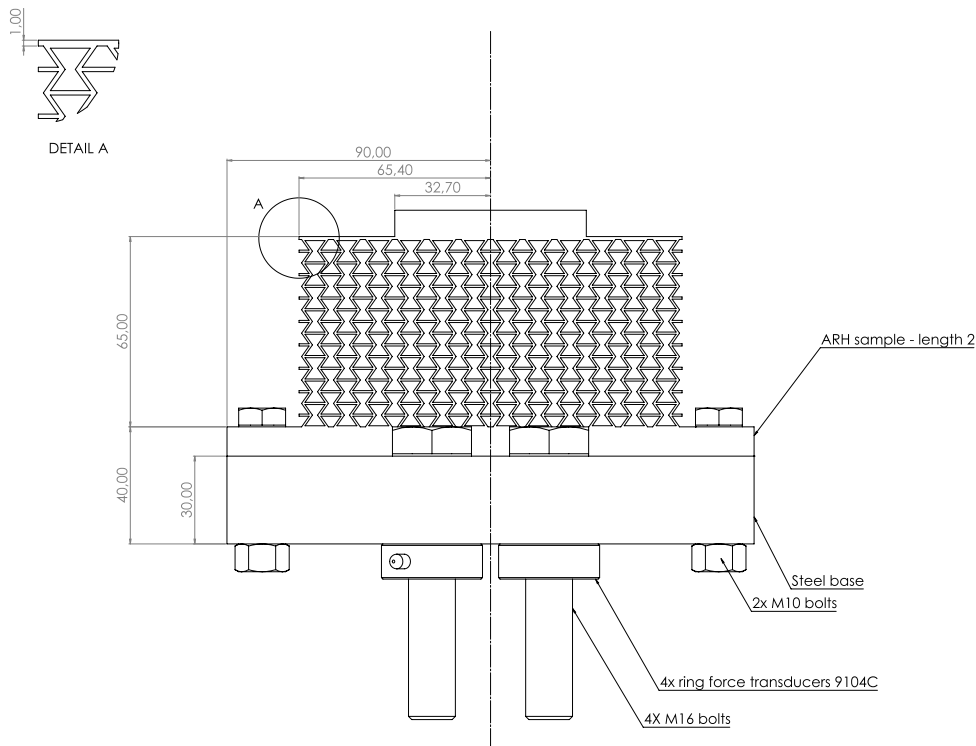


Figure 5.8.: Side view of the sample mounting in the experimental set-up with main dimensions and components - dimensions in mm.

For the test series, the lattice samples manufactured by EDM were attached to a 30 mm thick steel base using four M10 bolts. A construction drawing of this set-up can be found in Figure 5.8. The base was then attached to a stiff boundary using four M16 bolts and 4 Piezoelectric ring force transducers from the brand Kistler, type 9104C. The Kistler ring force transducers have a load limit of 160 kN and an axial stiffness of  $7.5 \text{ kN } \mu\text{m}^{-1}$  per transducer. All lattice samples were impacted by a plunger with a mass of 1.2 kg and made of aluminium. The experimental set-up is shown in Figure 5.9, while drawings of the plunger are shown in Appendix B.1. All tests are carried out with a nominal impact velocity of  $70 \text{ m s}^{-1}$ . The experimental



(a) Position of the camera with Fresnel lens.  
 (b) Shooting barrel and camera pointing at the sample.

Figure 5.9.: Experimental set-up.

procedure was recorded digitally by two high-speed cameras at 25 000 fps, one directed at the lattice to capture its performance, and the other at the plunger mid-flight to assess the projectile orientation and velocity. A schematic overview over the entire set-up can be found in Figure 5.7.

### 5.3.2. CONTINUUM-BASED FE

Explicit non-linear FE analyses were performed using the commercial software package ABAQUS. An example of a simulated assembly is given in Figure 5.10, which consists out of the lattice specimen and the plunger impacting the specimen. The specimen is fully fixed at its support and the 1.2 kg weighing plunger is given an initial vertical velocity, matching that of the experiments. The plunger was modelled in a simplified manner, as a rectangle of 20 mm height and 65.4 mm width (compare Figure 5.10). Note that, in order to maintain the mass of the plunger the density of this block was adjusted to  $36\ 703\ \text{kg m}^{-3}$ . All contact interactions were modelled by hard normal contact and frictionless tangential behaviour. The simulation were

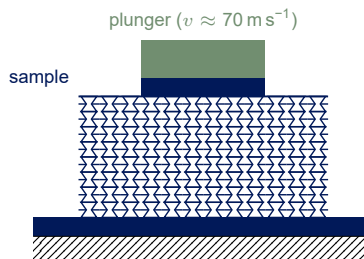


Figure 5.10.: Geometry, boundary conditions and initial conditions for the FE analyses.

performed in 2D, assuming plane strain, where the depth of the specimen and the plunger were set to 25 mm. Four-node quadrilateral elements with reduced integration (type CPE4R), having an average element size of 0.12 mm, were used. This

resulted for the ARH sample of *Length* 2 in 192 520 elements and 438 206 DOFs. A close-up of the mesh showing two unit cells is given in Figure 5.11. As indicated

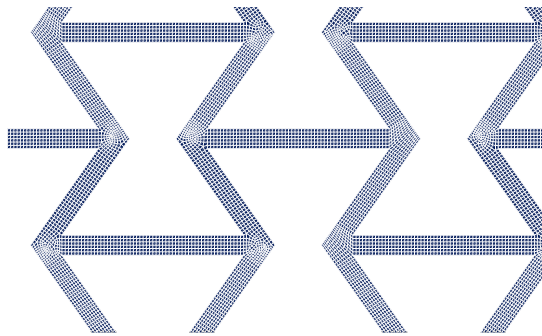


Figure 5.11.: Close-up of the mesh for two unit cells.

earlier, the lattice is made out of stainless steel and the plunger out of aluminium. Both materials were simulated using a Johnson-Cook plasticity model to account for strain rate effects [JC85]. In this model, the von Mises yield surface is described by

$$\bar{\sigma} = \left[ A + B (\bar{\varepsilon}^{\text{pl}})^n \right] \left[ 1 + C \ln \left( \frac{\dot{\varepsilon}^{\text{pl}}}{\dot{\varepsilon}_0} \right) \right], \quad (5.1)$$

with the equivalent plastic strain  $\bar{\varepsilon}^{\text{pl}}$ , the equivalent reference strain rate  $\dot{\varepsilon}_0$  and the numerical parameters  $A, B, C, n$ . These properties and parameters used for both materials, following from literature [Spr11; UMO07], are given in Table 5.5.

Table 5.5.: Material properties and parameters for the FE simulation.

Material	$E$ [GPa]	$\nu$ [-]	$A$ [MPa]	$B$ [MPa]	$C$ [-]	$n$ [-]	$\dot{\varepsilon}_0$ [-]	$\rho$ [ $\text{kg m}^{-3}$ ]
Stainless Steel [UMO07]	210	0.265	280	1750	0.1	0.8	0.02	8000
Aluminium [Spr11]	72	0.33	103	350	0.12	0.4	0.001	36 703*

\* Note that the density of aluminium is chosen such that the plunger mass is equal to 1.2 kg and is therefore not equal to the real density of aluminium.

### 5.3.3. BEAM-BASED FE

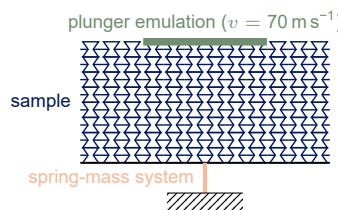


Figure 5.12.: Geometry and boundary conditions for the JIVE analyses.

The structures investigated can be viewed as a collection of beams into a lattice. In order to accelerate and simplify the simulations described in Section 5.3.2, and to allow for a faster processing of different configurations, these lattice structures are also implemented as a collection of Simo-Reissner beams as described in Chapters 2 and 3. This results for the ARH sample of *Length* 2 in 16 824 DOFs, which is a reduction by more than one order of magnitude compared to the continuum-based model in Section 5.3.2.

The material of the structure is modelled as elastoplastic beams with kinematic hardening as presented in Chapter 3. For the elastic behaviour a Young's modulus of 210 GPa and a Poisson's ratio of 0.265 are assumed in accordance with the assumptions in the solid model. The beams are modelled as square beams with a side length of 0.75 mm and the shear correction coefficient is set to 5/6. The yield function

$$\Phi = \left| \frac{N_1}{71.8 \text{ N} - N_1^h} \right|^{2.68} + \left| \frac{N_3}{164 \text{ N} - N_3^h} \right|^{1.75} + \left| \frac{M_2}{30.8 \text{ N mm} - M_2^h} \right|^{1.93} - 1, \quad (5.2)$$

with the stress resultants  $N_1$  for the shear force,  $N_3$  for the axial force,  $M_2$  for the bending moment, and the corresponding hardening contributions  $N_1^h$ ,  $N_3^h$ ,  $M_2^h$ , is accompanied by the kinematic hardening tensor

$$\mathbf{H} = \begin{bmatrix} 936 \text{ N} & 1630 \text{ N} & 618 \text{ N mm} \\ & 2800 \text{ N} & 907 \text{ N mm} \\ \text{sym.} & & 443 \text{ N mm}^2 \end{bmatrix}. \quad (5.3)$$

Further details on the elastoplastic beam formulation and their scaling for different beam sizes can be found in [Gär<sup>&al</sup>25b; SKS20] and are not part of this contribution.

For an adequate model of the beam connections slight modifications to the beam geometry have been applied. In accordance with [Kap<sup>&al</sup>23], the last elements in each beam are assumed purely elastic and thickened by a factor of 1.25 for the stiffness calculation and thinned by a factor of 0.75 for the inertia calculation. For the contact of the beams, all contact penalty parameters described in Section 2.3 are set to  $\varepsilon_{STS} = \varepsilon_{NTS} = \varepsilon_{NTN} = 4 \times 10^6$ . No self-contact within a singular beam is modelled, as this effect is not observed in the experiments.

The set-up for the beam-based FE analyses is shown in Figure 5.12. Notable differences to the solid-based analyses in Section 5.3.2 are the emulation of the impactor at the upper side by adding a virtual mass totalling 1.2 kg to the nodes on the impact surface, as well as the replacement of the lower plate by a “beam” acting as a spring-mass system emulating the baseplate.

## 5.4. RESULTS

To ensure the comparability of the different models, they were in a first step compared to each other. For this comparison ARH samples of both lengths were used. The total force recorded at the back face is shown over the time for all three models in Figure 5.13. One should note here, that the stopping points for all models are

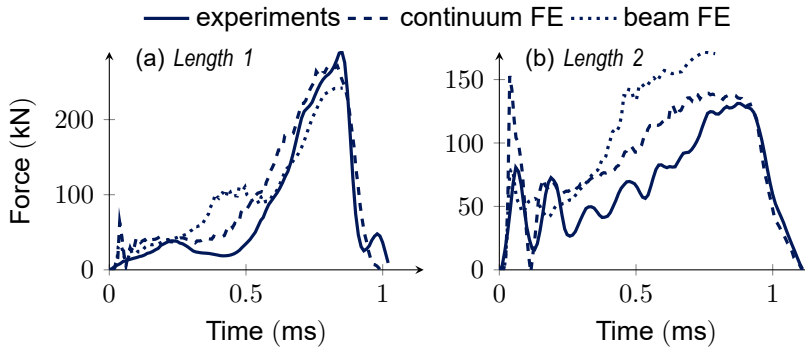


Figure 5.13.: Comparison of the three models from Section 5.3 for ARH samples of (a) Length 1 and (b) Length 2.

different, the experiment stops as soon as the total recorded force reaches 0 N, the continuum bases simulations are run for 1.3 ms and the beam-based simulations are run until the plunger velocity reaches  $0 \text{ m s}^{-1}$ .

When comparing the force recordings, an overestimation of the forces in the FE models can be observed. Such overestimation can be explained by the fact, that in the experiment the backing is not infinitely stiff, whereas the simulations assume a fully rigid boundary condition. In the high-speed videos a flexing motion of the backplate is observed, despite the best efforts to obtain a stiff test set-up. This effect of overestimating the force levels is also seen for all other simulations of the experimental cases described in Table 5.6. The comparisons for other architectures are shown in Appendix B.2. In general all simulations show higher force levels as well as a higher initial peak. Both of these phenomena can be explained by the rigid backing assumed in the simulation.

As the over-prediction of the force is a phenomenon observed in the correlation of all simulations with their respective experimental cases and not severe, the simulations were deemed trustworthy for the assessment of differences in the behaviour of different architectures. However, it was decided to exclude the first 0.15 ms from the computation of integral measures, such as the average or maximum pressure, in order to exclude the effects of the higher initial peak.

Further illustration for all models is provided in Figure 5.14. In this figure, the Length 2 ARH sample is shown in all three investigation settings after 0.25 ms. Here, it is observable, that both FE models show a stronger indentation of the plunger compared to the experimental model, which is again explained by the higher forces due to the rigid backing. Other than that, despite not matching the deformation

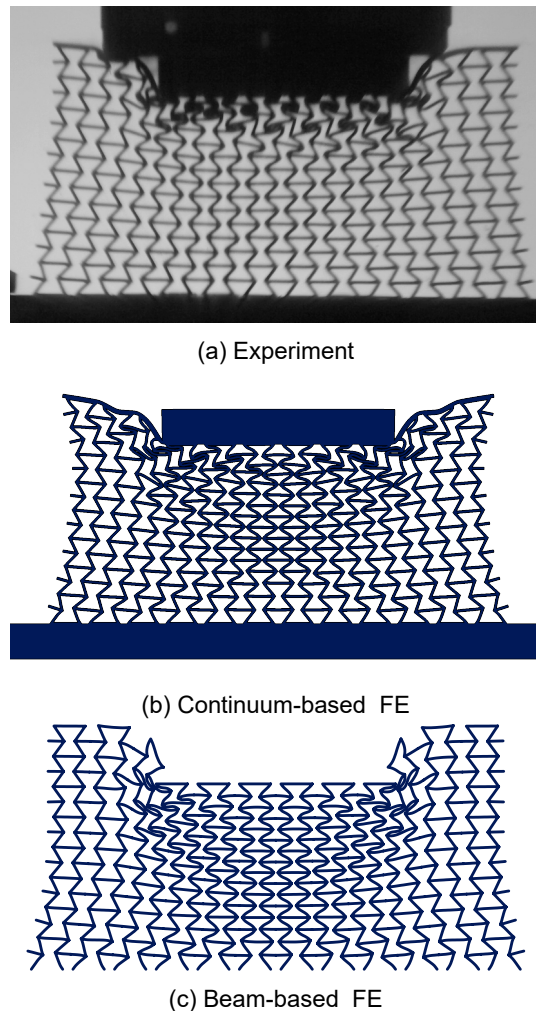


Figure 5.14.: Comparison of the deformation of the *Length 2* ARH sample at 0.25 ms. (a) is showing the experimental image, (b) the continuum-based FE result, and (c) the beam-based FE result.

of each singular member in the lattice precisely, the overall deformation pattern between the experiments and the FE models match closely. Especially the start of the densification in the upper end of the sample as well as stronger densification around the edges of the strike-face are matched well. This confirms the assessment based on the total force recordings, that the models are comparable and valuable insights can be gained by exploring all three models available.

### 5.4.1. EXPERIMENTS

## 5

The first set of experiments were conducted on the baseline ARH for both patch configurations, *Length 1* and *Length 2*. Both samples are displayed in an undeformed state in Figure 5.6. The corresponding recorded forces on the back-face are shown in Figure 5.15 over time measured from the initial contact between the plunger and the front face of the sample. In this figure it is observed that the initial part of the

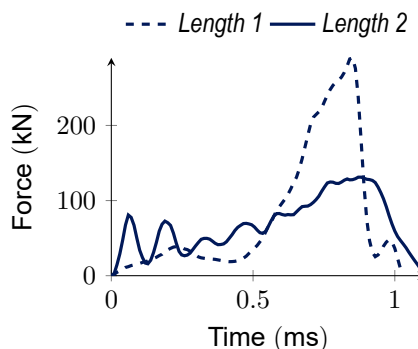


Figure 5.15.: Experimental comparison of samples sizes for ARH.

load is lower and more stable for the globally impacted sample of length 1. However, a large peak in the measured reaction force occurs after 0.8 s, followed by a subsequent sharp drop to 0 N. In contrast, the sample of *Length 2* exhibits a more dispersed impact load (and, consequently, impact energy) over time, maintaining a relatively constant transmitted force until the plunger is fully stopped. This comparison indicates that the surrounding material is crucial for the determination of the protection level of a structure. From the level of force, a localized impact is to be preferred in order to spread out the momentum transfer over a longer time resulting in a lower peak force throughout the time.

Subsequent experiments were conducted to compare other auxetic and non-auxetic architectures, as specified in Table 5.3, with the baseline ARH sample described above. The actual impact velocity and masses of each plunger were measured and are described in Table 5.6. In the first series, all four samples were designed to have the same initial elastic stiffness. Figure 5.16a shows the force summed up over the sensors plotted over time. Note that the force measurements due to the rebound of the plunger are not shown here as they are not the focus of this research. Both auxetic structures—ARH and ARH90 SS—show a distinct peak

Table 5.6.: Recorded plunger velocities and masses.

Unit cell		velocity ( $\text{m s}^{-1}$ )	mass (g)
SS	ARH	Length 1	74
	ARH	Length 2	71
	ARH90	Length 2	76
SM	CHW	Length 2	75
	CHL	Length 2	75
	ARH90	Length 2	72
SM	CHW	Length 2	77
	CHL	Length 2	73
			1199
			1202
			1202
			1199
			1202
			1199
			1192

in the force curve. Upon examination of the high-speed videos, it can be observed that this correlates with the point at which the material is approaching complete densification. Consequently, the subsequent deceleration of the plunger is solely due to material compression, requiring significantly greater forces compared to the lattice deformation in the earlier stages of the impact. Stills from the high speeds videos of both—ARH and ARH90 SS—can be found in Figure 5.17. In contrast, the conventional honeycombs in both orientations do not show a distinct peak, but rather a slower deceleration at lower forces. Here, due to the positive Poisson's ratio of the material, the structural members of the lattice are laterally pushed away from the impact location. This effect spreads the load over a larger area, as the laterally pushed away material deforms as well. This lateral deformation can be observed in Figure 5.18, where stills of the high speed videos throughout the deformation are shown for both CH SS configurations. The details of this spatial load distribution were investigated further in the numerical experiments.

Another comparison is undertaken with the lattices designed to exhibit a similar mass as the ARH baseline architecture. The corresponding measured forces over time are shown in Figure 5.16b. The ARH curve is the same as in Figure 5.16a, as this architecture is used as baseline. The rotated auxetic structure (ARH90) possesses a less distinct, more flat peak. The CH curves are higher than the

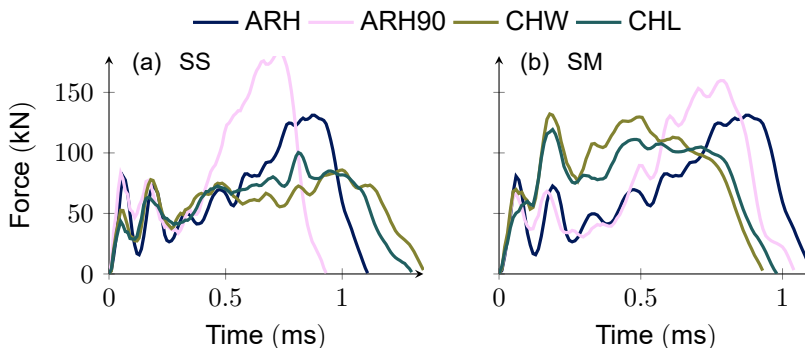


Figure 5.16.: Force comparison for same (a) stiffness and (b) mass from the physical tests.

5

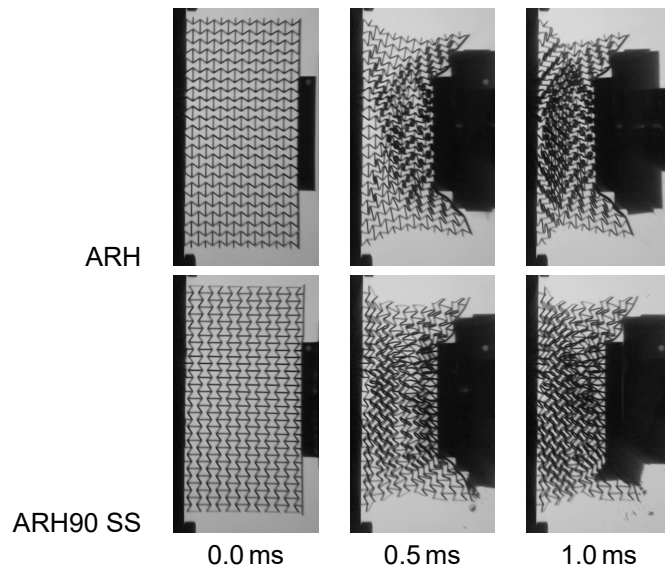


Figure 5.17.: Stills from the high-speed recordings for both auxetic architectures.

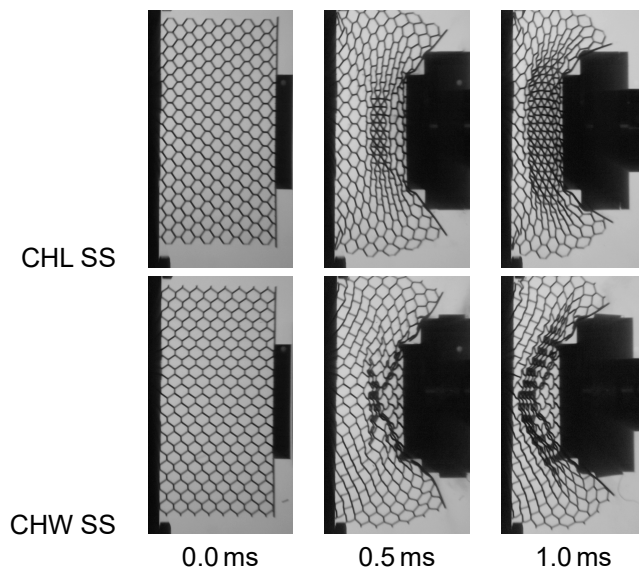


Figure 5.18.: Stills from the high-speed recordings for both non-auxetic architectures.

Figure 5.16a curves, due to the higher stiffness resulting from the thicker beams due to the equivalent mass design target. These higher initial stiffnesses are recorded Table 5.1. Both conventional honeycombs show the same peak-less behaviour as described for Figure 5.16a, but at a higher level.

### 5.4.2. CONTINUUM-BASED FE

In order to enhance understanding of the physical experiments, numerical simulations were conducted as detailed in Section 5.3.2. Simulations allow the extraction of data from any point, without any physical restrictions and effects on the results. Of special interest in the context of impact mitigation is not only the total force transmitted to the back of the protective structure, but also the pressure distribution over the back face. For this the average and maximum pressure onto locations of the back-face were computed over time, with the exclusion of the first 0.15 ms as described above. The average pressure over the back-face is shown in Figure 5.19b for all architectures with the same stiffness. This average pressure distribution in

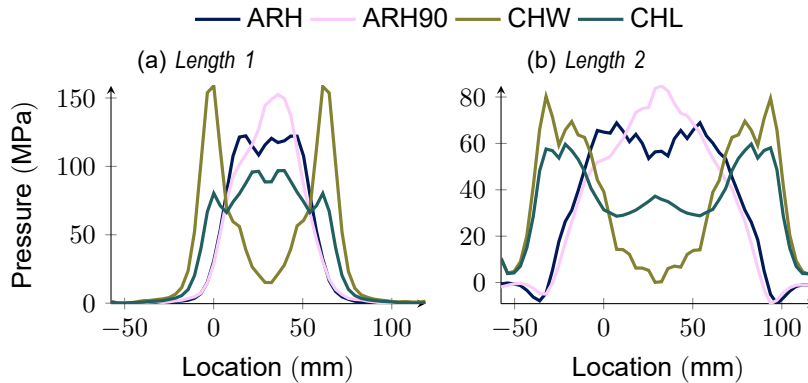


Figure 5.19.: Comparison of the average pressure over the back-face for the SS configuration using the continuum-based model.

Figure 5.19b shows that the auxetic densification leads to a concentration of the forces on a smaller area, resulting in a higher pressure onto the protected structure at the back of the plate. It should be mentioned that the highest average pressures for the non-auxetic structures are at the edges of the lattice structure, indicating, that the length of the CH samples is not sufficient to spread the load effectively. This is emphasized by the observation of similar pressure distributions in the samples with only the single width, as shown in Figure 5.19a. Here the auxetic samples concentrate the force in the centre, resulting in higher pressures onto the backside, whereas the non-auxetic samples distribute force to the boundaries. A point to note here is that the CHL architecture also shows a slight peak in the centre of the structure. This can be explained by the deformation of this unit cell leading to auxetic behaviour, as discussed in Chapter 4.

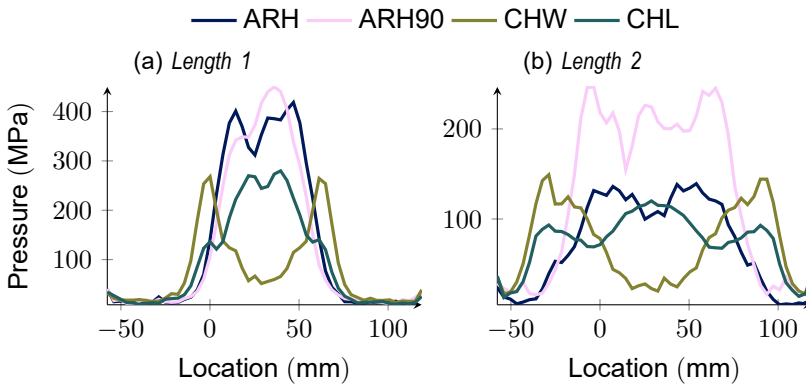


Figure 5.20.: Comparison of the maximum pressure over the back-face for the SS configuration using the continuum-based model.

Similar observations can be made upon examination of the maximum pressure on the backside. For the *Length 2* samples, this is shown in Figure 5.20b and for the *Length 1* samples in Figure 5.20a. The load spreading effect is less distinct, but still observable in the plot showcasing the *Length 2* samples. In the plot with the *Length 1* samples the discussed effects of CHL architectures becoming auxetic is even more prevalent. This is also observable in the deformation throughout the physical experimentation in Figure 5.18. Similar behaviour can be seen in Appendix B.3 for the SM configuration.

#### 5.4.3. BEAM-BASED FE

Using the more efficient beam-based model, investigations into wider samples are available for fast computation. For this, all SS samples reported in Table 5.1 as *Length 2* are elongated in the horizontal direction again, leading to a doubling of the unit cells in  $x$ -direction, whilst all other boundary conditions are kept the same. In Figure 5.21, again, the recorded total force on the back-face is shown over time. The solid lines represent the samples of *Length 2*, whereas the samples of *Length 4* are shown in dashed lines. No substantial difference between the two sample widths can be observed, indicating together with the results from the continuum-based simulation, that the increase in length does not affect the total force transmission profile, but only the pressure distribution. The same accordance between the configurations can be found when examining the results for the SM configurations in Appendix B.3.

Another additional study enabled by the structural FE modelling is the change of the unit cell size. For this, unit cell sizes are halved and the number of unit cells reported in Table 5.1 in each direction is doubled in order to have the same outer measures for each sample. This leads to a quadrupling of the overall number of unit cells whilst keeping the mass the same. In Figure B.6 the comparison between the two investigated sizes is plotted for the samples of *Length 1* in the SS configuration.

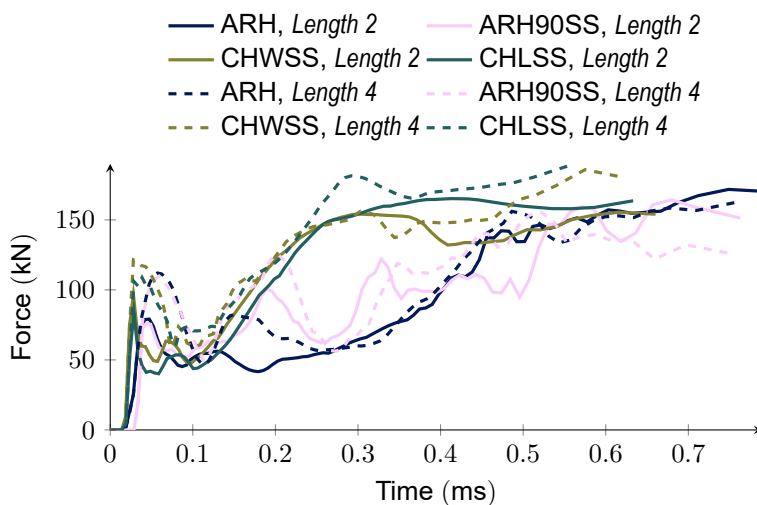


Figure 5.21.: Comparison of longer samples for the SS configuration.

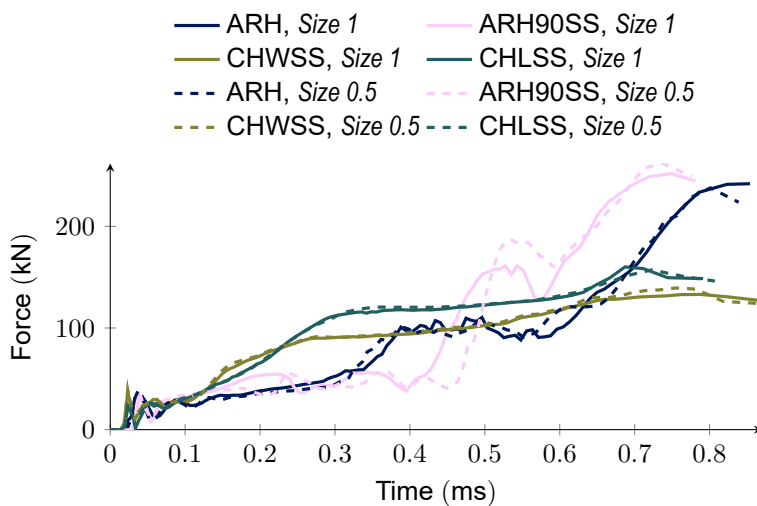


Figure 5.22.: Comparison of smaller unit cells for the SS configuration of *Length 1* using the beam-based model.

In this graph, the force on the back-face is shown for all different unit cells over the time. The default unit cells of Size 1 are shown in solid lines, whereas the adapted unit cells of Size 0.5 are depicted with dashed lines. In the graph it can be observed, that reducing the size of the unit cells does not lead to any significant change in the transmitted forces. The same effect is also seen in the *Length 2* samples, as well as in the *SM* configuration samples, which can be found in [Appendix B.3](#).

5

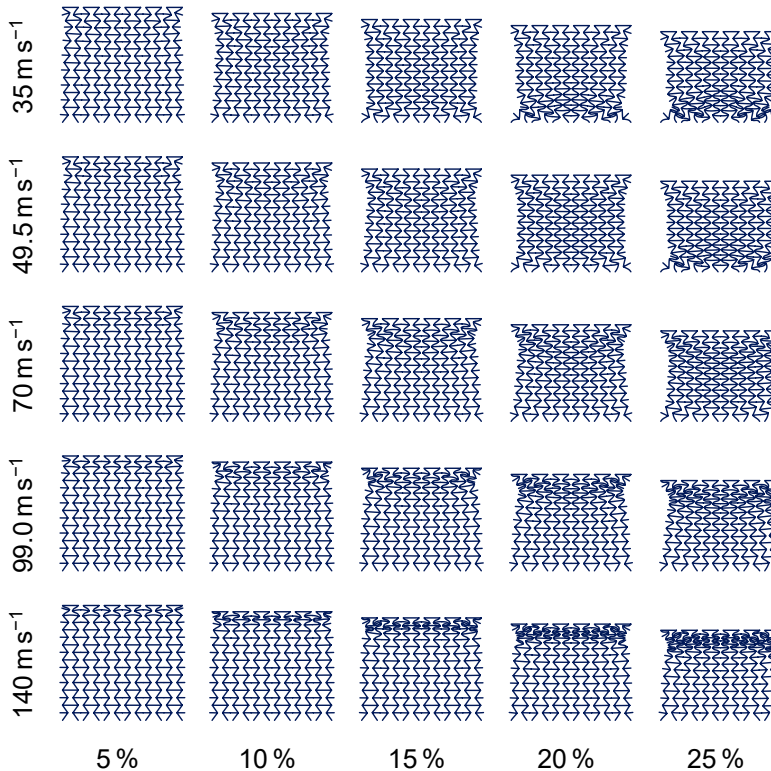


Figure 5.23.: Deformation patterns of the ARH sample of *Length 1* at different impact velocities and compression states.

In order to appreciate the effect of velocity additional studies at different velocities were carried out. In these investigations, the mass of the impactor was kept the same, but the speed was adapted, so that the kinetic energy or the impulse of the impactor were doubled and halved, respectively. For a doubling of kinetic energy, the velocity of the impactor needs to be multiplied by  $\sqrt{2}$ , and for halving it divided by  $\sqrt{2}$  likewise. This resulted in the list of 35 m/s, 49.5 m/s, 70 m/s, 99.0 m/s and 140 m/s as investigated speeds, including the original study. In [Figure 5.23](#), the ARH architecture is showcased for all 5 investigated speeds and at 5 %, 10 %, 15 %, 20 % and 25 % compression each. One should note, that the visualizations at the same compression level do not correspond to the same time, as the compression occurs faster at higher impactor velocities. In the central row, the speed

discussed in the previous parts of this study is shown. The deformation pattern emerging at this speed showcases a V-shaped manner, similar to the transitional mode discussed in [Rua<sup>&al</sup>03]. As reported in literature, for higher velocities a transition and concentration of the dynamic collapse zone towards the strike face can be observed. For lower velocities, we observe the emergence of the collapse pattern from the bottom of the patch. When inspecting the lateral contraction, the Poisson effect appears to be weakening with increased impact velocities. At the target velocity for this study of  $70 \text{ m s}^{-1}$ , the lateral contraction is still clearly visible throughout the sample, indicating the applicability of this speed for studying the effects of the Poisson effect. This can also be seen in Figure 5.24, where at lower speeds the effect of the negative Poisson's ratio is showcased by material being pulled towards the centre, whereas for higher speeds, the effect is subdued by the inertia of the material. Similar effects can be observed for the other investigated materials as well, they are shown in Appendix B.4.

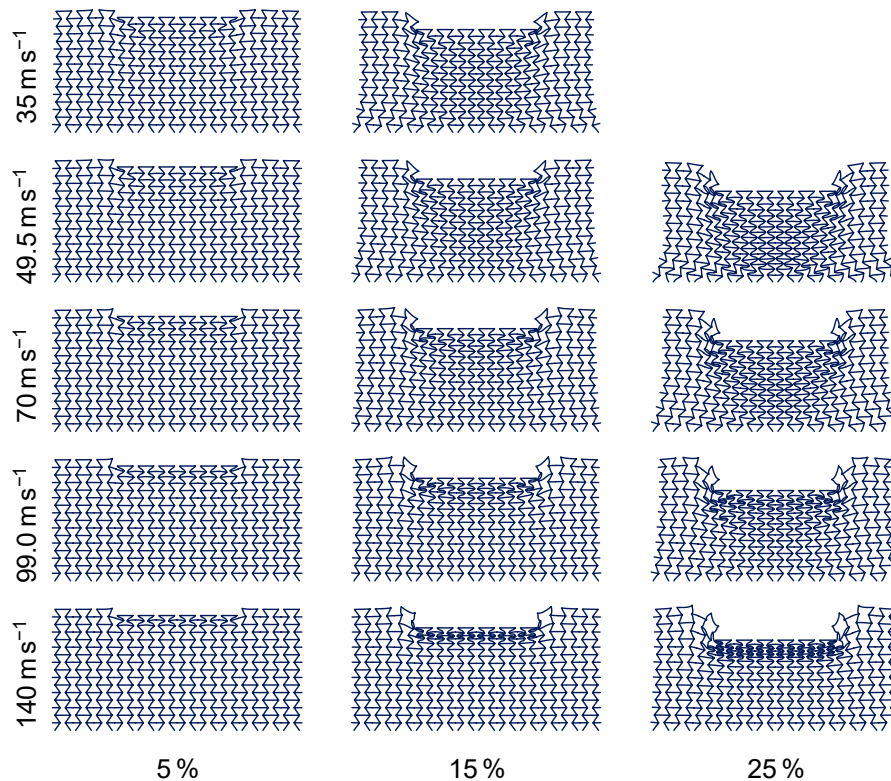


Figure 5.24.: Deformation patterns of the ARH sample of *Length 2* at different impact velocities and compression states.

## 5.5. DISCUSSION & CONCLUSION

Looking back at the experimental campaign that resulted in the transmitted force onto the underlying material after a localized impact, it is first observed, that higher stiffness leads to more direct force transmission. Whilst all samples are able to absorb the impact energy, this showcases CH structures outperforming ARH structures when the main concern is energy absorption in a limited area with a given weight, as they were able to do so in a shorter time. Reducing this stiffness allows the energy absorption to be spread out over a longer time for the CH samples, that are not stiffening unlike the ARH samples. This spread of the energy absorption results in lower total force levels on the back-face of the protective structure, potentially reducing the load on the precious load being protected by the lattice, which is beneficial for the protection as reported by Gupta and Ding [GD02]. While under blast loading, the more compliant edges can help distribute the force, as reported by [Boh<sup>&al</sup>22], due to the external load spread inherent to a blast. Under ballistic impact, the load is naturally concentrated and thus negative Poisson's ratio and the corresponding densification and stiffening lead to a further concentration of the load.

These finding are reinforced by the additional numeric studies into the load spread on the back-face of the material. Here, it can be summarized, that in the given context, a negative Poisson's ratio in the material leads to higher peaks in the loading on the backside of the protective structure also in space. This effect is especially pronounced when comparing the structures with comparable stiffness. When looking at structures with equivalent mass, the higher stiffness of the conventional architectures has a stronger effect compared to its load distribution effect. Overall it has been shown, that higher stiffness improves the energy absorption qualities in a confined space, but also lead to worse protective properties due to higher force peaks onto the back-face of the protective structure.

Thus, it can be concluded that the impact mitigation efficacy of auxetic materials only appears in the case, where energy absorption and the need to limit the deformation of the protective structure at a given stiffness are the main measures. In other cases, especially when the spreading of the load or lightweight design of the protective structures are of interest, auxetic structures are not able to spread the load of a localized impact and perform worse than conventional honeycombs when considering equal mass even in pure energy absorption measures.

Lastly, investigations with different scenarios as well as size effects using faster, albeit less accurate, beam-based simulations were conducted to explore other patch configurations. In the first trial, the investigation into even longer samples lead to no significant difference between patches of *Length* 2 and *Length* 4, emphasizing the assumption that the earlier investigations are representative of a local impact onto a wide structure. The contradiction with Chapter 4, where wider samples are suggested to be required for assessment of the performance of the structure, can be explained by the limitation to elasticity in that study, whereas plasticity, especially in this dynamic environment, can lead to higher localization, which prevents further spreading of the load. To this end as well, different unit cell sizes were compared in another investigation. Here no significant effect was observed, leading to the

conclusion, that the investigated number of unit cells reported in Table 5.3 can be taken as sufficient to not experience significant boundary effects. This is especially valuable when considering the physical tests, where smaller unit cells would require more refined manufacturing, that might be limited by technological or budgetary constraints.

This full-scale, physical testing campaign is needed to ensure all physical phenomena have been considered. Physical tests, especially when considering ballistic impact studies, require tremendous effort and resources to be conducted and have, as was demonstrated, difficulties to ensure the boundary conditions envisioned are met with certainty. To this end numerical tests enable faster and less resource-intensive assessment with properly idealized boundary conditions. In numerical investigations, the placement of sensors is not a matter of physical practicality, but rather of limiting the amount of data, enabling a better understanding of the inside processes in the material and the detailed interactions with the surrounding structure. As there are different levels of refinement and discretization of structures, one needs to make good use of all available resources in order to speed up the design and research process and to further facilitate the understanding and development of protection concepts.

Summarizing the findings of this contribution, the existing primer of literature, that auxetics perform better for impact mitigation, has been challenged by data of force distribution, where simple non-auxetic honeycombs were shown to exhibit better performance in multiple configurations. Also, the simple use of energy absorption as assessment tool for impact mitigation is insufficient in cases where not only the total energy absorbed by the structure is relevant for the safety of the protected structure, but also the distribution of the transmitted forces. To this end various numerical tools were shown to be effective supplements to the physical experiments in order to gain a deeper understanding, which can be used for the design of protective structures and further research on this topic. For this further research, the assessment of different auxetic and non-auxetic structures will be valuable for the community to ensure that findings can be generalized, as well as a deeper investigation into the interdependency of the inelastic, strain-rate dependent response and different unit cell architectures.

## REFERENCES

**5**

- [Boh<sup>&al</sup>22] R. P. Bohara et al. 'Performance of an auxetic honeycomb-core sandwich panel under close-in and far-field detonations of high explosive'. *Compos. Struct.* **280**, 114907 (2022).
- [Boh<sup>&al</sup>23] R. P. Bohara et al. 'Anti-blast and -impact performances of auxetic structures: A review of structures, materials, methods, and fabrications'. *Eng. Struct.* **276**, 115377 (2023).
- [Cri<sup>&al</sup>13] R. Critchley et al. 'A review of the manufacture, mechanical properties and potential applications of auxetic foams'. *phys. status solidi (b)* **250** (2013), pp. 1963–1982.
- [Fin00] B. K. Fink. 'Performance Metrics for Composite Integral Armor'. *J. Thermoplast. Compos. Mater.* **13** (2000), pp. 417–431.
- [Gal<sup>&al</sup>24] R. Galea Mifsud et al. 'Auxetics and FEA: Modern Materials Driven by Modern Simulation Methods'. *Mater. (Basel)* **17**, 1506 (2024).
- [Gär<sup>&al</sup>24] T. Gärtner et al. 'Geometric effects on impact mitigation in architected auxetic metamaterials'. *Mech. Mater.* **191**, 104952 (2024).
- [Gär<sup>&al</sup>25a] T. Gärtner et al. '(In)efficacy of auxetic metamaterials for impact mitigation'. *Int. J. Impact Eng.* **206**, 105402 (2025).
- [Gär<sup>&al</sup>25b] T. Gärtner et al. 'A strategy for scaling the hardening behavior in finite element modelling of geometrically exact beams'. *Comput. Mech.* **75** (2025), pp. 1471–1482.
- [GD02] Y. M. Gupta and J. L. Ding. 'Impact load spreading in layered materials and structures: concept and quantitative measure'. *Int. J. Impact Eng.* **27** (2002), pp. 277–291.
- [Gib<sup>&al</sup>97] L. J. Gibson et al. 'The mechanics of two-dimensional cellular materials'. *Proc. R. Soc. Lond., A. Math. Phys. Sci.* **382** (1997), pp. 25–42.
- [JC85] G. R. Johnson and W. H. Cook. 'Fracture characteristics of three metals subjected to various strains, strain rates, temperatures and pressures'. *Eng. Fract. Mech.* **21** (1985), pp. 31–48.
- [Kap<sup>&al</sup>23] K. Kappe et al. 'Multi-objective optimization of additive manufactured functionally graded lattice structures under impact'. *Int. J. Impact Eng.*, 104789 (2023).
- [Liu<sup>&al</sup>16] W. Liu et al. 'In-plane dynamic crushing of re-entrant auxetic cellular structure'. *Mater. & Des.* **100** (2016), pp. 84–91.
- [Qi<sup>&al</sup>17] C. Qi et al. 'Impact and close-in blast response of auxetic honeycomb-cored sandwich panels: Experimental tests and numerical simulations'. *Compos. Struct.* **180** (2017), pp. 161–178.
- [Ren<sup>&al</sup>18] X. Ren et al. 'Auxetic metamaterials and structures: a review'. *Smart Mater. Struct.* **27**, 023001 (2018).
- [Rua<sup>&al</sup>03] D. Ruan et al. 'In-plane dynamic crushing of honeycombs—a finite element study'. *Int. J. Impact Eng.* **28** (2003), pp. 161–182.

[SDC16] K. K. Saxena, R. Das and E. P. Calius. 'Three Decades of Auxetics Research – Materials with Negative Poisson's Ratio: A Review'. *Adv. Eng. Mater.* **18** (2016), pp. 1847–1870.

[SKS20] Smriti, A. Kumar and P. Steinmann. 'A finite element formulation for a direct approach to elastoplasticity in special Cosserat rods'. *Int. J. Numer. Methods Eng.* (2020), pp. 1262–1282.

[Spr11] T. J. Spradlin. *Process Sequencing for Fatigue Life Extension of Large Scale Laser Peened Components*. PhD thesis. Wright State University, 2011.

[UMO07] D. Umbrello, R. M'Saoubi and J. C. Outeiro. 'The influence of Johnson-Cook material constants on finite element simulation of machining of AISI 316L steel'. *Int. J. Mach. Tools Manuf.* **47** (2007), pp. 462–470.

[Wee<sup>&a/</sup>23] O. Weeger et al. 'Inelastic finite deformation beam modeling, simulation, and validation of additively manufactured lattice structures'. *Addit. Manuf. Lett.* **4**, 100111 (2023).



# 6

## **INELASTIC BEHAVIOUR UNDER DIFFERENT STRAIN RATE REGIMES**

*Materials engineered with an internal architecture in order to achieve unusual properties, so-called mechanical metamaterials, are a promising candidate in the ongoing quest for lightweight impact mitigation. During impact events, these materials are subject to high strain rates, and the forces occurring due to the deceleration of the impactor are transmitted in a non-uniform way. The prevailing research in the field of impact mitigation focuses largely on the global effects of architected materials, with less attention being paid to the internal mechanisms of these structured materials. While there have been recent studies on the distribution of forces throughout an impact event, less research is devoted to the transmission of forces and the distribution of energy dissipation. The objective of this study is to examine the transition from static deformation patterns to dynamic phenomena for different types and sizes of microstructure, and to understand both the force transmission through the patch and the energetic distributions in different strain rate regimes. To enable this investigation discretized—geometrically as well as materially—nonlinear Timoshenko-Ehrenfest beams are used in implicit and explicit finite element schemes. The transmitted force levels and energy dissipation are investigated for two auxetic architectures (one for each mechanism resulting in a negative Poisson's ratio) and one non-auxetic architecture. The dynamic force levels transmitted to the back face exhibit an initial peak of a similar magnitude for all investigated strain rates and stabilize to the static stress plateau for each architecture. While the global amount of potential energy remains largely unchanged for all investigated rates, the amount of dissipation and kinetic energy demonstrates a non-linear increase from static deformation to slow and high rate deformation. The phenomena observed in different architectures are highlighted, and the differences are explained and related back to the configurations of the lattices. Notably, the prevalent notion in literature asserting the superiority of negative Poisson's ratio materials for impact mitigation applications is not replicated in this study.*

## 6.1. INTRODUCTION

The engineered microstructure of architected materials achieving unusual mechanical properties, resulting in so-called mechanical metamaterials, presents new opportunities for designers and engineers as well as new challenges for researchers [Bon<sup>&al</sup>24; Jia<sup>&al</sup>23; SP25]. Of particular interest is the design of metamaterials for impact mitigation. Impact events, necessitating protective measures, exist in a wide range of fields, from sports [San<sup>&al</sup>14] over space travel [PA99], metal roofs in hailstorms [SS19], collisions between cars and civil infrastructure [Pan<sup>&al</sup>18] to personal protective equipment [Cro19]. In all these applications, the aim of the protective structure is to limit the energy and impulse transmitted from the impactor to the protected structure, be it a living being or an otherwise fragile material.

In this quest, auxetic (negative Poisson's ratio) materials have gained considerable interest in the research community in recent years, as evidenced by the reviews [Boh<sup>&al</sup>23; Ren<sup>&al</sup>18; SDC16; TZH22]. The negative Poisson's ratio, which characterizes auxetic materials, leads to lateral material contraction under compression, as shown in Figure 6.1. For impact mitigation, auxetic materials are of special interest due to reported higher indentation resistance [AGS12] as well as shear resistance [CL92]. Other promising properties for impact mitigation include increased fracture toughness [CL96] and enhanced energy absorption [JH17]. Auxetic materials naturally compress themselves underneath the impacted area, reportedly allowing for more mass-efficient protective solutions. However, these assumptions are based on homogeneous, isotropic materials under infinitesimal, quasi-static deformation.

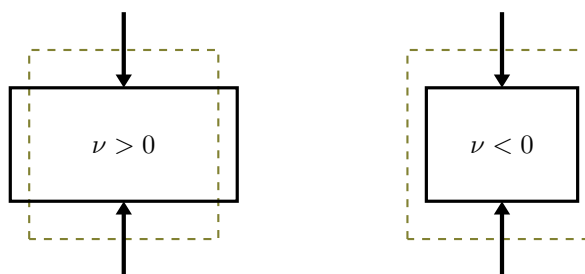


Figure 6.1.: Auxetic materials concept.

As no relevant natural auxetic materials exist, this negative Poisson effect needs to be artificially created through mechanical metamaterials. Whilst mechanical metamaterials can be constructed from shells [Mey<sup>&al</sup>22], plates [GYM22; MTM24], or as foams [Cri<sup>&al</sup>13], the focus in this work is on auxetic structures based on structured beam-lattices. These architected materials are inherently *not* isotropic and, as they also undergo large deformations, their material properties vary throughout deformation. In beam lattices, the individual beams are re-oriented, leading to a change in the effective material properties, as shown in Chapter 4.

As shown in [Chapter 5](#) not only the pure energy absorption capability of a structure is of importance for impact mitigation, but also the—temporal and spatial—distribution of forces. In this chapter, further investigation is conducted into the distribution of energy dissipation within the structure at varying strain rates for different refinement levels, alongside the subsequent effects on the force transmission from the impactor to the protected structure.

The investigation into the energy absorption of protective structures has thus far focused mostly on the energy dissipated by compression of the structure, and its conclusions focus on the higher amount of energy dissipated by auxetic lattices [[Liu<sup>et al.</sup> 16](#); [Qi<sup>et al.</sup> 17](#)]. However, little attention is given to the internal mechanisms and the distribution of the energies in comparable metamaterials of different architectures. Investigations of different collapse patterns under high speed compression were undertaken as early as the 1980s [[CE84](#)], where a comparison between two types of structures and their internal collapse mechanism is shown. Ruan et al. [[Ruan<sup>et al.</sup> 03](#)] investigated different modes of collapse occurring throughout different speeds in non-auxetic conventional honeycombs with different wall-thicknesses. More recently, investigations into the static mechanisms in the deformation of metamaterials, either driven by the boundary conditions [[CKvH17](#)] or by the interaction between local and global collapse patterns [[Zhang<sup>et al.</sup> 25](#)] have been conducted. However, only one type of fundamental architecture was investigated in all these works, and a comparison between different auxetic and non-auxetic architectures is yet to be made. The link between the collapse patterns, dynamic loading and the corresponding force transmission for different types of unit cells is explored in this chapter. To provide a first insight into this topic, numerical experiments are conducted using beam-based finite element analyses. For these analyses, three different fundamental unit cells, are investigated: **a)** the most common auxetic type, a re-entrant honeycomb (cf. [[Gib<sup>et al.</sup> 97](#)]); **b)** an auxetic cell based on a rotation mechanism, the so-called missing ribs or chiral unit cell (cf. [[SGE00](#)]); and **c)** a non-auxetic unit cell, the regular honeycomb. The three unit cells are designed to exhibit the same relative density as well as initial stiffness (cf. [Chapter 4](#)). Knowledge of the behaviour of these architectures will allow for better insight into the mechanisms of collapse under different strain rates. Here, special attention will be paid to the effects of microstructural refinement and transmission of forces from the strike face of the protective layer, i.e. the side of the structure subjected to the impact, to its back face, i.e. the interface with the opposing structure. This enables design engineers to decide on a protection concept fit for the expected impact events.

The architecture designs for the investigated metamaterials are presented in [Section 6.2](#), and in [Section 6.3](#) the numerical framework to conduct the investigation is laid out. In [Section 6.4](#), an investigation into the static behaviour of different sizes of unit cells in a patch is presented, which forms the basis for the investigation into the force transmission at different rates through the patch in [Section 6.5](#). To understand the processes involved in this force transmission better and obtain insight into the deformation patterns, in [Section 6.6](#), the distribution of energies is presented and discussed. The chapter closes in [Section 6.7](#) with a short discussion of the obtained results, limitations of this study and recommendations for further research.

## 6.2. INVESTIGATED ARCHITECTURES

The investigated auxetic architectures in this chapter are the same as in [Chapter 4](#). All architectures investigated are designed to exhibit a Young's modulus of 300 MPa in vertical direction and a relative density with regard to the base material of 0.1. The material of which the architectures are constructed from is taken to be a steel with a Young's modulus of 210 GPa, a Poisson's ratio of 0.3, and a density of  $7850 \text{ kg m}^{-3}$ . An in-depth discussion on the static, elastic properties of these architectures, as well as the design process, can be found in [Chapter 4](#). It should, however, be noted that the absolute dimensions of the unit cells do not matter for the determination of the Young's modulus or the relative density, so that the unit cell can be directly scaled to the desired measures for the investigations conducted in this chapter.

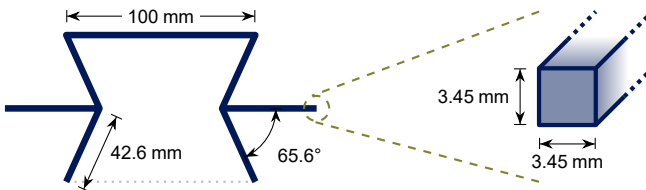


Figure 6.2.: Re-entrant unit cell used throughout this investigation.

The first investigated unit cell is the most common auxetic architecture, the re-entrant honeycomb (cf. [\[Gib&al97\]](#)). Its configuration is shown in [Figure 6.2](#). The horizontal beam has a length of 100 mm, the tilted beams a length of 42.6 mm and the angle between the tilted beams and the horizontal is set to be  $65.6^\circ$ . The beams itself have a square cross-section with a side length of 3.45 mm.

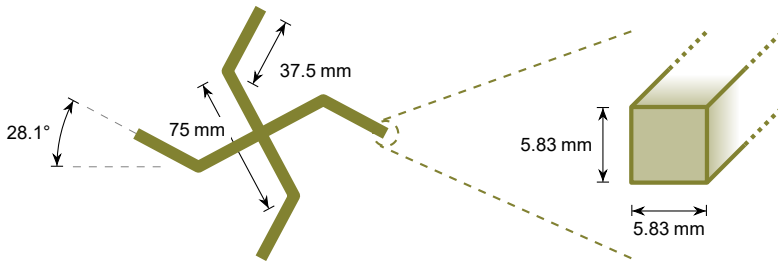


Figure 6.3.: Chiral unit cell used throughout this investigation.

In order to also capture unit cells with a fundamentally different deformation mechanism, chiral, sometimes called missing ribs, unit cells (cf. [\[SGE00\]](#)) are investigated. Whilst the Poisson effect of re-entrant honeycombs is driven largely by inwards folding, the deformation of chiral unit cells is driven by rotation of the joints, resulting in a mechanism that can also be found in rotating squares unit cells (e.g. [\[CKvH17\]](#)). The chiral unit cell is depicted in [Figure 6.3](#). The length of a single beam in the centre is 75 mm and the angle between the horizontal (or vertical) axis and

the beams is set to  $28.1^\circ$ . This results in a width of the entire unit cell of 132 mm and together with a square cross-section of 5.83 mm side length, the relative density of 0.1 and the effective Young's modulus of 300 MPa in vertical direction are obtained as for the re-entrant unit cell.

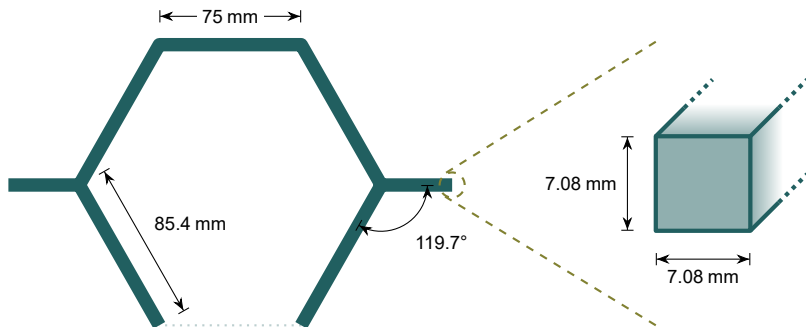


Figure 6.4.: Honeycomb unit cell used throughout this investigation.

The final investigated unit cell is the non-auxetic honeycomb as depicted in Figure 6.4. The horizontal beam has a length of 75 mm and the tilted beams are 85.4 mm long. The beams have a square cross-section with a side length of 7.08 mm and the angle between the tilted beams and the horizontal is set to  $119.7^\circ$ . Again, the resulting Young's modulus and relative density are 300 MPa in vertical direction and 0.1, respectively.

All three unit cells are subsequently assembled into patches. When assembling these patches, the unit cells are scaled down, to ensure that the overall patch has the same outer dimensions for each architecture. For the scaling, all geometric dimensions, the length of the beams, as well as the dimensions of their cross-sections are scaled by the same factor. The thickness in the third direction is thus changing for a different number of unit cells, which is accounted for in the later analyses. A comparison between two patches consisting of  $2 \times 2$  and  $12 \times 12$  unit cells is shown in Figure 6.5. In this illustration, the scaling of the singular unit cells to achieve the same outer dimension is shown.

### 6.3. NUMERICAL FRAMEWORK

In order to model patches made from the unit cells described above, the lattices are subsequently modelled as a collection of nonlinear Timoshenko-Ehrenfest beams as described in Chapter 2. The elastoplastic behaviour of the materials is modelled as laid out in Chapter 3. A Young's modulus of  $E = 210$  MPa and a Poisson's ratio of  $\nu = 0.3$  are assumed. The yield function and hardening parameters for a reference quadratic cross-section of side length 0.75 mm is taken to be the same

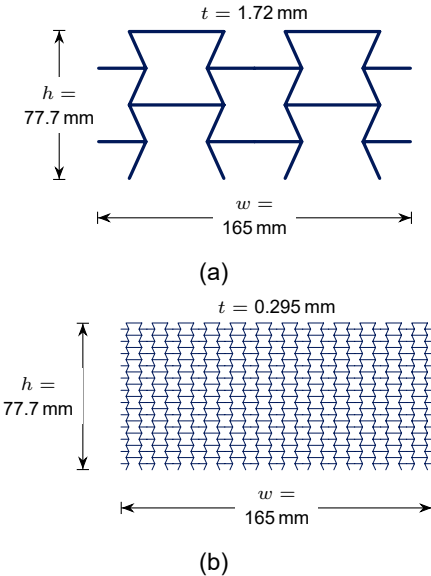


Figure 6.5.: Patches from  $2 \times 2$  and  $12 \times 12$  unit cells, scaled to ensure the same outer dimensions.

as in [Chapter 5](#) and can be found in [Equations \(5.2\)](#) and [\(5.3\)](#). These parameters resulted from scaling the reported values from literature [[HKS21](#); [HKS22](#)] to the physical material parameters of the steel used in the experiments in [Chapter 5](#). Scaling of these parameters follows the approaches laid out in [Chapter 3](#).

Contact between the beams is assumed using the approach laid out in [Section 2.3](#). In order to scale the contact stiffness with the size of the contact points, the penalty parameters are adapted with the thickness of the beams  $t$

$$\varepsilon_{STS} = \varepsilon_{NTS} = \varepsilon_{NTN} = 10^7 \cdot \left( \frac{t}{1 \text{ mm}} \right)^2, \quad (6.1)$$

as the contact radii around all beams are set to half the beam thickness

$$r = \frac{t}{2}. \quad (6.2)$$

For the static investigations an implicit Newton-Raphson scheme is employed, whilst the dynamic investigations are computed using an explicit scheme with adaptive time stepping as laid out in [Section 2.4](#).

Throughout the analysis, different stress and energy measures are recorded. The stress on the strike face is the sum of the resulting nodal forces in vertical direction on the top boundary divided by the width of the sample  $w$  and the thickness  $t$  of a beam. A similar computation is employed for the back face. As the resulting forces on the strike face are typically acting downwards (in negative direction) a factor of

-1 is added to obtain positive values:

$$\sigma_{\text{strike}} = -1 \cdot \frac{\sum f_{\text{strike}}}{wt}, \quad (6.3)$$

$$\sigma_{\text{back}} = \frac{\sum f_{\text{back}}}{wt}. \quad (6.4)$$

The SEA, i.e. the external work put into the system, is calculated by integrating the sum of the resulting forces on the strike face over the displacement of the strike face  $u_{\text{strike}}$  and normalizing it by the mass of the patch  $m_{\text{patch}}$ :

6

$$\text{SEA}(u) = \frac{1}{m_{\text{patch}}} \int_0^u \left( \sum f_{\text{strike}} \right) du_{\text{strike}}, \quad (6.5)$$

where the integration is executed using the discrete values recorded during the simulation using Simpson's rule. The potential, kinetic and dissipated energies are recorded on a nodal basis. The kinetic energy is directly computed from the nodal velocities and the global mass matrix, whereas the potential and dissipated energies are calculated per element and subsequently integrated for each node using standard finite element procedures.

As the time-steps for the different simulations are not identical, and the dynamic simulations conducted show high-frequency oscillations due to the absence of damping in the model, all reported measures are created from the average of bins stretching 0.5 % compression each. E.g. the point plotted at 15 % compression is the average of the recorded values between 14.75 % and 15.25 % compression.

### 6.3.1. BOUNDARY CONDITIONS

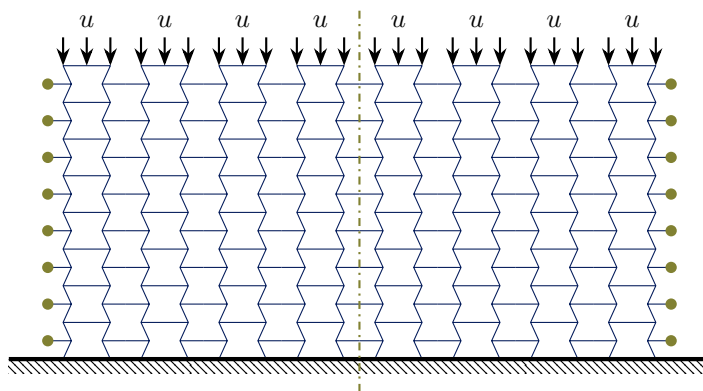


Figure 6.6.: Boundary conditions applied in this investigation at the example of an  $8 \times 8$  patch.

In order to estimate the behaviour of different patch configurations, a set of boundary conditions mimicking a constant strain-rate setup is applied. An overview of these boundary conditions can be found in Figure 6.6. On the bottom side, the patch is fully fixed, whilst at the top side, horizontal movement is prevented and a vertical, compressive displacement  $u = u_{\text{strike}}$  is enforced. The boundary nodes on the left and on the right side are enforced to deform symmetrically with respect to a symmetry plane corresponding to the centre of the patch, in order to prevent globally asymmetric deformation.

Throughout this chapter, different compression rates  $\dot{u}/h$  are investigated. As a reference case *static* compression is analysed. For the dynamic investigations, the investigated strain rates are  $\dot{u}/h = 250 \text{ s}^{-1}$ ,  $\dot{u}/h = 1000 \text{ s}^{-1}$ , and  $\dot{u}/h = 4000 \text{ s}^{-1}$ . These rates will be called in the remainder of the chapter *slow rate compression* ( $\dot{u}/h = 250 \text{ s}^{-1}$ ), *medium rate compression* ( $\dot{u}/h = 1000 \text{ s}^{-1}$ ), and *fast rate compression* ( $\dot{u}/h = 4000 \text{ s}^{-1}$ ).

## 6.4. EFFECTS OF THE NUMBER OF UNIT CELLS

As a first investigation, using the boundary conditions described above, the effect of the number of unit cells within the patch is analysed. For this, unit cells of different size are assembled into patches of the same overall size, ensuring the same elastic tangent properties, as explained in Section 6.2 and shown in Figure 6.5. This scaling results in e.g. each individual unit cell in a  $2 \times 2$  patch to be twice as high and wide as each individual unit cell in a  $4 \times 4$  patch. The resulting changes in the thickness of the patch in the third dimension  $t$  are explicitly accounted for when calculating the stresses in Equations (6.3) and (6.4) and implicitly via the total mass  $m_{\text{patch}}$  when calculating the SEA in Equation (6.5).

### 6.4.1. RE-ENTRANT UNIT CELLS

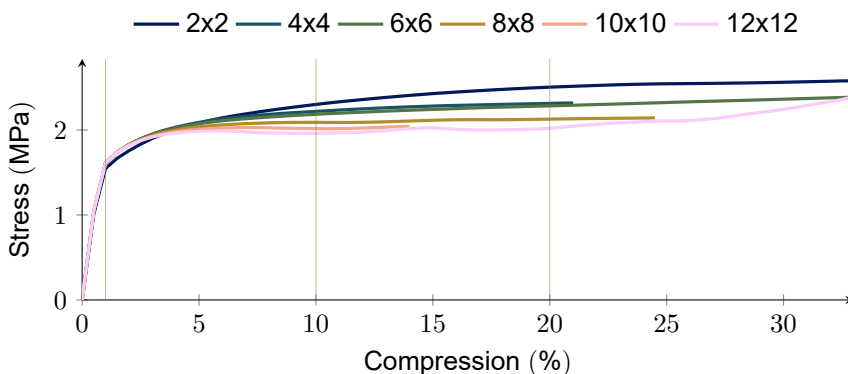


Figure 6.7.: Stress-strain curves of patches with a different number of re-entrant unit cells under *static* compression.

The behaviour of different re-entrant patches under *static* compression is investigated first. In [Figure 6.7](#) the *static* stress-strain curves at the strike face for different numbers of re-entrant unit cells under compression are shown. All investigated patches show onset of plasticity at 1 % compression. Prior to the onset of plasticity, there is some loss of stiffness corresponding with the re-orientation of beams and the subsequent shift in load-carrying capacity as discussed in [Chapter 4](#). After the onset of plasticity, as the load carrying capacity of the beams is limited at yield, nearly no stiffness remains upon further deformation. When the unit cell size is decreased, a more brittle response is observed. This phenomenon is attributed to the more pronounced localization resulting from the smaller unit cells, and thus in less material undergoing large deformations. The hardening in later stages of the response, most clearly seen for the  $12 \times 12$  patch, is an effect of contact within the unit cells.

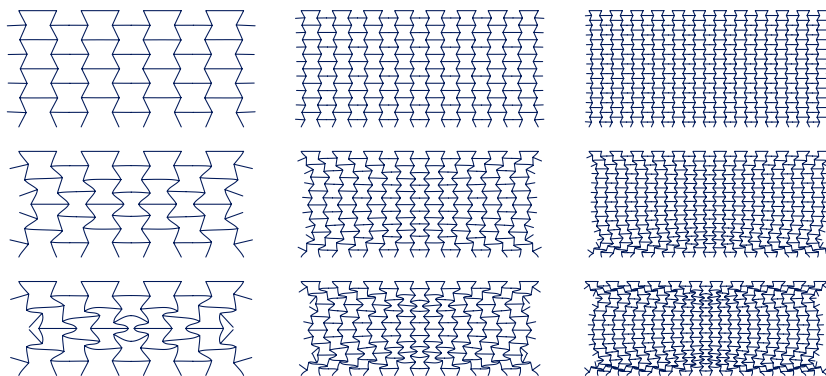


Figure 6.8.: Re-entrant  $4 \times 4$  (left),  $8 \times 8$  (centre), and  $12 \times 12$  (right) unit cell patches under *static* deformation at 1 %, 10 % and 20 % compression.

The deformation patterns in [Figure 6.8](#) support this observation. In this figure, the deformed configurations of  $4 \times 4$ ,  $8 \times 8$ , and  $12 \times 12$  unit cell patches are showcased for 1 %, 10 % and 20 % compression. These compression levels are indicated by vertical lines in [Figure 6.7](#) as well. Here, it can be seen, that 1 % compression coincides with the loss of stiffness due to plasticity. During the initial, mostly elastic deformation (depicted in the top row), the patches are deformed uniformly. At a deformation of 10 %, differences in deformation are visible: Whereas in the  $4 \times 4$  and the  $8 \times 8$  patch, on the left and in the centre, the deformation appears symmetric both along the vertical axis as well the horizontal axis, the  $12 \times 12$  patch on the right side of the figure shows a break of symmetry along the horizontal axis, i.e. the deformation of the top half does not mirror the deformation of the bottom half. This is due to a localization of deformation near the bottom edge. A stronger deformation within a single row of unit cells leads to a stronger loss in stiffness and a more brittle response. Once such a weak spot appears, the remaining deformation concentrates around it. In the last row of [Figure 6.8](#), the deformation state for 20 % compression is shown. Here, the localization is intensified and becomes visible for

the  $8 \times 8$  unit cell patch in the centre of the figure as well, whilst the  $4 \times 4$  patch on the left maintains both symmetries. All investigated patches suffer from loss of convergence in the global Newton-Raphson scheme at different stages of compression. The common cause of these numerical problems is the contact between free ends of beams at the left and right boundaries of the patch, as can be seen for example in the centre of the  $4 \times 4$  unit cell patch at both sides between the second and third unit cell.

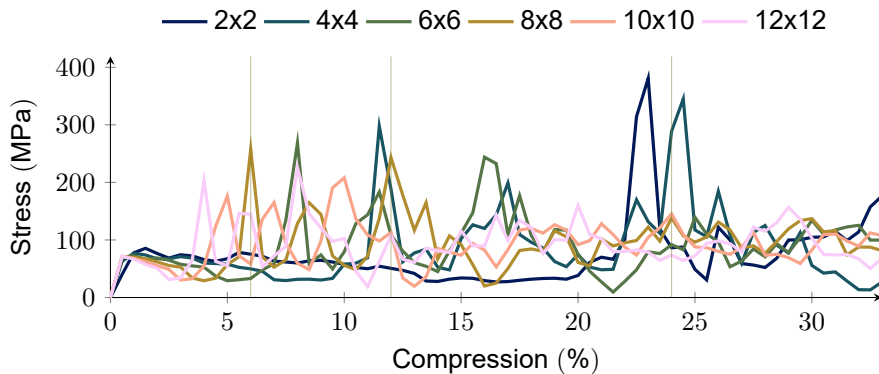


Figure 6.9.: Stress-strain curves of patches with a different number of re-entrant unit cells under *fast* rate compression.

For the investigations of the impact behaviour of architected metamaterials, the consideration of dynamic deformation is of crucial importance. To this end, the effects of different numbers of unit cells on the dynamic response of a patch are investigated as well. In Figure 6.9 the stress-strain curves measured at the strike face for *fast* rate compression are shown. For all patches, an initial rise in the stress can be observed, followed by a loss in stiffness, that is occurring earlier for smaller unit cells. Prior to the onset of plasticity at around 1 %, smaller unit cells show a more stiff response, attributed to differences in the distribution of inertia within the patches. After this, smaller unit cells show a more brittle behaviour, as already seen for the *static* case in Figure 6.7. For a better understanding of the dynamic behaviour of the different patches, again,  $4 \times 4$ ,  $8 \times 8$ , and  $12 \times 12$  unit cell patches are shown at 6 %, 12 % and 24 % compression in Figure 6.10. As can be seen in the higher stress levels in Figure 6.9 compared with Figure 6.7 and the concentration of the deformation near the moving boundary in the patches in Figure 6.10, the response is driven by inertia and not by the structural response. This is due to the fact that the accelerating forces are beyond the yield limit of the upper parts of the structure. These forces lead to a localized collapse of the structure near the strike face. The peaks observed throughout the stress-strain curves in Figure 6.9 put further emphasis on this observation. 6 % compression corresponds with the first peak for the  $8 \times 8$  unit cell patch, as indicated by the thin vertical line in Figure 6.9. At this compression level, it can be seen from Figure 6.10 that the first half unit cell is fully collapsed and the corresponding horizontal row of beams starts to come

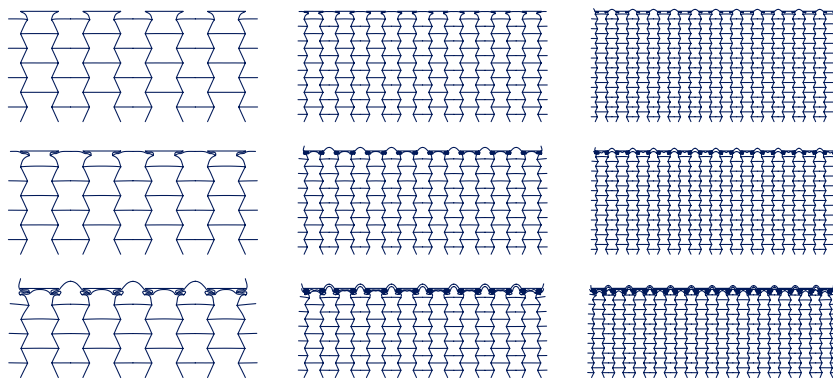


Figure 6.10.: Re-entrant  $4 \times 4$  (left),  $8 \times 8$  (centre), and  $12 \times 12$  (right) unit cell patches under *fast* rate deformation at 6 %, 12 % and 24 % compression.

into contact. The acceleration of this horizontal row of beams is the explanation for the increased stress experienced at the strike face. The size of half a unit cell in horizontal direction would correspond to 6.25 % of the length for an  $8 \times 8$  patch. The effect occurs already at lower compression levels due to the finite sized beams coming into contact already earlier. At 12 % compression, showcased in the centre row of Figure 6.10, first contact can be seen for the  $4 \times 4$  patch as well as contact with the second row of horizontal beams for the  $8 \times 8$  patch. This corresponds well with the peaks in Figure 6.9. This observation provides a rationale for the earlier occurrence of peaks in the stress response for a smaller unit cell size. After a nominal compression of 24 %, all deformation is concentrated at the top and the lower parts do not show any deformation. One should note here, that the bulging of the beams through the upper boundary is not an error, but a limitation of the employed boundary conditions only constraining the nodes at the top boundary in the undeformed configuration. The limitation is acceptable as the bulging elements are not causing numerical issues and are connected to the rest of the lattice. Furthermore, they are sufficiently far from the bottom boundary, which is the focus of the remaining investigations. The remaining stress-strain curves for *slow* and *medium* compression as well as the corresponding deformation patterns are shown in Appendix C.1.1.

#### 6.4.2. CHIRAL UNIT CELLS

Next to the re-entrant unit cell, the behaviour of patches from chiral unit cells is analysed. The *static* stress-strain curves are shown in Figure 6.11. Also for this architecture, in these curves the onset of plasticity can be seen at 1 %. Similar to the re-entrant patches in Figure 6.7, all structures initially show a hardening re-

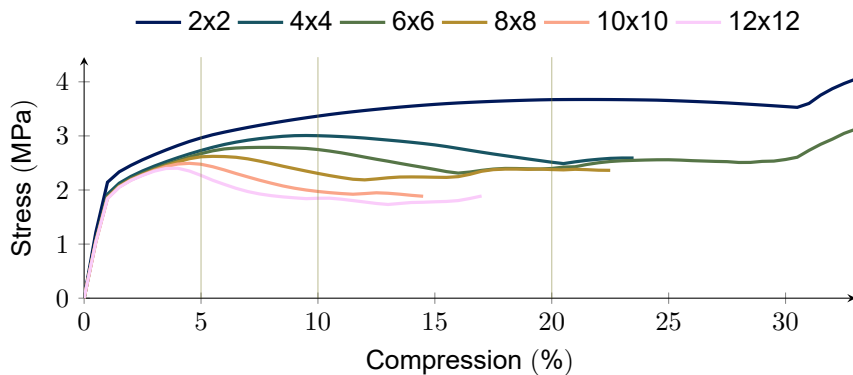


Figure 6.11.: Stress-strain curves of patches with a different number of chiral unit cells under *static* compression.

6

response. This hardening response is then followed by a softening response, which is more pronounced for smaller unit cells. This is consistent with earlier observed tendencies, that smaller unit cells lead to an earlier and stronger localization of the deformation.

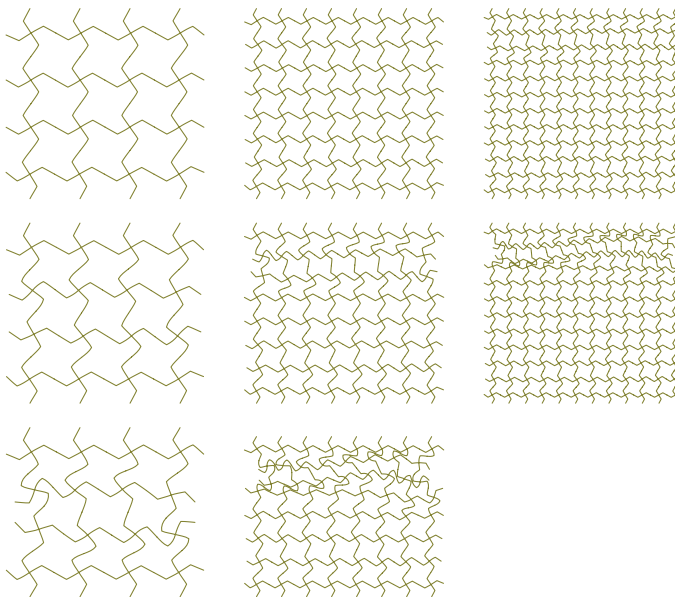


Figure 6.12.: Chiral  $4 \times 4$  (left),  $8 \times 8$  (centre), and  $12 \times 12$  (right) unit cell patches under *static* deformation at 5 %, 10 % and 20 % compression.

The deformed configurations for  $4 \times 4$ ,  $8 \times 8$ , and  $12 \times 12$  patches at 5 %, 10 % and 20 % are visualized in Figure 6.12. These compression levels are marked in Figure 6.11 by thin vertical lines. In the stress-strain curves, it can be seen, that at 5 % compression both the  $4 \times 4$  on the left and  $8 \times 8$  patches in the centre are still in the first hardening phase, whilst the  $12 \times 12$  patch on the right is already in the softening phase. Upon inspection of the deformation patterns, it can be seen, that the  $12 \times 12$  patch exhibits localizations of deformation (near the top of the patch), whilst the other two still showcase uniform deformation. At 10 % compression, the  $12 \times 12$  patch on the right side of the figure shows contact, leading to a slightly stiffer response. The  $8 \times 8$  patch in the centre has also entered the softening phase and showcases clearly localized deformation as well. The  $4 \times 4$  patch on the left is near the peak of its stress level and when examining the deformation patterns, the start of localized deformation can be seen as well. At the last investigated compression level of 20 %, the  $8 \times 8$  patch shows multiple points of internal contact, which corresponds to the global hardening of the patch. On the other hand, the  $4 \times 4$  patch shows no contact yet, which is consistent with the ongoing softening behaviour of the overall patch as seen in Figure 6.11. After further deformation, beams within the patch will come into contact, marking the transition from the softening phase to the re-hardening phase. It should be noted, that chiral patches show strong local asymmetries in their behaviour despite the enforced global symmetry, due to the rotating mechanism responsible for the negative Poisson effect. For the chiral unit cells, as is the case for the re-entrant ones, the static solution scheme suffers from loss of convergence after a larger number of beams or the free ends of beams come into contact.

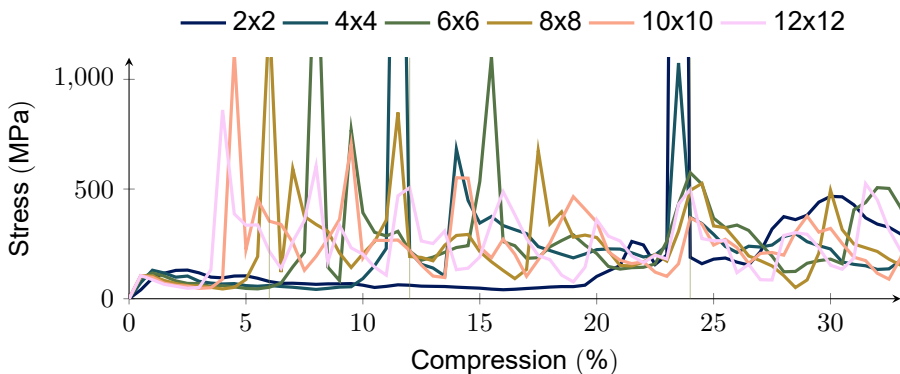


Figure 6.13.: Stress-strain curves of patches with a different number of chiral unit cells under *fast* rate compression.

The dynamic behaviour is investigated for the chiral unit cells as well and the resulting stress-strain curves for *fast* compression are shown in Figure 6.13. An initial maximum appears around the onset of plasticity at 1 % deformation. Here, as is the case for re-entrant patches, smaller unit cells show a stiffer response not seen in static deformation, attributed again to differences in the distribution of inertia

within the patches. Furthermore, smaller unit cells show a more brittle response after the first peak around 1 % compression, as seen earlier for the re-entrant unit cells in Figure 6.9, consistent with the *static* behaviour of both auxetic unit cells. Afterwards all investigated patches show further peaks, appearing later for larger unit cells, i.e. patches with a smaller number of unit cells. In order to understand

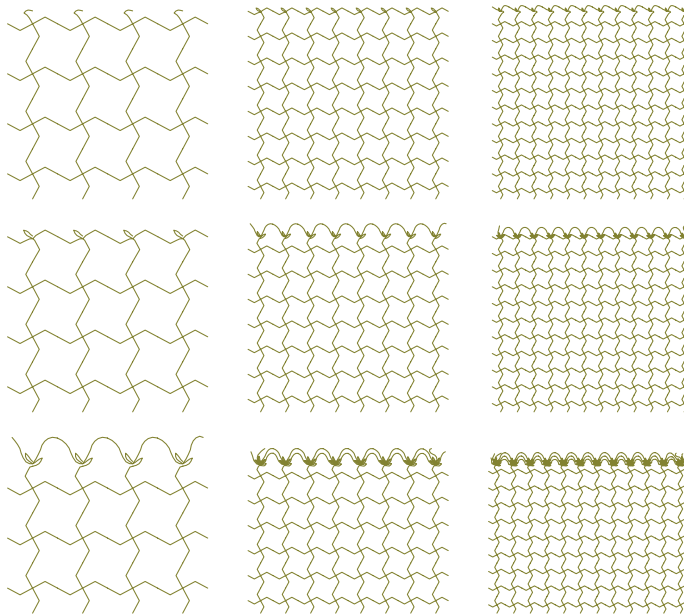


Figure 6.14.: Chiral  $4 \times 4$  (left),  $8 \times 8$  (centre), and  $12 \times 12$  (right) unit cell patches under fast rate deformation at 6 %, 12 % and 24 % compression.

the reason behind these peaks, the deformed patches are plotted for 6 %, 12 % and 24 % compression and shown in Figure 6.14. All patches show a clear localization of the deformation at the top and no deformation of the remaining parts of the structure. At 6 % deformation, for the  $8 \times 8$  patch, half a unit cell is compressed, and contact between the upper nodes as well as the next horizontal row of beams is achieved. The acceleration of these beams corresponds with a peak in the stress-strain curve seen in Figure 6.13. The same phenomenon can be seen in the  $4 \times 4$  patch at 12 % deformation, both in the deformation plots in Figure 6.14 and the stress-strain curve in Figure 6.13. The peaks are cut off in the figure for better visibility, but larger elements show peaks of higher magnitude, i.e. from the peak for  $12 \times 12$  unit cells at about 800 MPa the stress level rises over approximately 2000 MPa for  $6 \times 6$  unit cells to roughly 6000 MPa for the  $2 \times 2$  unit cell patch. These phenomena are similar to the ones observed in the re-entrant patch. Additional stress-strain curves for *slow* and *medium* compression as well as the corresponding deformation patterns are shown in Appendix C.1.2.

### 6.4.3. HONEYCOMB UNIT CELLS

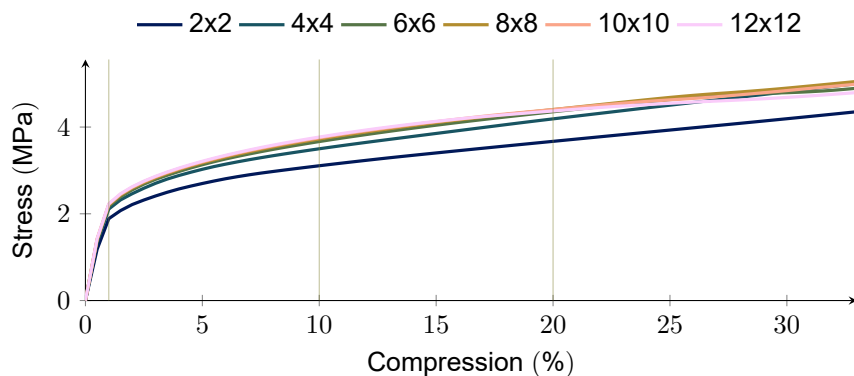


Figure 6.15.: Stress-strain curves of patches with a different number of honeycombs unit cells under *static* compression.

In order to make a comparison with the auxetic unit cells, regular honeycomb unit cell patches with a positive Poisson's ratio are investigated. The corresponding static stress-strain curves are shown in Figure 6.15. We observe the same kink in the curve at the onset of plasticity as for the patches with re-entrant and chiral unit cells. For smaller unit cells neither the reduction in the hardening response, observed for the re-entrant architecture, nor earlier softening, as for the chiral architecture, is observed. This is also confirmed in the deformation patterns

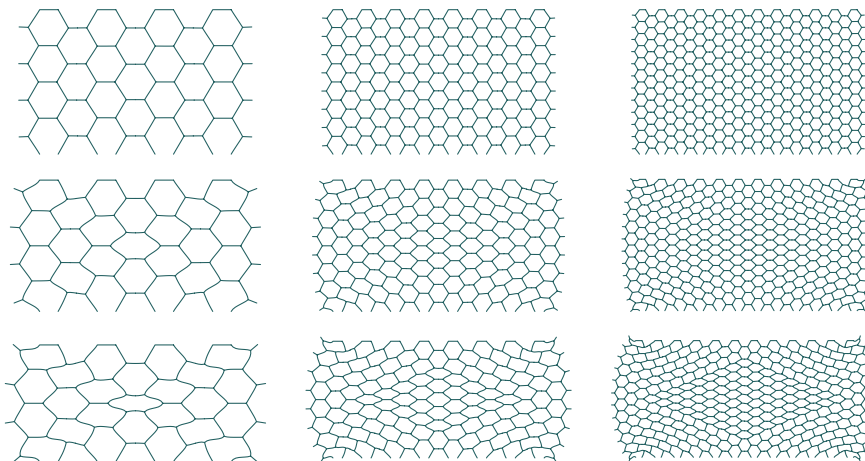


Figure 6.16.:  $4 \times 4$  (left),  $8 \times 8$  (centre), and  $12 \times 12$  (right) unit cell patches under static deformation at 1 %, 10 % and 20 % compression.

of  $4 \times 4$ ,  $8 \times 8$ , and  $12 \times 12$  unit cell patches in Figure 6.16. Global barrelling is clearly

visible for the  $8 \times 8$  and  $12 \times 12$  cases, in the centre and on the right side respectively. As the barrelling response is a global pattern we can, in Figure 6.15, observe a convergence of the response already at smaller numbers of unit cells compared to the two investigated auxetic structures in Figures 6.7 and 6.11, in which localized deformation is occurring.

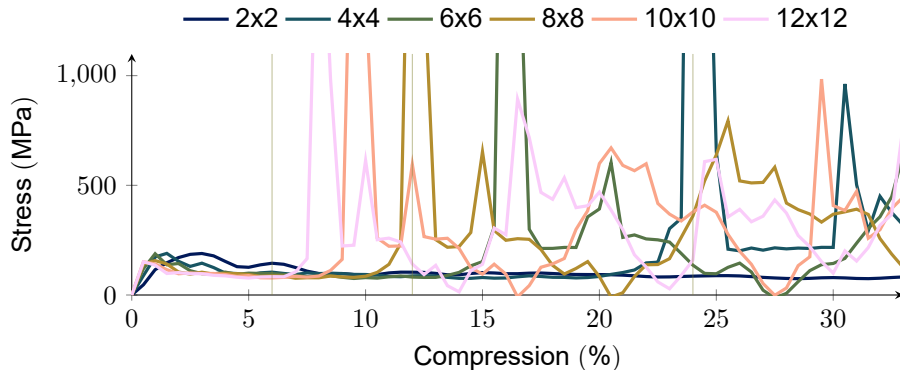
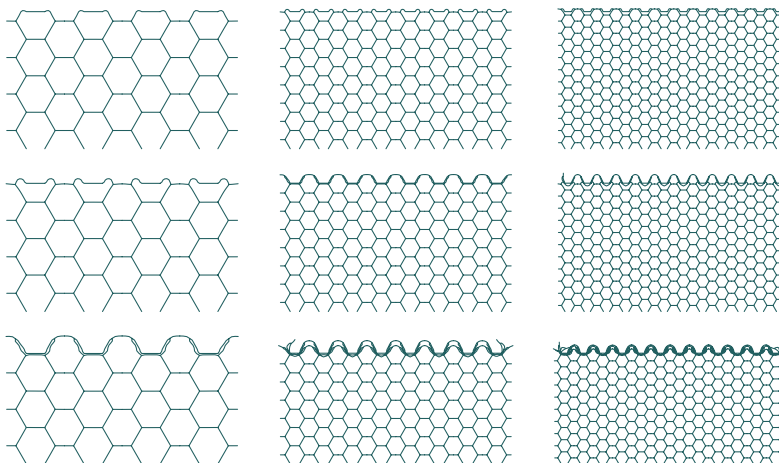


Figure 6.17.: Stress-strain curves of patches with a different number of honeycombs unit cells under *fast* rate compression.

For the dynamic investigation of different honeycomb patches, again the stress-strain curves under *fast* compression are examined, as shown in Figure 6.17. The initial response, prior to the onset of plasticity at 1% shows, opposed to the observations in static deformation, a stiffer response for smaller unit cells, motivated again by differences in the distribution of inertia for different sizes of unit cells. After this onset of plasticity, a more brittle response is observed for smaller unit cells, in agreement with the observations made for both auxetic architectures. In the stress-strain curves, peaks are seen at lower compression for smaller unit cells and at higher compression levels for larger unit cells as already seen in the responses of the two auxetic architectures. Nevertheless, fewer peaks are observed than for the two auxetic architectures. To illustrate the reason behind this, in Figure 6.18, the deformed shapes of  $4 \times 4$ ,  $8 \times 8$ , and  $12 \times 12$  unit cell patches at compression levels of 6%, 12% and 24% are shown. Whereas both auxetic structures show peaks in their stress response at a compression level of 6%, this peak is not seen in the response of the non-auxetic patches. In the deformed shapes in Figure 6.18, it can be seen, that none of the patches show any contact yet, as the beams at the upper boundary do not come into contact with the beams at half a unit cell height due to the convex structure of the honeycomb architecture. For this same reason, a full unit cell of compression is needed for the non-auxetic honeycomb structures to experience contact. At this point, shown in the centre row at 12% compression for the  $8 \times 8$  patch in the central columns and in the bottom row at 24% compression for the  $4 \times 4$  patch on the left side, contact is seen. This corresponds with the stress peaks in Figure 6.17, where the first peak for the  $8 \times 8$  patch occurs at 12% and the first peak of the  $4 \times 4$  patch at 24%. These values are again marked by



6

Figure 6.18.:  $4 \times 4$  (left),  $8 \times 8$  (centre), and  $12 \times 12$  (right) unit cell patches under fast rate deformation at 6 %, 12 % and 24 % compression.

thin vertical lines. For better readability of the graph, the peaks are again cut off but are rising from about 2000 MPa for the  $12 \times 12$  patch up to about 4000 MPa for the  $4 \times 4$  patch. The  $2 \times 2$  unit cell patch does not show a peak in the first 33 % compression. The other stress-strain curves for *slow* and *medium* compression as well as the corresponding deformation patterns are shown in [Appendix C.1.3](#).

#### 6.4.4. COMPARISON OF UNIT CELLS

Balancing the convergence behaviour in the *static* case, the dynamic behaviour and the computational cost, it is decided to take  $8 \times 8$  unit cell patches as representative. Thus,  $8 \times 8$  patches are used in the dynamic investigations in [Sections 6.5](#) and [6.6](#) on force transmission and energy distribution.

A first comparison between  $8 \times 8$  patches using the three architectures is shown in [Figure 6.19](#). In this figure, the stress-strain curves are shown for the investigated rates. During *static* compression, both investigated auxetic architectures, re-entrant and chiral, show a similar level of stress, whereas the honeycomb architecture not only shows a higher overall level, but also a significant hardening throughout the compression. This difference is explained by the fundamentally different deformation modes in the patches: localized collapse in the case of the re-entrant and chiral architectures versus global barrelling in the case of the honeycomb. Also for *slow* compression, the honeycomb shows higher stress levels at the strike face compared to the auxetic architectures. As the *static* deformation patterns are less relevant at higher speeds, in the *medium* rate, peaks begin to appear, as discussed above. Here the re-entrant structure remains at a low stress level, and both the chiral and honeycomb patches show a large fluctuation of similar magnitude. This is even further emphasized for the *fast* rate, where the chiral and honeycomb structures

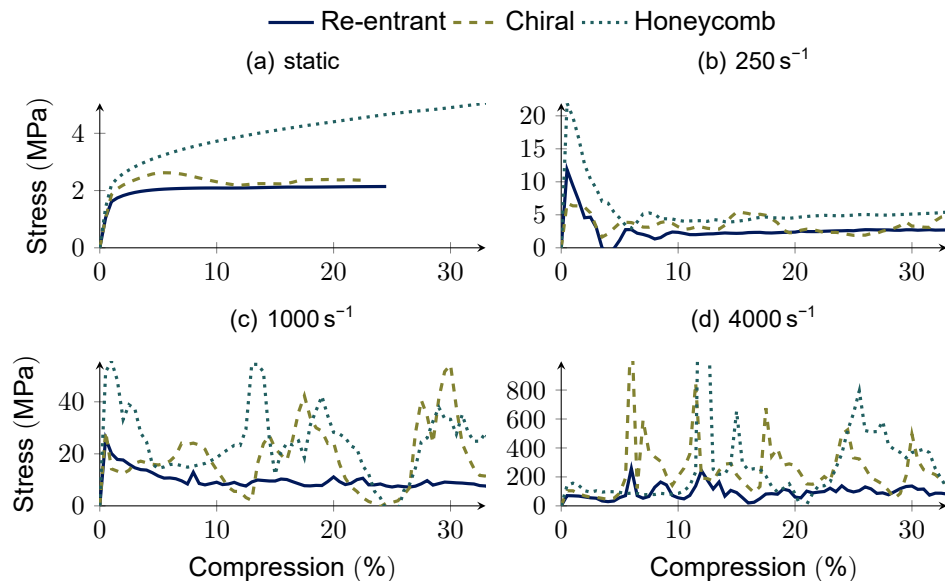


Figure 6.19.: Comparison of the stress-strain curves at the strike face for  $8 \times 8$  patches of different architectures for the four investigated strain rates.

again exhibit peaks of comparable magnitude, with the re-entrant patch remaining at a lower stress level, despite a few distinct peaks. From this it can be concluded that in all loading scenarios, the honeycomb structure outperforms the auxetic ones regarding the stress needed to compress the patch to the same level. For all investigated architectures, whilst the *static* deformation modes differ and only the auxetic patches show localized deformation, during *fast* compression, the response is dominated by inertial effects, leading to a more brittle behaviour for smaller unit cells of all architectures, as discussed in the previous sections. Dynamic effects within the patches will be investigated in more detail in the following.

## 6.5. EFFECTS OF STRAIN RATE ON THE FORCE TRANSMISSION

In order to assess the efficacy of a protection concept, one not only needs to assess the forces exhibited at the strike face, but also the transmission of those forces through the protective layer, as was done in [Chapter 5](#) for an emulated impact event with focus on the local distribution of these forces. The measurement of the forces acting on the strike face during an impact event has little information regarding the forces acting on the back face, thus the next investigation focuses on the transmission of forces from the strike face to the back face.

### 6.5.1. RE-ENTRANT PATCH

6

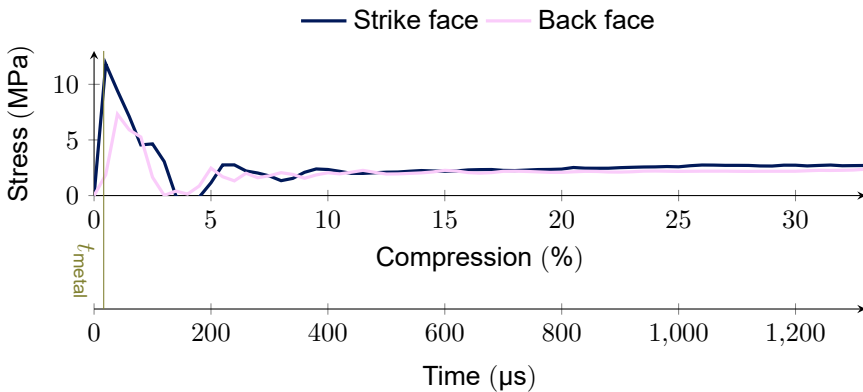


Figure 6.20.: Comparison of the stress on the strike face and the back face under *slow* compression for an  $8 \times 8$  re-entrant patch.

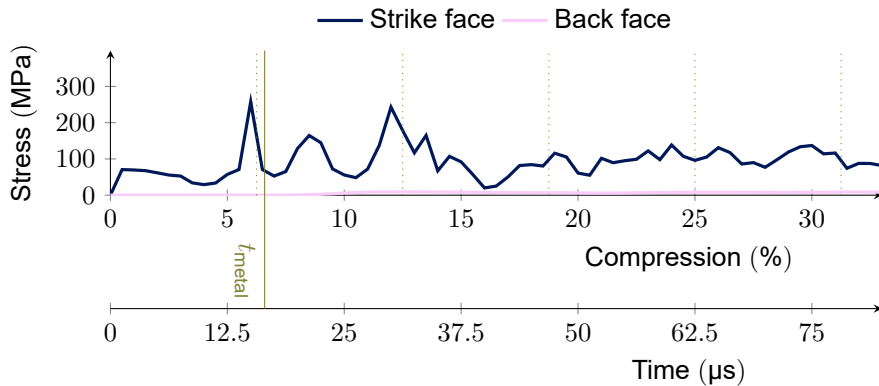
To investigate this transmission of the force through the protective layer, a first comparison is done between the stresses on the strike face and the back face for the *slow* rate compression. The corresponding stresses, both on the strike face (the top boundary in Figure 6.6) and on the back face (the bottom boundary in Figure 6.6), are shown over the compression in Figure 6.20. An additional abscissa is given depicting the time corresponding to the amount of compression at this strain rate. The stress on the back face follows the stress on the strike face with a delay, and both finally converge towards the same stress level. The magnitude of the delay, especially in the first rise of the stress, can be explained by the time needed for the elastic pressure wave to travel through the patch. Given the material parameters laid out in Section 6.3, the pressure wave speed through a beam is

$$c_{\text{metal}} = \sqrt{\frac{210 \text{ GPa}}{7850 \text{ kg m}^{-3}}} \approx 5172 \text{ m s}^{-1}. \quad (6.6)$$

Together with the height of the patch of  $h = 77.7 \text{ mm}$  and the angle between the beams and the vertical of  $\alpha = 24.4^\circ$ , the time required for the pressure wave to reach the bottom equals

$$t_{\text{metal}} = \frac{h / \cos(\alpha)}{c_{\text{metal}}} \approx 16.5 \mu\text{s}. \quad (6.7)$$

This time is marked in Figure 6.20 with a thin vertical line and corresponds with the first rise in stress being recorded at the back face.



6

Figure 6.21.: Comparison of the stress on the strike face and the back face under fast compression for an  $8 \times 8$  re-entrant patch.

The behaviour of the patch under *fast* rate compression is then investigated, and the resulting stresses recorded at the strike face and the back face are shown in Figure 6.21. The delay in the stress on the back face is again visible and corresponds with the time required for the stress wave through the metal  $t_{\text{metal}}$ . In this graph, the peaks in the stresses on the strike face at intervals of 6.25 %, corresponding to half the height of a unit cell, as discussed in Section 6.4 can be seen as well.

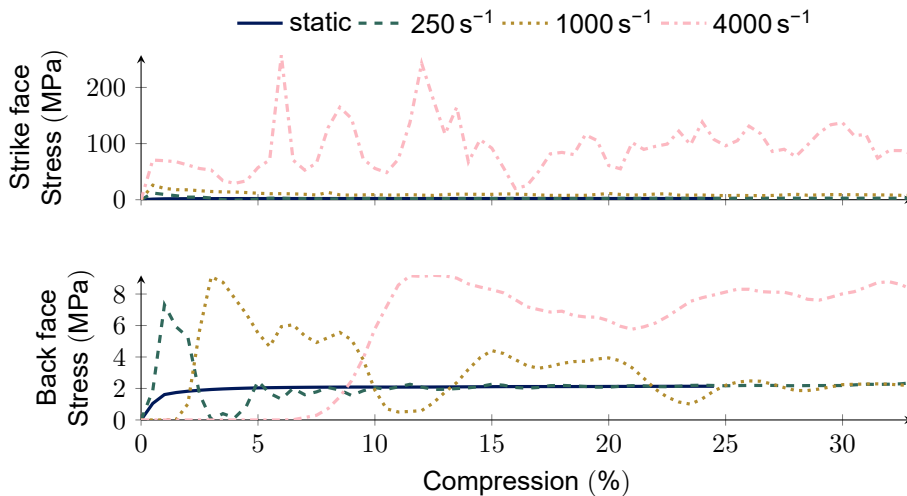


Figure 6.22.: Stresses on both faces for the re-entrant patch for different compression rates.

To compare different rates, in Figure 6.22, the stresses on both faces are plotted for the investigated compression rates. On the strike face, we can observe an increase of the stresses needed to compress the patch at the given rates. This increase is moderate for *slow* and *medium* rate compression when compared to *static* compression, but increases significantly for *fast* rate compression. On the back face, it is clearly observed, that the stresses for both *slow* and *medium* rate compression approach *static* compression stress, despite the increase seen on the strike face. For the *fast* compression case, this cannot be observed. The increase seen here between the different compression rates is however small, when compared to the increase in stresses on the strike face, leading to the assumption, that the stress transmitted to the back face, after an initial peak, is in a first approximation independent of the compression rate. These initial peaks show similar magnitudes irrespective of the compression rate. The stresses transmitted to the back face are reduced when compared to the stress experienced at the strike face. This is mostly due to an increase in the dynamic stresses at the strike face, whilst the stresses at the back face have about the same magnitude. The mechanisms of dissipation of these forces will be discussed in Section 6.6. Plots comparing the stresses at the strike face and the back face for *static* and *medium* rate compression can be found in Appendix C.2.1.

### 6.5.2. CHIRAL PATCH

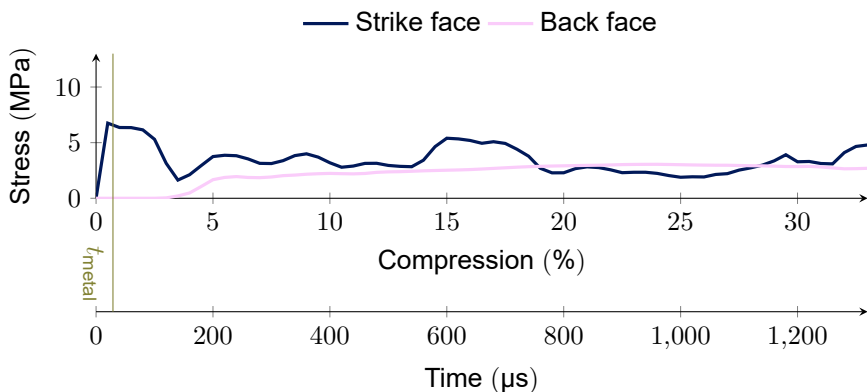


Figure 6.23.: Comparison of the stress on the strike face and the back face under *slow* compression for an  $8 \times 8$  chiral patch.

Next to the re-entrant architecture also the dynamic effects in the chiral architecture are investigated. The stresses on both faces for *slow* compression are shown in Figure 6.23. In this figure, the stresses are plotted over both the compressive strain, and the corresponding time. As for the re-entrant case, the theoretical time needed for a pressure wave travelling through a beam  $t_{\text{metal}} \approx 28.9 \mu\text{s}$  is indicated by a vertical line. This time is different from the re-entrant patch due to a different geometry

(more explanation given in Appendix C.2.2). It can be seen in Figure 6.23, that the pressure wave reaches the bottom significantly later than would be expected by a wave travelling unhindered through a metal beam. This is attributed to the impedance jumps at the sharp kinks in the chiral unit cell, leading to partial reflection and conversion from pressure to shear waves. Similar to the re-entrant patch, also for the chiral patch, the stress on both faces converge towards the same value. This convergence is slower than for the re-entrant patch, which is consistent with the longer times required for the stress waves to transverse the patch.

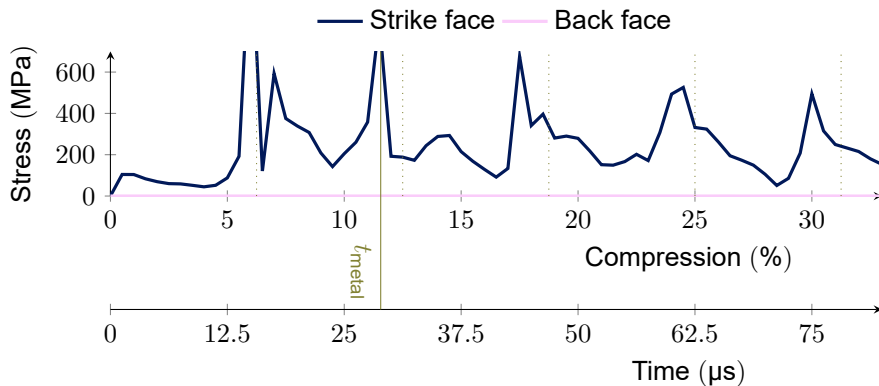


Figure 6.24.: Comparison of the stress on the strike face and the back face under fast compression for an  $8 \times 8$  chiral patch (the values of the peaks outside the figure axis are approximately 1250 MPa at 6 % compression and approximately 800 MPa at 11.5 % compression).

In Figure 6.24 the stresses for fast compression of the chiral patch are depicted. The peaks can again be attributed to the acceleration of horizontal rows of beams at half unit cells. A delay of the pressure waves reaching the bottom of the patch, as discussed above for slow compression, can be seen again for the fast compression case. The point where the stress on the back face starts to be observable is well beyond the plotted range of 82.5  $\mu$ s. Prior to this, stress on the back face is insignificant at well below 1 MPa.

In order to get a better estimation of the effect different strain rates have on the response of the chiral patch, the stresses on both faces for different strain rates are compared in Figure 6.25. As is the case for the re-entrant patch, the chiral patches show an increase of stress needed for the compression of the patch at the strike face with an increase in rate. This increase is moderate for slow and medium rate compression, and again significantly more pronounced for the fast rate. The stresses on the back face are less evidently approaching a common value as is the case for the re-entrant patch. Although the compression at static, slow, and medium rates seem to converge towards the same value, a longer time interval is needed in order to assess this effect in more detail. This longer time interval is also needed to be able to give an indication on the effects of the fast compression onto

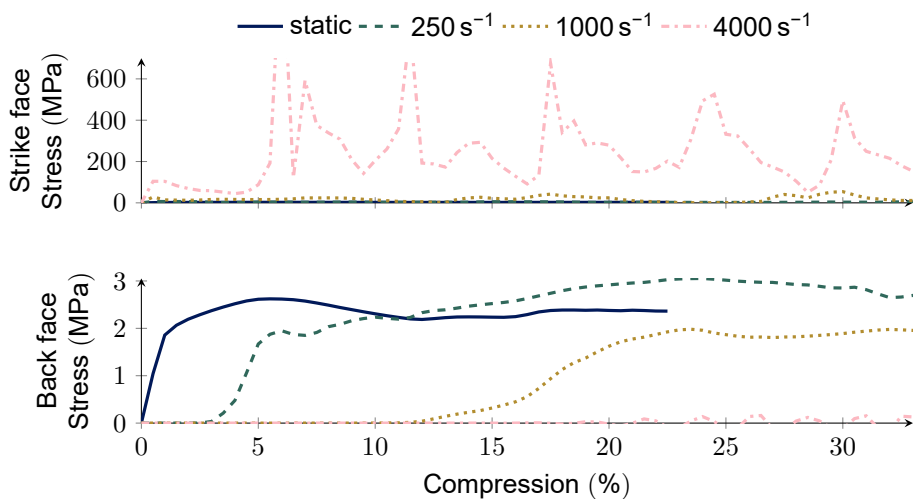


Figure 6.25.: Stresses on both faces for the chiral patch for different compression rates.

the stresses seen at the back face, as the pressure waves through the material need more time to reach the back face of the patch. This longer time interval relates to higher compression, which results in densification and thus a response more akin to a solid material and no longer a heterogeneous metamaterial. At this stage of densification, the formulation of the contact stiffness reaches a limit as well, and a more sophisticated modelling of the contact would be required. It is thus opted not to conduct these simulations. Plots comparing the stresses at the strike face and the back face for *static* and *medium* rate compression can be found in [Appendix C.2.2](#).

### 6.5.3. HONEYCOMB PATCH

The behaviour of non-auxetic honeycombs under dynamic compression is investigated as well. The stresses on the strike face and back face for the honeycomb patches, at *slow* rate compression, can be seen in [Figure 6.26](#). The time for the pressure wave to propagate through the metal  $t_{\text{metal}} \approx 32.9 \mu\text{s}$  is indicated by a vertical line (see [Appendix C.2.3](#)). The general behaviour of the honeycomb unit cell patch, does not deviate from the auxetic unit cell patches. The time delay for the stresses at the back face to rise roughly corresponds with the metal wave speed. Later on stresses on both the front and strike face converge towards a common plateau.

The behaviour of the honeycomb patch for the *fast* rate compression, as seen in [Figure 6.27](#), shows again lower stresses on the back face compared to the stresses on the strike face. This is consistent with the observations for the auxetic patches.

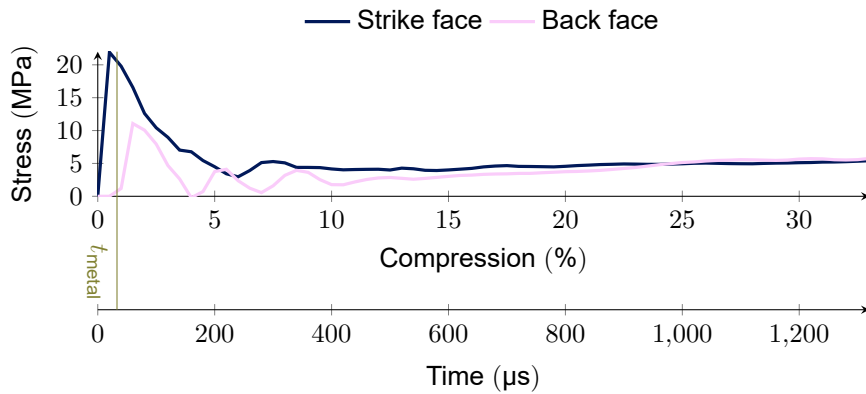


Figure 6.26.: Comparison of the stress on the strike face and the back face under slow compression for an  $8 \times 8$  honeycomb patch.

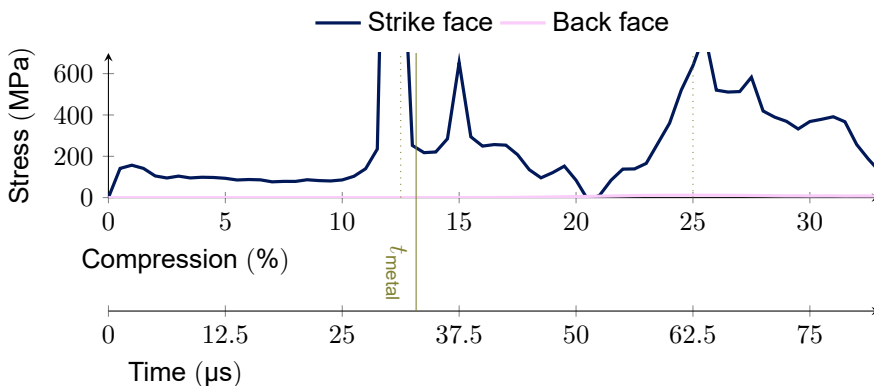


Figure 6.27.: Comparison of the stress on the strike face and the back face under fast compression for an  $8 \times 8$  honeycomb patch (the values of the peaks outside the figure axis are approximately 2500 MPa at 12 % compression and approximately 900 MPa at 25 % compression).

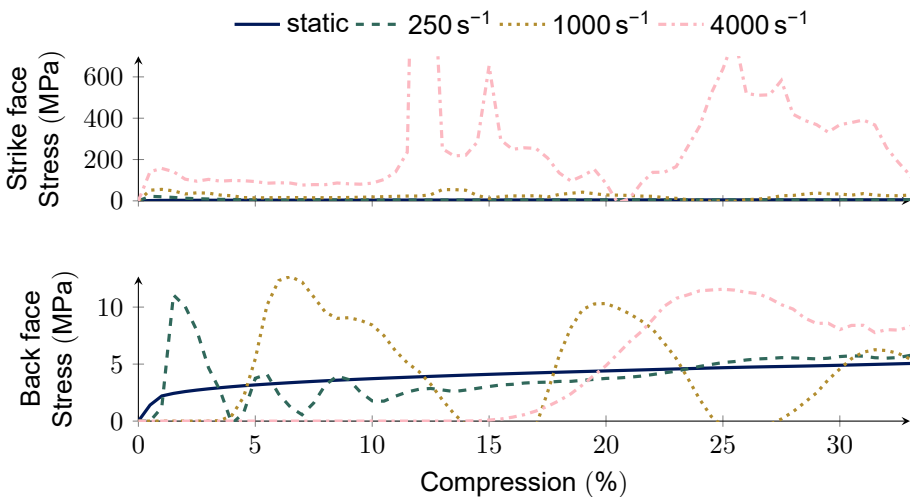


Figure 6.28.: Stresses on both faces for the honeycomb patch for different compression rates.

For a better understanding of the strain rate effect in the non-auxetic patch, the stresses on both faces are shown for the different investigated strain rates in Figure 6.28. As with the auxetic patches, we can see the stress on the back face for *slow* compression approaching the stress level for the *static* compression. The stress for *medium* compression shows large oscillations around the same level as well. Finally, at *fast* compression, the stress appears to be higher, which is in agreement with the observations made for the auxetic unit cells. This increase is however negligible when compared to the increase in stress at the strike face. A much higher increase in stress on the strike face is needed to compress the patch at the *fast* rate compared to the *medium*, *slow*, and *static* compression cases, which is seen in the auxetic patches as well. Plots comparing the stresses at the strike face and the back face for *static* and *medium* rate compression can be found in Appendix C.2.3.

#### 6.5.4. COMPARISON OF PATCHES

Summarizing the findings of this section, two observations can be made: Firstly, that the speed of the pressure waves through the metal is a lower bound for the stress to reach the back face. This theoretical phenomenon can also be observed in the simulations. This lower bound is approached when more straight beams and fewer kinks and joints are present within an architecture, resulting the chiral patch in a significant delay after the theoretical lower limit. Secondly, the stress amplitudes experienced at the back face appear to be largely unaffected by the strain rate. The peak stresses experienced in all investigated rates can be regarded as equivalent, and the final, constant stress level approaches the static compression

value for all investigated structures. However, this is only a first approximation; a full understanding of the impact protection effect of the different patches requires the consideration of the force-time record and subsequent effects on the protected material.

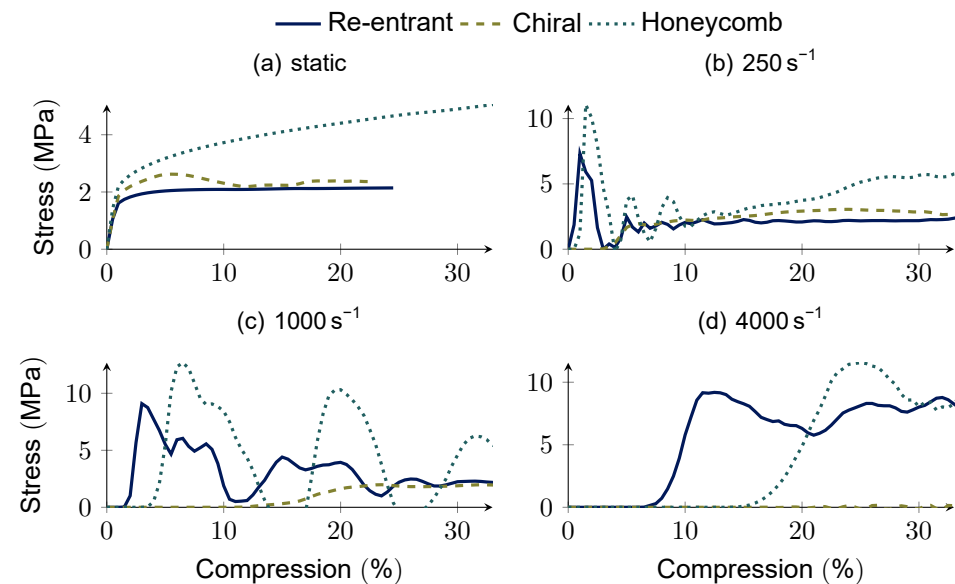


Figure 6.29.: Comparison of the stresses at the back face for  $8 \times 8$  patches of different architectures for the four investigated strain rates.

Both observations can also be seen by comparing the stress curves at the back face of the three patches in Figure 6.29. In this figure, the first effect is clearly observable as the rise in stress level appears later for patches with less straight connections between the top and the bottom. For instance, both the re-entrant and the honeycomb unit cell can be considered. The beams of the re-entrant patch are  $24.4^\circ$  off the vertical, whereas the beams for the honeycomb patch are  $29.7^\circ$  off, meaning the re-entrant patch offers a more straight vertical line for the pressure waves to the bottom compared to the honeycomb patch. The angle is however not the only factor for the time of the waves reaching the back face, as can be seen by the much later rise in stress for the chiral patch, of which the beams are only  $28.1^\circ$  off the vertical, but exhibit more kinks and joints when compared to the other two architectures. The chiral architecture contains beams meeting in  $90^\circ$  angles at their joints, amplifying this effect. Comparing the stress levels at the back face between the architectures, *static* compression shows the same graph as the strike face, resulting in Figure 6.29a being identical to Figure 6.19a. Considering higher compression rates, the chiral architecture appears to show the lowest stress levels at the back face, despite showing similarly high stress levels at the strike face compared to the honeycomb structure. This observation is based on the *slow and medium*

compression rates, as in the *fast* compression rate, the stress does not reach the back face for the chiral patch within the investigated time, however a qualitatively similar result is to be expected. These results indicate the chiral architecture as a good candidate for impact mitigation.

## 6.6. LOCAL ENERGY DISTRIBUTIONS

6

In order to facilitate a more thorough understanding of the mechanisms exhibited in the previous section, the SEA, as defined by Equation (6.5) spent on compression of the patches and its subsequent distribution into various components of energy throughout the patches is analysed. For the present analyses, the global specific energy is split into elastic potential energy, inelastic dissipated energy, and kinetic energy. The spatial distribution of the elastic, dissipated, and kinetic energy measures over the two directions of the patch, based on the nodal energy levels as explained in Section 6.3, will be analysed as well.

### 6.6.1. RE-ENTRANT PATCH

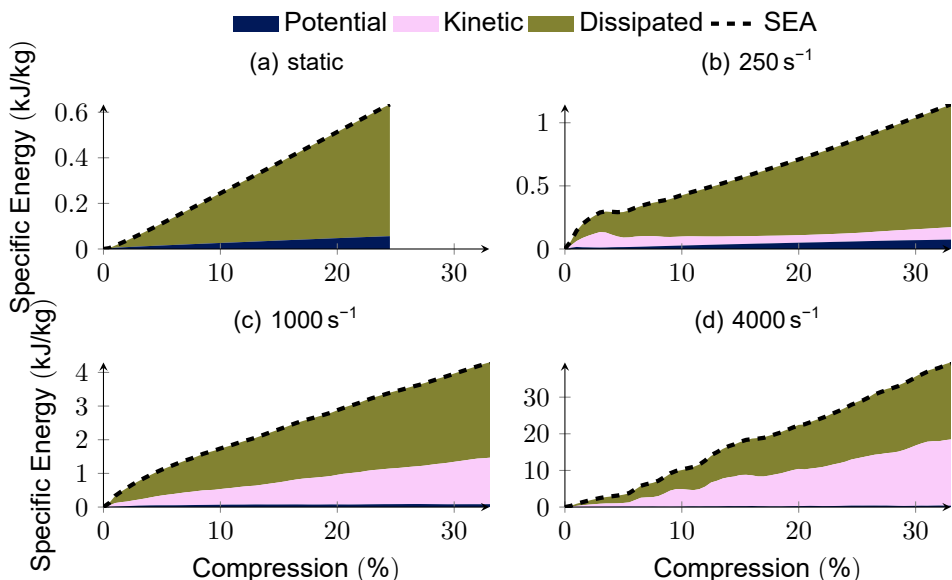


Figure 6.30.: Distribution of the SEA into different types of energy for the  $8 \times 8$  re-entrant patches at different strain rates.

The first comparison is the distribution of energy in the patch at different compression rates shown in Figure 6.30 for the re-entrant patch. In Figure 6.30a, static deformation is shown. At around 1 %, plastic deformation starts to occur, which coincides with the loss in stiffness seen in Figure 6.7. During the remainder of the analysis, the majority of the SEA put into the system is dissipated through plastic deformation, and only a minor increase in elastically stored potential energy can be observed. This increase can be related to the hardening present in the material model. In Figure 6.30b, the distribution of energy for slow compression is shown. The ratio between dissipated and potential energy remains roughly the same and the kinetic energy contributes only a minor part to the total SEA spent on compressing the material. In Figure 6.30c, the distribution of energy in the medium compression scenario is shown. While the dissipated energy is still the dominant form of energy present in the system, the amount of kinetic energy increases whilst the potential energy vanishes. This effect is visible in a more pronounced way in Figure 6.30d, showing both contributions of the kinetic and dissipated energy being at similar levels. Note, that the force peaks observed in Figure 6.21, can be seen in the energy plots as well. At the half unit cell points—at multiples of 6.25 %—the kinetic energy shows a sharp increase.

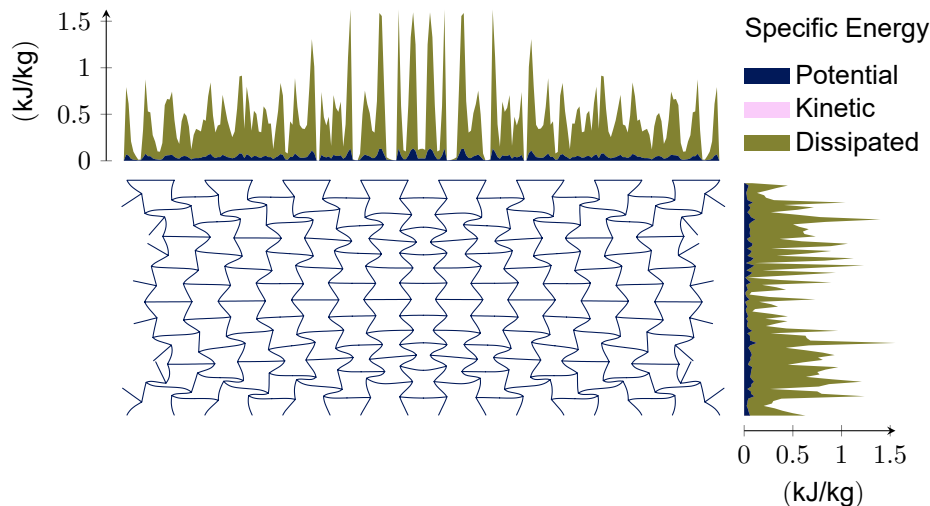


Figure 6.31.: Local distribution of energy at 20 % compression for *static* compression of the  $8 \times 8$  re-entrant patch.

Next to the distribution of energy for different physical mechanisms, the distribution of energy across the lattice structure is investigated. In Figure 6.31, the deformation after 20 % *static* compression is depicted with marginal distributions of the energy density split into the different physical mechanisms shown at the top

and the right of the patch. While the symmetry between the left and the right side remains intact, the top-bottom symmetry is broken by the more localized deformation near the bottom. The plastic nature of this collapse is emphasized by a higher specific dissipated energy near the bottom of the patch.

6

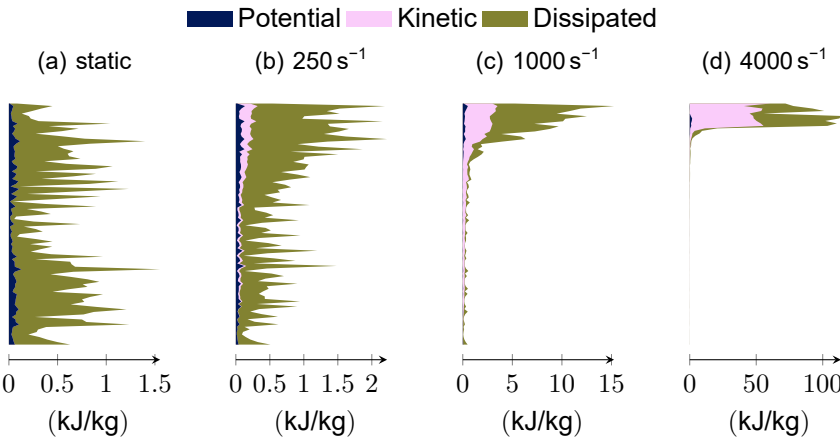


Figure 6.32.: Vertical distribution of energy at 20 % compression for all investigated compression rates in the  $8 \times 8$  re-entrant patch.

In Figure 6.32 the vertical distribution of the absorbed energy is shown for the four investigated rates. Comparing the *static* results to the *slow* rate compression case, in Figures 6.32a and 6.32b respectively, confirms the observation from Figure 6.30, that the dissipated energy is responsible for the majority of the SEA needed to compress the patch. Only a minor portion of the SEA is stored in potential energy, and at *slow* compression, the kinetic energy contributions are of course comparatively small. A shift of the energy distributions towards the strike face at the top of the patch is however observed. This shift in the distributions can be seen more pronounced in Figure 6.32c for the *medium* rate, where the dissipated energy still takes up the majority of SEA, as discussed above. At *medium* compression, although the bulk of the energy is dissipated near the top, still a significant part of the energy is present in the lower parts of the patch. This is no longer the case for the *fast* compression rate seen in Figure 6.32d. For this rate, the amounts of energy seen at the lower parts of the structure appear negligible, and the energy distributions show a clear increase in the relative share of kinetic energy, which is in agreement with the observations from Figure 6.30. This negligible amount of energy in the lower parts of the structure is in agreement with the deformation patterns shown in Figure 6.10. As discussed above, the deformations remain small in the lower parts of the patch at this *fast* rate, as also can be seen by the lack of lateral contraction at the boundaries, that would be expected from the negative Poisson's ratio of this structure, resulting in negligible amounts of energy in the lower parts of the patch.

### 6.6.2. CHIRAL PATCH

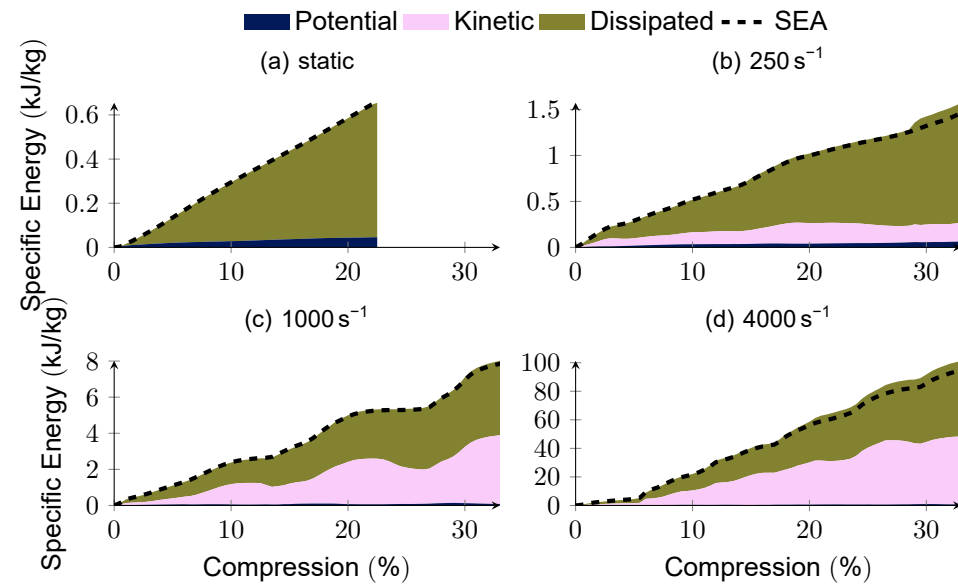


Figure 6.33.: Distribution of the SEA into different types of energy for the  $8 \times 8$  chiral patches at different strain rates.

The energy distribution in the chiral patch under different deformation rate is analysed in the same manner. In Figure 6.33, the distribution of the SEA in potential, kinetic, and dissipated energy is shown for different rates. The observations made for the re-entrant patch hold for the chiral patch as well. At *static* deformation, the majority of the SEA spent on compressing the material is dissipated throughout the deformation and only a minor increase in potential energy due to hardening of the material can be seen. At higher strain rates, the total SEA increased, as well as the share of kinetic energy. The share of kinetic energy at the *medium* rate is already half of the total energy, whereas for the re-entrant patch, this only happens at the *fast* rate, indicating an increased rate sensitivity of the chiral lattice. The higher sum of the different forms of specific internal energy compared to the externally computed SEA seen in Figures 6.33b and 6.33d is due to interpenetration of singular beams, that lead to divergence in the *static* case (Figure 6.33b) and represent an unphysical source of energy in the dynamic simulations. Since this effect is small and does not influence the global behaviour of the lattice, it is deemed acceptable.

The strain rate sensitivity of the chiral patch, can also be seen when comparing the vertical distributions of energy in Figure 6.34. In this figure, the vertical distribution of energy throughout the patch is plotted for the four investigated rates. In Figures 6.34c and 6.34d, depicting the *medium* and *fast* rate compression, the complete concentration of energy at the top is shown. This is consistent with the

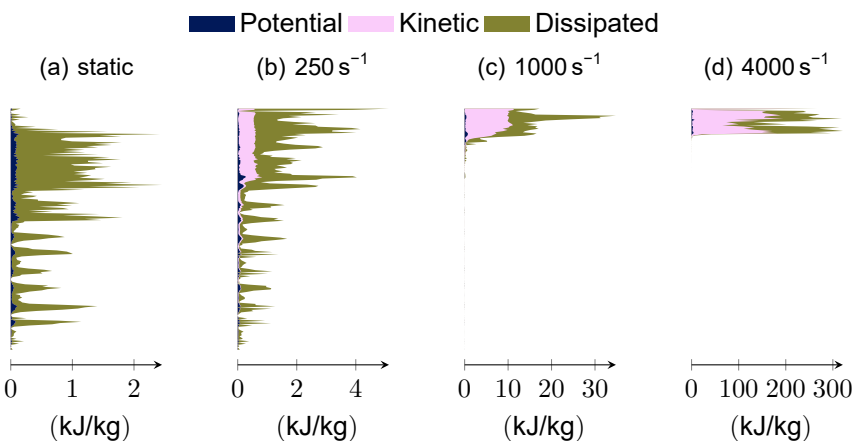


Figure 6.34.: Vertical distribution of energy at 20 % compression for all investigated compression rates in the  $8 \times 8$  chiral patch.

observations made in Figure 6.33 and further emphasizes the increased strain rate sensitivity of the chiral architecture when compared to the re-entrant architecture. The chiral patch at *low* rate compression, shows a similar trend compared to the re-entrant patch. A small shift of energy towards the top can be observed, with the energy in lower parts being more uniformly distributed. A similar shift of energy towards the top can be observed in *static* compression in Figure 6.34a, this is however explained by the localized deformation in singular rows of unit cells, as shown in Figure 6.12, where the deformation corresponding to this distribution is shown for the  $8 \times 8$  patch at 20 % compression. The localization of deformation around the unit cells corresponds with a significant increase in energy dissipated and only a minor increase in elastically stored energy, as shown in Figure 6.34a.

### 6.6.3. HONEYCOMB PATCH

Finally, the distribution of energy in the honeycomb patch is investigated. In Figure 6.35, the different forms of energy are again compared for *static*, *slow*, *medium* and *fast* rates of compression. Here, the phenomena observed in the re-entrant and chiral patch, can be seen as well. The majority of the energy is dissipated and the fraction of kinetic energy rises with increasing compression rate. Two observations are noteworthy: Firstly, the peaks in force on the strike face observed at *fast* compression, seen in Figure 6.27, correspond with the sudden rise of kinetic energy in Figure 6.35d as well. In Figure 6.18 the acceleration of horizontal bars is illustrated, leading to both force peaks and a fast rise in kinetic energy. Secondly, at *medium* rate compression, the kinetic energy takes less than half of the energy in the patch, resembling the behaviour of the re-entrant patch, distinct from the chiral patch. This is seen by the vertical distributions of energy in Figure 6.36 as well. Here, at *medium* rate, the energies are shifted to the upper boundary, but still a significant amount of

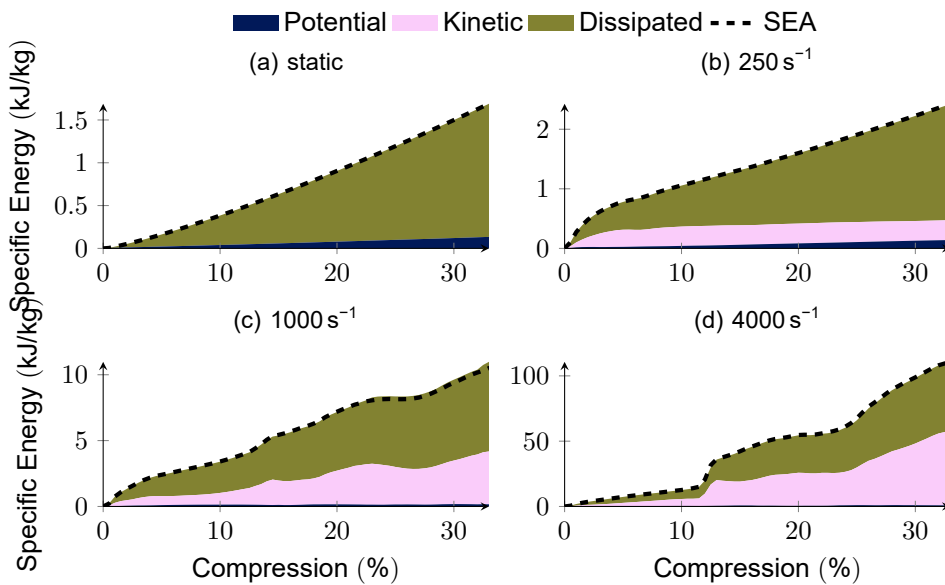


Figure 6.35.: Distribution of the SEA into different types of energy for the  $8 \times 8$  honeycomb patches at different strain rates.

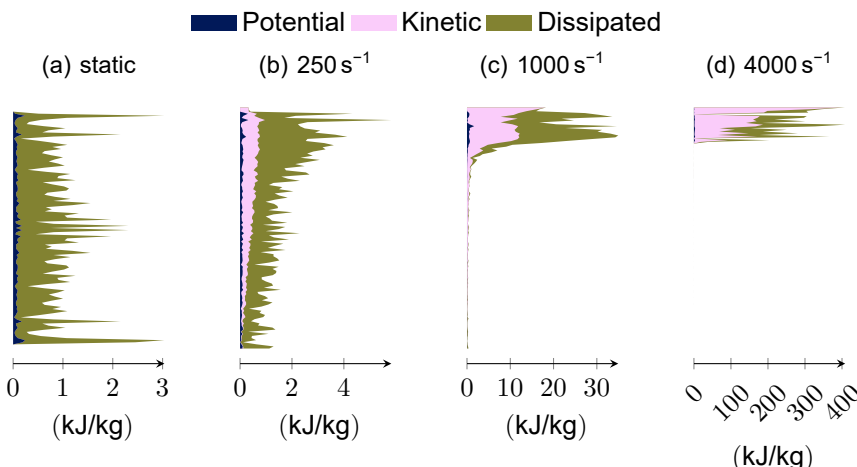


Figure 6.36.: Vertical distribution of energy at 20 % compression for all investigated compression rates in the  $8 \times 8$  honeycomb patch.

energy is in the bottom part of the lattice, similar to the observations made for the re-entrant patch. This is no longer the case for the *fast* rate, where energy is fully concentrated at the upper part near the strike face. At *slow* compression, a nearly linear distribution of all energies rising from the bottom to the top can be seen, with more energy dissipated close to the strike face. *Static* compression shows a bulge in the centre of the patch, consistent with the global barrelling seen in Figure 6.16. The peaks near the top and the bottom of the distribution are attributed to the strong deformation of elements at the fixed boundaries.

## 6

#### 6.6.4. COMPARISON OF PATCHES

There are two commonalities between different metamaterial architectures when considering the energy distributions. Firstly, the majority of energy spent on compressing the material is dissipated by plastic deformation of the material throughout all compression rates. At higher rates the amount of kinetic energy approaches the level of plastically dissipated energy in the patch. This corresponds to the second common effect at higher rates, noted in earlier sections. The behaviour is not determined by the transmission of forces, but rather by the inertial forces that result from the distribution of mass within the lattice.

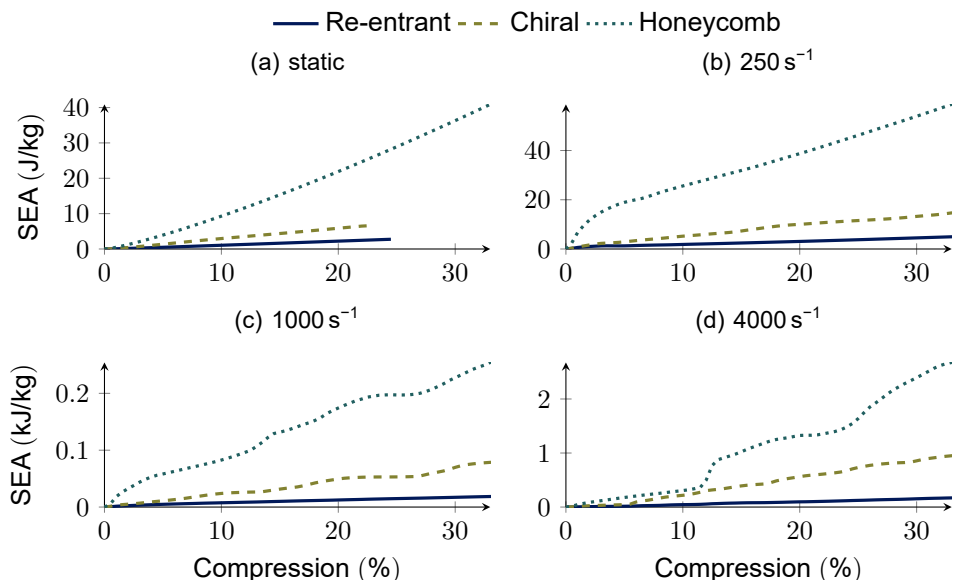


Figure 6.37.: Comparison specific absorbed energies for  $8 \times 8$  patches of different architectures for the four investigated strain rates.

For a fair comparison of the different architectures, the SEA is plotted against the compression for the three investigated architectures. In Figure 6.37a, the SEA can be seen for *static* compression. Here, the honeycomb architecture shows the highest levels, which is consistent with the higher levels of pressure seen for this architecture in Figure 6.19. The honeycomb patches show the highest SEA for the investigated strain rates. For *fast* compression, it is noteworthy, that the chiral patch shows similar levels of energy absorption as the honeycomb architecture up to 12 %, at which compression levels the first contact occurs for the honeycomb leading to a steep rise in absorbed energy. This emphasizes the dominance, that inertial effects have over the structural response of the different architectures at high rates of deformation.

## 6.7. CONCLUSION

The investigations presented in this chapter offer a novel perspective on the high-rate deformation mechanisms in different architected metamaterials employed for impact mitigation.

It has been shown in Section 6.4, that localized failure within the investigated auxetic architectures—re-entrant and chiral—leads to a stronger softening effect for smaller unit cells due to a more pronounced localization of the deformation. However, honeycombs, as an investigated non-auxetic architecture, show a global deformation pattern, leading to a stiffer response when considering patches with more unit cells. For higher rates, there is a shift towards deformation localizing at the strike face, leading to a more brittle response and unit cell size dependence for all architectures. The subsequent deformation resistance is dominated by inertia effects, that are directly related to the geometry of the microstructure of the patch.

Next to the stresses at the strike face, also the stress levels at the back face have been investigated in Section 6.5. In this investigation it has been shown, that the force exerted on the back face is delayed by the wave transmission through the lattice of the metamaterials. The magnitude of the transmitted forces has been shown to be, in a first approximation, independent of the compression rate. Only at the highest investigated compression rate the forces start to rise. This suggests, that for an initial estimation of the force exerted at the back of the protective structure, a set of two calculations, i.e. a static to estimate the terminal level of stress and a high rate analysis to quantify the dynamic pulses at the rear face, might be sufficient to estimate the force transmitted through an architected metamaterial.

The distribution of different types of energy throughout the structure of the architected metamaterials has been investigated as well in Section 6.6. In the static case, the concentration of energy at the moment of localized deformation is observed for the auxetic architectures, whereas for the globally barrelling honeycomb structure, the energy is more evenly distributed. At higher strain rates, the distribution of energy is concentrated at the top of the lattice near the strike face, consistent with the localized deformation patterns seen in Section 6.5. The chiral architecture shows the highest sensitivity to strain rate, whilst the honeycomb architecture shows the largest amount of SEA across the investigated cases.

Throughout this study no beneficial contribution from a negative Poisson's ratio for impact mitigation can be found. The obtained results allow designers of protection concepts to make an informed decision on the architecture and the size of the unit cells based on force transmission during static compression together with an estimation of the maximum force pulse during higher rate compression. Next to the practical applications, also new research avenues have been opened into impact resistant metamaterials away from simply auxetic structures towards architectures that focus on the limitation of the transmitted forces.

## REFERENCES

[AGS12] I. I. Argatov, R. Guinovart-Díaz and F. J. Sabina. 'On local indentation and impact compliance of isotropic auxetic materials from the continuum mechanics viewpoint'. *Int. J. Eng. Sci.* **54** (2012), pp. 42–57.

[Boh<sup>&al</sup>23] R. P. Bohara et al. 'Anti-blast and -impact performances of auxetic structures: A review of structures, materials, methods, and fabrications'. *Eng. Struct.* **276**, 115377 (2023).

[Bon<sup>&al</sup>24] S. Bonfanti et al. 'Computational design of mechanical metamaterials'. *Nat Comput. Sci.* **4** (2024), pp. 574–583.

[CE84] C. R. Calladine and R. W. English. 'Strain-rate and inertia effects in the collapse of two types of energy-absorbing structure'. *Int. J. Mech. Sci.* **26** (1984), pp. 689–701.

[CKvH17] C. Coulais, C. Kettenis and M. van Hecke. 'A characteristic length scale causes anomalous size effects and boundary programmability in mechanical metamaterials'. *Nat. Phys.* **14** (2017), pp. 40–44.

[CL92] J. B. Choi and R. S. Lakes. 'Non-linear properties of metallic cellular materials with a negative Poisson's ratio'. *J. Mater. Sci.* **27** (1992), pp. 5375–5381.

[CL96] J. B. Choi and R. S. Lakes. 'Fracture toughness of re-entrant foam materials with a negative Poisson's ratio: experiment and analysis'. *Int. J. Fract.* **80** (1996), pp. 73–83.

[Cri<sup>&al</sup>13] R. Critchley et al. 'A review of the manufacture, mechanical properties and potential applications of auxetic foams'. *phys. status solidi (b)* **250** (2013), pp. 1963–1982.

[Cro19] I. G. Crouch. 'Body armour – New materials, new systems'. *Def. Technol.* **15** (2019), pp. 241–253.

[Gär<sup>&al</sup>25] T. Gärtner et al. 'Force transmission and dissipation in dynamic compression of architected metamaterials'. *engrXiv* (2025). Preprint.

[Gib<sup>&al</sup>97] L. J. Gibson et al. 'The mechanics of two-dimensional cellular materials'. *Proc. R. Soc. Lond., A. Math. Phys. Sci.* **382** (1997), pp. 25–42.

[GYM22] M.-F. Guo, H. Yang and L. Ma. '3D lightweight double arrow-head plate-lattice auxetic structures with enhanced stiffness and energy absorption performance'. *Compos. Struct.* **290**, 115484 (2022).

[HKS21] L. Herrnböck, A. Kumar and P. Steinmann. 'Geometrically exact elastoplastic rods: determination of yield surface in terms of stress resultants'. *Comput. Mech.* **67** (2021), pp. 723–742.

[HKS22] L. Herrnböck, A. Kumar and P. Steinmann. 'Two-scale off-and online approaches to geometrically exact elastoplastic rods'. *Comput. Mech.* **71** (2022), pp. 1–24.

[JH17] L. Jiang and H. Hu. 'Low-velocity impact response of multilayer orthogonal structural composite with auxetic effect'. *Compos. Struct.* **169** (2017), pp. 62–68.

[Jia<sup>&al</sup>23] P. Jiao et al. 'Mechanical metamaterials and beyond'. *Nat. Commun.* **14**, 6004 (2023).

[Liu<sup>&al</sup>16] W. Liu et al. 'In-plane dynamic crushing of re-entrant auxetic cellular structure'. *Mater.& Des.* **100** (2016), pp. 84–91.

[Mey<sup>&al</sup>22] P. P. Meyer et al. 'Graph-based metamaterials: Deep learning of structure-property relations'. *Mater.& Des.* **223**, 111175 (2022).

[MTM24] P. P. Meyer, T. Tancogne-Dejean and D. Mohr. 'Non-symmetric plate-lattices: Recurrent neural network-based design of optimal metamaterials'. *Acta Mater.* **278**, 120246 (2024).

[PA99] C. Pardini and L. Anselmo. 'Assessing the Risk of Orbital Debris Impact'. *Space Debris* **1** (1999), pp. 59–80.

[Pan<sup>&al</sup>18] J. Pan et al. 'Study on the performance of energy absorption structure of bridge piers against vehicle collision'. *Thin-Walled Struct.* **130** (2018), pp. 85–100.

[Qi<sup>&al</sup>17] C. Qi et al. 'Impact and close-in blast response of auxetic honeycomb-cored sandwich panels: Experimental tests and numerical simulations'. *Compos. Struct.* **180** (2017), pp. 161–178.

[Ren<sup>&al</sup>18] X. Ren et al. 'Auxetic metamaterials and structures: a review'. *Smart Mater. Struct.* **27**, 023001 (2018).

[Rua<sup>&al</sup>03] D. Ruan et al. 'In-plane dynamic crushing of honeycombs—a finite element study'. *Int. J. Impact Eng.* **28** (2003), pp. 161–182.

[San<sup>&al</sup>14] M. Sanami et al. 'Auxetic Materials for Sports Applications'. *Procedia Eng.* **72** (2014), pp. 453–458.

[SDC16] K. K. Saxena, R. Das and E. P. Calius. 'Three Decades of Auxetics Research – Materials with Negative Poisson's Ratio: A Review'. *Adv. Eng. Mater.* **18** (2016), pp. 1847–1870.

[SGE00] C. W. Smith, J. N. Grima and K. E. Evans. 'A novel mechanism for generating auxetic behaviour in reticulated foams: missing rib foam model'. *Acta Mater.* **48** (2000), pp. 4349–4356.

[SP25] J. U. Surjadi and C. M. Portela. 'Enabling three-dimensional architected materials across length scales and timescales'. *Nat. Mater.* **24** (2025), pp. 493–505.

[SS19] D. Saini and B. Shafei. 'Prediction of extent of damage to metal roof panels under hail impact'. *Eng. Struct.* **187** (2019), pp. 362–371.

[TZH22] D. Tahir, M. Zhang and H. Hu. 'Auxetic Materials for Personal Protection: A Review'. *phys. status solidi (b)* **259**, 2200324 (2022).

[Zha<sup>&al</sup>/25] J. Zhang et al. 'Buckle-Barrel Correspondence Based on Topological Polarization Conversion in Mechanical Metamaterials'. *Adv. Mater.* **37**, 2415962 (2025).



# 7

## **CONCLUSION & OUTLOOK**

*Given the pace of technology,  
I propose we leave math to the machines  
and go play outside.*

Calvin

**T**HIS dissertation has challenged the prevalent opinion of previous literature regarding the benefits of auxetic materials for impact mitigation purposes. In doing so, a numerical model was developed and implemented, to enable the fast and accurate analysis of different lattice materials in series of virtual experiments, answering *Research Question #1*. Using this model, different material architectures were designed to exhibit the same mass and stiffness and were subsequently analysed. Together with a series of physical tests, *Research Question #2* was answered. In a final step, *Research Question #3* was investigated using the developed numerical model for different microstructural sizes of both auxetic and non-auxetic materials. The answers given to the questions are given in the following sections:

## 7.1. COMPUTATIONAL MODELLING OF ARCHITECTED METAMATERIALS

In [Chapters 2](#) and [3](#), the analytical description and numerical discretization used for an efficient and accurate description of the behaviour of the nonlinear dynamic behaviour of architected materials was presented. The discussed methods were implemented using the [\[JIVE\]](#)-framework as a basis for later investigations.

For the kinematic description, geometrically exact beams following Crisfield and Jelenić [\[CJ99\]](#) and Simo and Vu-Quoc [\[SV86\]](#) were used. These beams were supplemented with a contact formulation following Wriggers [\[Wri06\]](#). Time marching needed for the dynamic processes during impact mitigation was achieved by an explicit time stepping scheme for fast computation at high speeds requiring small time steps for precise detection of contact events. Accuracy of the scheme was ensured by adapting the time step size based on the error estimate from a Milne-device of the predictor-corrector pairing employed.

For the material response of the beams in [Chapter 3](#), the plasticity constants from literature (cf. [\[HKS21; HKS22\]](#)) were augmented to allow for arbitrary geometric scaling of the inelastic material behaviour. This allowed to describe the plastic hardening behaviour of the investigated material to be applied to a wide range of metamaterial architectures. In this context the approach proposed by Smriti, Kumar and Steinmann [\[SKS20\]](#) for the direct implementation of elastoplasticity in the beam-type strains and stresses was adapted using an explicit return mapping scheme to allow for a fast computation during global explicit time marching.

This allows for answering the first research question as follows:

### RESEARCH QUESTION #1

How can lattice structures be efficiently and accurately modelled using numerical tools?

**Geometrically nonlinear beams contribute to a numerically efficient method for the modelling of lattice structures and allow for inclusion of material non-linearities, contact, and proper geometric scaling in an accurate manner.**

The efficiency of the model has been shown in [Chapter 5](#), where the number of DOFs in comparison with a continuum-based model was reduced by more than one order of magnitude. The accuracy of the model was demonstrated by comparison with physical as well as other numerical models in [Chapter 5](#) and by validating with results from literature in [Chapters 2 and 3](#).

## CONTRIBUTIONS

- Development of a geometrically consistent scaling strategy for the kinematic hardening behaviour of elastoplastic beams.
- Application of an explicit return mapping scheme to the direct modelling of inelastic material behaviour in beams.
- Application of geometrically exact beams with inelastic material behaviour to static and dynamic problems.
- Implementation of a modular research code, incorporating numerical benchmarks and detailed documentation [[dynLattice](#)].<sup>1</sup>

7

## 7.2. INFLUENCE OF THE POISSON EFFECT ON ENERGY ABSORPTION

[Chapter 4](#) established a set of unit cells from different architectures with the same effective properties to enable an unbiased comparison between different material architectures. The development of these elastic properties under compression and shear was evaluated and related to the deformations of the beams in the architecture. It was demonstrated, that the Poisson's ratio does not provide a satisfactory explanation for the difference in energy absorption under localized impact phenomena. For an impact scenario, the stiffness of the material in impact direction and its development during the deformation was identified as a crucial component for energy absorption, together with the lateral stress wave velocity as a proxy for energy dispersion. Both must remain sufficiently high throughout the deformation for all unit cells in the patch to enable high absorption of energy from the impactor. These initial results were subsequently verified experimentally using lattice architectures of the same mass in [Chapter 5](#). Re-entrant and conventional honeycomb unit cells were designed to exhibit similar mass for one comparison and similar stiffness for a second. Patches of these unit cells were manufactured and experimentally subjected to localized high-rate deformation. In this study, no effect of the Poisson's ratio on the energy absorption could be seen as well. The materials with a negative Poisson's ratio densified earlier, leading to reduced duration for energy absorption, resulting in higher stresses exerted at the protected side of the structure.

The second research question can thus be answered:

<sup>1</sup>available at <https://github.com/hortulanusT/dynLattice>

**RESEARCH QUESTION #2**

How does the Poisson effect influence energy absorption in architected materials?

**The Poisson effect in itself does not influence the energy absorption capacity of an architected material.**

**CONTRIBUTIONS**

- Development of distinct sets of equivalent unit cells from ten different metamaterial architectures.
- Analysis of the evolution of the stiffness properties throughout the static deformation of unit cells.
- Determination of the elastic energy absorption capabilities at different strain rates and sizes of impactors.
- Experimental investigation of same mass and same stiffness metamaterial patches under high-speed impact and analysis of the temporal and local force distribution.

7

## 7.3. INFLUENCE OF THE POISSON EFFECT ON FORCE TRANSMISSION

Next to the global effects experimentally investigated, in [Chapter 5](#) also the distributions of the force transmission throughout the different lattices were investigated. The experimental studies demonstrated that auxetic architectures showcase a higher maximum total load on the protected side attributed to earlier densification of the lattice. Accompanying the experimental study, numerical models showed, that the local distribution of the pressure onto the protected side throughout the impact is concentrated for auxetic materials. These concentrations result in higher pressures for the auxetic architectures and lower pressures for the patches with a positive Poisson's ratio. This behaviour in force transmission was further investigated in [Chapter 6](#) for different compression rates using the architectures developed in [Chapter 4](#) to exhibit equivalent density and stiffness. Here, auxetic architectures exhibited a trend towards localized deformation during static compression, whereas the investigated non-auxetic architecture showed a stable, global deformation pattern. For higher strain rates, the static deformation patterns disappear, and the deformation concentrates at the face subjected to impact loading. This leads to a stronger influence of the geometric distribution of masses. Even at the highest strain rates the size of the unit cells was seen to determine the behaviour of the patch at the loading edge.

These investigations lead to the answer for the third research question:

**RESEARCH QUESTION #3**

How does the Poisson effect influence force transmission in architected materials?

**A negative Poisson's ratio concentrates the load over a smaller time frame and a narrower zone.**

**CONTRIBUTIONS**

7

- Analysis of the pressure distributions on the protected side for different meta-material architectures under impact loading.
- Determination of the energy absorption capabilities at different strain rates including material non-linearities.
- Determination of force transfer mechanisms at different strain rates and their relation to the size of the unit cells.

**7.4. CONCLUSION**

In this dissertation, the high rate compressive behaviour of architected auxetic metamaterials was compared rigorously with non-auxetic metamaterials and the evolution of properties in architected materials under high-rate compression were thoroughly scrutinized. It was shown using both numerical and physical tests, that auxetic architected materials offer no benefit in energy absorption capabilities and transmitted forces. [Chapter 4](#) showed worse performance of all auxetic architectures compared to the non-auxetic ones regarding the elastic potential to absorb energy in the majority of investigated scenarios. [Chapter 5](#) showed higher peak pressures being exerted on the protected side of the protective structure at the same levels of absorbed energy for all three variants of the auxetic re-entrant honeycomb compared to all four variants of the non-auxetic conventional honeycomb at both equivalent mass and stiffness properties. [Chapter 6](#) demonstrated lower absorbed energies and higher transmitted forces of the auxetic architectures compared to the non-auxetic architecture at all investigated rates. All results thus lead to the following answer for the title question:

**TITLE QUESTION**

Are auxetics better for protection?

**Auxetics are *not* better for protection.**

A set of auxetic structures, that cover variants of the two different auxetic mechanisms, were rigorously compared to a single non-auxetic architecture. By showing that the non-auxetic structure is able to absorb more specific energy as well as showing, that an auxetic structure concentrates forces, the general claim "Auxetics are better for protection" is disproven.

## 7.5. RECOMMENDATIONS FOR FURTHER RESEARCH

Whilst challenging the basis for auxetic architected metamaterials for impact mitigation, the present work serves as a starting point for further research into other architected materials for this purpose.

Especially promising is the class of aperiodic, but ordered structures (e.g. [Qi<sup>&al</sup>24; Ros<sup>&al</sup>25]), showing staggered buckling and thus a less pronounced drop in stiffness as observed for the investigated structures. An intriguing question here is the interaction between quasi-static deformation patterns and the dynamic concentration of deformation near the loading edge in different aperiodic patterns. Of interest as well are the analysis of transmission of waves throughout the aperiodic lattice. These dynamic properties are yet unexplored, but appear promising in the quest for more lightweight materials mitigating impacts.

Another promising approach would be the investigation of graded metamaterials (e.g. [Fu<sup>&al</sup>24; GKS24; Kap<sup>&al</sup>23; VW24]) under different strain rates, in which the concentration of different types of energy and collapse patterns could be either taken advantage of or mitigated for better distribution of energies throughout the structure.

Next to the use of grading of a single material, also the use of multiple architected materials throughout the structure, would be a promising avenue for upcoming research. A noteworthy mention here are so-called interpenetrating lattices (e.g. [Fit<sup>&al</sup>24; WGB23; Whi<sup>&al</sup>21]), that consist of two independent structures made from separate materials. These materials have already shown remarkable properties with regard to an increased fracture toughness (cf. [WGB23]), that could make them an interesting candidate for protective applications.

Finally, the investigations presented in this dissertation are only concerned with the behaviour of plain auxetic architected materials. In practical protection concepts, they are usually embedded in a layered structure. Investigation of the effects of different lattice architectures in these structures would be of great interest and required before a final answer regarding the efficacy of any material in a wider protection concept can be given.

Besides impact scenarios, the developed numerical toolkit also allows for the investigation of lattice architectures in other scenarios. Especially the vibration transmission behaviour of lightweight structures in for example satellite launches would be of interests. The in Chapters 2 and 3 developed toolkit also allows the simulation of three-dimensional structures, which was not done in this dissertation. The modelling of three-dimensional structures would allow the investigation of more complex loading scenarios as well as architectures. Of particular interest here would be to examine how the tangent properties of metamaterials change throughout deformation, e.g. can a transversely isotropic material be architected to retain this property during finite compression or shear?

Next to investigations using the present tools, the developed numerical tools can be extended as well. The discussed inclusion of elastoplastic parameters should be extended to a more general set of cross-sections for the beam. The inclusion of viscous effects in the material into the modelling of the beam would be of interest to capture a wider range of material behaviour in the formulation for the beam, as done

by Le Barbenchon and Lißner [LL24]. Whilst this is done conceptually already (cf. [SHT84; Wee<sup>&al</sup>23]), a direct link relating the microstructural behaviour to constants on beam-level is yet to be found. Besides the discussion of single beams, in the modelling of lattice structures, the modelling of material accumulation near the joints has in this dissertation only been done through numerical fitting of simple hardening of single elements. A more robust approach, that could also account for different joint angles is needed.

Besides beam structures, also shell structures could be modelled intrinsically using Kirchhoff-Love or Reissner-Mindlin theories. These shell structures would allow for a wider range of architected materials, see e.g. [GYM22; Mey<sup>&al</sup>22; MTM24]. Especially the description of inelastic phenomena prevalent during impact scenarios in shell structures could allow for further investigations into the possibilities of architected materials for lightweight impact protection.

## REFERENCES

[CJ99] M. A. Crisfield and G. Jelenić. 'Objectivity of strain measures in the geometrically exact three-dimensional beam theory and its finite-element implementation'. *Proc. R. Soc. A-Math. Phys. Eng. Sci.* **455** (1999), pp. 1125–1147.

[dynLattice] T. Gärtner and F. P. van der Meer. *dynLattice: A finite element environment for dynamic simulation of beam networks and lattice metamaterials*. Version 1.11. 13th Aug. 2025.

[Fit<sup>&al</sup>24] K. M. Fitzgerald et al. 'Structural metamaterials with innate capacitive and resistive sensing'. *J. Mater. Sci.* **59** (2024), pp. 15469–15490.

[Fu<sup>&al</sup>24] T. Fu et al. 'Impact dynamic response of stiffened porous functionally graded materials sandwich doubly-curved shells with Arc-type auxetic core'. *Int. J. Impact Eng.* **191**, 105000 (2024).

[GKS24] V. Gupta, A. Kidane and M. Sutton. 'Dynamic characteristics of density-graded cellular materials for impact mitigation'. *Int. J. Solids Struct.*, 112816 (2024).

[GYM22] M.-F. Guo, H. Yang and L. Ma. '3D lightweight double arrow-head plate-lattice auxetic structures with enhanced stiffness and energy absorption performance'. *Compos. Struct.* **290**, 115484 (2022).

[HKS21] L. Herrnböck, A. Kumar and P. Steinmann. 'Geometrically exact elastoplastic rods: determination of yield surface in terms of stress resultants'. *Comput. Mech.* **67** (2021), pp. 723–742.

[HKS22] L. Herrnböck, A. Kumar and P. Steinmann. 'Two-scale off-and online approaches to geometrically exact elastoplastic rods'. *Comput. Mech.* **71** (2022), pp. 1–24.

[JIVE] Dynaflow Research Group. *JIVE*. Version 3.0. 1st Apr. 2021.

[Kap<sup>&al</sup>23] K. Kappe et al. 'Multi-objective optimization of additive manufactured functionally graded lattice structures under impact'. *Int. J. Impact Eng.*, 104789 (2023).

[LL24] L. Le Barbenchon and M. Lißner. 'On the dynamic performance of additively manufactured visco-elastic meta-materials'. *Mater. Lett.* **359**, 135823 (2024).

[Mey<sup>&al</sup>22] P. P. Meyer et al. 'Graph-based metamaterials: Deep learning of structure-property relations'. *Mater. & Des.* **223**, 111175 (2022).

[MTM24] P. P. Meyer, T. Tancogne-Dejean and D. Mohr. 'Non-symmetric plate-lattices: Recurrent neural network-based design of optimal metamaterials'. *Acta Mater.* **278**, 120246 (2024).

[Qi<sup>&al</sup>24] G. Qi et al. 'Compressive properties of aperiodic but ordered cellular materials inspired by Penrose tilings'. *Thin-Walled Struct.* **204**, 112287 (2024).

[Ros<sup>&al</sup>25] M. I. N. Rosa et al. 'Enhanced Deformability Through Distributed Buckling in Stiff Quasicrystalline Architected Materials'. *Adv. Mater.*, 2505125 (2025).

[SHT84] J. C. Simo, K. D. Hjelmstad and R. L. Taylor. 'Numerical Formulations of Elasto-Viscoplastic Response of Beams Accounting for the Effect of Shear'. *Comput. Methods Appl. Mech. Eng.* **42** (1984), pp. 301–330.

[SKS20] Smriti, A. Kumar and P. Steinmann. 'A finite element formulation for a direct approach to elastoplasticity in special Cosserat rods'. *Int. J. Numer. Methods Eng.* (2020), pp. 1262–1282.

[SV86] J. C. Simo and L. Vu-Quoc. 'A three-dimensional finite-strain rod model. part II: Computational aspects'. *Comput. Methods Appl. Mech. Eng.* **58** (1986), pp. 79–116.

[VW24] I. Valizadeh and O. Weeger. 'Rate-dependent energy dissipation of graded viscoelastic structures fabricated by grayscale vat photopolymerization'. *Smart Mater. Struct.* **33**, 065006 (2024).

[Wee<sup>&al</sup>23] O. Weeger et al. 'Inelastic finite deformation beam modeling, simulation, and validation of additively manufactured lattice structures'. *Addit. Manuf. Lett.* **4**, 100111 (2023).

[WGB23] B. C. White, A. Garland and B. L. Boyce. 'Toughening by interpenetrating lattices'. *Matter* **6** (2023), pp. 570–582.

[Whi<sup>&al</sup>21] B. C. White et al. 'Interpenetrating lattices with enhanced mechanical functionality'. *Addit. Manuf.* **38**, 101741 (2021).

[Wri06] P. Wriggers. *Computational Contact Mechanics*. 2nd ed. Springer, 2006.







## **ELASTIC BEHAVIOUR UNDER IMPACT**

---

this appendix corresponds to Chapter 4

## A.1. STRUCTURAL CONFIGURATIONS

A more detailed description of the tuning process for each architecture is described here. As can be seen in Figure 4.4a, the re-entrant honeycomb has three variables that define the geometry, namely the sizes of the base  $b$  and the tilted bars  $l$  as well as the angle of these tilted bars  $\alpha$ . Finally, the thickness of the bars  $d$  is a parameter to be determined. This study assumes (linear) elastic material behaviour. Structures with geometric similitude can be assumed to have no difference in their behaviour. Therefore, the values of  $b$ ,  $l$ , and  $d$  by themselves are not important, but the ratio between them is. We chose the ratio of the tilted bar length to the base length  $r = \frac{l}{b}$  and the ratio of the thickness to the base length  $t = \frac{d}{b}$ . In this study, the angle  $\alpha$  ranges from  $20^\circ$  to  $85^\circ$ , the beam length ratio  $t$  ranges from  $\frac{1}{3}$  to  $\frac{4}{3}$ , and the beam thickness ratio  $t$  ranges from 0.01 to 0.1. For small angles, the re-entrant beams may not intersect, so the additional constraint  $r < \frac{1}{2\cos\alpha}$  is introduced.

The arrowhead structure is defined by the two angles  $\alpha \in (5^\circ, 60^\circ)$ ,  $\beta \in (45^\circ, 75^\circ)$  (see Figure 4.5a) and the thickness of the beams relative to the height of the structure  $t = \frac{d}{h} \in (0.01, 0.1)$ , as can be seen in Figure 4.5a. To get realistic structures, the constraint  $3\tan\alpha < \tan\beta$  was added.

For the second auxetic mechanism, as explained in Section 4.2.1, a chiral and an anti-chiral lattice have been selected. As can be seen in Figure 4.2a and Figure 4.3a, the only parameters to set are the angle  $\alpha \in (5^\circ, 60^\circ)$  and the thickness of the beams relative to the width of the unit cell  $t = \frac{d}{b} \in (0.01, 0.1)$ . Since the antichiral unit cell is based on the chiral one, the parameters and their respective ranges are identical.

Finally, the properties of a non-auxetic architecture are also examined for comparison. For simplicity, the same parameter range is chosen as for the re-entrant honeycomb, but with angles  $\alpha \in (95^\circ, 145^\circ)$ , resulting in a positive Poisson's ratio (see [Gib<sup>&al</sup>97]).

For each considered architecture, in a first step, the elastic properties in the undeformed configuration are recorded for all valid combinations in a full factorial exploration space. These results are then used to create a (linearized) mapping for the four linear elastic constants of an orthotropic material in 2D as well as the relative density  $\mathcal{P} \mapsto (E_y, E_x, \nu_{yx}, G, \rho_{\text{rel}})$ . Where  $\mathcal{P}$  is the point in the design space that describes the variables described above. Using this mapping, a target function is defined by calculating the root sum squared of the error terms. In the case of the desired vertical Young's modulus  $E_y^* = 300$  MPa and relative density  $\rho_{\text{rel}}^* = 0.1$ , this results in the following objective function

$$t(\mathcal{P}) = \sqrt{\left(\frac{E_y(\mathcal{P}) - E_y^*}{E_y^*}\right)^2 + \left(\frac{\rho_{\text{rel}}(\mathcal{P}) - \rho_{\text{rel}}^*}{\rho_{\text{rel}}^*}\right)^2} \quad (\text{A.1})$$

This objective function is now minimized in the parameter spaces shown in Table 4.1 with the reported constraints using the `scipy`<sup>1</sup> implementation of the DIRECT optimizer.

<sup>1</sup>version 1.9.2

With the procedure described above, all architectures are tuned to exhibit the desired properties. All combinations of  $E_y^* = 200 \text{ MPa}$ ,  $300 \text{ MPa}$  and  $400 \text{ MPa}$  and  $\rho_{\text{rel}}^* = 0.067$ ,  $0.100$  and  $0.133$  are designed. The resulting orthotropic material properties are given in Tables A.1 to A.9 accepting some discrepancy between the linearized target function space and the actual computations. The corresponding configurations are shown below the tables.

Table A.1.: Resulting properties and unit cells for  $E_y^* = 200 \text{ MPa}$ ,  $\rho_{\text{rel}}^* = 0.067$   
Angles  $\alpha, \beta$  are in and the moduli  $E_x, E_y, G_{xy}, G_{yx}$  in MPa.

Geometry	$t$	$\alpha$	$\beta$	$r$	$\rho_{\text{rel}}$	$E_y$	$E_x$	$\nu_{yx}$	$\nu_{xy}$	$G_{xy}$	$G_{yx}$
re-entrant	0.032	75.59	—	0.82	0.067	198	14	-3.77	-0.26	2	2
re-entrant (90°)	0.028	84.99	—	0.39	0.067	195	2,465	-0.21	-2.69	5	5
arrowhead (90°)	0.025	8.55	53.06	—	0.067	194	8	-4.79	-0.20	1,291	1,291
chiral	0.058	21.71	—	—	0.067	199	199	-0.38	-0.38	67	4
antichiral	0.061	19.01	—	—	0.067	198	198	-0.70	-0.70	3	3
honeycomb	0.050	111.82	—	0.82	0.067	201	96	1.42	0.68	16	16
honeycomb (90°)	0.045	127.38	—	0.72	0.067	201	56	1.87	0.52	18	18

A

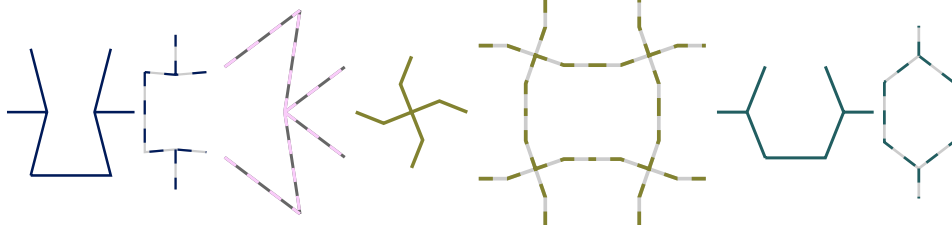


Table A.2.: Resulting properties and unit cells for  $E_y^* = 200 \text{ MPa}$ ,  $\rho_{\text{rel}}^* = 0.100$   
Angles  $\alpha, \beta$  are in and the moduli  $E_x, E_y, G_{xy}, G_{yx}$  in MPa.

Geometry	$t$	$\alpha$	$\beta$	$r$	$\rho_{\text{rel}}$	$E_y$	$E_x$	$\nu_{yx}$	$\nu_{xy}$	$G_{xy}$	$G_{yx}$
re-entrant	0.037	65.33	—	0.62	0.100	198	74	-1.60	-0.60	6	6
re-entrant (90°)	0.034	63.18	—	0.46	0.100	196	208	-0.94	-1.00	6	6
arrowhead	0.025	5.27	70.70	—	0.100	198	1,873	-0.25	-2.39	1,398	1,397
arrowhead (90°)	0.031	15.91	62.35	—	0.100	199	60	-1.77	-0.53	1,555	1,559
chiral	0.073	31.56	—	—	0.100	200	200	-0.38	-0.38	97	68
antichiral	0.080	30.17	—	—	0.100	199	200	-0.70	-0.70	9	9
honeycomb	0.094	124.94	—	1.13	0.100	202	309	0.79	1.21	97	97
honeycomb (90°)	0.095	116.11	—	1.16	0.100	202	396	0.69	1.36	82	82

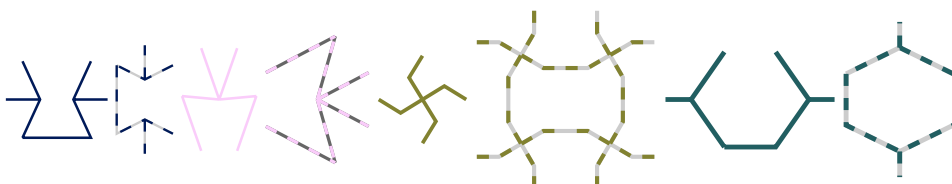
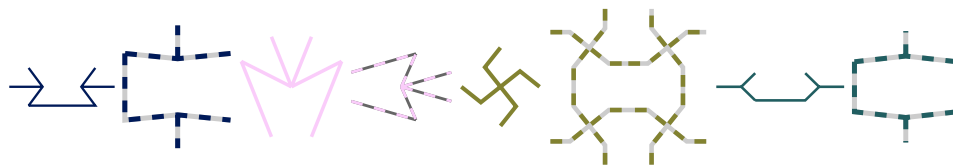


Table A.3.: Resulting properties and unit cells for  $E_y^* = 200$  MPa,  $\rho_{\text{rel}}^* = 0.133$   
 Angles  $\alpha, \beta$  are in and the moduli  $E_x, E_y, G_{xy}, G_{yx}$  in MPa.

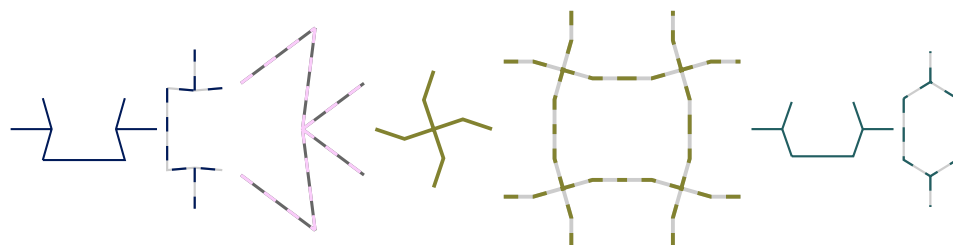
Geometry	$t$	$\alpha$	$\beta$	$r$	$\rho_{\text{rel}}$	$E_y$	$E_x$	$\nu_{yx}$	$\nu_{xy}$	$G_{xy}$	$G_{yx}$
re-entrant	0.035	53.37	—	0.35	0.133	199	801	-0.47	-1.89	11	11
re-entrant (90°)	0.075	84.29	—	0.80	0.133	199	8,025	-0.11	-4.55	36	36
arrowhead	0.035	26.84	68.20	—	0.133	198	125	-1.22	-0.77	1,401	1,401
arrowhead (90°)	0.028	23.86	73.89	—	0.133	199	462	-0.63	-1.46	1,136	1,136
chiral	0.082	38.53	—	—	0.133	200	200	-0.38	-0.38	19	178
antichiral	0.091	38.87	—	—	0.133	200	200	-0.69	-0.69	17	17
honeycomb	0.052	135.63	—	0.39	0.133	200	3,916	0.20	3.93	57	57
honeycomb (90°)	0.099	96.35	—	1.03	0.133	201	8,033	0.12	4.70	73	73



A

Table A.4.: Resulting properties and unit cells for  $E_y^* = 300$  MPa,  $\rho_{\text{rel}}^* = 0.067$   
 Angles  $\alpha, \beta$  are in and the moduli  $E_x, E_y, G_{xy}, G_{yx}$  in MPa.

Geometry	$t$	$\alpha$	$\beta$	$r$	$\rho_{\text{rel}}$	$E_y$	$E_x$	$\nu_{yx}$	$\nu_{xy}$	$G_{xy}$	$G_{yx}$
re-entrant	0.025	74.07	—	0.39	0.067	296	138	-1.40	-0.66	3	3
re-entrant (90°)	0.027	85.00	—	0.34	0.069	292	2,611	-0.24	-2.17	5	5
arrowhead (90°)	0.025	7.15	53.27	—	0.067	290	9	-5.59	-0.17	1,353	1,353
chiral	0.060	18.55	—	—	0.067	299	299	-0.38	-0.38	10	-16
antichiral	0.063	15.84	—	—	0.067	298	298	-0.69	-0.69	4	4
honeycomb	0.035	109.26	—	0.47	0.067	301	255	1.04	0.88	10	10
honeycomb (90°)	0.036	121.56	—	0.51	0.067	301	95	1.73	0.55	12	12

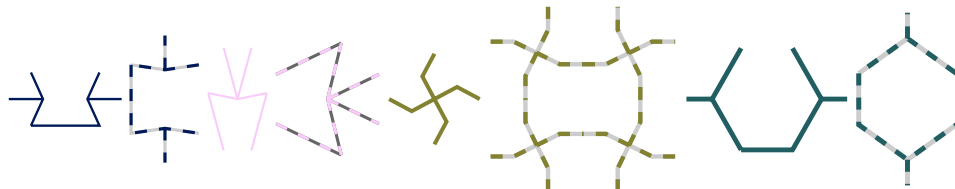


## A.2. BOUNDARY CONDITIONS AND TANGENT PROPERTIES

In this Appendix, a more detailed description of the implementation of the PBCs and the subsequent computation of the elastic tangent properties using these, as discussed in Section 4.3.1, is given.

Table A.5.: Resulting properties and unit cells for  $E_y^* = 300 \text{ MPa}$ ,  $\rho_{\text{rel}}^* = 0.100$   
 Angles  $\alpha, \beta$  are in and the moduli  $E_x, E_y, G_{xy}, G_{yx}$  in MPa.

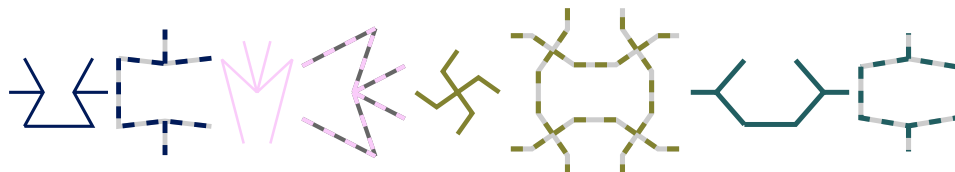
Geometry	$t$	$\alpha$	$\beta$	$r$	$\rho_{\text{rel}}$	$E_y$	$E_x$	$\nu_{yx}$	$\nu_{xy}$	$G_{xy}$	$G_{yx}$
re-entrant	0.035	65.62	—	0.43	0.100	297	273	-1.00	-0.92	8	8
re-entrant (90°)	0.046	81.67	—	0.50	0.100	297	2,937	-0.26	-2.60	15	15
arrowhead	0.021	11.60	74.90	—	0.100	296	468	-0.73	-1.16	924	924
arrowhead (90°)	0.030	13.81	64.34	—	0.100	295	80	-1.85	-0.50	1,583	1,583
chiral	0.078	28.11	—	—	0.100	299	299	-0.38	-0.38	53	19
antichiral	0.085	26.09	—	—	0.100	299	299	-0.69	-0.69	10	10
honeycomb	0.094	119.69	—	1.14	0.100	302	246	1.08	0.88	88	88
honeycomb (90°)	0.096	125.63	—	1.17	0.100	302	189	1.23	0.77	101	101



A

Table A.6.: Resulting properties and unit cells for  $E_y^* = 300 \text{ MPa}$ ,  $\rho_{\text{rel}}^* = 0.133$   
 Angles  $\alpha, \beta$  are in and the moduli  $E_x, E_y, G_{xy}, G_{yx}$  in MPa.

Geometry	$t$	$\alpha$	$\beta$	$r$	$\rho_{\text{rel}}$	$E_y$	$E_x$	$\nu_{yx}$	$\nu_{xy}$	$G_{xy}$	$G_{yx}$
re-entrant	0.045	61.08	—	0.57	0.133	298	191	-1.21	-0.78	11	11
re-entrant (90°)	0.070	83.33	—	0.69	0.133	298	6,987	-0.15	-3.55	37	37
arrowhead	0.025	42.99	75.37	—	0.133	294	24	-3.43	-0.28	686	686
arrowhead (90°)	0.041	18.86	62.75	—	0.133	299	133	-1.44	-0.64	1,911	1,911
chiral	0.089	35.19	—	—	0.133	300	300	-0.38	-0.38	156	35
antichiral	0.099	34.70	—	—	0.133	299	299	-0.69	-0.69	19	19
honeycomb	0.097	131.09	—	0.83	0.133	303	1,333	0.45	1.99	163	163
honeycomb (90°)	0.099	99.51	—	0.94	0.133	303	5,152	0.20	3.42	86	86

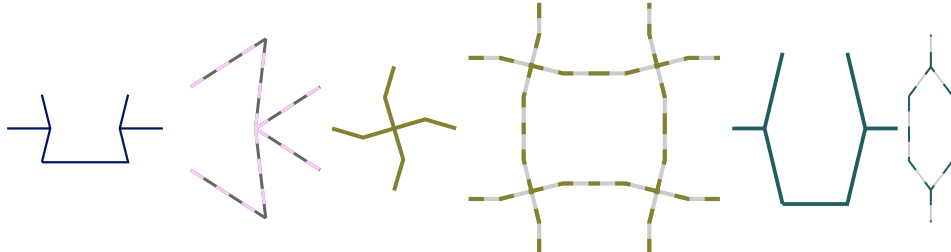


### A.2.1. PERIODIC BOUNDARY CONDITIONS

As can be seen in Figure A.1, the boundary of a (rectangular) unit cell is split into 4 sections  $\Gamma_T, \Gamma_R, \Gamma_B, \Gamma_L$  such that  $\Gamma_T$  represents all the nodes on the top side of the unit cell,  $\Gamma_R$  all the nodes on the right side,  $\Gamma_B$  all on the bottom side, and finally  $\Gamma_L$  the nodes on the left side. This figure shows for all 5 investigated unit cells (re-entrant honeycomb unit cell in Figure A.1a, arrowhead unit cell in Figure A.1b, chiral unit cell in Figure A.1c, antichiral unit cell in Figure A.1d, and the regular

Table A.7.: Resulting properties and unit cells for  $E_y^* = 400$  MPa,  $\rho_{\text{rel}}^* = 0.067$   
 Angles  $\alpha, \beta$  are in and the moduli  $E_x, E_y, G_{xy}, G_{yx}$  in MPa.

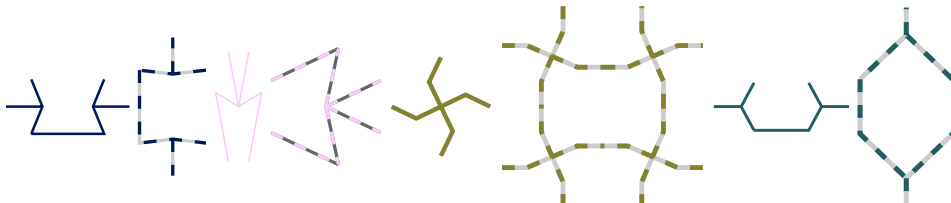
Geometry	$t$	$\alpha$	$\beta$	$r$	$\rho_{\text{rel}}$	$E_y$	$E_x$	$\nu_{yx}$	$\nu_{xy}$	$G_{xy}$	$G_{yx}$
re-entrant	0.026	76.05	—	0.40	0.067	398	136	-1.63	-0.56	4	4
arrowhead (90°)	0.023	6.54	57.28	—	0.067	392	14	-5.12	-0.18	1,386	1,386
chiral	0.061	16.44	—	—	0.067	399	399	-0.37	-0.37	2	-1
antichiral	0.064	13.85	—	—	0.067	395	395	-0.68	-0.68	4	4
honeycomb	0.059	103.41	—	1.20	0.067	399	28	3.67	0.26	15	15
honeycomb (90°)	0.031	143.10	—	0.56	0.067	399	13	5.50	0.17	10	10



A

Table A.8.: Resulting properties and unit cells for  $E_y^* = 400$  MPa,  $\rho_{\text{rel}}^* = 0.100$   
 Angles  $\alpha, \beta$  are in and the moduli  $E_x, E_y, G_{xy}, G_{yx}$  in MPa.

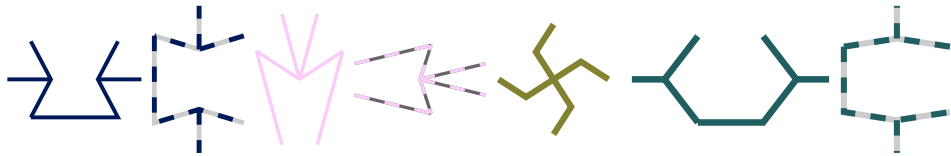
Geometry	$t$	$\alpha$	$\beta$	$r$	$\rho_{\text{rel}}$	$E_y$	$E_x$	$\nu_{yx}$	$\nu_{xy}$	$G_{xy}$	$G_{yx}$
re-entrant	0.035	67.69	—	0.40	0.100	397	343	-1.02	-0.88	8	8
re-entrant (90°)	0.045	83.36	—	0.46	0.100	394	4,132	-0.23	-2.41	16	16
arrowhead	0.015	31.67	79.43	—	0.099	380	36	-3.18	-0.30	435	435
arrowhead (90°)	0.030	12.18	64.54	—	0.100	395	85	-2.05	-0.44	1,633	1,633
chiral	0.081	25.65	—	—	0.100	399	399	-0.37	-0.37	33	44
antichiral	0.088	23.33	—	—	0.100	398	398	-0.69	-0.69	11	11
honeycomb	0.054	118.49	—	0.49	0.100	402	937	0.61	1.43	37	37
honeycomb (90°)	0.092	133.79	—	1.17	0.100	401	97	1.99	0.48	107	107



honeycomb unit cell in Figure A.1e) the empty corners. We therefore add 'ghost' nodes, not connected to the rest of the mesh, in the corners for the application of boundary conditions as described in the following. The four nodes in the corners start with node 0 at the bottom left side and are then numbered counter-clockwise.

Table A.9.: Resulting properties and unit cells for  $E_y^* = 400 \text{ MPa}$ ,  $\rho_{\text{rel}}^* = 0.133$   
 Angles  $\alpha, \beta$  are in and the moduli  $E_x, E_y, G_{xy}, G_{yx}$  in MPa.

Geometry	$t$	$\alpha$	$\beta$	$r$	$\rho_{\text{rel}}$	$E_y$	$E_x$	$\nu_{yx}$	$\nu_{xy}$	$G_{xy}$	$G_{yx}$
re-entrant	0.045	62.12	—	0.49	0.133	397	340	-1.03	-0.89	13	13
re-entrant (90°)	0.056	73.13	—	0.54	0.133	398	1,497	-0.47	-1.78	23	23
arrowhead	0.026	33.15	74.81	—	0.133	397	71	-2.30	-0.41	896	896
arrowhead (90°)	0.025	18.09	76.47	—	0.133	395	747	-0.67	-1.27	978	978
chiral	0.094	32.74	—	—	0.133	399	399	-0.37	-0.37	28	-69
honeycomb	0.100	127.62	—	0.83	0.133	404	1,208	0.55	1.64	162	162
honeycomb (90°)	0.092	98.75	—	0.82	0.133	404	5,988	0.20	3.03	80	80



## A

The sets for corresponding sides need to be ordered in a way, such that they correspond towards each other, i.e. in a rectangular unit cell for every node on the bottom edge, we need to find a node on the top edge, for which the relationship

$$\mathbf{X}_T = \mathbf{X}_B + \begin{bmatrix} 0 \\ h \end{bmatrix} \quad (\text{A.2})$$

of the respective reference position vectors  $\mathbf{X}$  holds, where  $h$  is the height of the unit cell. With its width  $w$ , a similar relationship holds to identify corresponding nodes between the left and right edges:

$$\mathbf{X}_R = \mathbf{X}_L + \begin{bmatrix} w \\ 0 \end{bmatrix}. \quad (\text{A.3})$$

After having identified all nodes that need to be taken into account, it is made sure that the rotation of one node is equal to the rotation of the corresponding node on the opposite side by enforcing the following two boundary conditions on the rotational displacement vectors  $\vartheta$ :

$$\vartheta_{iT} = \vartheta_{iB}, \quad \forall iT \in \Gamma_T, iB \in \Gamma_B \mid \mathbf{X}_{iT} = \mathbf{X}_{iB} + \begin{bmatrix} 0 \\ h \end{bmatrix}, \quad (\text{A.4})$$

$$\vartheta_{iR} = \vartheta_{iL}, \quad \forall iR \in \Gamma_R, iL \in \Gamma_L \mid \mathbf{X}_{iR} = \mathbf{X}_{iL} + \begin{bmatrix} w \\ 0 \end{bmatrix}. \quad (\text{A.5})$$

The translational displacement vectors  $\mathbf{u}$  are now coupled via the controlling nodes at the corresponding sides as (sets are omitted for better readability)

$$\mathbf{u}_{iT} = \mathbf{u}_{iB} + (\mathbf{u}_3 - \mathbf{u}_0), \quad (\text{A.6})$$

$$\mathbf{u}_{iR} = \mathbf{u}_{iL} + (\mathbf{u}_1 - \mathbf{u}_0), \quad (\text{A.7})$$

while the corner nodes are fixed to enforce the desired displacement gradient  $H_{ij} = \frac{\partial u_i}{\partial X_j}$ ,

$$\mathbf{u}_0 = \begin{bmatrix} 0 \\ 0 \end{bmatrix} \quad \mathbf{u}_1 = \mathbf{H} \cdot \begin{bmatrix} w \\ 0 \end{bmatrix} \quad \mathbf{u}_3 = \mathbf{H} \cdot \begin{bmatrix} 0 \\ h \end{bmatrix}. \quad (\text{A.8})$$

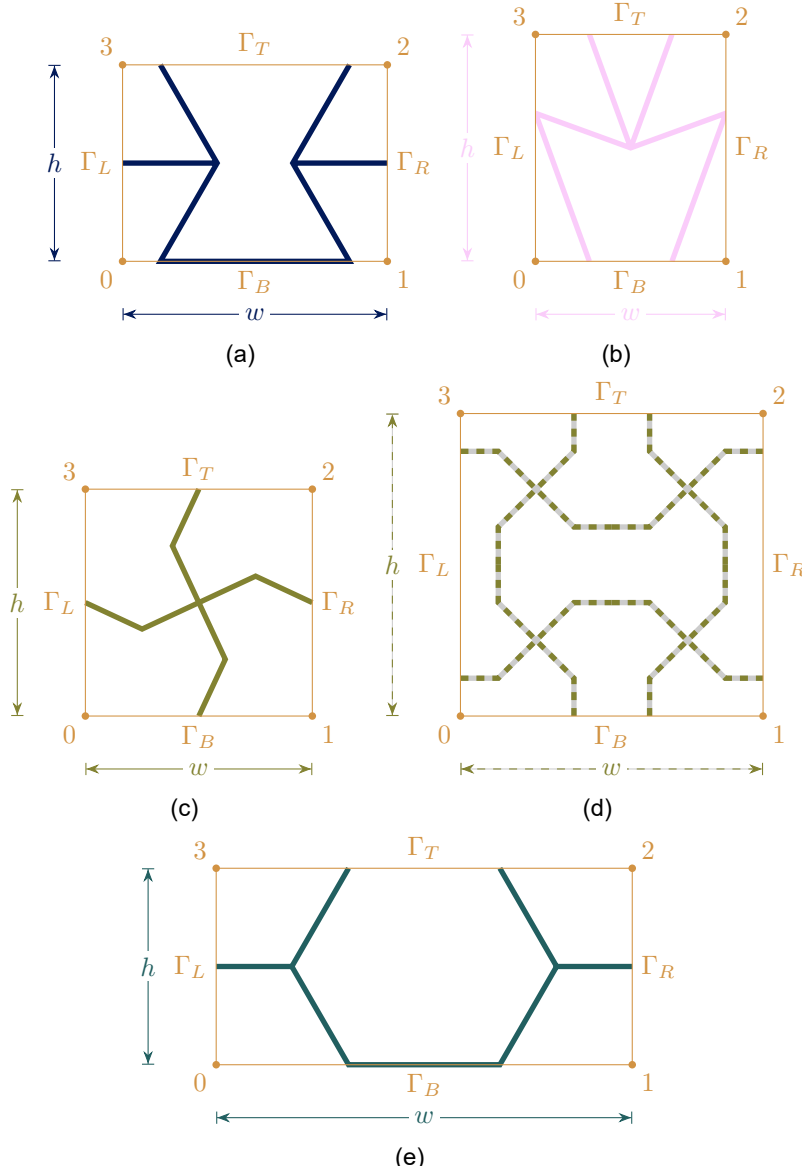


Figure A.1.: Unit cells of (a) the re-entrant honeycomb, (b) the arrowhead structure, (c) the chiral structure, (d) the antichiral structure, and (e) the honeycomb structure with notation used for establishing the PBCs.

A

It should be noted, that the *ghost* nodes are not connected to any element in the FE implementation and thus do not contribute to the internal force vector or stiffness matrix, but their effect stems from constraining the system whilst using them as helper nodes. Also, in order to prevent rigid body movement, a single node connected to the structure needs to have all translational DOFs being equal to 0.

The 1st Piola-Kirchhoff stress tensor  $\mathbf{P}$  is subsequently calculated based on its definition

$$\frac{\mathbf{f}}{\Gamma_0} = \mathbf{P} \mathbf{n}_0. \quad (\text{A.9})$$

Where  $\mathbf{f}$  are the forces on the surface,  $\Gamma_0$  is the area of the undeformed surface and  $\mathbf{n}_0$  is the normal to the undeformed surface. One can now rearrange it for the different surfaces and average over two opposite surfaces for numerical accuracy:

$$P_{11} = \frac{f_1(R) - f_1(L)}{\Gamma_R + \Gamma_L} \quad (\text{A.10})$$

$$P_{12} = \frac{f_1(T) - f_1(B)}{\Gamma_T + \Gamma_B} \quad (\text{A.11})$$

$$P_{21} = \frac{f_2(R) - f_2(L)}{\Gamma_R + \Gamma_L} \quad (\text{A.12})$$

$$P_{22} = \frac{f_2(T) - f_2(B)}{\Gamma_T + \Gamma_B} \quad (\text{A.13})$$

A

## A.2.2. COMPUTATION OF THE TANGENT PROPERTIES

We start from the relationships

$$\delta \mathbf{P} = \mathbb{C}^4 : \delta \mathbf{H} \quad (\text{A.14})$$

and

$$\delta \mathbf{H} = \mathbb{S}^4 : \delta \mathbf{P}. \quad (\text{A.15})$$

In order to simplify notation,  $\mathbf{P}, \mathbf{H}$  are now column-vectors and  $\mathbb{S}^4, \mathbb{C}^4$  are now the matrices  $[\mathbf{S}], [\mathbf{C}]$

$$\delta \begin{bmatrix} P_{11} \\ P_{12} \\ P_{21} \\ P_{22} \end{bmatrix} = \begin{bmatrix} c_{1111} & c_{1112} & c_{1121} & c_{1122} \\ c_{1211} & c_{1212} & c_{1221} & c_{1222} \\ c_{2111} & c_{2112} & c_{2121} & c_{2122} \\ c_{2211} & c_{2212} & c_{2221} & c_{2222} \end{bmatrix} \delta \begin{bmatrix} H_{11} \\ H_{12} \\ H_{21} \\ H_{22} \end{bmatrix} \quad (\text{A.16})$$

or with the index combination  $(11) \Rightarrow 1, (12) \Rightarrow 2, (21) \Rightarrow 3, (22) \Rightarrow 4$

$$\delta \begin{bmatrix} P_1 \\ P_2 \\ P_3 \\ P_4 \end{bmatrix} = \begin{bmatrix} c_{11} & c_{12} & c_{13} & c_{14} \\ c_{21} & c_{22} & c_{23} & c_{24} \\ c_{31} & c_{32} & c_{33} & c_{34} \\ c_{41} & c_{42} & c_{43} & c_{44} \end{bmatrix} \delta \begin{bmatrix} H_1 \\ H_2 \\ H_3 \\ H_4 \end{bmatrix}. \quad (\text{A.17})$$

The tangent stiffness matrix  $[\mathbf{C}]$  is computed as described in Section 4.3.1 and the tangent compliance matrix  $[\mathbf{S}]$  is afterwards computed by

$$[\mathbf{S}] = (0.5[\mathbf{C}] + 0.5[\mathbf{C}]^T)^{-1}, \quad (\text{A.18})$$

where the symmetrization of the stiffness is done to minimize numerical errors.

For the derivation of the (linearized) Young's modulus and Poisson's ratio, we need a relation between  $\delta P_i$  and  $\delta H_i$ , where the orthogonal stress is zero, whilst the orthogonal strain is free

$$\begin{bmatrix} \delta H_1 \\ 0 \\ 0 \\ \delta H_2 \end{bmatrix} = \begin{bmatrix} s_{11} & s_{12} & s_{13} & s_{14} \\ s_{21} & s_{22} & s_{23} & s_{24} \\ s_{31} & s_{32} & s_{33} & s_{34} \\ s_{41} & s_{42} & s_{43} & s_{44} \end{bmatrix} \begin{bmatrix} \delta P_1 \\ \delta P_2 \\ \delta P_3 \\ 0 \end{bmatrix}. \quad (\text{A.19})$$

Starting with the third line of (A.19), we obtain

$$0 = s_{31}\delta P_1 + s_{32}\delta P_2 + s_{33}\delta P_3, \quad (\text{A.20})$$

$$\delta P_3 = \frac{-s_{31}}{s_{33}}\delta P_1 + \frac{-s_{32}}{s_{33}}\delta P_2, \quad (\text{A.21})$$

$$\delta P_3 = f_{31}\delta P_1 + f_{32}\delta P_2. \quad (\text{A.22})$$

Inserting now (A.22) in the second line of (A.19), we obtain

$$0 = s_{21}\delta P_1 + s_{22}\delta P_2 + s_{23}\delta P_3, \quad (\text{A.23})$$

$$0 = s_{21}\delta P_1 + s_{22}\delta P_2 + s_{23}(f_{31}\delta P_1 + f_{32}\delta P_2), \quad (\text{A.24})$$

$$0 = (s_{21} + s_{23}f_{31})\delta P_1 + (s_{22} + s_{23}f_{32})\delta P_2, \quad (\text{A.25})$$

$$\delta P_2 = \frac{-s_{21} - s_{23}f_{31}}{s_{22} + s_{23}f_{32}}\delta P_1, \quad (\text{A.26})$$

$$\delta P_2 = f_{21}\delta P_1. \quad (\text{A.27})$$

This can now be inserted into (A.22)

$$\delta P_3 = f_{31}\delta P_1 + f_{32}\delta P_2, \quad (\text{A.28})$$

$$\delta P_3 = (f_{31} + f_{32}f_{21})\delta P_1, \quad (\text{A.29})$$

which gives for the first line of (A.19)

$$\delta H_1 = s_{11}\delta P_1 + s_{12}\delta P_2 + s_{13}\delta P_3, \quad (\text{A.30})$$

$$\delta H_1 = s_{11}\delta P_1 + s_{12}f_{21}\delta P_1 + s_{13}(f_{31} + f_{32}f_{21})\delta P_1, \quad (\text{A.31})$$

$$\delta H_1 = (s_{11} + s_{12}f_{21} + s_{13}(f_{31} + f_{32}f_{21}))\delta P_1. \quad (\text{A.32})$$

Here we use

$$\delta H_1 = \frac{1}{E_1}\delta P_1 \quad (\text{A.33})$$

to determine the Young's modulus.

In order to derive the Poisson's ratio, we need to consider the last equation of (A.19) and insert all previous results:

$$\delta H_4 = s_{41}\delta P_1 + s_{42}\delta P_2 + s_{43}\delta P_3, \quad (\text{A.34})$$

$$\delta H_4 = (s_{41} + s_{42}f_{21} + s_{43}(f_{31} + f_{32}f_{21}))\delta P_1, \quad (\text{A.35})$$

$$\delta H_4 = \frac{s_{41} + s_{42}f_{21} + s_{43}(f_{31} + f_{32}f_{21})}{s_{11} + s_{12}f_{21} + s_{13}(f_{31} + f_{32}f_{21})}\delta H_1. \quad (\text{A.36})$$

Again we use the relationship

$$\delta H_4 = -\nu_{14}\delta H_1 \quad (\text{A.37})$$

to determine the Poisson's ratio. Other properties are obtained again in a similar fashion by exchanging the indices.

For the derivation of the linearized modulus of constrained motion in one direction, we need a relation between  $\delta P_i$  and  $\delta H_i$  from

$$\begin{bmatrix} \delta H_1 \\ 0 \\ 0 \\ 0 \end{bmatrix} = \begin{bmatrix} s_{11} & s_{12} & s_{13} & s_{14} \\ s_{21} & s_{22} & s_{23} & s_{24} \\ s_{31} & s_{32} & s_{33} & s_{34} \\ s_{41} & s_{42} & s_{43} & s_{44} \end{bmatrix} \begin{bmatrix} \delta P_1 \\ \delta P_2 \\ \delta P_3 \\ \delta P_4 \end{bmatrix}. \quad (\text{A.38})$$

Using the last line of (A.38), we get

$$0 = s_{41}\delta P_1 + s_{42}\delta P_2 + s_{43}\delta P_3 + s_{44}\delta P_4, \quad (\text{A.39})$$

$$\delta P_4 = -\frac{s_{41}}{s_{44}}\delta P_1 - \frac{s_{42}}{s_{44}}\delta P_2 - \frac{s_{43}}{s_{44}}\delta P_3, \quad (\text{A.40})$$

$$\delta P_4 = f_{41}\delta P_1 + f_{42}\delta P_2 + f_{43}\delta P_3. \quad (\text{A.41})$$

Now putting (A.41) into the third line of (A.38) results in

$$0 = s_{31}\delta P_1 + s_{32}\delta P_2 + s_{33}\delta P_3 + s_{34}\delta P_4, \quad (\text{A.42})$$

$$0 = s_{31}\delta P_1 + s_{32}\delta P_2 + s_{33}\delta P_3 + s_{34}(f_{41}\delta P_1 + f_{42}\delta P_2 + f_{43}\delta P_3), \quad (\text{A.43})$$

$$(s_{33} + s_{34}f_{43})\delta P_3 = (-s_{31} - s_{34}f_{41})\delta P_1 + (-s_{32} - s_{34}f_{42})\delta P_2, \quad (\text{A.44})$$

$$\delta P_3 = \frac{-s_{31} - s_{34}f_{41}}{s_{33} + s_{34}f_{43}}\delta P_1 + \frac{-s_{32} - s_{34}f_{42}}{s_{33} + s_{34}f_{43}}\delta P_2, \quad (\text{A.45})$$

$$\delta P_3 = f_{31}\delta P_1 + f_{32}\delta P_2. \quad (\text{A.46})$$

Inserting this back into (A.41) gives

$$\delta P_4 = f_{41}\delta P_1 + f_{42}\delta P_2 + f_{43}(f_{31}\delta P_1 + f_{32}\delta P_2), \quad (\text{A.47})$$

$$\delta P_4 = (f_{41} + f_{43}f_{31})\delta P_1 + (f_{42} + f_{43}f_{32})\delta P_2. \quad (\text{A.48})$$

Now (A.46) and (A.48) can be inserted into the second row of (A.38) giving:

$$0 = s_{21}\delta P_1 + s_{22}\delta P_2 + s_{23}\delta P_3 + s_{24}\delta P_4, \quad (\text{A.49})$$

$$\begin{aligned} 0 = s_{21}\delta P_1 + s_{22}\delta P_2 + s_{23}(f_{31}\delta P_1 + f_{32}\delta P_2) \\ + s_{24}((f_{41} + f_{43}f_{31})\delta P_1 + (f_{42} + f_{43}f_{32}))\delta P_2, \end{aligned} \quad (\text{A.50})$$

$$\begin{aligned} (s_{22} + s_{23}f_{32} + s_{24}(f_{42} + f_{43}f_{32}))\delta P_2 = \\ (-s_{21} - s_{23}f_{31} - s_{24}(f_{41} + f_{43}f_{31}))\delta P_1, \end{aligned} \quad (\text{A.51})$$

$$\delta P_2 = \frac{-s_{21} - s_{23}f_{31} - s_{24}(f_{41} + f_{43}f_{31})}{s_{22} + s_{23}f_{32} + s_{24}(f_{42} + f_{43}f_{32})} \delta P_1, \quad (\text{A.52})$$

$$\delta P_2 = f_{21}\delta P_1. \quad (\text{A.53})$$

Again this can be inserted back into (A.46) and (A.48):

$$\delta P_3 = (f_{31} + f_{32}f_{21})\delta P_1, \quad (\text{A.54})$$

$$\delta P_4 = (f_{41} + f_{43}f_{31} + (f_{42} + f_{43}f_{32})f_{21})\delta P_1. \quad (\text{A.55})$$

Finally, (A.53), (A.54), and (A.55) are inserted back into (A.38) to give

$$\begin{aligned} \delta H_1 = & (s_{11} + s_{12}f_{21} + s_{13}(f_{31} + f_{32}f_{21}) \\ & + s_{14}(f_{41} + f_{43}f_{31} + (f_{42} + f_{43}f_{32})f_{21}))\delta P_1. \end{aligned} \quad (\text{A.56})$$

Now by comparing this to

$$\delta H_1 = \frac{1}{M_1} \delta P_1 \quad (\text{A.57})$$

we can calculate the constrained modulus.

The other constrained modulus as well as the shear moduli are obtained in the same fashion.

## REFERENCES

[Gib<sup>&al</sup>97] L. J. Gibson et al. 'The mechanics of two-dimensional cellular materials'. *Proc. R. Soc. Lond., A. Math. Phys. Sci.* **382** (1997), pp. 25–42.





# B

## **EFFICACY OF AUXETICS IN PHYSICAL IMPACT SIMULATIONS**

---

this appendix corresponds to Chapter 5

## B.1. CONSTRUCTION DRAWINGS

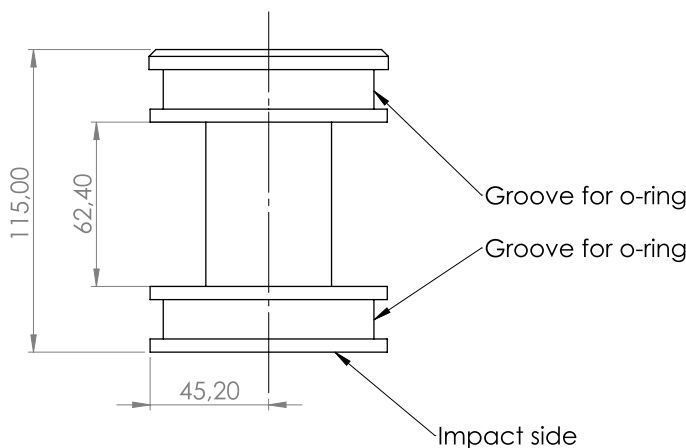


Figure B.1.: Plunger with main dimensions in mm.

B

## B.2. EXPERIMENTAL AND NUMERICAL COMPARISONS

— ARH90 experiments	— CHW experiments	— CHL experiments
- - - ARH90 continuum FE	- - - CHW continuum FE	- - - CHL continuum FE
.... ARH90 beam FE	.... CHW beam FE	.... CHL beam FE

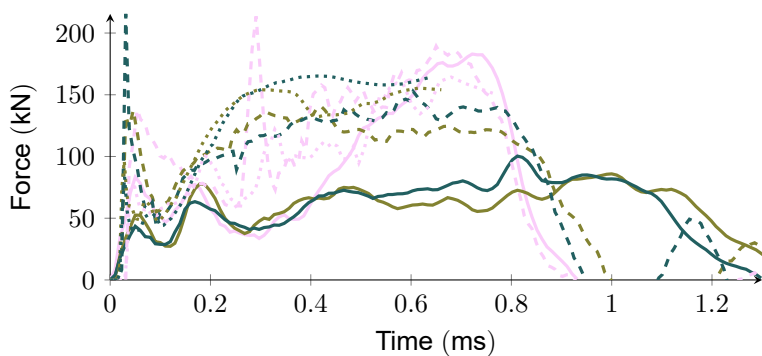


Figure B.2.: Comparison of experimental and numerical results for the SS configuration.

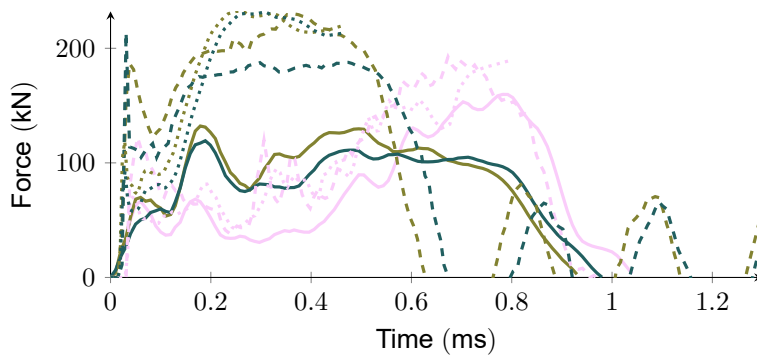


Figure B.3.: Comparison of experimental and numerical results for the SM configuration.

**B**

### B.3. STRUCTURAL SAMPLES COMPARISONS

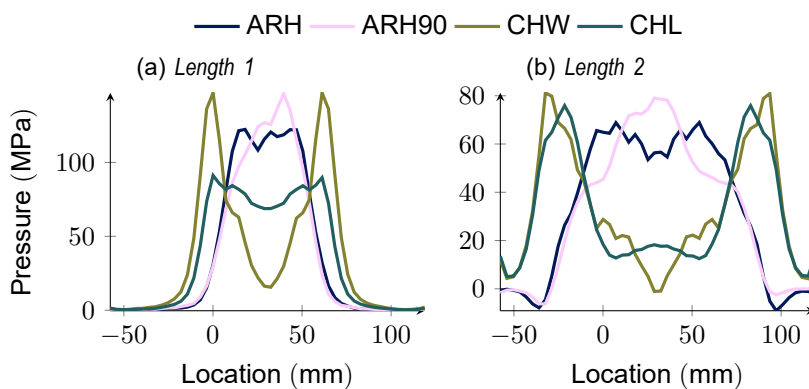


Figure B.4.: Comparison of the average pressure over the back-face for the SM configuration using the continuum-based model.

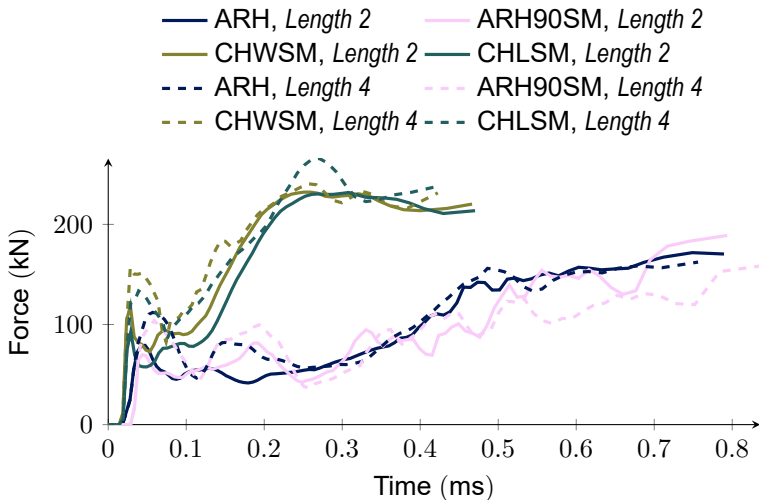


Figure B.5.: Comparison of wider samples for the SM configuration using the beam-based model.

B

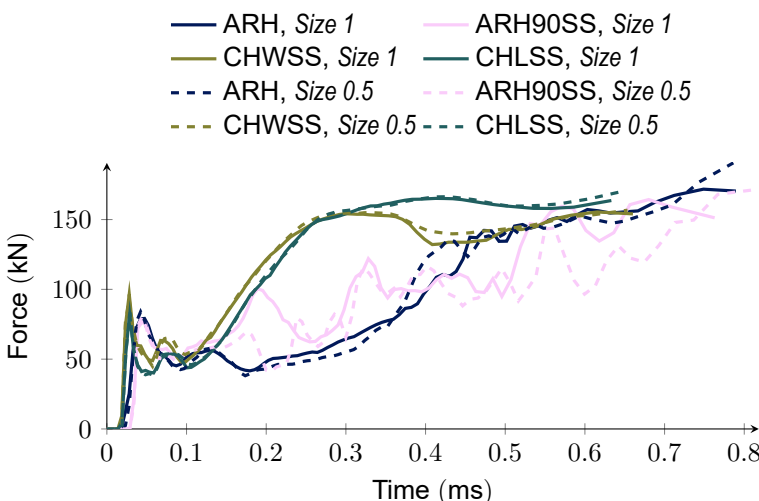


Figure B.6.: Comparison of smaller unit cells for the SS configuration of Length 2 using the beam-based model.

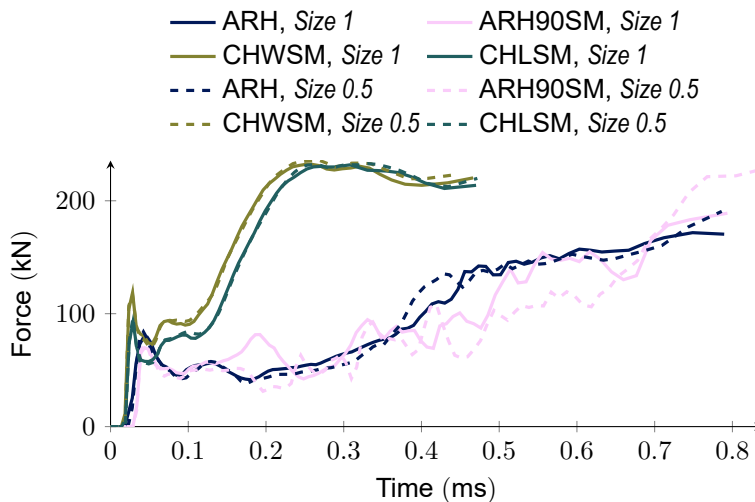


Figure B.7.: Comparison of smaller unit cells for the SM configuration using the beam-based model.

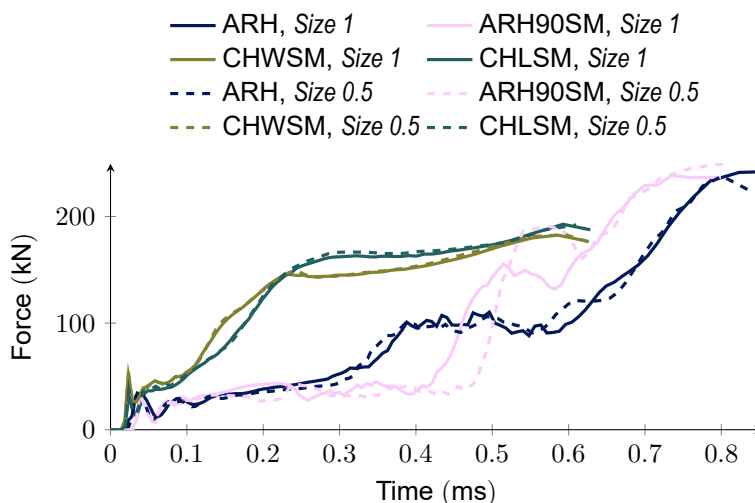


Figure B.8.: Comparison of smaller unit cells for the SM configuration *Length 1* using the beam-based model.

## B.4. DEFORMATION PATTERNS AT DIFFERENT SPEEDS

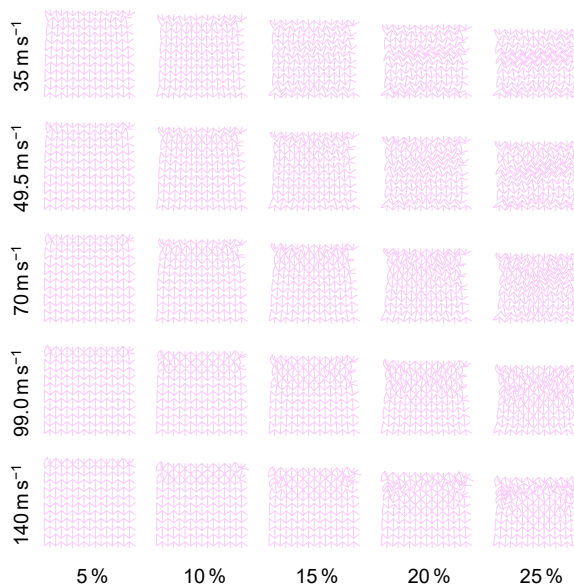


Figure B.9.: Deformation patterns of the ARH90 SM sample of *Length 1* at different impact velocities and compression states.

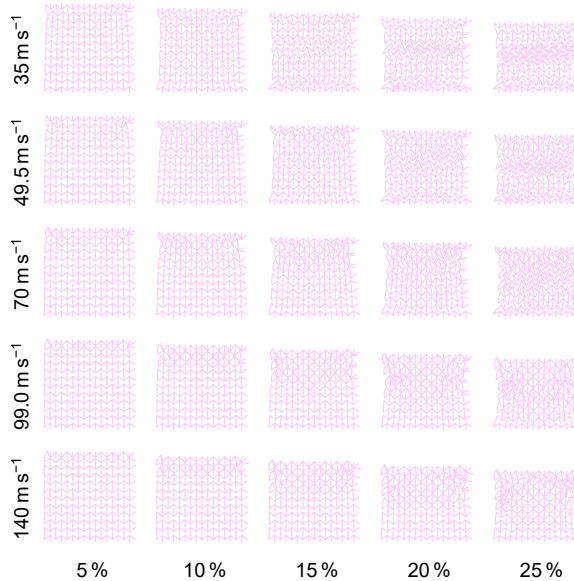
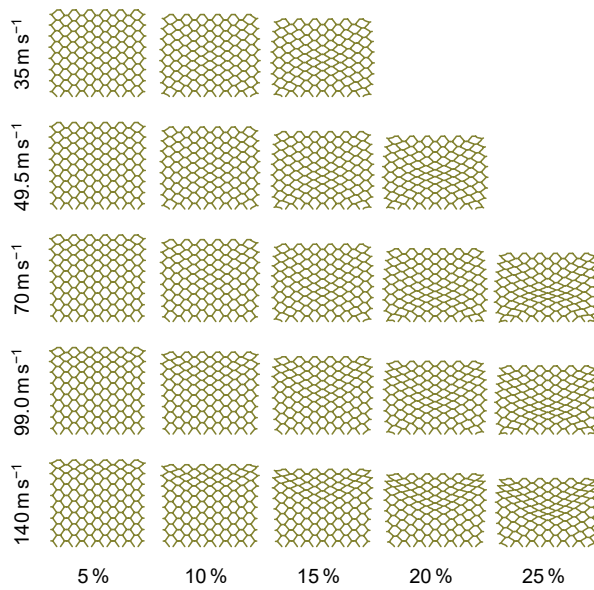


Figure B.10.: Deformation patterns of the ARH90 SS sample of *Length 1* at different impact velocities and compression states.



B

Figure B.11.: Deformation patterns of the CHW SM sample of *Length 1* at different impact velocities and compression states.

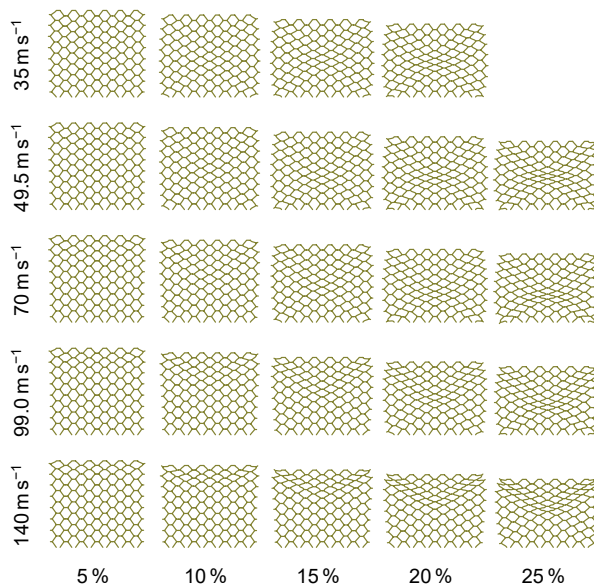


Figure B.12.: Deformation patterns of the CHW SS sample of *Length 1* at different impact velocities and compression states.

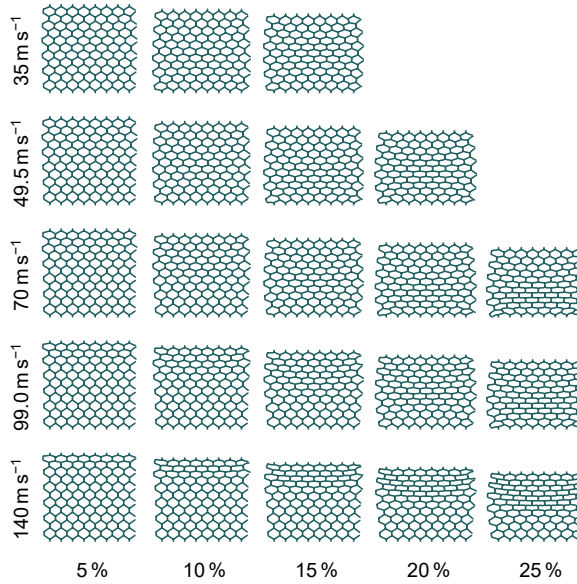


Figure B.13.: Deformation patterns of the CHL SM sample of *Length 1* at different impact velocities and compression states.

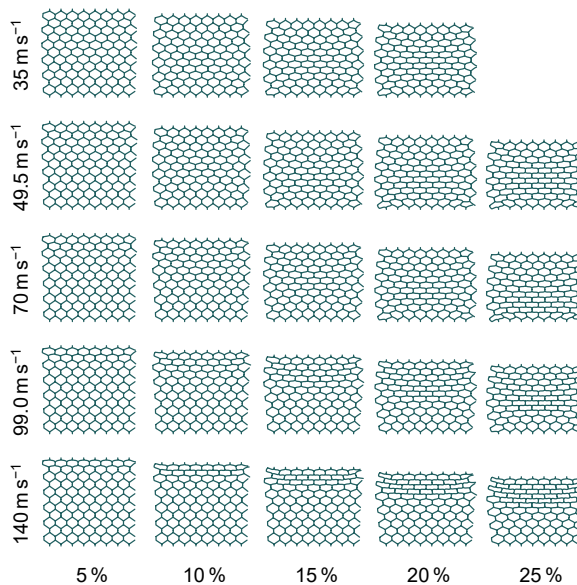


Figure B.14.: Deformation patterns of the CHL SS sample of *Length 1* at different impact velocities and compression states.

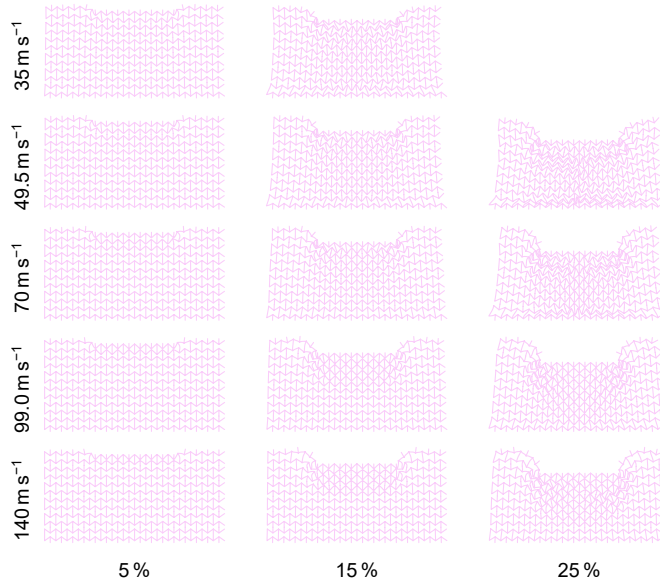


Figure B.15.: Deformation patterns of the ARH90 SM sample of *Length 2* at different impact velocities and compression states.

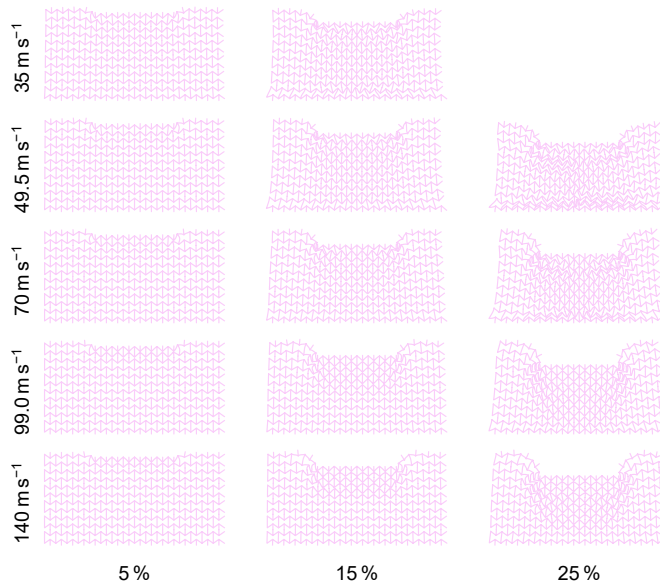


Figure B.16.: Deformation patterns of the ARH90 SS sample of *Length 2* at different impact velocities and compression states.

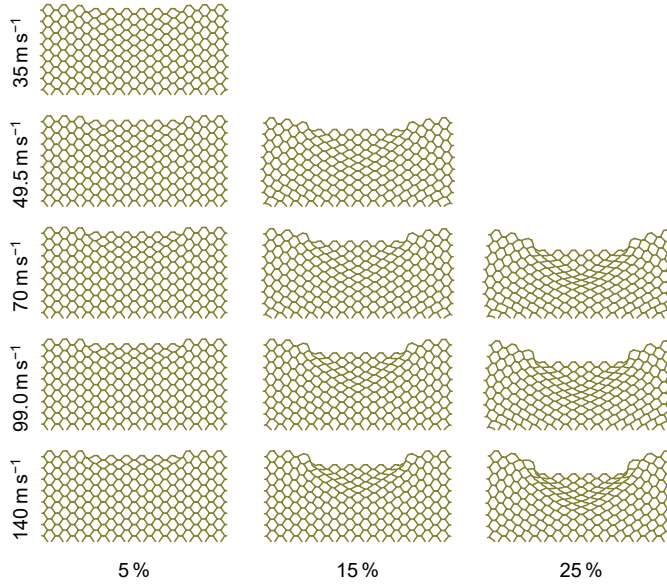


Figure B.17.: Deformation patterns of the CHW SM sample of *Length 2* at different impact velocities and compression states.

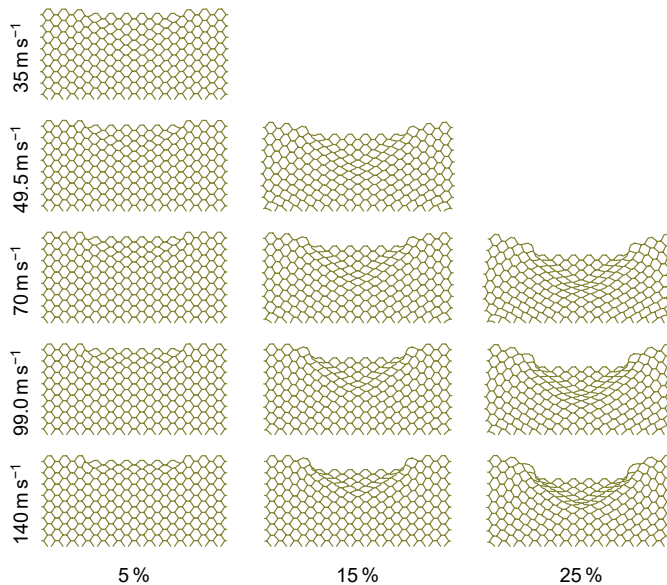


Figure B.18.: Deformation patterns of the CHW SS sample of *Length 2* at different impact velocities and compression states.

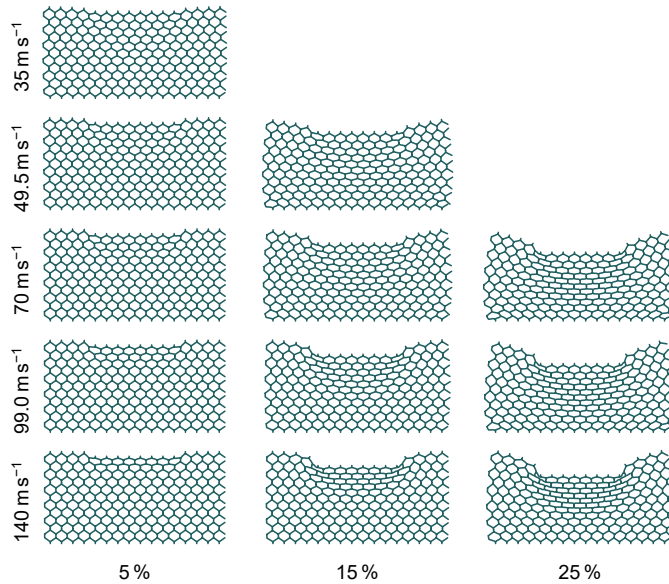


Figure B.19.: Deformation patterns of the CHL SM sample of *Length 2* at different impact velocities and compression states.

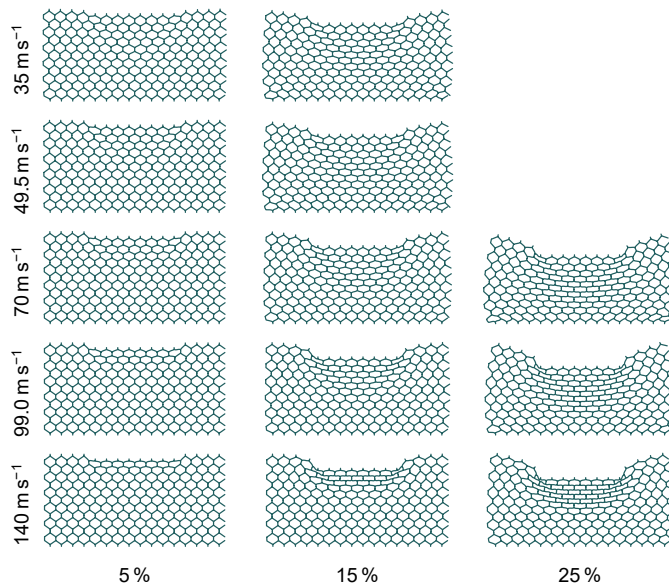
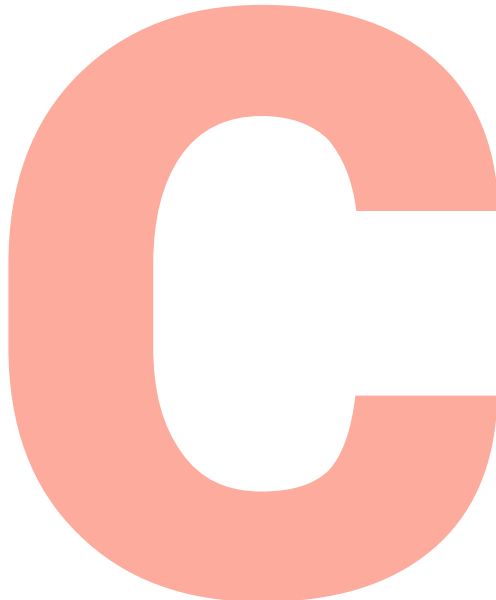


Figure B.20.: Deformation patterns of the CHL SS sample of *Length 2* at different impact velocities and compression states.







# **INELASTIC BEHAVIOUR UNDER DIFFERENT STRAIN RATE REGIMES**

---

this appendix corresponds to Chapter 6

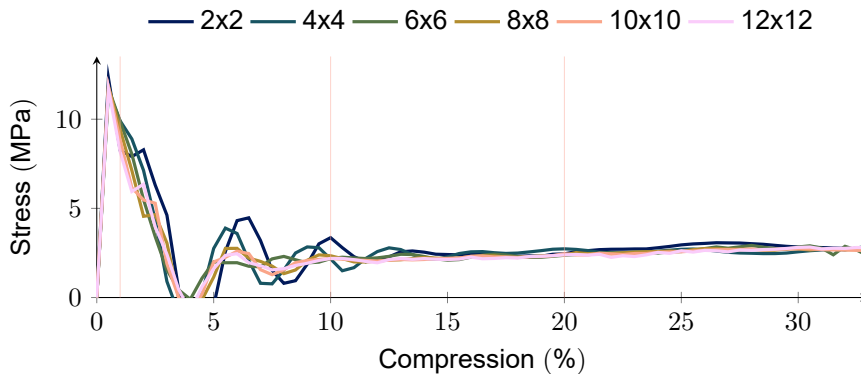
**c.1. ADDITIONAL NUMBER OF UNIT CELLS PLOTS****c.1.1. RE-ENTRANT UNIT CELLS**

Figure C.1.: Stress-strain curves of patches with a different number of re-entrant unit cells under slow rate compression.

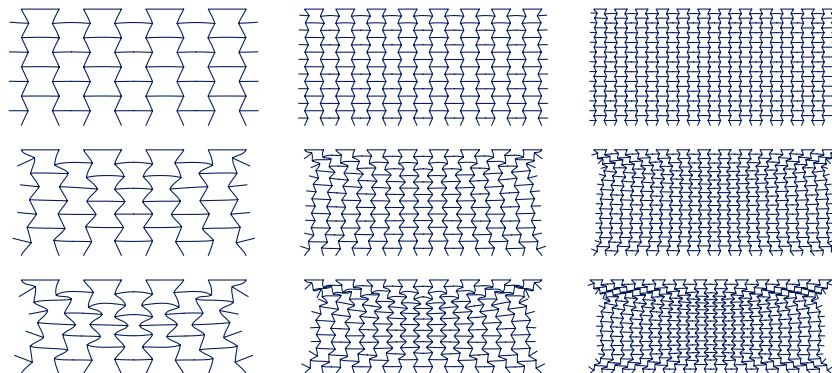


Figure C.2.: Re-entrant  $4 \times 4$  (left),  $8 \times 8$  (centre), and  $12 \times 12$  (right) unit cell patches under slow rate deformation at 1%, 10 % and 20 % compression.

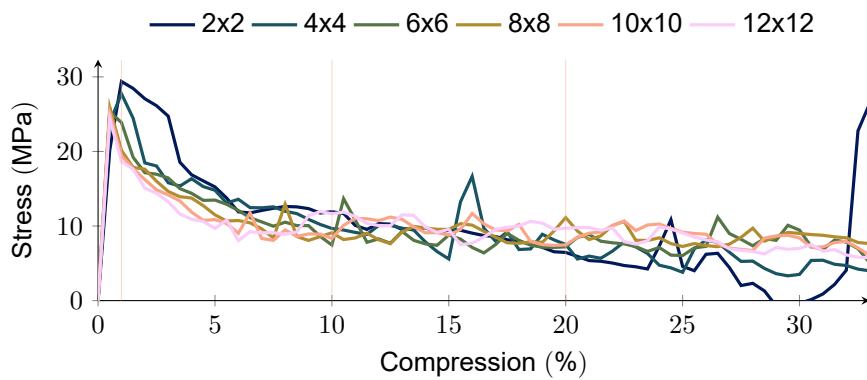


Figure C.3.: Stress-strain curves of patches with a different number of re-entrant unit cells under *medium* rate compression.

C

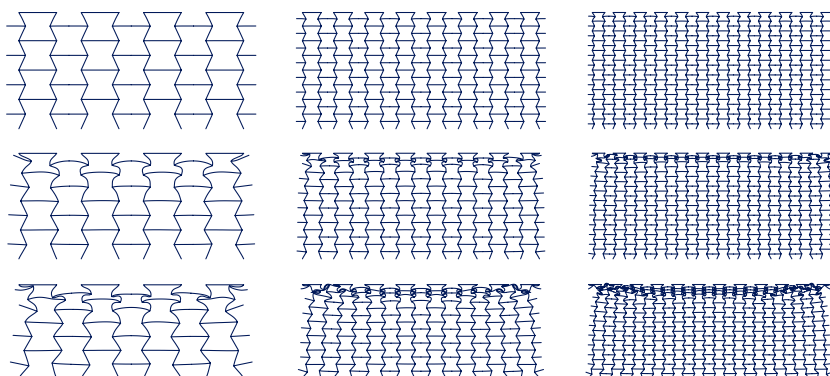


Figure C.4.: Re-entrant  $4 \times 4$  (left),  $8 \times 8$  (centre), and  $12 \times 12$  (right) unit cell patches under *medium* rate deformation at 1 %, 10 % and 20 % compression.

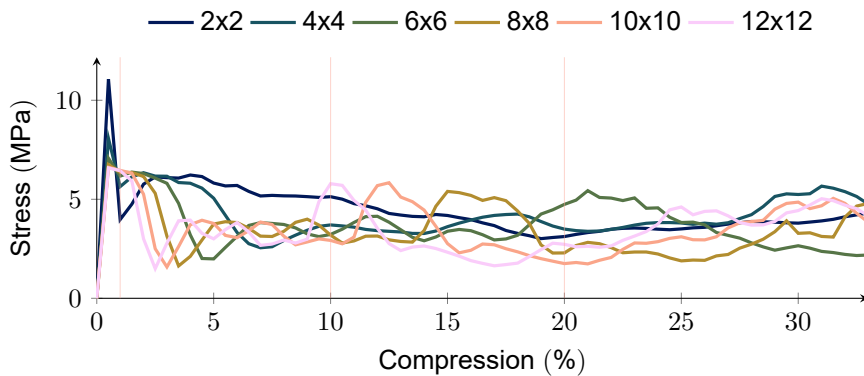
**c.1.2. CHIRAL UNIT CELLS**

Figure C.5.: Stress-strain curves of patches with a different number of chiral unit cells under *slow rate* compression.

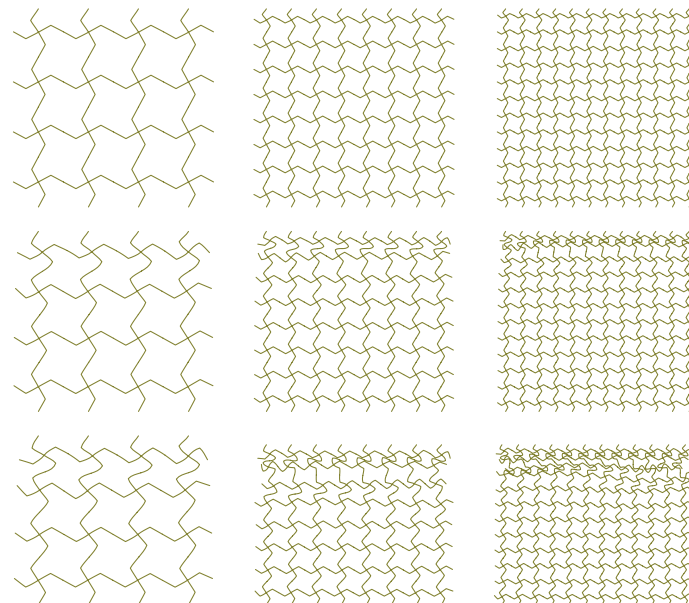


Figure C.6.: Chiral  $4 \times 4$  (left),  $8 \times 8$  (centre), and  $12 \times 12$  (right) unit cell patches under *slow rate* deformation at 1%, 10% and 20% compression.

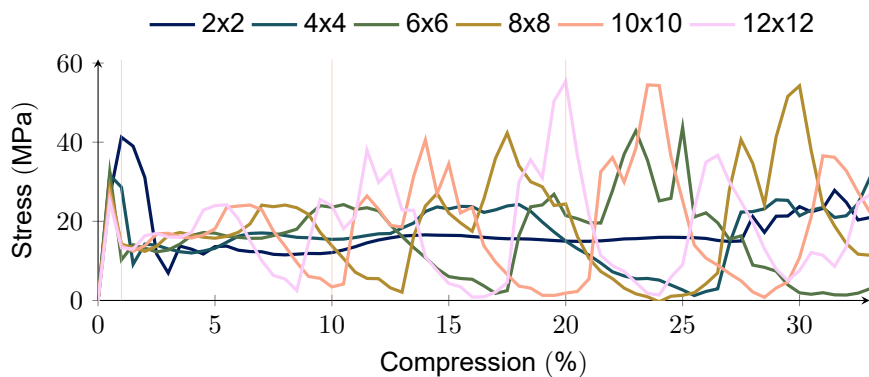


Figure C.7.: Stress-strain curves of patches with a different number of chiral unit cells under *medium* rate compression.

C

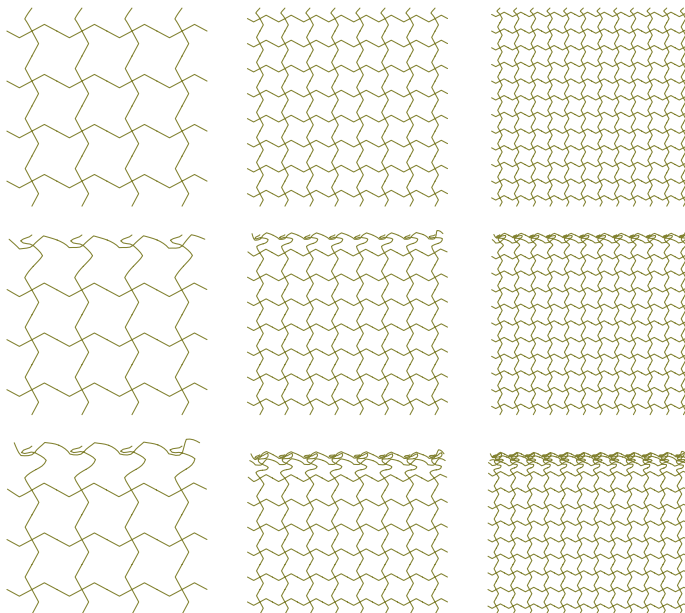


Figure C.8.: Chiral  $4 \times 4$  (left),  $8 \times 8$  (centre), and  $12 \times 12$  (right) unit cell patches under *medium* rate deformation at 1 %, 10 % and 20 % compression.

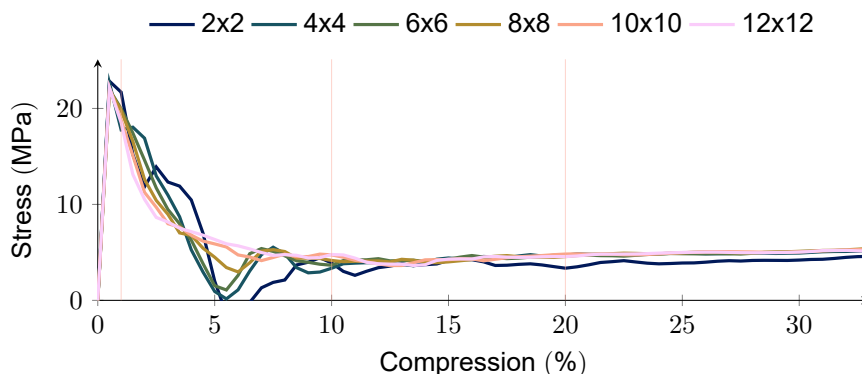
**c.1.3. HONEYCOMB UNIT CELLS**

Figure C.9.: Stress-strain curves of patches with a different number of honeycombs unit cells under slow rate compression.

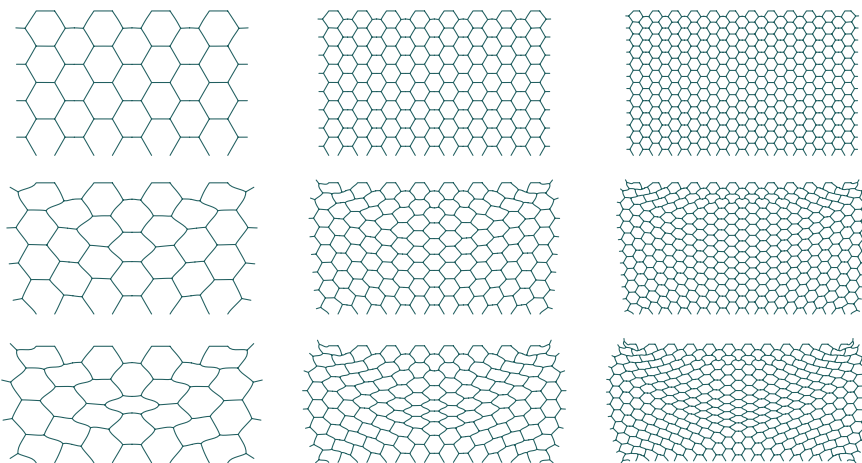


Figure C.10.: 4 × 4 (left), 8 × 8 (centre), and 12 × 12 (right) unit cell patches under slow rate deformation at 1 %, 10 % and 20 % compression.

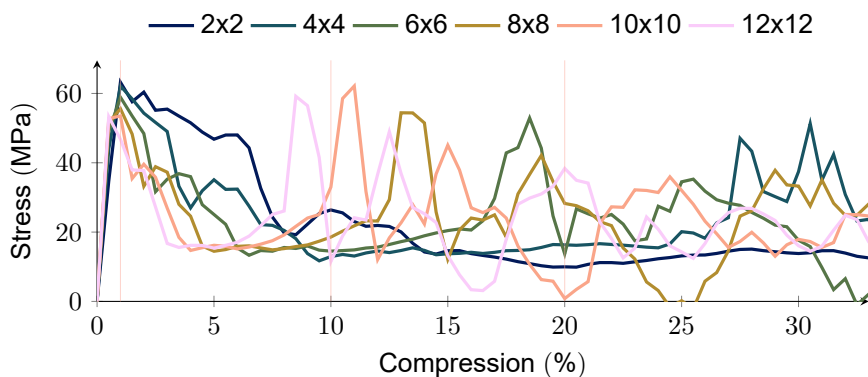


Figure C.11.: Stress-strain curves of patches with a different number of honeycombs unit cells under *medium* rate compression.

C

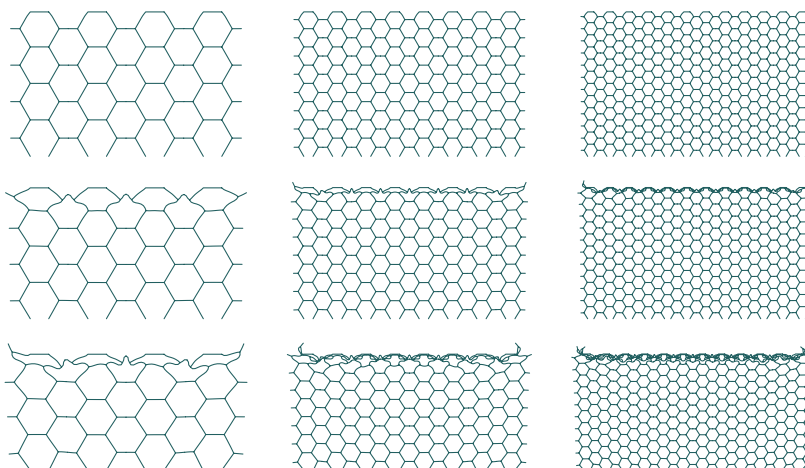


Figure C.12.:  $4 \times 4$  (left),  $8 \times 8$  (centre), and  $12 \times 12$  (right) unit cell patches under *medium* rate deformation at 1 %, 10 % and 20 % compression.

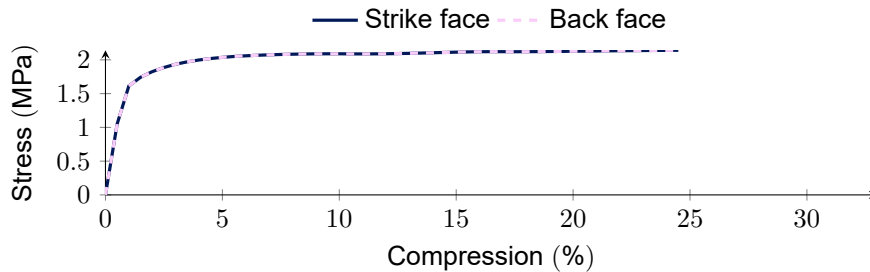
**c.2. ADDITIONAL STRAIN RATE PLOTS****c.2.1. RE-ENTRANT PATCH**

Figure C.13.: Comparison of the stress on the strike face and the back face under static compression for an  $8 \times 8$  re-entrant patch.

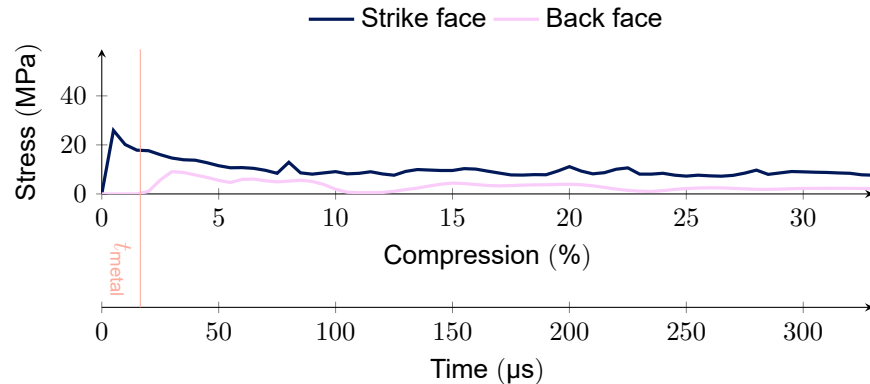


Figure C.14.: Comparison of the stress on the strike face and the back face under medium compression for an  $8 \times 8$  re-entrant patch.

### c.2.2. CHIRAL PATCH

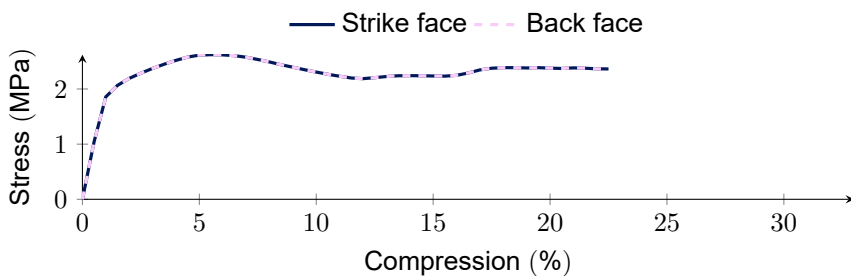


Figure C.15.: Comparison of the stress on the strike face and the back face under *static* compression for an  $8 \times 8$  chiral patch.

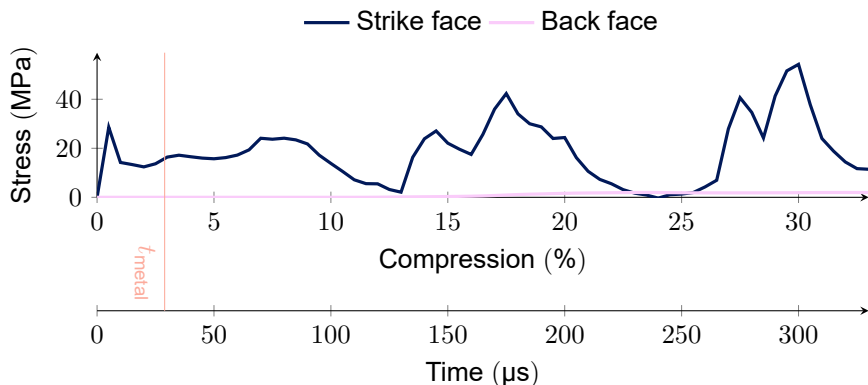


Figure C.16.: Comparison of the stress on the strike face and the back face under *medium* compression for an  $8 \times 8$  chiral patch.

For the chiral patch, the time needed for a pressure stress wave to travel through the metal is computed from the height of the patch  $h = 132$  mm and the angle between the beams and the vertical of  $\alpha = 28.1^\circ$ :

$$t_{\text{metal}} = \frac{h / \cos(\alpha)}{c_{\text{metal}}} \approx 28.9 \mu\text{s.} \quad (\text{C.1})$$

### c.2.3. HONEYCOMB PATCH

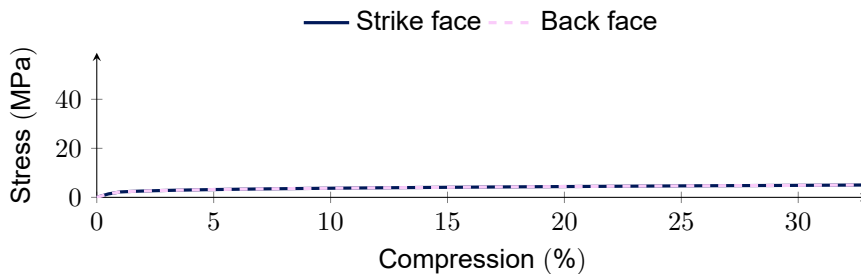


Figure C.17.: Comparison of the stress on the strike face and the back face under static compression for an  $8 \times 8$  honeycomb patch.

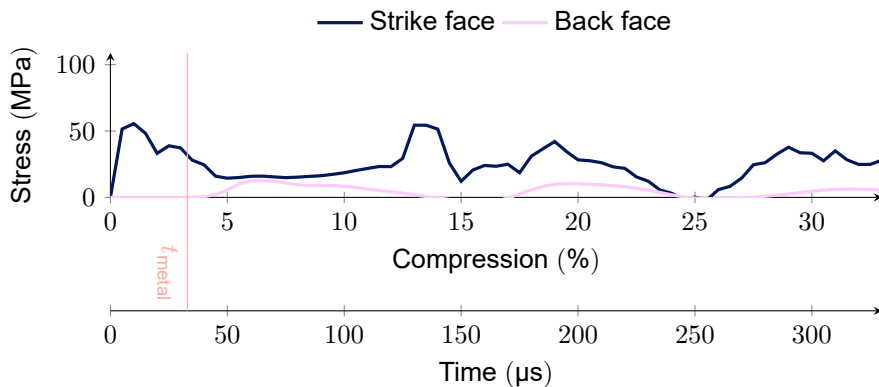


Figure C.18.: Comparison of the stress on the strike face and the back face under medium compression for an  $8 \times 8$  honeycomb patch.

For the honeycomb patch, the time needed for a pressure stress wave to travel through the metal is computed from the height of the patch  $h = 148$  mm and the angle between the beams and the vertical of  $\alpha = 29.7^\circ$ :

$$t_{\text{metal}} = \frac{h / \cos(\alpha)}{c_{\text{metal}}} \approx 32.9 \mu\text{s.} \quad (\text{C.2})$$



# ACKNOWLEDGEMENTS

*He travels fastest who goes alone,  
He travels farthest who pulls with his team.*

Cyrus H. McCormick

Although only one name appears on the title page of this booklet, I was fortunate enough to be part of a team that pulled together throughout my journey.

Allereerst is er mijn supervisieteam. Ik ben zeer dankbaar voor jullie open deuren, waar ik meermalen gebruik heb van gemaakt – wellicht zelfs te vaak. Jullie hebben me echter altijd aangemoedigd om terug te komen, vragen te stellen en fouten te maken, en dit heeft me uiteindelijk geholpen om de belangrijkste kennis te vergaren. Tijdens een marathon is het niet alleen een kwestie van de ene voet voor de andere zetten; je hebt ook voldoende voeding nodig tijdens de race. Jullie zijn een groot deel van de voeding geweest die me op de been hield. Voor dit alles ben ik jullie enorm dankbaar.

In addition to my supervisory team, there is a list of names on page iv of this booklet of the independent members of the committee who assessed my research work from the past years. I would like to thank you all for your availability and willingness to take part in this rite of passage.

Naast de universiteit heb ik ook samengewerkt met TNO. Mijn dissertatie was onderdeel van een groter project van de *Advanced Materials* groep, waar ik met plezier onderdeel van ben geweest. Het was meer dan een stukje papier – getekend na gesteggel van de juridische afdelingen – dat mij met de groep verbond: ik heb enorm genoten van de gezelligheid bij koffiemachine en de teamuitjes. Daarnaast heeft de groep het voor mij mogelijk gemaakt mezelf te kunnen verbreden naar een toegepaste onderzoeker en heeft TNO daarmee een grote bijdrage geleverd aan dit proefschrift – in het bijzonder aan Hoofdstuk 5. Ik bedank de groep daarom graag voor het verwelkomen van mij als volwaardig lid van de groep en de geslaagde samenwerking.

Al mijn werk is mogelijk gemaakt door de inzet en vriendelijkheid van het secretariaat van de afdeling; mijn tijd aan de afdeling is door hen aanzienlijk verlicht. Jullie waren een enorme hulp in de strijd tegen de bureaucratie van de universiteit. Dankzij jullie heb ik mijn verstand kunnen behouden.

Neben meiner akademischen Laufbahn möchte ich auch meine Zeit bei Bosch nicht unerwähnt lassen. In den drei Abteilungen, in denen ich die Entwicklung elektrischer Maschinen begleiten durfte, habe ich Erfahrungen gesammelt, die mich – und damit auch diese Dissertation – geprägt haben. Für diese Erfahrungen und die Kontakte, die ich dabei knüpfen konnte, bin ich enorm dankbar.

Het leven in Nederland is meer dan alleen werken. Het is ook wonen, waarvoor ik graag mijn buren wil bedanken. Jullie tijd en onze gesprekken, een korte ontmoeting in de gang op weg naar de wasmachine, bier en wijn op het balkon, of gewoon een kaartspel of een film kijken; dit alles heeft me een gevoel van thuis gegeven dat ik niet had verwacht te vinden in een vreemd land met een vreemde taal.

University is about more than just science; it is also a community of people bound together by common aspirations. Throughout my education, I have been part of different communities, and I would like to thank everyone I have encountered during my studies. Over the last four and a half years, I had the privilege of being part of an inspirational research group. Although I rarely attended conferences with any of you, the times we played board games or went into the city were great fun. My time on the PhD council was enlightening, helping me to understand the usually opaque workings of the university's administrative apparatus. It also gave me the chance to meet amazing people from other disciplines. Thank you all for the good times! A large part of my sanity was preserved by playing tennis and reading books. I would like to thank not only the few players who stuck around for as long as me, but also everyone else I met throughout my sporting endeavours.

All dies wäre ohne die Freunde in Deutschland und auf der ganzen Welt nicht möglich gewesen. Zunächst sind da diejenigen, die mich während meines Studiums in Darmstadt und Blacksburg begleitet haben. Sie haben nicht nur diese Zeit, sondern auch mein Leben bereichert und tun dies noch immer. Neben den Freunden aus meinem Studium muss ich mich insbesondere bei allen bedanken, die ich während meiner Schulzeit kennengelernt habe und die den Kontakt zu mir gehalten haben. Neben den Erfahrungen, die ich in den letzten drei Jahren meiner Schulzeit machen durfte, waren sie mir eine enorme Hilfe auf meinem Weg. Die regelmäßigen virtuellen Skatrunden, die zahlreichen Telefonate und die wechselseitigen Besuche gaben mir einen Halt, den ich manchmal mehr gebraucht habe, als ich mir eingestehen wollte. Ich bin sicher, dass sich unsere Wege auch in Zukunft immer wieder kreuzen werden und wir gute Freunde bleiben werden, selbst wenn Jahre und Länder uns trennen.

Schließlich und vor allem möchte ich mich bei meiner Familie bedanken. Ich hoffe, ihr erkennt euch in diesem Büchlein wieder. Für manche ist das vielleicht einfacher als für andere: Manche finden ihren Anteil auf dem Umschlag, manche auf der ersten Seite, manche auf der letzten Seite und manche erst in diesem Satz. Seid euch aber sicher: Ohne euren Einfluss während meiner Entwicklung wäre ich nicht hier. Ich hätte nicht die Neugier und das Durchhaltevermögen, die es braucht, um dieses Buch zu schreiben und zu verteidigen. Auch wenn ich durch schwierige Zeiten gehen musste, wart ihr mit Rat und Tat an meiner Seite und habt mir all die Unterstützung gegeben, von der ich nur träumen konnte. Ich hoffe, ich kann euch zumindest ein wenig von dem zurückgeben, was ihr mir gegeben habt.

# CONTRIBUTIONS

## JOURNAL ARTICLES

5. T. Gärtner, S. J. van den Boom, J. Weerheijm and L. J. Sluys. 'Force transmission and dissipation in dynamic compression of architected metamaterials'. *engrXiv* (2025). Preprint
4. T. Gärtner, R. Dekker, D. van Veen, S. J. van den Boom and L. Amaral. '(In)efficacy of auxetic metamaterials for impact mitigation'. *Int. J. Impact Eng.* **206**, 105402 (2025)
3. T. Gärtner, S. J. van den Boom, J. Weerheijm and L. J. Sluys. 'A strategy for scaling the hardening behavior in finite element modelling of geometrically exact beams'. *Comput. Mech.* **75** (2025), pp. 1471–1482
2. T. Gärtner, S. J. van den Boom, J. Weerheijm and L. J. Sluys. 'Geometric effects on impact mitigation in architected auxetic metamaterials'. *Mech. Mater.* **191**, 104952 (2024)
1. T. Gärtner, M. Fernández and O. Weeger. 'Nonlinear multiscale simulation of elastic beam lattices with anisotropic homogenized constitutive models based on artificial neural networks'. *Comput. Mech.* **68** (2021), pp. 1111–1130

## RESEARCH SOFTWARE

1. T. Gärtner and F. P. van der Meer. *dynLattice: A finite element environment for dynamic simulation of beam networks and lattice metamaterials*. Version 1.11. 13th Aug. 2025

## CONFERENCE PRESENTATIONS

8. T. Gärtner, S. J. van den Boom, J. Weerheijm and L. J. Sluys. *Numerical Investigation into Rate Effects in Architected Metamaterials under Extreme Loading Conditions*. 8th International Conference on Computational Modelling of Fracture and Failure of Materials and Structures (Porto, 4th–6th June 2025). oral presentation
7. T. Gärtner, S. J. van den Boom, J. Weerheijm and L. J. Sluys. *Architectural Choices for Auxetic Metamaterials and their Effects on Impact Mitigation*. 27th Engineering Mechanics Symposium (Arnhem, 22nd–23rd Oct. 2024). invited oral presentation
6. T. Gärtner, L. Amaral, R. Dekker, A. M. Diederens, A. Niessen, D. van Veen and S. J. van den Boom. *(In)Efficacy of Auxetic Metamaterials for Impact Mitigation: Investigations of Energy Absorption and Force Distribution*. 14th International Conference on the Mechanical and Physical Behaviour of Materials under Dynamic Loading (Zürich, 8th–13th Sept. 2024). poster presentation

5. **T. Gärtner**, S. J. van den Boom, J. Weerheijm and L. J. Sluys. *Effects of different architectural choices for auxetic metamaterials on impact mitigation*. 16th World Congress on Computational Mechanics (Vancouver, 21st–26th July 2024). oral presentation
4. **T. Gärtner**, S. J. van den Boom, J. Weerheijm and L. J. Sluys. *Kinematic Hardening and Size Effects in Elastoplastic Nonlinear Timoshenko Beams*. 94th Annual Meeting of the International Association of Applied Mathematics and Mechanics (Magdeburg, 18th–22nd Mar. 2024). oral presentation
3. **T. Gärtner**, S. J. van den Boom, J. Weerheijm and L. J. Sluys. *Effects of Material Architecture in Elastic Impact Mitigation*. 2nd International Conference on Computational Modeling of Complex Materials Across the Scales (Eindhoven, 10th–13th Oct. 2023). poster presentation
2. **T. Gärtner**, S. J. van den Boom, J. Weerheijm and L. J. Sluys. *Architectural Choices for Auxetic Metamaterials and their Effects on Impact Mitigation*. 17th U. S. National Congress on Computational Mechanics (Albuquerque, 23rd–27th July 2023). oral presentation
1. **T. Gärtner**, S. J. van den Boom, J. Weerheijm and L. J. Sluys. *Modelling Impact Behavior of Auxetic Meta-Materials using Geometrically Nonlinear Lattices*. 9th GACM Colloquium on Computational Mechanics (Essen, 21st–23rd Sept. 2022). oral presentation

## SUPERVISED STUDENTS

4. P. van IJzendoorn. *Multiscale Modelling of Lattice Materials: a novel approach using Beam Neural Networks*. MSc Thesis. Technische Universiteit Delft, 29th Nov. 2024
3. A. Alami. *Finite Element Analysis of Structures. Comparing Large and Small-Scale Structures in Linear and Non-linear Behaviour*. BSc Report. Technische Universiteit Delft, 25th June 2024
2. J. Smit. *Stiffness of architected materials*. BSc Report. Technische Universiteit Delft, 24th June 2024
1. A. Niessen. *GNNs and Beam Dynamics. Investigation into the application of Graph Neural Networks to predict the dynamic behaviour of lattice beams*. MSc Thesis. Technische Universiteit Delft, 12th Dec. 2022

## REVIEWS

- Progress in Additive Manufacturing
- Scientific Reports
- Engineering with Computers
- Mechanics of Materials 2x
- Journal of Applied and Computational Mechanics



# CURRICULUM VITAE

## Til GÄRTNER

15. 04. 1996 Born in Hanau, Germany

### EDUCATION

2025	Ph.D. Computational Mechanics Delft University of Technology, The Netherlands
2020	M.Sc. Mechanical and Process Engineering Technical University of Darmstadt, Germany
2017	B.Sc. Mechanical Engineering Virginia Polytechnic Institute and State University, USA
2017	B.Sc. Mechanical and Process Engineering Technical University of Darmstadt, Germany
2014	Abitur Oberstufengymnasium Schloss Hansenberg, Germany

### PROFESSIONAL

2021–2025	Ph.D. Candidate Delft University of Technology, The Netherlands
2021–2025	Visiting Scientist TNO, The Hague, The Netherlands
2021	Student Assistant Technical University of Darmstadt, Germany
2019–2020	Working Student Robert Bosch GmbH, Schwieberdingen, Germany
2017–2018	Computation Engineer Robert Bosch GmbH, Schwieberdingen, Germany